# Transient Thermal Modelling of Cooling Methods in Green Bi-Propellant Thrusters for CubeSat Applications

A numerical and experimental comparison of regenerative cooling and radiation cooling in a CubeSat scale propulsion system.

Peter Martijn van den Berg

**Master thesis report**
Faculty of Aerospace Engineering
Department of Space Engineering

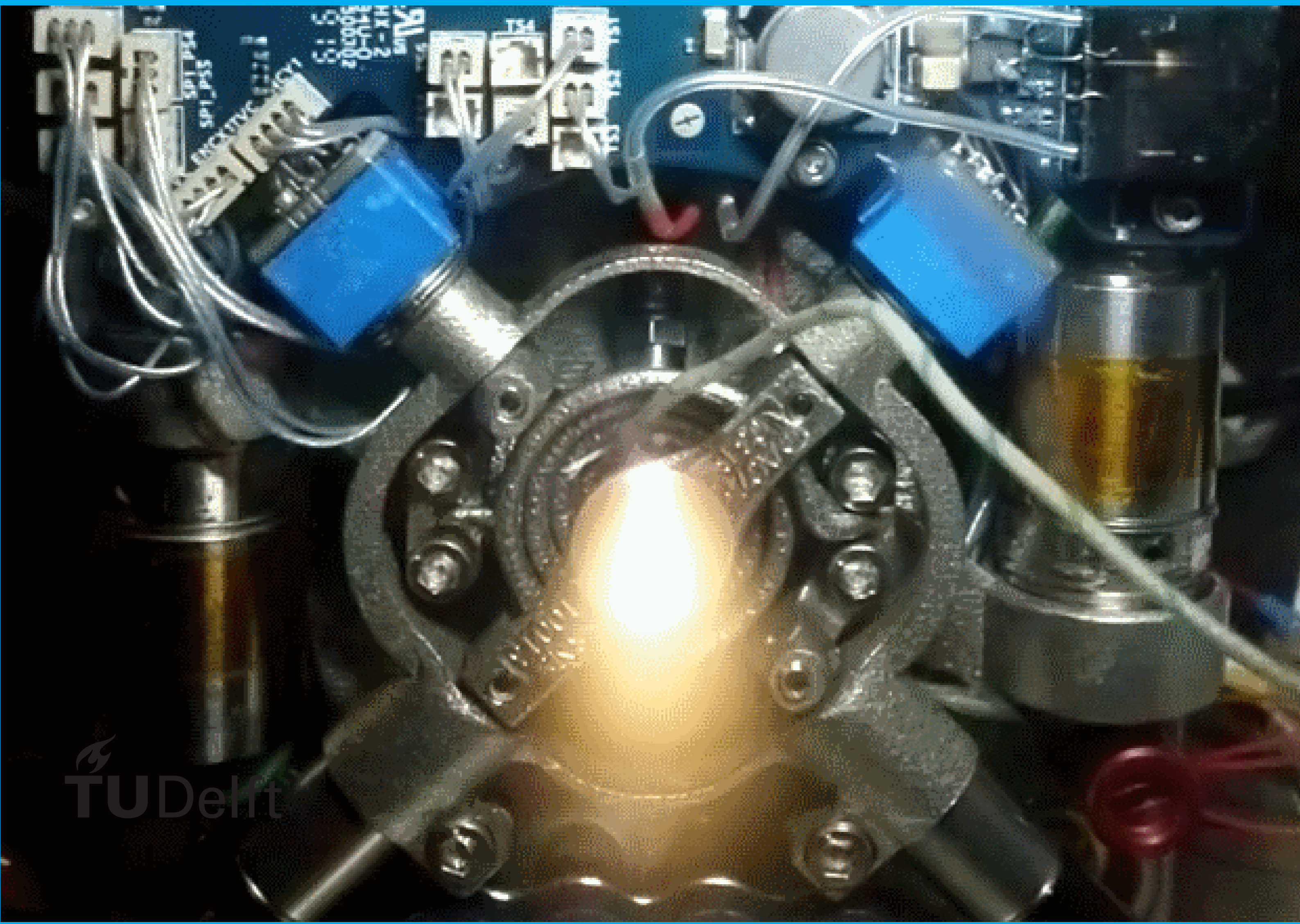

(This page was intentionally left blank)

# Transient Thermal Modelling of Cooling Methods in Green Bi-Propellant Thrusters for CubeSat Applications

## A numerical and experimental comparison of regenerative cooling and radiation cooling in a CubeSat scale propulsion system.

by

Peter Martijn van den Berg

In partial fulfilment of the requirements for the degree of
**Master of Science in Aerospace Engineering**
at the Delft University of Technology,
to be defended publicly on Monday November 30th, 2020 at 10:00 AM.

| | | |
|---|---|---|
| Student number: | 4207696 | |
| Supervisor: | Dr. B.V.S. Jyoti | |
| Thesis committee: | Prof. Dr. E.K.A. Gill | TU Delft |
| | Dr. B.V.S. Jyoti | TU Delft |
| | ir. R. Noomen | TU Delft |
| | R.J.G. Hermsen Msc. | Dawn Aerospace |

*This thesis is confidential and cannot be made public until November 30th, 2022.*

TU Delft

(This page was intentionally left blank)

# Preface

This thesis is the culmination of many years of studying at Delft University of Technology and its completion marks the end of my student life. As such I would like to thank the people who helped me in the realisation of this thesis, as well as those who ensured that my time as a student is a time that I will look back on fondly.

First of all I would like to thank my TU Delft Thesis supervisor Dr. Botchu Jyoti for her guidance and feedback during the whole project. Our bi-weekly meetings helped keep me on track with the project and her positive attitude was motivating.

I would also like to thank the people at Dawn Aerospace, who welcomed me with open arms and allowed me to do my thesis project within the company. In particular I would like to thank Rob Hermsen, who was my supervisor within Dawn Aerospace. He often gave valuable feedback on my project and was not afraid to be critical of my work. I also owe him thanks for helping me with some of the experiments performed during the thesis research. Besides Rob, I also owe thanks to Ralph Huijsman with whom I had many discussions during the early stages of the project regarding the programming of the model presented within this report, Michał Grendysz for his help with some of the experiments performed during this thesis, Jeroen Wink and Tobias Knop for allowing me to do my thesis within their company and for helping me get started up, and Charlie North for helping me out with the production of the research thrusters.

My thanks also go out to the many friends I made during my student time. A special shout out goes out to my friends within Delft Aerospace Rocket Engineering, with whom I worked long days and late nights to design, build, and fire the worlds most powerful student built rocket engine for the Stratos III rocket and with whom I got to experience the record breaking launch of the Stratos II+ rocket. These experiences and many others made my student time truly unforgettable. Another shout out goes out to Stijn Koehler, Angelos Karagiannis, Bas Krijnen, Thomas Haex and Kapeel Samarawickrama, who were doing their thesis at the same time as me and with whom I had occasional but useful discussions about the work performed.

Lastly I would like to thank my family, especially my parents Ben and Marian and my brother Robert, who have always supported me during my studies, even during the few times when things were not going exactly as planned. I couldn't have wished for more support.

Thank you all

*Peter Martijn van den Berg*
*Delft, November 2020*

(This page was intentionally left blank)

# Summary

The Dutch/New Zealand based aerospace company Dawn aerospace has developed a 0.5N green bi-propellant propulsion system for use in CubeSat applications called the PM200. This thruster uses gaseous nitrous oxide and propylene as propellants. Currently, the burn time of this thruster is limited to 10 seconds after which cool down of the thruster is required. This burn time limit was set quite arbitrarily as no thermal analysis nor any thermal experimentation was performed on the thruster. In this study the thermal limits of the PM200 and similar thrusters was explored. In doing so designs with two particular cooling methods were analysed in detail: designs with Regenerative cooling and designs with Radiation cooling. The overall goal of the project was to assess the thermal performance of the thruster and to see which of the two cooling methods would be most beneficial to implement.

In order to perform the thermal analysis a transient numerical model was created based on the finite volume method in combination with ideal rocket theory and several semi-empirical relationships. The model is able to calculate the temperature distribution and heating rate for several different thruster- and cooling system designs. The model results were verified by comparing the results of the model with the results from commercially available software. A good agreement was found with all results matching within 5-8% or less.

Because the model relied on several semi-empirical relationships, test firings were performed using the PM200 and a heat-sink/radiation cooled version of the PM200 specifically designed for this study to determine two empirical constants required to calibrate the model. In total, 325 tests were performed. During these tests, temperature measurements were taken on various locations on the thruster. After the model was calibrated, the model was validated by checking the model results for different starting conditions with temperature measurements from test firings with corresponding starting conditions. It was found that the model was able to reproduce the temperature distribution measured in the tests within 15% for all cases (with the exception of one particular 2s burn case).

With the validated model, a number of regenerative cooling channel designs and radiation cooled designs was simulated for a reference thruster similar to the PM200. It was determined that with regenerative cooling the maximum wall temperature could be lowered by up to 23% for the reference thruster. This reduction in temperature was sufficient to lower the maximum wall temperature (to ~1090 K) below the maximum operating temperature (1150 K) of the stainless steel alloy used. A simulation of the PM200 design was also performed and a similar result was found; with regenerative cooling a maximum wall temperature of ~1020 K is predicted for the PM200.

For the radiation cooled designs, the wall temperatures exceeded the allowable temperature of 1150 K for both cases. The reference thruster design reached a maximum temperature of ~1420 K and the PM200 reached a maximum temperature of ~1320 K. For radiation cooling to be feasible a different more temperature resistant wall material is thus required. As this would come at an increase in cost, it was concluded that it is more beneficial to use regenerative cooling for the PM200.

While regenerative cooling was found to be effective, it was found that for a given type of cooling channel the design parameters have relatively little effect on the cooling performance due to the small size of the thruster. For all designs (with ribs) the variation in temperature was less than 82 K.

(This page was intentionally left blank)

# Contents

(This page was intentionally left blank)

# List of Figures

# List of Tables

(This page was intentionally left blank)

# List of Symbols

(Sorted by alphabetical order and lower and upper case)

**Scalars**

| Symbol | Description | Unit |
|---|---|---|
| $a$ | Empirical constant for convective heat transfer coefficient | - |
| $a_C$ | Orthogonal components of the diffusion flux going out of the current cell C | W/K |
| $a_C^t$ | Flux component representing the mass flow through the cell due to density or volume changes at the current time value | kg/s |
| $a_C^{t-\Delta t}$ | Flux component representing the mass flow through the cell due to density or volume changes at the previous time value | kg/s |
| $a_F$ | Orthogonal components of the diffusion flux going into current cell C from a neighbouring cell F | W/K |
| $A$ | Local cross sectional area | $m^2$ |
| $A_c$ | Coolant channel cross sectional area | $m^2$ |
| $A_m$ | Empirical constant for the determination of thermal conductivity (dependent on temperature) | W/m |
| $A^*$ | Nozzle throat area | $m^2$ |
| $b_C$ | Non-linear and boundary value heat flow contributions to the current cell C | W |
| $B$ | Empirical constant for determination of thermal conductivity (independent of temperature) | W/(mK) |
| $c$ | Empirical constant for convective heat transfer coefficient for the coolant heat transfer | - |
| $c_p$ | Specific heat capacity (at constant pressure) | J/K |
| $c_{p,g}$ | Specific heat capacity (at constant pressure) | J/K |
| $c_v$ | Specific heat capacity (at constant volume) | J/K |
| $c^*$ | Characteristic velocity | m/s |
| $d_{Cf}$ | Distance between the central centroid C and the integration point f | m |
| $d_{fF}$ | Distance between the neighbouring centroid F and the integration point f | m |
| $D$ | Local combustion chamber/nozzle diameter | m |
| $D_h$ | Hydraulic diameter | m |
| $D_t$ | Nozzle throat diameter | m |
| $e_f$ | Channel roughness | m |
| $E_f$ | Magnitude of the orthogonal component of the surface vector $\mathbf{E}_f$ | $m^2$ |
| $f$ | Integration point on the cell surface boundary | - |
| $f_i$ | Friction factor | - |
| $g_c$ | Geometric interpolation factor | - |
| $h$ | Cooling channel height | mm |
| $h_a$ | Convective heat transfer coefficient | $W/(m^2K)$ |
| $h_c$ | Coolant side convective heat transfer coefficient | $W/(m^2K)$ |
| $I_{sp}$ | Specific impulse | s |
| $k$ | Thermal conductivity | W/(mK) |

| | | |
|---|---|---|
| $k_c$ | Coolant thermal conductivity | W/(mK) |
| $L$ | Axial coordinate of the coolant inlet | mm |
| $L$ | Discretization of all non transient (heat flow) terms | W |
| $L_e$ | Effective radiative path length | m |
| $L_{helicalsection}$ | The lenght of a section of a helical cooling channel | m |
| $\dot{m}$ | Mass flow | kg/s |
| $\dot{m}_c$ | Coolant mass flow | kg/s |
| $\dot{m}_{coolant}$ | Coolant mass flow | kg/s |
| $M$ | Mach number | - |
| $n_T$ | Number of times a cell has been flagged (for flux limiter) | - |
| $N$ | Number of cooling channels | - |
| $N_\Lambda$ | Number of helix windings (for cooling channel) | - |
| $Nu$ | Nusselt number | - |
| $p$ | Pressure | Pa |
| $p_c$ | Chamber pressure | Pa |
| $p_{co_2}$ | Partial pressure for $CO_2$ | Pa |
| $p_{H_2O}$ | Partial pressure for $H_2O$ | Pa |
| $p_t$ | Total pressure | Pa |
| $Pr$ | Prandtl number | - |
| $q$ | Heat flux | W/m$^2$ |
| $q_b$ | Boundary value flux | W/m$^2$ |
| $q_{conv,wc}$ | Convective heat flux between the combustion chamber wall to the coolant | W/m$^2$ |
| $q_r$ | Radiation heat flux (to the environment) | W/m$^2$ |
| $q_{rad}$ | Total radiation heat flux (from combustion gases) | W/m$^2$ |
| $\dot{q}_{rad,CO_2}$ | Radiation heat flux due to $CO_2$ | W/m$^2$ |
| $\dot{q}_{rad,H_2O}$ | Radiation heat flux due to $H_2O$ | W/m$^2$ |
| $q_{wc}$ | Heat flux from between the combustion chamber wall to the coolant | W/m$^2$ |
| $Q$ | Heat flow | W |
| $Q^\phi$ | Source term | W |
| $r$ | Local radius | m |
| $r$ | Recovery factor | - |
| $r_c$ | Local combustion chamber radius | m |
| $r_c$ | Longitudinal throat radius | m |
| $R$ | Universal gas constant | J/K |
| $Re$ | Reynolds Number | - |
| $t$ | Time | s |
| $t_{TBC}$ | Thermal barrier coating thickness | mm |
| $T$ | Temperature | K |
| $T_{amb}$ | Ambient temperature | K |
| $T_b$ | Coolant bulk temperature | K |
| $T_c$ | Combustion temperature in the combustion chamber | K |
| $T_{crit}$ | Critical temperature (of the cooling fluid) | K |
| $T_F$ | Temperature at failure | K |
| $T_w$ | Wall temperature | K |
| $T_{w_{ad}}$ | Adiabatic wall temperature | K |
| $T_{w,g}$ | Combustion chamber wall temperature on the hot gas side | K |
| $T_0$ | Stagnation temperature | K |
| $v$ | Flow velocity | m/s |
| $v_c$ | Coolant flow velocity | m/s |
| $V$ | Volume | m$^3$ |
| $V_c$ | Control volume/Cell volume | m$^3$ |
| $w_c$ | Coolant channel width | m |

**Scalars (Greek)**

| Symbol | Description | Unit |
|---|---|---|
| $\alpha$ | Helmholtz energy | J |
| $\alpha_c$ | Coolant channel angular width | Deg |
| $\alpha^r$ | Helmholtz energy of the real gas | J |
| $\alpha_{rib}$ | Rib angular width | Deg |
| $\alpha^0$ | Helmholtz energy of the ideal gas | J |
| $\gamma$ | Specific heat ratio | - |
| $\Gamma^\phi$ | Material diffusivity (here equal to the thermal conductivity) | W/(mK) |
| $\Gamma^\phi_C$ | Material diffusivity at the central centroid C (here equal to the thermal conductivity) | W/(mK) |
| $\Gamma^\phi_{eff}$ | Effective diffusivity (Used for interfaces between two different materials) | W/(mK) |
| $\Gamma^\phi_F$ | Material diffusivity at the neighbouring centroid F (here equal to the thermal conductivity) | W/(mK) |
| $\delta$ | Density ratio between fluid density and the critical fluid density | - |
| $\epsilon$ | Emissivity of material | - |
| $\Lambda$ | Coolant channel helix pitch | m |
| $\Lambda$ | Sum of all non transient (heat flow) terms | W |
| $\mu$ | Viscosity | Pa |
| $\mu_c$ | Viscosity of cooling fluid | Pa |
| $\rho$ | Density | $kg/m^3$ |
| $\rho_{crit}$ | Critical density (of the cooling fluid) | $kg/m^3$ |
| $\rho_{t-1}$ | Density at the previous time step | $kg/m^3$ |
| $\sigma$ | Stefan–Boltzmann constant | $Wm^{-2}K^{-4}$ |
| $\tau$ | Temperature ratio between the fluid temperature and the critical fluid temperature | - |
| $\phi$ | Correction factor for property variation across the boundary layer (for Bartz equation) | - |
| $\phi$ | Temperature | K |
| $\phi_C$ | (Average) temperature at centroid C | K |
| $\phi^t_C$ | (Average) temperature at centroid C at time step t | K |
| $\phi_f$ | Temperature at integration point f | K |
| $\phi_F$ | (Average) temperature at centroid F | K |
| $\phi_n$ | Temperature at nodes/vertices | K |
| $\phi_t$ | Temperature at the current time step t | K |
| $\phi_{t+\Delta t}$ | Temperature at the next time step t+Δt | K |
| $\Psi$ | Burn time extension factor | s |
| $\omega$ | Relaxation factor | - |

**Vectors and Matrices**

| Symbol | Description | Unit |
|---|---|---|
| $\mathbf{A}$ | Matrix containing linear components of the flux | N/A |
| $\mathbf{b}$ | Matrix containing all non-linear components of the flux | N/A |
| $\mathbf{B}$ | The iteration matrix | N/A |
| $\mathbf{C}$ | Matrix containing all the $a_C^{t-\Delta t}$ coefficients | N/A |
| $\mathbf{e}$ | Unit (surface) vector on the line which connects two centroids C and F (The orthogonal component) | $m^2$ |
| $\mathbf{E}_f$ | Orthogonal component of the surface vector **S** | $m^2$ |
| $\mathbf{n}$ | Unit (surface) vector in the direction of the surface vector **S** | $m^2$ |
| $\mathbf{P}$ | Preconditioner matrix | N/A |
| $\mathbf{r}_C$ | Position vector for the central centroid C | m |

| | | |
|---|---|---|
| $\mathbf{r}_F$ | Position vector for a neighbouring centroid F | m |
| $\mathbf{S}$ | Surface vector | $m^2$ |
| $\mathbf{S}_b$ | Surface vector at a boundary | $m^2$ |
| $\mathbf{S}_f$ | Surface vector at the integration point f | $m^2$ |
| $\mathbf{t}$ | Unit (surface) vector for the non-orthogonal component of the heat flux | $m^2$ |
| $\mathbf{T}_f$ | Non-orthogonal component of the surface vector **S** | $m^2$ |
| $\mathbf{v}$ | (Coolant) velocity vector | m/s |

**Vectors and Matrices (Greek)**

| Symbol | Description | Unit |
|---|---|---|
| $\boldsymbol{\phi}^n$ | Matrix containing all temperature values after iteration | N/A |
| $\boldsymbol{\phi}^{n-1}$ | Matrix containing all temperature values before iteration | N/A |
| $\boldsymbol{\phi}^t$ | Matrix containing all temperature values for the current time step | N/A |
| $\boldsymbol{\phi}^{t-\Delta t}$ | Matrix containing all temperature values for the previous time step | N/A |

# 1 Introduction

In recent years there has been a steady increase in the amount of CubeSat missions performed. While between 2002 and 2005 there were a total of 10 cubesat missions launched, by 2017 this number had risen to 287 [47]. Nanosats database[1] predicts that this number will continue to rise even further with a predicted 458 launches for 2020 and up to 545 predicted launches by 2023. This increase in launches can be explained by the fact that while in the past the development of CubeSats was mainly driven by educational purposes, in recent year CubeSats have caught the interest of governments and industry, increasing their capabilities and expanding their mission profiles immensely. As these mission profiles expanded, the economic exploitation of CubeSats became limited by the lack of available propulsion systems [29]. Because of this, in recent years multiple efforts have popped up to develop propulsion systems for CubeSats, although the technology is still in its infancy [29]. To complicate matters even more, in 2011 the European Commission decided to include hydrazine, a common propellant used for spacecraft, on the list of substances which pose a serious concern in the Registration of Evaluation Authorisation and Restriction of Chemicals (REACH) framework.[2] As a result Hydrazine could be banned within the European Union as soon as 2021. Recent studies have therefore focused on the development of alternative propulsion systems which use so-called “green propellants”; propellants which exhibit a low amount of dangerous properties and which are easy to handle.

The Dutch/New Zealand based aerospace company Dawn Aerospace has developed such a green propulsion system for use in CubeSat applications called the PM200. The PM200 is a bi-propellant thruster using gaseous Nitrous Oxide and gaseous Propylene as propellants with a nominal thrust of 0.5 N. The burn time of the PM200 is currently limited to 10 seconds, after which the thruster needs to cool down to prevent overheating. Due to the rapid development of CubeSat technology in the last few years, the need has arisen for CubeSat propulsion systems to be able to perform longer burns in order to allow for more complex mission profiles. In order to do this a cooling system thus has to be implemented into the PM200. However, due to the novelty of green propellants and CubeSat scale propulsion systems, little information is available in literature about the thermal management of such systems, especially for the propellant combination used by the PM200. Because of the rather scarce amount of information available, it is difficult to determine what would be an effective cooling mechanism for the PM200. Therefore, the study presented in this report aims to investigate the thermal behaviour of green bi-propellant CubeSat propulsion systems with a primary focus on determining the feasibility of the implementation of two cooling methods: regenerative cooling and radiation cooling. This investigation will be performed using a combination of numerical modelling and experimentation using the PM200 propulsion system.

[1] Nanosats database, Erik Kulu, Updated: April 19th 2020, Available online at: https://www.nanosats.eu/ (Accessed 05-08-2020)
[2] The REACH documentation is available online on the website of the European Commission: https://ec.europa.eu/environment/chemicals/reach/reach_en.htm (Accessed 21-01-2020)

The structure of this report is as follows: In chapter 2 the scientific context of the study as well as background knowledge required for understanding the rest of the report is provided. In this chapter the research objective and the research questions are also presented. In chapter 3 the numerical model which was developed will be presented. Chapter 4 focuses on the validation of the model as well as on the tests which were performed for the validation of the model. Chapter 5 presents and discusses the results found by the model. In chapter 5 the sub research questions will also be answered. Conclusions and recommendations based on the discussion in the previous chapters are given in chapter 6. In this chapter the primary research question will also be answered.

# 2

# Scientific Context and Theoretical Basis

In chapter 1 the PM200 CubeSat propulsion system developed by Dawn Aerospace was introduced. It was stated that the burn time of the thruster was currently limited to 10s and that in literature only little information was available about the thermal behaviour of CubeSat scale propulsion systems. Further explanation was however not given. This chapter aims to elaborate on these statements by first giving an overview of the PM200 design in section 2.1. Afterwards the theoretical foundation for the rest of the report will be laid by discussing several different cooling methods which are commonly used in rocket engines in section 2.2. With this theoretical foundation in place, the current state of the art when it comes to cooling methods for CubeSat scale propulsion systems is discussed in section 2.3. Within this discussion the motivation for the current research will become clear. Based on the findings presented in section 2.3 the research objective and research questions of this study are specified in section 2.4. The overall goal of this chapter is to give the reader sufficient context to understand the remainder of the report.

## 2.1. PM200

The PM200 module is the smallest propulsion system developed by Dawn Aerospace in a line of green bi-propellant propulsion systems. The system is intended for use in CubeSats and can act as a completely stand-alone system. It has a nominal thrust level of 0.5 N and is standardly available in a 0.7U or a 1U form factor although other sizes are also possible if required. The module consists of the thruster, a tank module, valves, a thrust vector control system, and electronics. The thruster itself is called the BT400.10, although throughout this text the name PM200 will be used interchangeably to refer to both the thruster and the module as a whole. Besides the PM200, Dawn Aerospace has also developed or partially developed several other thrusters in the same thruster family, a brief overview of these thrusters will be given in section 2.1.3.

### 2.1.1. General overview of the thruster

To get a better idea of the PM200 thruster/system a short overview of the thruster design will be given here. Additional information about the system can also be found in [49]. As was mentioned before, the PM200 module consists of a thruster, a tank, valves and a thrust vector control system. The module can be seen in figure 2.1. As can be seen the thruster is completely contained within the module. The cross-like structure seen around the thruster is the thrust vector control mechanism which provides stabilisation of the satellite during a burn.

In figure 2.2 a render of the BT400.10/PM200 thruster can be seen with various components of the thruster labelled. The thruster is a chemical bi-propellant thruster using a propellant combination of Propylene and Nitrous Oxide. The total propellant mass is 170 or 310 gram and the total system mass is 1170 or 1410 gram depending on whether or not the 0.7U or 1U

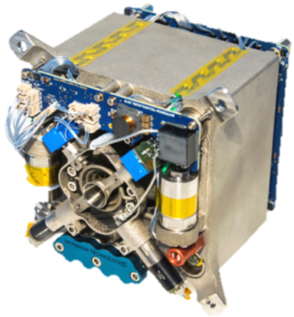

Figure 2.1: The PM200 module

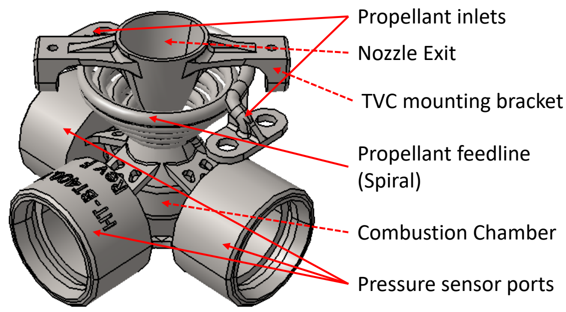


Figure 2.2: The BT400.10 thruster

module is used. As is characteristic for bi-propellant thrusters, the PM200 has a relatively high specific impulse with a specific impulse of approximately 285 s. This specific impulse is amongst the highest for chemical CubeSat propulsion systems currently in development and/or available on the market [45]. Because the PM200 is a chemical propulsion system, the power consumption of the thruster is also relatively low, requiring less than 6 W of power to operate [49]. As a downside, bi-propellant thrusters typically have a relatively high combustion temperature, leading to a high thermal load.

Because of the expected high thermal load, the burn time of the thruster is currently limited to 10 seconds after which the thruster has to cool down. This limit of 10 seconds was chosen because it was proven safe to fire the thruster for this amount of time (see also Appendix A, which contains the original project assignment from Dawn Aerospace). It was however not known whether or not this 10 second limit is the true limit of the thruster, as longer burns have not been attempted. No thermal analysis nor thermal experimentation had been performed on the thruster, so the (theoretical) thermal limits of the thruster were unknown. To mitigate the heat loading, a cooling channel was added to the PM200 thruster design. However, since no thermal analysis nor thermal experimentation was performed on the thruster the effectiveness of the cooling channel design was largely unknown.

In figure 2.2 it can be seen that on the combustion chamber body of the PM200 three pressure sensors ports are placed. By placing pressure sensors in these ports they can be used to measure the combustion chamber pressure and the injection pressure for both the fuel and oxidiser. Two pressure sensors are also mounted on the two tanks, which can be used to monitor the tank pressures. Typical pressure measurements from a test can be seen below in figure 2.3. Note that the data is normalised with respect to an average chamber pressure value, which can be assumed to be 3.5 bar. An interesting phenomenon to note is that the oxidiser injection pressure rises slowly during the burn. This is because the oxidiser is used as the coolant in the aforementioned regenerative cooling channel. As the oxidiser heats up the pressure at the injector increases. It can also be seen that the fuel injection pressure increases slightly, although less so than the oxidiser injection pressure, this is because the fuel is not used as coolant and thus heats up less.

On and around the nozzle, mounting brackets and a spiral mechanism can be seen. These are attached to the thrust vector control mechanism and allow the thruster to be rotated around its axes. The spiral is a compliant mechanism which contains the propellant feed lines.

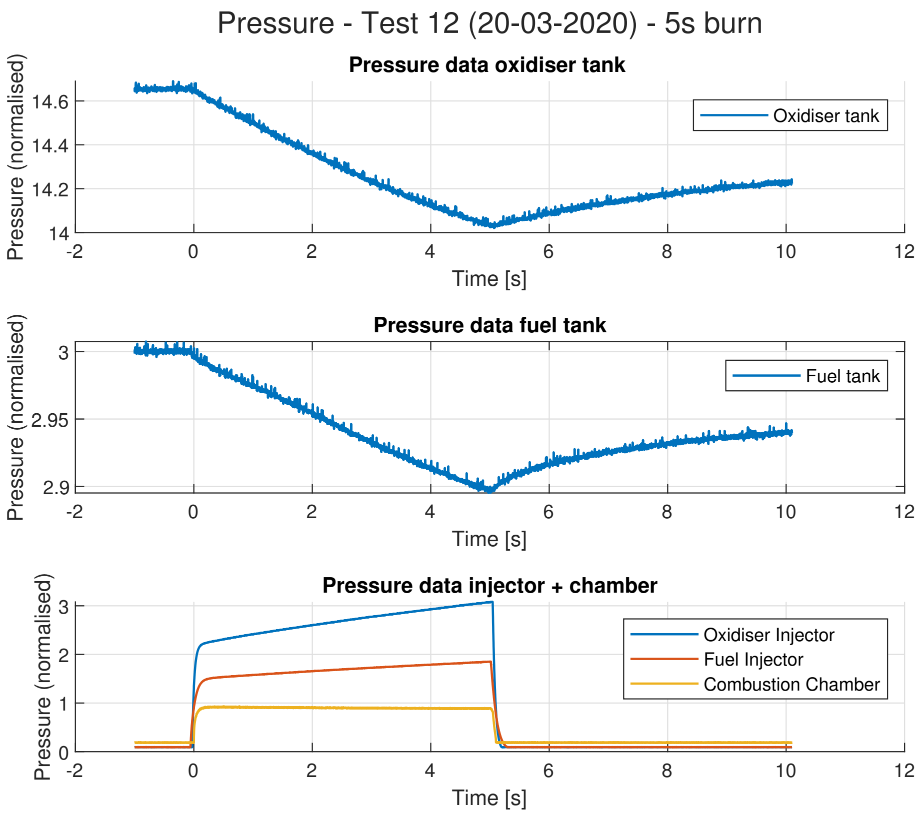


Figure 2.3: Pressures for the PM200 as recorded during test 12 on (20-03-2020).

### 2.1.2. Propellants

The propellants used within the PM200 are Propylene (fuel) and Nitrous Oxide (oxidiser). These propellants are known as so-called “green propellants”, which means they exhibit a low amount of toxicity and other dangerous properties which makes them relatively easy to handle and store in contrast with traditional propellants used for in-space propulsion systems such as hydrazine.

Propylene and Nitrous Oxide are self-pressurising propellants, which means that their vapour pressure at room temperature is sufficiently high that it can be used as a feed pressure. The propellants are stored under saturation conditions in the tank with part of the propellants being in a gaseous phase and part being in a liquid phase. For the PM200 the gaseous part of the propellant is used. As the tanks are emptied the liquid part of the propellants will boil to refill the volume of gas lost which has a pressurising effect. The propellant (tank) pressure therefore drops less quickly than would otherwise be expected during firing. A small drop in pressure is still present as can be seen in figure 2.3. When the engine is turned off the tank pressure will rise again until saturation conditions are restored. The advantage of such self-pressuring propellants is that no separate pressurant is needed, reducing the system complexity and mass.

Since the PM200 is a blow-down system, the performance of the thruster is dependent on the tank pressure. Because the propellants are stored under saturation conditions, the tank pressure is dependent on the ambient temperature. This is shown graphically in figure 2.4. It can be seen that the trend in pressure is almost exactly the same for both propellants with the difference between the two propellant pressures being mainly in the magnitude of the pressure value. Because of this, the efficiency of the thruster remains roughly the same independent of ambient temperature. The thrust produced however does not remain constant with ambient temperature but varies instead, with a higher ambient temperature corresponding to a higher thrust level (for more details see [49]). Furthermore, because the mass flow of the propellants is directly related to the tank pressure, the chamber pressure of the thruster is also dependent on the ambient temperature. In section 3.1 it will be shown that the heat transfer to the thruster wall is proportional to the chamber pressure and because of this the final temperature reached by the thruster after a burn is in turn dependent on the ambient temperature.

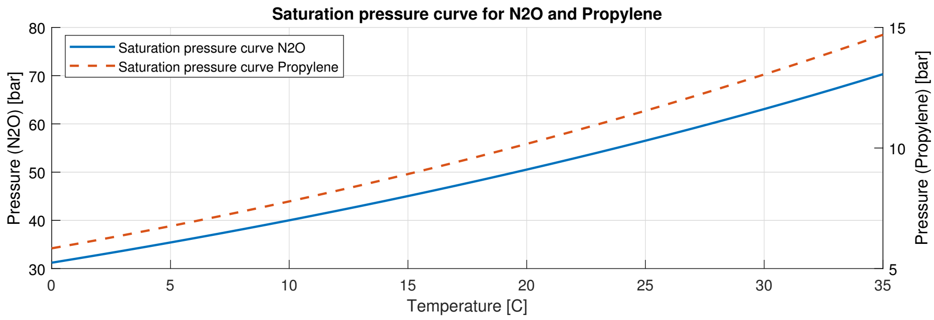


Figure 2.4: Saturation pressure curves for Nitrous Oxide and Propylene (data generated using REFPROP)

### 2.1.3. Other thrusters within the PM200 family

Dawn Aerospace has developed several other thrusters within the PM200 family. These thrusters are all similar in design, use similar propellants and similar materials. Three different thrusters currently exist within the PM200 family and they are in varying stages of development: the PM400, the B20 and the NP120. Throughout this report various references will be made to some of these thrusters and therefore they are introduced briefly here to aid the comprehension of the reader. The B20 thruster in particular will be referred to often. This is because in chapter 4 some of the test data gathered from tests with the B20 thruster will be used for the calibration and validation of the model developed within this study.

**PM400 thruster**

The PM400 thruster is a 1N thruster developed for CubeSat applications similar to the PM200. It was developed in parallel to the PM200 and both were derived from the same prototype. The PM400 module has a 2U form factor. The module was successfully tested several times and was commercial available in the past. Currently development on the module has halted in favour of developing the PM200 further. More details about the PM400 module can be found in [34].

**NP120 thruster**

The NP120 thruster is a 120N (sea level, 200N vacuum) thruster. It was developed to power Dawn Aerospace's Mk.1 space plane prototype. This prototype is a small scale technology demonstrator used to demonstrate some of the key technologies required for the Mk.2 Aurora suborbital space plane currently under development at Dawn Aerospace. The thruster uses the same propellants as the PM200 although in liquid form. Furthermore the NP120 also uses regenerative cooling using the oxidiser. For the NP120 is has been shown that this cooling is effective as several static fire tests were performed in which it was shown that the thruster reached a steady state [48]. The NP120 has been tested during static fire tests several times, it has also been successfully used in several flights of the Mk.1 prototype.

**B20 thruster**

The B20 thruster is a 20N thruster used for small satellites. The thruster was derived from the PM200 and uses the same propellants. The B20 thruster is similar to the PM200 design except that it is slightly larger and has a slightly different geometry as a result. A picture of the B20 thruster will be shown in chapter 4 (figure 4.33). The B20 thruster uses the same stainless steel alloy as the PM200 as a wall material. The thruster uses regenerative cooling to cool the nozzle throat and combustion chamber. A limited amount of thermal measurements has been performed on this thruster to characterise the thermal behaviour. These measurements include measurements of the cooling channel at the start and end of the cooling channel. In chapter 4 these measurements will be used to calibrate the model developed in this study.

### 2.1.4. Reference thruster

Since the PM200 thruster is a product developed by Dawn Aerospace, details about the internal geometry of the thruster are proprietary. Because of this, a theoretical reference thruster will be used throughout this report which has similar but slightly different design parameters as the PM200. This thruster will be used throughout the report for any figures where it is required that the internal geometry of the thruster is shown. It will be used to indicate trends and to conceptually explain phenomena which were observed during the study. The design parameters of this reference thruster are shown in table 2.1. Throughout this report this thruster will simply be referred to as “the reference thruster”. A contour plot showing the internal thruster wall geometry and the outer thruster wall geometry of the reference thruster can be seen in figure 2.5.

Table 2.1: Reference thruster parameters

| Parameter | Parameter value [unit] |
|---|---|
| Thrust | 0.7 [N] |
| Chamber Pressure | 3 [bar] |
| Area Ratio (Supersonic) | 90 [-] |
| Area Ratio (Subsonic) | 45 [-] |
| Wall thickness | 1.5 [mm] |
| Fuel | Propylene [-] |
| Oxidizer | Nitrous Oxide [-] |
| O/F Ratio | 8 [-] |
| Material Thermal Conductivity | 15 [W/mK] (kept constant) |

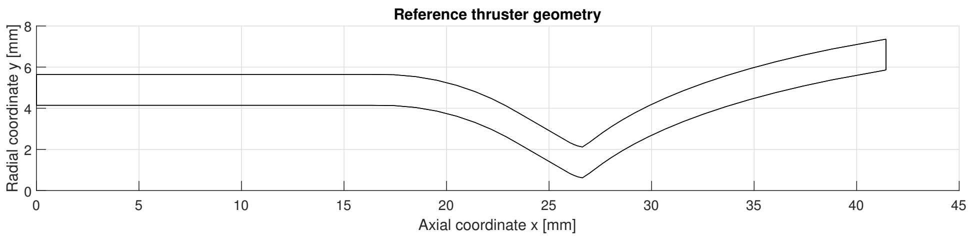


Figure 2.5: Geometry of the reference thruster

## 2.2. Theoretical background on cooling methods

In this section a theoretical background will be given on typical cooling methods used within rocket engines. First an overview of all cooling methods identified in literature will be given and afterwards a more detailed theoretical background on Regenerative cooling, Radiation cooling and Thermal barrier coatings will be given. The main goal of this section is to give the reader a sufficient basic understanding of these cooling methods in order to better understand the remainder of the report.

### 2.2.1. Cooling methods used in rocket engines

Several different cooling methods exist for cooling rocket engines. These cooling methods can be grouped into two different groups: active and passive cooling methods. Active cooling methods use one of the propellants or a separate coolant to cool (part) of the rocket engine while passive cooling methods rely solely on the material properties or the rocket engine geometry to provide cooling. An overview of the cooling methods found in literature and their applications can be seen below in table 2.2.

Table 2.2: Cooling methods for rocket engines and their characteristics

| Cooling method | Type | Applicable duration | Indefinite restarts possible? |
|---|---|---|---|
| Regenerative Cooling | Active | Unlimited | Yes |
| Film Cooling | Active | Unlimited | Yes |
| Transpiration Cooling | Active | Unlimited | Yes |
| Dump Cooling | Active | Unlimited | Yes |
| Heat-Sink Cooling | Passive | Seconds | Yes |
| Ablation Cooling | Passive | Seconds/Minutes | No[1] |
| Insulation/Thermal Barrier Coatings | Passive | Unlimited | Yes/No[2] |
| Radiation Cooling | Passive | Unlimited | Yes |

During a literature study preceding this thesis study [45], it was determined that for the PM200 the most promising cooling methods were regenerative cooling and radiation cooling, although with the side note that it was unclear whether or not regenerative cooling was possible on the small scale required for the PM200. Thermal Barrier Coatings (TBC) were also considered feasible as an addition to either of the two aforementioned cooling methods if a coating could be found with a high enough resistance to cracking. Therefore in the remainder of this report the focus will be on regenerative cooling and radiation cooling, with also some attention given to TBCs. The general working principles of each of these cooling methods will be discussed to give the reader the knowledge required to understand the remainder of the report.

### 2.2.2. Radiation cooling

Radiation cooling is a passive cooling method which is one of the easier cooling methods to implement and model. In radiation cooling the wall material is allowed to heat up to such a high temperature that the heat radiated away from the thruster balances the heat input from the combustion gases. This is possible because the heat radiated away is proportional to the wall temperature to the fourth power. Nevertheless, high wall temperatures are usually required before an equilibrium is reached and radiation cooling actually becomes effective. Because such high wall temperatures are required, radiation cooling usually comes at a cost: specialised materials with a high temperature resistance such as refractory metals have to be used. These materials are often more expensive and more difficult to work with than other materials typically used in rocket engines. Furthermore, it can be difficult to connect the radiation cooled parts of the thruster to the rest of the system without causing these systems to overheat.

By definition radiation cooling can only be used in steady state, as long as steady state is not yet reached radiation cooling is simply equal to heat-sink cooling. Throughout this report, the term radiation cooling will however often be used interchangeably to refer to both heat-sink cooling and radiation cooling for simplicity. Schematically, the concept of radiation cooling can be seen in figure 2.6.

[1] Amount of restarts is limited by amount of ablative material.

[2] Amount of restarts is limited by lifetime of coating. Depending on the coating this can however be considered indefinite for practical purposes.

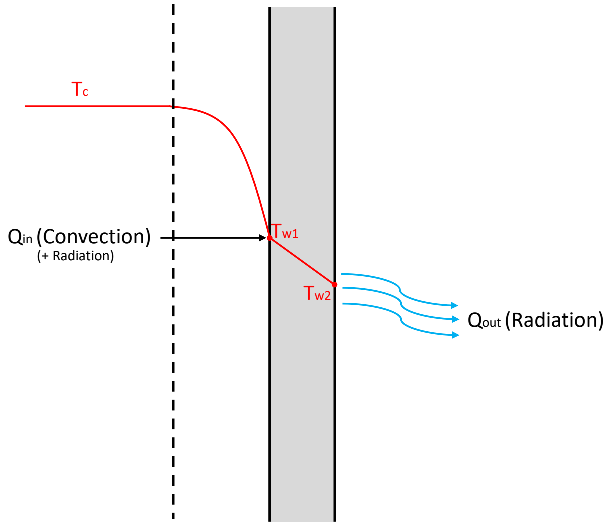


Figure 2.6: Working principle of radiation cooling

### 2.2.3. Regenerative cooling

Regenerative cooling is an active cooling method in which one (or both) of the propellants is (are) circulated around the combustion chamber wall and/or nozzle before being injected into the main combustion chamber. While the propellant is being circulated around the combustion chamber walls it acts as a coolant picking up heat from the hot combustion chamber walls. Regenerative cooling is one of the more efficient active cooling methods that exists because none of the propellants are solely used for the purpose of cooling and all coolants are injected into the main combustion flow after being used as a coolant. Furthermore, because the propellants are used as a coolant before being injected into the combustion chamber, their enthalpy increases leading to an increase in specific impulse. Because of this, regenerative cooling is a popular cooling method which is often used in rocket engines. Regenerative cooling can also be used in parallel with other cooling methods such as film cooling or thermal barrier coatings.

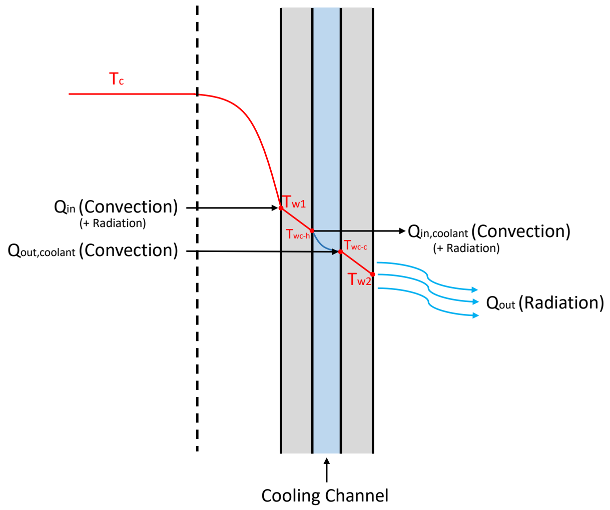


Figure 2.7: Working principle of regenerative cooling

The cooling channels for regenerative cooling can have various geometries. In this report three different types will be distinguished: Cooling sleeves, axial channels with ribs and helical channels.

In a cooling sleeve the coolant flow covers the entire thruster circumference. The combustion chamber consists of two coaxial shells and coolant is injected in between these shells. The case for axial channels with ribs is essentially the same as the coolant sleeve, except in this case ribs are present between the inner and outer shell of the combustion chamber. These ribs add structural strength to the thruster and subdivide the cooling channel into multiple smaller cooling channels. Because of the smaller cooling channel size, a higher coolant flow velocity is achieved at the cost of a larger pressure drop. Furthermore, the wall surface which is in contact with the coolant is increased as the ribs are also in contact with the coolant, leading to a higher amount of heat transfer to the coolant. The third category: helical channels, consists of one or more channels which are wound around the combustion chamber in a helical pattern. The advantage of this design is that the effective coolant channel length increases, meaning that more heat can be transferred to the coolant for a given section of the combustion chamber wall compared to the case where axial channels are used. However, the downside of this design is that the increase in the effective cooling channel length comes at the cost of a higher pressure drop.

### 2.2.4. Thermal Barrier Coatings

Thermal barrier coatings are a passive cooling method which works by applying a thin layer of material with a very low thermal conductivity at the parts of the thruster which see the highest heat loading, usually the inside of the combustion chamber and nozzle. Heat flux by conduction is dependent on the thermal conductivity of the wall material as well as the temperature drop over the wall. The lower thermal conductivity of the thermal barrier coating layer thus results in a large temperature drop over the thermal barrier coating, meaning that the structural part of the wall is exposed to a lower temperature and heat flux. The temperature at the hot side of the thermal barrier coating is usually higher than what would be the highest temperature on a wall without a coating, however the thermal barrier coating material has a higher operational temperature than the structural wall material to prevent failure of the coating. The working principle of a thermal barrier coating can be seen below in figure 2.8.

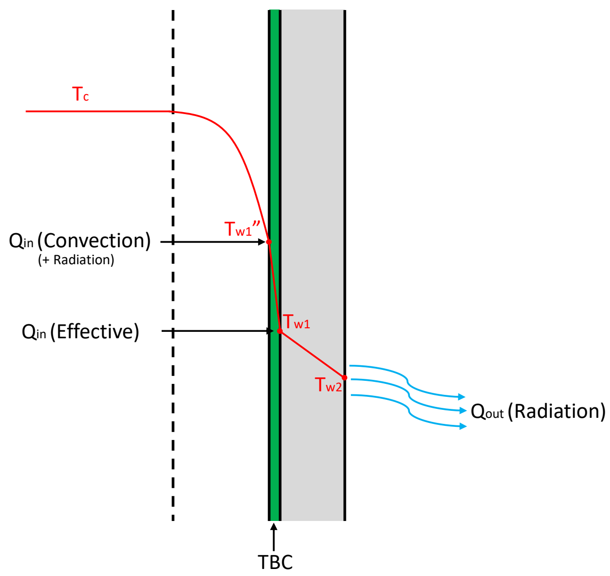


Figure 2.8: Working principle of a thermal barrier coating

Thermal barrier coatings can be used as a stand-alone solution to lower the heat flux, or they can be used in parallel with another cooling method such as regenerative cooling. A downside of thermal barrier coatings is that they can crack after multiple load cycles due to the high thermal gradients applied during each load cycle.

## 2.3. State of the art & motivation for research

In recent years several propulsion systems tailored towards Cubesats have entered development [45]. From literature, it appears that most of these use passive cooling methods; mostly radiation cooling and sometimes heat-sink cooling [45]. Both of these cooling methods have however some drawbacks. Heat-sink cooling can only be used for short burn times, making it unsuitable for many types of missions. Radiation cooling, while effective and relatively simple to model, requires specialised materials and manufacturing techniques, making it almost prohibitively expensive for usage in CubeSat applications.

An attractive alternative solution could be regenerative cooling. With the advent of additive manufacturing techniques the complex geometries of regeneratively cooled engines can be manufactured easily and at low cost. Regenerative cooling is typically used in large scale liquid propellant rocket engines. This is because the cooling efficiency of regenerative cooling scales with engine size, with larger engines being easier to cool than smaller engines [50]. Because of this, it is unclear whether or not regenerative cooling could work on the small scale required for a thruster used in CubeSats. Another factor which complicates the use of regenerative cooling is that the PM200 uses gaseous propellants and that for regeneratively cooled engines, cooling effectiveness decreases by an order of magnitude when gaseous coolants are used instead of liquid coolants [3, 50].

Since the PM200 is a very small engine for bi-propellant standards and because the PM200 uses gaseous propellants it is unsure whether or not regenerative cooling could be a feasible solution for thrusters like the PM200. On the other hand, in literature it was found that for smaller rocket engines the heat transfer from the combustion gases to the chamber wall is in general somewhat lower than expected compared to large rocket engines [18, 38, 50]. Furthermore, the PM200 also operates at a relatively low chamber pressure with typical chamber pressures ranging between 2 and 6 bar [49], this low chamber pressure further reduces the heat transfer to the wall. The question thus becomes whether or not the reduction in heat transfer to the wall can balance the low cooling efficiency of regenerative cooling in small rocket engines. As a starting point for answering this question literature was explored to see if any thrusters on a CubeSat scale could be identified which utilised regenerative cooling. Multiple examples could be found and a brief overview of these systems will be given below:

Mechatronics GmbH in collaboration with the European Space Agency has been working on the development of a small scale rocket engine which utilises regenerative cooling and which could be used in CubeSat applications. This engine has a similar scale and almost identical dimensions to the PM200 but uses Hydrogen Peroxide and Ethanol as propellants [25]. The thrust of the engine is around 1 N. Multiple tests were performed using this thruster and long burn times of over 1000 s were achieved although performance was lower than expected [37]. A detailed thermal analysis of this design was performed by Campolo and Soldati [7] and they concluded that regenerative cooling was a feasible cooling method for this design. The cooling used in this thruster was however somewhat special, the hydrogen peroxide was first decomposed and the water vapour resulting from this reaction was used as the coolant. Because of the decomposition reaction the inlet temperature of the cooling fluid was relatively high at 207 ° C. Nevertheless the cooling solution was effective as shown from the simulation and test results. This is likely because water has a relatively high heat capacity, making it a very effective coolant even at high temperatures. By decomposing the oxidiser before entering the cooling channel the risk of coolant decomposition due to temperature rise is also mitigated, allowing for the coolant to reach higher temperatures. The cooling channel design consisted of a 0.5 mm thick cooling sleeve for the combustion chamber, while for the convergent nozzle section sixteen ribs were added to locally increase the heat transfer to the coolant. In literature no information could be found which indicates that this system has had any flight heritage.

Massachusetts institute of technology (MIT) worked on the development of a micro-scale propulsion system which used regenerative cooling. While this thruster was not particularly designed for CubeSat applications, its dimensions are of a similar scale as CubeSat sized propulsion systems [6]. The thruster developed at MIT initially was designed to use LOX and ethanol, but later versions of the design used Hydrogen Peroxide in combination with JP7 [6]. Two studies could be identified in literature which studied the heat transfer to the cooling channels for this engine [6, 13]. Both of these studies however simplified the problem by only considering the heat transfer to Hydrogen peroxide in a micro-channel and both studies were mostly experimental in nature. Joppin [13] did extrapolate the experimental results to a micro rocket engine design but notes that significant differences were present between the experimental set-up used and a real rocket engine design and that the results may therefore not be representative. Successful ground firing tests were performed using this engine at 10% of the maximum thrust value resulting in a thrust of around 1N [22]. In literature no information could be found which indicates that this system has had any flight heritage.

Both engines mentioned above used hydrogen peroxide as an oxidiser/coolant and therefore their behaviour may not be representative for an engine using nitrous oxide as an oxidiser/-coolant. Perhaps the most similar design to the PM200 were two thrusters developed around 2013 at the University of Miyazaki in Japan [15, 43]. Like the PM200, these thrusters used self-pressurising propellants, in particular nitrous oxide in combination with dimethyl ether (DME). The thrusters had a design thrust of 0.4 N and 1 N. For the 0.4 N thruster no cooling method was specified in literature. For the 1 N thruster however it was stated that regenerative cooling was used and a schematic detailing the cooling channel design was given in a paper by Kakami et al. [15]. Unlike the PM200, this thruster uses the (gaseous) DME fuel as a coolant instead of the nitrous oxide. This is possible for this engine because the optimum O/F of DME in combination with nitrous oxide is lower than the optimum O/F for propylene in combination with nitrous oxide [45]. This means that a larger amount of fuel mass flow is available, which makes it possible to use the fuel as a coolant. DME has slightly better cooling properties (higher heat capacity) than nitrous oxide [45] which is a small advantage. The mass flow of the DME must however always be lower than the nitrous mass flow due to the optimum O/F occurring at around 5.5 [45].

From the schematics given in [15] it appears that the design uses a 2 mm cooling sleeve that starts at the start of the nozzle convergent. It appears that only the chamber is cooled and the nozzle is uncooled. The paper by Kakami et al. [15] does not go into details about the effectiveness of the cooling channel design although relatively long burn times of up to 70s are reported. These long burn times seem promising, although it should be noted that low $c^*$ and $I_{sp}$ efficiencies were reported. It could be the case that these long burn times were only achieved because the heat transfer to the thruster wall was limited due to the low performance of the thruster. An attempt was made to contact the authors of the study to get more details and clarification about the effectiveness of the cooling channel design, but unfortunately more details could not be obtained.

As stated in section 2.1 the PM200 also has a regenerative cooling channel. This cooling channel was however not optimised and at the start of this study the effectiveness of this cooling channel was completely unknown. Some thermal measurements were available in literature on an early prototype thruster which eventually evolved into the PM200 and PM400 designs [33]. The design of this prototype was however substantially different from the current PM200 design as it used a different wall material, had a different regenerative cooling channel geometry, a different internal combustion chamber geometry, had a higher thrust level, operated at higher chamber pressures, used a different fuel, and used liquid propellants instead of gaseous propellants. Thermal measurements were performed on both regeneratively cooled versions of the thrusters and heat-sink cooled versions of the thruster. However, few tests were performed and due to a loss of data the results were highly inconclusive. Because obtaining temperature data was not the primary focus of the study, additional tests which would have allowed for comparison were not performed. A CFD analysis was performed on this design as well [33], however the effectiveness of adding the cooling channel was not determined; it was just checked if the design requirements were met.

In conclusion, from literature it can be seen that regenerative cooling has been applied in CubeSat sized propulsion systems. However in most cases the effectiveness of the regenerative cooling channel design was not studied in detail except for a thruster using a different propellant combination. Furthermore, the only design for which a detailed thermal analysis was published was rather unconventional and used the decomposition products of the oxidiser as the coolant. No thermal analysis could be identified in literature which analysed a conventional regenerative cooling channel design for a thruster used in CubeSat applications. Furthermore, no thermal analysis could be identified in literature which analysed the a regenerative cooling channel design for a thruster using similar propellants to the PM200.

## 2.4. Research Objective and Research Questions

In the previous section it was explained that most CubeSat scale propulsion systems use radiation cooling. Furthermore it was explained that regenerative cooling could be an attractive alternative solution but that the feasibility of using regenerative cooling on the small scales required for CubeSats was uncertain. From literature it became apparent that some CubeSat scale propulsion systems have been developed in the past which used regenerative cooling. The effectiveness of (traditional) regenerative cooling in thrusters used for CubeSat applications was however never established and results from literature are inconclusive. Based on this, the following research objective was formulated:

**Research Objective:** *To assess the effectiveness of regenerative cooling and radiation cooling in a small green bi-propellant thruster in order to increase the maximum attainable burn time while taking into account practical constraints* by developing a numerical model that will simulate the heat distribution within the thruster and by implementing one of the two cooling methods in a real life thruster.*

*Practical constraints: The term “practical constraints” in the research objective is quite ambiguous, therefore a clarification of this term will be given here: the main point is that the proposed solution must be a solution that can actually be implemented relatively easily in real life applications. Solutions which require for example materials which only exist in theory are therefore not allowed.

In order to achieve the research objective a research question was formulated which was subdivided into several subquestions. Based on the research objective, the following primary research question was established:

**Primary Research Question:** *Is it more beneficial to use regenerative cooling or radiation cooling using refractory metals for a self-pressurising green bi-propellant rocket engine used in CubeSat applications?*

This research question can be answered by answering the following sub-questions:

- **SQ-1:** Is it possible to achieve sufficient cooling using regenerative cooling in a thrust chamber which is small enough to be used in CubeSat applications?
  - **SSQ-1.1:** How is the temperature distributed within the thruster?
  - **SSQ-1.2:** Is it possible to achieve sufficient cooling with gaseous nitrous oxide?
  - **SQ-1.3:** Are the thrust levels and corresponding (coolant) mass flows used in CubeSat scale propulsion systems sufficient to make regenerative cooling feasible?

- **SQ-2:** Which design parameters are the main drivers for selecting a cooling method for a CubeSat scale propulsion system?
  - **SSQ-2.1:** What is the influence of the different design parameters on the heat loads experienced by the thruster?

  - **SSQ-2.2:** What is the influence of the different design parameters on the cooling performance of each cooling method?

- **SQ-3:** Is it possible to eliminate potential limitations imposed by the outcomes of sub-question 1 and 2 by changing certain design parameters? If so, what changes can be made?
- **SQ-4:** From a thermal point of view, what factors on a system level besides cooling of the thruster body should be taken into account when implementing a cooling system design for a thruster used in CubeSat applications?

With the research questions above answered, it will be possible to determine the feasibility of Regenerative cooling and Radiation cooling for a CubeSat scale propulsion system like the PM200. In case both methods are feasible it will also be possible to determine which of the two methods is more beneficial.

# 3
# Numerical Model

A numerical model was developed to evaluate the heat transfer within the engine. This was done for three reasons: the first reason was that prior to this study there was very little understanding of the thermal behaviour of the PM200. While the thermal behaviour can in part be characterised by performing measurements, it is not feasible to measure the temperature at every location of the thruster. Therefore, characterisation of the thermal behaviour of the thruster can be improved by making a model. The second reason for the development of the model was to evaluate the performance of the current cooling methods implemented in the PM200 and potential new cooling methods which could be implemented within the PM200. The final reason for the development of the model was to create a tool which could be used to predict the thermal behaviour of the thruster beyond the 10 second burn times which were achieved currently.

The numerical model which was developed is a hybrid between a full sized computational finite volume method and a more simple model using equations from ideal rocket theory. By choosing this hybrid strategy an accurate solution can be obtained at the points most critical for evaluating cooling system designs while at the same time keeping the simulation somewhat simple, lowering the computational cost required.

The model can perform both transient and steady state heat transfer simulations, with the main the focus being on the transient simulations. The choice for a transient model rather than only a steady state model was motivated by two reasons: The first reason was that it was unsure whether or not the PM200 thruster could reach a steady state, so it would be difficult to validate the model if the model could only perform steady state calculations. The second reason was that it was also unknown after approximately how many seconds the PM200 thruster would reach a steady state. The original project assignment (see Appendix A) states that one of the goals of the project is to figure out whether or not the burn time of the PM200 could be extended to 60 seconds. If the steady state is not yet reached at this 60 seconds mark, a steady state simulation would be useless to investigate whether or not this 60 seconds mark can be reached. Furthermore, since it was unknown after how many seconds a steady state was reached, it was also difficult to estimate how close the current design was to reaching a steady state operating mode. It is therefore clear that a transient model is required. From a scientific point of view investigating the transient thermal behaviour of rocket engines is also interesting as during the literature study preceding this project [45] it became clear that the vast majority of studies in the scientific literature only consider the steady state.

In this chapter the complete set-up of the numerical model will be described. It should be noted that in this chapter a large number of equations will be shown, for each of these equations all parameters can be assumed to be expressed in SI units unless stated otherwise. The chapter is set up as follows: First the flow parameter and heat transfer modelling is discussed. This is followed by a discussion on how each of the several cooling methods are modelled. First radiation cooling is discussed in section 3.2, followed by regenerative cooling and thermal barrier coatings. In the section on radiation cooling the general conduction modelling and the time stepping scheme used for the transient solution is also discussed. In section 3.5 some additional transient solution methods are discussed which are useful to speed up the solution process for some cases. In this section it will also be discussed how the model can solve for the steady state solution directly. After this section the majority of the functions of the program are explained and the last three sections therefore focus more on the characteristics and verification of the model. In section 3.6 the meshing strategy used in the program is discussed, as a first verification step it will also be shown that grid convergence is achieved within the model. In section 3.7 a detailed verification of all aspects of the program is performed. Finally in section 3.8 a sensitivity analysis is performed on some input parameters which are somewhat uncertain to see what the effect of input errors is on the model results.

## 3.1. Flow parameter and heat transfer modelling

In this section the modelling of the flow parameters and heat transfer will be discussed. The models described here are applicable to the phenomena that occur within the combustion chamber itself and therefore these phenomena are independent of the cooling method chosen (at least for the cooling methods under consideration within this study). The section is divided in four subsections: first the modelling of the flow parameters within the combustion chamber will be discussed, followed by the heat transfer from the combustion gases to the wall. Afterwards the heat transfer within the wall is discussed followed by the heat transfer from the thruster to the environment.

### 3.1.1. Flow conditions

To calculate the heat transfer from the combustion gases to the combustion chamber wall it is first required to calculate the flow properties of the combustion gases itself. Within the model it is assumed that the flow of the combustion gases is steady. This assumption can be made because the transient behaviour of the combustion flow is relatively short compared to the time it takes for the thruster to heat up. Therefore the transient effects present during start-up of the engine are assumed to have a negligible effect on the heating “profile” of the thruster.

For an ideal rocket motor, the flow conditions of the combustion gases can be determined using the isentropic flow relationships. Three relationships in particular are of interest: equation 3.1 which can be used to determine the local Mach number of the flow, equation 3.2 which can be used to determine the local pressure of the flow and equation 3.3 which can be used to determine the local temperature of the flow.

$$\frac{A}{A^*} = \left(\frac{\gamma+1}{2}\right)^{-\frac{\gamma+1}{2(\gamma-1)}} \cdot \frac{\left(1+\frac{\gamma-1}{2}M^2\right)^{\frac{\gamma+1}{2(\gamma-1)}}}{M} \tag{3.1}$$

With $\gamma$ the specific heat ratio, M the mach number, $A$ the local cross sectional area of the combustion chamber/nozzle and $A^*$ the nozzle throat area. For a given design the values $A$ and $A^*$ are known and $\gamma$ can be determined. Using equation 3.1 the Mach number M can then be determined. As can be seen equation 3.1 is an implicit equation and needs to be solved iteratively. For a given area ratio two solutions can be found: a subsonic and a supersonic solution. In the model the Mach number is calculated for each cell, for cells before the nozzle throat only subsonic solutions for the Mach number are iterated while for the cells after the nozzle throat only supersonic solutions for the Mach number are used in the iteration. To decrease the computation time the Mach number of the previous cell is used as an initial guess for the Mach number in the next cell, reducing the amount of iterations required.

With the Mach number known in each station the local pressure was calculated using equation 3.2.

$$\frac{p}{p_t} = \left(1 + \frac{\gamma - 1}{2} M^2\right)^{\frac{-\gamma}{\gamma - 1}} \tag{3.2}$$

With $p_t$ being the total pressure and p being the local pressure at a given cross sectional area. In a somewhat similar fashion, the static temperature at each cell was calculated using equation 3.3.

$$T_c = T_o \cdot \left(1 + \frac{\gamma - 1}{2} \cdot M^2\right)^{-1} \tag{3.3}$$

With $T_o$ being the stagnation temperature.

To solve equations 3.1,3.2 and 3.3 values are required for $\gamma$, the total pressure, and the stagnation temperature. These values were determined using NASA CEA. NASA CEA is a chemical equilibrium tool which is developed and maintained by NASA's Glenn Research Center and which is freely available.[1] The CEA program works using a standardised input file. To link the CEA program with the MATLAB model a MATLAB function was written which automatically generates this input file, then runs CEA, and then reads out the output file. Besides the parameters $\gamma$, $p_t$ and $T_o$, NASA CEA is able to calculate many more flow parameters and some of these were also used within the model. A complete overview of the inputs and outputs of the CEA program as used within the model can be seen below in table 3.1.

Table 3.1: NASA CEA Inputs and Outputs as used within the model

| **Inputs** | **Outputs** |
|---|---|
| Chamber pressure | $\gamma$ |
| Ambient pressure | $T_c$ |
| Oxidiser used | $I_{sp}$ |
| Fuel used | $c^*$ |
| Oxidiser inlet temperature | $\mu$ |
| Fuel inlet temperature | Pr |
| O/F ratio | $p_{co2}$ |
| Supersonic area ratio (nozzle) | $p_{h_2o}$ |
| Subsonic area ratio (nozzle) | $C_p$ (frozen flow) |
| | Pr (frozen flow) |

CEA was used to compute the flow conditions along four stations in the combustion chamber as can be seen in figure 3.1: the combustion chamber/injector (station 1), the entrance of the convergent nozzle section (station 2), the nozzle throat (station 3), and the nozzle exit (station 4). Between these stations the value of the parameters are determined by interpolation.
It obviously would be more accurate to evaluate the flow parameters at more stations, however this would come at the cost of a larger code complexity. An investigation of the flow parameters evaluated by CEA shows that their variation is relatively small up until the nozzle throat where the heat flux is highest. In figure 3.2 the normalised flow parameters as interpolated from CEA can be seen. It can be seen that all parameters vary less than 10% between the injector and the nozzle throat. Because it is expected that the true functions representing the flow parameters do not have very large fluctuations it can be expected that the error that is introduced by interpolation for the analysis between the injector and the nozzle is small. In figure 3.2 it can also be seen that between the nozzle throat and the nozzle exit the flow parameters do vary by relatively large margins in some cases (up to 55%). Because the variation after the nozzle throat is larger the potential error could also be somewhat larger (but still << 55%). This was however not considered an issue as the heat flux is generally smaller in the divergent section of the nozzle, meaning that the analysis of the divergent

[1] Chemical Equilibrium with Applications, NASA Glenn Research Center, Christopher A. Snyder ,04/02/2016, Available online at: https://www.grc.nasa.gov/WWW/CEAWeb/

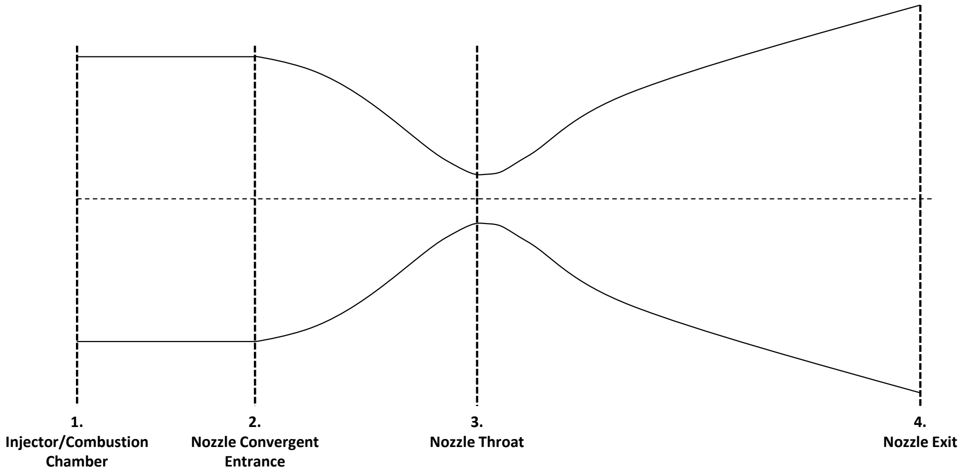


Figure 3.1: Stations in the combustion chamber for which CEA evaluates the flow properties

section of the nozzle is not the most critical from a thermal perspective. Therefore a slightly larger error was considered permissible here. The parameters which could potentially have a large error are also only relevant for the radiation heat transfer of the combustion gases, which usually accounts for only a small portion of the total heat transfer from the combustion gases. Furthermore, the analysis of this type of heat transfer was also only added to the program as an optional feature.

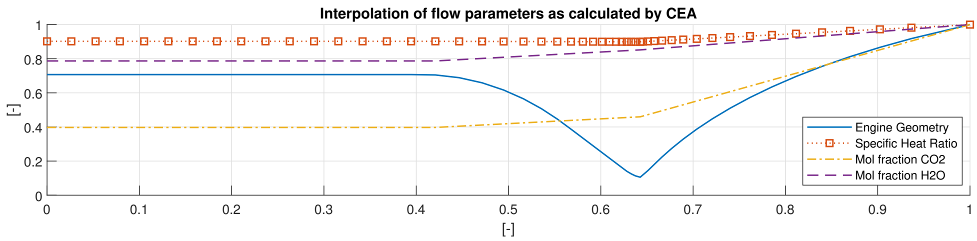


Figure 3.2: Various flow properties as a function of combustion chamber x-coordinate as interpolated from NASA CEA (all parameters normalised)

Another important parameter required for the determination of the heat transfer from the combustion gases to the combustion chamber wall is the adiabatic wall temperature. The adiabatic wall temperature represents a reference temperature which is used to calculate the heat transfer from the combustion gases to the wall. This reference temperature is required because in rocket engines there is significant heat transfer from the low speed flow near the wall to the free stream flow inside the chamber. This in turn causes the stagnation temperature of the fluid near the chamber wall to be less than the free stream temperature and therefore the free stream temperature can not be used to calculate the heat transfer from the combustion gases to the wall [12]. The adiabatic wall temperature can be calculated using equation 3.4.

$$T_{w_{ad}} = T_c \cdot \left(1 + r \cdot \frac{\gamma - 1}{2} \cdot M^2\right) \tag{3.4}$$

With $T_c$ being the local static temperature and $r$ being the recovery factor. The recovery factor is calculated using equation 3.5.

$$r = Pr^{1/3} \tag{3.5}$$

With Pr being the Prandtl number which can either be taken directly from CEA or which can be calculated using equation 3.6 [2].

$$Pr = \frac{4\gamma}{9\gamma - 5} \tag{3.6}$$

### 3.1.2. Heat transfer from the combustion gases

The heat transfer from the combustion gases to the combustion chamber wall is mainly governed by convection. The convective heat flux can be calculated using equation 3.7.

$$q = h_a \cdot (T_{w_{ad}} - T_w) \tag{3.7}$$

With $T_{w_{ad}}$ the adiabatic wall temperature as calculated earlier, $T_w$ the local wall temperature and $h_a$ the convective heat transfer coefficient. The main difficulty in solving this equation is finding the convective heat transfer coefficient. Several relations have been developed over the years to calculate the heat transfer coefficients in rocket engines. Two equations have been implemented within the program. The first and perhaps the most widely used of these equations is the Bartz equation which can be seen in equation 3.8 [2].

$$h_a = \left[\left(\frac{a}{D_t^{0.2}}\right) \cdot (\mu^{0.2} \cdot c_{p,g}/Pr^{0.6}) \cdot \left(\frac{p_c}{c^*}\right)^{0.8} \cdot \left(\frac{D_t}{r_c}\right)^{0.1}\right] \cdot \left(\frac{D_t}{D}\right)^{1.8} \cdot \phi \tag{3.8}$$

With the factor "a" being an empirical constant, usually taken to be 0.026, $D_t$ being the throat diameter, $\mu$ the viscosity of the combustion gases, $c_{p,g}$ the specific heat capacity of the combustion gases, $c^*$ the characteristic velocity, $r_c$ the longitudinal throat radius and D the local combustion chamber diameter. The parameters between the rectangular brackets are to be evaluated at total conditions, meaning that the heat transfer coefficient only varies with the local area ratio. Furthermore, it should be noted that the parameters $c_{p,g}$ and $Pr$ in equation 3.8 are evaluated at frozen flow conditions. The parameter $\phi$ is a correction factor to account for property variations across the boundary layer which can be calculated using equation 3.9.

$$\phi = \frac{[1 + M^2 \cdot (\gamma - 1)/2]^{-0.12}}{[0.5 + 0.5 \cdot (T_{w,g}/T_o) \cdot (1 + M^2 \cdot (\gamma - 1)/2)]^{0.68}} \tag{3.9}$$

The second equation which was implemented within the program was an equation by Cornelisse et al. which can be seen in equation 3.10 [14].

$$h_\alpha = 1.213 \cdot a \cdot \dot{m}^{0.8} \mu^{0.2} \cdot c_p \cdot Pr^{-2/3} \cdot D^{-1.8} \tag{3.10}$$

With "a" an empirical constant which is usually taken to be 0.023 for cross sections before the nozzle throat and between 0.025 and 0.028 for cross sections about one throat diameter after the nozzle throat [14].

It should be noted that equations 3.8 and 3.10 are semi-empirical and that these equations were not specifically developed for the thrusters considered within this study. The Bartz equation for example was specifically derived to be most accurate in the nozzle throat and the divergent section of the nozzle [2]. Both equations listed were also not specifically developed to predict heat transfer in the transient state although Di Matteo et al. [24] have shown that the Bartz equation is relatively accurate even when used for modelling heat transfer in the transient state. Still, equations such as equation 3.8 and 3.10 generally only give a rough estimate of the convective heat transfer coefficient and are therefore commonly calibrated for a specific application using experimental data [18, 23, 40]. In this study such a calibration will also be performed using experimental data. This will be discussed in more detail in chapter 4.

Besides convection, radiation from the combustion gases also contributes to the total heat transfer to the wall, although usually this contribution is relatively small [18, 40]. Calculating the contribution of radiation to the heat transfer precisely is a complex problem and usually multiple simplifications are made to get an approximate solution. One of the assumptions that is usually made is to assume that the combustion gases are a mixture of CO2 and H2O only. This assumption can be made because symmetrical molecules like H2, O2, and N2 contribute relatively little to the radiation heat transfer of the combustion gases while hetropolar gases like CO2 and H2O have relatively large contributions [40]. Another molecule which is present in the exhaust gases is CO, Kirchberger [18] studied heat transfer in small hydrocarbon based rocket engines and found that the contributions of CO to the radiation heat transfer can also be neglected, leaving CO2 and H2O as the main two radiating molecules within the combustion gas. Therefore the assumption that only CO2 and H2O are radiating within the combustion gases was also applied to the case studied here.

Kirchberger [18] gives several simple relationships which can be used to approximate the magnitude of the radiative heat transfer from CO2 and H2O for small hydrocarbon rocket engines. These can be seen below in equations 3.11 to 3.16.

$$\dot{q}_{rad,H_2O} = 4.07 \cdot \left(p_{H_2O}\right)^{0.8} \cdot (L_e)^{0.6} \cdot \left(\left[\frac{T_{wad}}{100}\right]^3 - \left[\frac{T_w}{100}\right]^3\right) \tag{3.11}$$

$$\dot{q}_{rad,CO_2} = 4.07 \cdot \left(p_{CO_2} \cdot L_e\right)^{0.33} \cdot \left(\left[\frac{T_{wad}}{100}\right]^{3.5} - \left[\frac{T_w}{100}\right]^{3.5}\right) \tag{3.12}$$

$$\dot{q}_{rad,H_2O} = (46.5 - 84.9 \cdot p_{H_2O} \cdot L_e) \cdot (p_{H_2O} \cdot L_e)^{0.6} \cdot \left[\frac{T_c}{100}\right]^{2.32+1.37\cdot\sqrt[3]{p_{H_2O}\cdot L_e}} \tag{3.13}$$

$$\dot{q}_{rad,CO_2} = 10.35 \cdot (p_{CO_2} \cdot L_e)^{0.4} \cdot \left[\frac{T_c}{100}\right]^{3.2} \tag{3.14}$$

$$\dot{q}_{rad,H_2O} = 5.74 \cdot (p_{H_2O} \cdot r_c)^{0.3} \cdot \left(\frac{T_c}{100}\right)^{3.5} \tag{3.15}$$

$$\dot{q}_{rad,CO_2} = 4 \cdot (p_{CO_2} \cdot r_c)^{0.3} \cdot \left(\frac{T_c}{100}\right)^{3.5} \tag{3.16}$$

Where $p_{CO_2}$ and $p_{H_2O}$ are the partial pressures of CO2 and H2O within the combustion gases respectively, $T_c$ is the temperature of the combustion gases as calculated using equation 3.3, $T_w$ is the wall temperature, and $r_c$ is the radius of the combustion chamber. $L_e$ is the so called effective radiation path and for a circular cylinder this can be calculated using equation 3.17 [17, 18].

$$L_e = 0.6 \cdot r_c \tag{3.17}$$

The partial pressures $p_{CO_2}$ and $p_{H_2O}$ are calculated by multiplying the local pressure as calculated using equation 3.2 with the local molar fraction of each of the respective species. The molar fractions of the two species are obtained using NASA CEA.

The total heat flux from radiation follows by simply summing the two heat flux terms as follows:

$$q_{rad} = \dot{q}_{rad,H_2O} + \dot{q}_{rad,CO_2} \tag{3.18}$$

Equations 3.13 to 3.16 were validated by Kirchberger in [17]. However the data available in literature is insufficient to perform an independent verification and validation of these equations. Therefore these equations were added to the program as an optional feature only.

### 3.1.3. Heat transfer within the combustion chamber walls

Within the combustion chamber wall the heat transfer is governed by conduction. The heat transfer by conduction can be calculated using the heat equation which is given below in equation 3.19.

$$\frac{\partial}{\partial x}\left(k_x\frac{\partial T}{\partial x}\right)+\frac{\partial}{\partial y}\left(k_y\frac{\partial T}{\partial y}\right)+\frac{\partial}{\partial z}\left(k_z\frac{\partial T}{\partial z}\right)+Q(x,y,z,t)=C\frac{\partial T}{\partial t} \tag{3.19}$$

In this equation the parameter k represent the thermal conductivity of the wall material, C represents the material heat capacity, x, y and z represent the spatial directions and t represents the time direction. A detailed overview of how this equation was implemented within the model will be given in section 3.2.

### 3.1.4. Heat transfer to the environment

Since the PM200 is intended to be used in space and is tested in a vacuum chamber, it is assumed that heat transfer to the environment is purely by radiation. Heat flux by radiation heat transfer can be calculated using equation 3.20.

$$q_r=\epsilon\cdot\sigma\cdot\left(T_w^4-T_{amb}^4\right) \tag{3.20}$$

Where $\epsilon$ is the emissivity of the material, $\sigma$ is the Stefan-Boltzmann constant $T_w$ is the temperature of the part of the wall exposed to the environment and $T_{amb}$ is the ambient temperature.

## 3.2. Radiation cooling / Conduction modelling

The temperature distribution of the thruster wall is of particular interest to determine the feasibility of a given thruster and cooling system design. As mentioned before, the temperature distribution within the thruster wall is governed by conduction. The conduction behaviour is for the most part modelled in the same way for all the cooling methods implemented within the model. The most simple case that can be modelled is that of a radiation cooled engine. Therefore this cooling method will be used as an example case to explain how the conduction modelling and time stepping was implemented within the model. It should be noted that this case is identical to the case of heat-sink / no cooling from a physical perspective and differs only in the sense that higher operating temperatures and a steady state are achieved when suitable materials are implemented to enable radiation cooling.

In the following text the logic of the program will be explained, within the program several different operators and discretised equations are used. In order to keep oversight the following conventions are used: scalar operators are written in *italic*, while vector and matrix operators are written in **boldface**. Furthermore, the notation used here corresponds in large part to the notation used in [27], which was one of the main references used for the derivation of the following equations and for the development of the numerical model. Because of this, temperature values which are calculated using ideal rocket theory and analytical equations will be represented using the parameter $T$ while the temperature values calculated using the numerical finite volume scheme will be indicated by the parameter $\phi$. There is a good reason to do this, as the set of assumptions that holds for $T$ is in general not equal to the set of assumptions that holds for $\phi$, in many cases within this report $\phi$ can however be used as a good approximation of $T$.

The main equation to be solved for determining the temperature distribution within the wall is the heat conduction equation given by equation 3.19. This equation is derived from several conservation laws, namely: conservation of Mass, Momentum and Energy. In a more general form these conservation laws lead to an equation which can be written as [27]:

$$\underbrace{\frac{\partial}{\partial t}(\rho\phi)}_{unsteady\ term}+\underbrace{\nabla\cdot(\rho\mathbf{v}\phi)}_{convection\ term}=\underbrace{\nabla\cdot(\Gamma^{\phi}\nabla\phi)}_{diffusion\ term}+\underbrace{Q^{\phi}}_{source\ term} \tag{3.21}$$

Note that $\phi$ in equation 3.21 does not necessarily have to represent temperature, $\phi$ can represent any intensive property [27]. In the remainder of this text it will however be assumed that $\phi$ represents a temperature. To determine the heating of the wall over time by conduction, only the first and third term in equation 3.21 are relevant. By adding the specific heat capacity $c_p$ the diffusion equation for heat conduction can be obtained [46]:

$$\frac{\partial}{\partial t}(\rho c_p \phi) = \nabla \cdot (\Gamma^{\phi} \nabla \phi) \tag{3.22}$$

With $\phi$ representing the temperature, $t$ the time value, $\rho$ the wall material density and $\Gamma^{\phi}$ the diffusivity, which in this case is equal to the thermal conductivity $k$. Note that this equation is identical to equation 3.19 minus the source term. To solve this equation the problem was split into two parts (the unsteady term and the diffusion term) which were each solved separately. The diffusion term was solved using a finite volume method while the unsteady term was solved using a finite difference method. The reason for this will become clear in the next two subsections where the implemented solution of equation 3.22 will be described.

### 3.2.1. Solution of the diffusion term (Finite Volume Method)

The diffusion term of equation 3.22 was solved using a finite volume method. In order to do so the thruster wall had to be divided into finite volumes and a mesh had to be generated. In doing so it was assumed that the temperature distribution varied only in the radial and axial direction and that the temperature distribution was axisymmetric. This assumption can be made as the thruster geometry is (for the most part) axisymmetric leading to the distribution of the heat flux from the combustion gases being axisymmetric as well. By making this assumption the mesh can be reduced from a 3D mesh to a 2D mesh which simplifies the calculations.

The thruster was meshed using a structured, non-orthogonal quadrilateral mesh (i.e. the mesh consists of quadrilaterals with arbitrary shape and each quadrilateral is connected to four other quadrilaterals with the exception of the cells at the boundaries). To keep the mesh somewhat simple the “vertical” vertices of the mesh were all made parallel to each other and perpendicular to the axis of symmetry while the “horizontal” vertices of the mesh were made to be parallel to the wall surfaces whenever possible. The program was set up such that these rules are not required for the mesh and in principle the program can work for any structured, non-orthogonal quadrilateral mesh. However, applying these restrictions to the mesh makes it easier to intuitively see what is going on within the program.

The amount of mesh cells can be specified beforehand by the user in both the x-direction and the radial direction. Throughout the cross section the amount of cells in x and radial direction are kept constant to keep the mesh structured. As a side effect this has the benefit that a smaller cell size is obtained at locations were the wall thickness is smaller. Besides the factors mentioned above the mesh was also made such that the cell size in the x direction at any given point is proportional to the local diameter. This ensures that cell sizes are smaller near the nozzle throat were the highest heat fluxes are expected to occur, leading to a more accurate solution. An example mesh as generated by the program can be seen in figure 3.3.

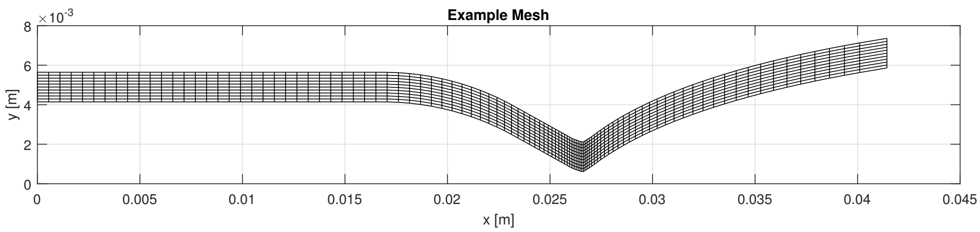


Figure 3.3: An example mesh for a reference thruster with 100 cells in the x direction and 10 cells in the radial direction

With the thruster geometry subdivided into a mesh the diffusion term (equation 3.23) can now be solved over the entire domain.

$$\nabla \cdot (\Gamma^{\phi} \nabla \phi) \tag{3.23}$$

The diffusion term will be solved on each of the elements within the domain. Integrating equation 3.23 over an arbitrary element C with volume $V_c$ and applying divergence theorem it can be shown that:

$$\int_{V_c} \nabla \cdot (\Gamma^{\phi} \nabla \phi) dV = \oint_{\partial V_c} (\Gamma^{\phi} \nabla \phi) \cdot d\mathbf{S} \tag{3.24}$$

With **S** being the surface vector of each of the boundary surfaces of the cell. Equation 3.24 basically states that the the sum of the temperature fluxes over the boundary surfaces is equal to the divergence in temperature over the element volume. The right hand-side of equation 3.24 can be simplified further using a Gaussian quadrature. If one integration point at the face centroid is used (this point will be designated as point f) the surface integral simply becomes the sum of the scalar product of each of the surface flux values ($\Gamma^{\phi} \nabla \phi_f$) and their surface vectors ($\mathbf{S}_f$) (left hand side in equation 3.29).

The surface vectors $\mathbf{S}_f$ follow from the geometry and the mesh selected. The evaluation of the surface flux requires the evaluation of the surface gradient, which is more complicated. To explain the general principle, the surface gradient in point f will first be determined for the orthogonal case. For an orthogonal grid the evaluation of the surface gradient is relatively straightforward and this can be done using equation 3.25.

$$(\nabla \phi \cdot \mathbf{e})_f = \left( \frac{\partial \phi}{\partial e} \right)_f = \frac{\phi_F - \phi_C}{||\mathbf{r}_F - \mathbf{r}_C||} \tag{3.25}$$

Where $\phi_C$ is the temperature value in the cell for which the integral is being evaluated, $\phi_F$ is the temperature value in one of the neighbouring cells, $\mathbf{r}_F$ and $\mathbf{r}_C$ are the position vectors of the centroids of each cell and **e** is the unit vector in the direction of the line which connects centroids C and F. The unit vector **e** is given by equation 3.26.

$$\mathbf{e} = \frac{\mathbf{r}_F - \mathbf{r}_C}{||\mathbf{r}_F - \mathbf{r}_C||} \tag{3.26}$$

Basically equation 3.25 states that the surface gradient at point f can be approximated as the difference between the temperature in two points divided by the distance between the two points.

In reality, the mesh is not orthogonal and in this case the surface vector is not in the direction of **e**. It then follows that the flux is not purely orthogonal and therefore the vector $\mathbf{S}_f$ has to be decomposed into a vector in the **e** direction ($\mathbf{E}_f$) representing the orthogonal contribution of the flux and a vector in the **t** direction ($\mathbf{T}_f$) representing the non-orthogonal contribution to the flux (see figure 3.4). Several different options exist for the decomposition of $\mathbf{S}_f$ into the vectors $\mathbf{E}_f$ and $\mathbf{T}_f$. The approach chosen here is the over-relaxed approach [27] a schematic of which can be seen in figure 3.4.

From figure 3.4 it can be seen that in the over-relaxed approach the vectors $\mathbf{E}_f$ and $\mathbf{T}_f$ can be calculated using equations 3.27 and 3.28 respectively.

$$\mathbf{E}_f = \frac{\mathbf{S}_f \cdot \mathbf{S}_f}{\mathbf{e} \cdot \mathbf{S}_f} \mathbf{e} \tag{3.27}$$

$$\mathbf{T}_f = \mathbf{S}_f - \mathbf{E}_f \tag{3.28}$$

Using the results obtained above and using a Gaussian quadrature with one integration point (point f in figure 3.4) the integral on the right hand side of equation 3.24 can be written as equation 3.29 which represents the solution of the diffusion term.

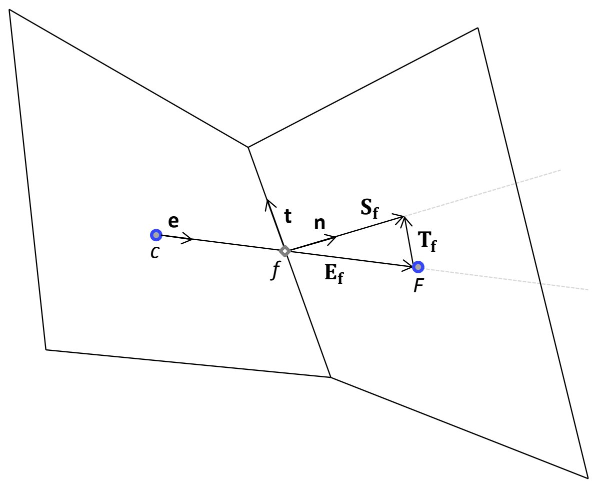


Figure 3.4: Definition of vectors used within the model (over-relaxed approach)

$$\sum_{f \,\epsilon\, C} \left( - \left(\Gamma^{\phi} \nabla \phi\right)_f \cdot \mathbf{S}_f \right) = \sum_{f \,\epsilon\, C} \left( - \left(\Gamma^{\phi} \nabla \phi\right)_f \cdot \mathbf{E}_f \right) + \sum_{f \,\epsilon\, C} \left( - \left(\Gamma^{\phi} \nabla \phi\right)_f \cdot \mathbf{T}_f \right) \tag{3.29}$$

For clarification in figure 3.5 a small section of a thruster is shown with the integration points, the cell centroids and the vectors $\mathbf{E}_f$, $\mathbf{T}_f$ and $\mathbf{S}_f$ indicated (vectors not to scale). The cell centroids are indicated by the blue circles, the integration points are indicated by the red circles, the $\mathbf{E}_f$ vectors are indicated by the blue vectors, the $\mathbf{T}_f$ vectors are indicated by the orange vectors and the $\mathbf{S}_f$ vectors are indicated by the green vectors.

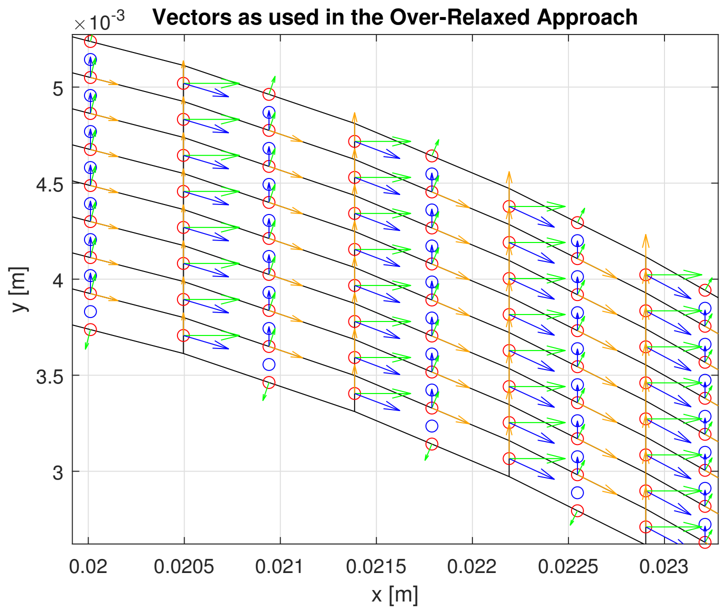


Figure 3.5: Example showing the vectors (not to scale), integration points and centroid locations for a small section of a thruster.

Before equation 3.29 can be applied, the temperature gradient $\nabla\phi_f$ at the integration point still has to be evaluated for the non orthogonal case. This evaluation was done by expressing the gradient $\nabla\phi_f$ as a function of the gradients in the centroids of the two surrounding cells as shown in equation 3.30.

$$\nabla\phi_f = g_c\nabla\phi_C + (1 - g_c)\nabla\phi_F \tag{3.30}$$

Where $g_c$ is a geometric interpolation factor which is calculated using equation 3.31.

$$g_c = \frac{d_{Cf}}{d_{Cf} + d_{fF}} \tag{3.31}$$

Where d represents the distance between the two points specified in the subscript.

For the calculation of the gradients $\nabla\phi_C$ and $\nabla\phi_F$ at the cell centroids divergence theorem can again be exploited. Using divergence theorem the gradients at the cell centroids can be written purely as a function of the temperature on the boundaries of each cell as can be seen in equation 3.32.

$$\int_V \nabla\phi dV = \oint_{\partial V} \phi d\mathbf{S} \tag{3.32}$$

The integral on the right hand side of this equation can again be approximated as the sum of the face centroid temperature value (the temperature in point f) multiplied by the surface vector. The left hand side of the equation can be evaluated using mean value theorem to obtain the average gradient at the centroid. The result can be seen in equation 3.33.

$$\nabla\phi_C = \frac{1}{V_C}\sum_{f\,\epsilon\,C} \phi_f \mathbf{S}_f \tag{3.33}$$

The question now becomes how to calculate $\phi_f$. For this the extended stencil method by B.K. Soni [39] was used. In this method the value of $\phi_f$ is estimated as the mean of the values of $\phi$ at the nodes of the surface boundary ($\phi_n$). The values of $\phi_n$ are in turn estimated using equation 3.34. This equation calculates the value of $\phi_n$ as the weighted average of the surrounding (known) $\phi_C$ values.

$$\phi_n = \frac{\sum_{k=1}^{NB(n)} \frac{\phi_{F_k}}{||\mathbf{r}_n - \mathbf{r}_{F_k}||}}{\sum_{k=1}^{NB(n)} \frac{1}{||\mathbf{r}_n - \mathbf{r}_{F_k}||}} \tag{3.34}$$

After the value of $\phi$ at the nodes is found the value of $\phi_f$ is found using equation 3.35.

$$\phi_f = \frac{\phi_{n_1} + \phi_{n_2}}{2} \tag{3.35}$$

Where $\phi_{n_1}$ and $\phi_{n_2}$ represent the temperature values at the two surface boundary nodes. Substituting equation 3.35 into equation 3.33 the following result can be obtained.

$$\nabla\phi_C = \frac{1}{V_C}\sum_{f\,\epsilon\,C} \left(\frac{\phi_{n_1} + \phi_{n_2}}{2}\right)_f \mathbf{S}_f \tag{3.36}$$

The approach described above has the advantage that it is fast, intuitive, and easy to implement. It also has two disadvantages, the first one is that information from the “wrong” side of the cell also contributes to the estimate being made [27]. The second disadvantage of this approach is that the $\phi_n$ values at the mesh boundaries will only be calculated using the $\phi_C$ values at the boundary cells, meaning that the heat flow into and out of the walls is not taken into account for the estimation of the $\phi_n$ values. This is however not a big problem as the heat flows at the mesh boundaries are defined by von Neumann boundary conditions and therefore these nodal values are not required for any actual calculations. However if one were to plot the temperature of the nodal values this error could cause confusion. This error decreases rapidly with cell size so this error can be made negligible if needed by refining the mesh. It is also possible to calculate the nodal values at the boundaries more accurately using different techniques [27], however since this has only a small impact on the solution, especially as the mesh gets more refined, it was decided to not implement this in order to keep code complexity down.

As mentioned before, in the case considered here the diffusivity $\Gamma^{\phi}$ is equal to the thermal conductivity $k$ of the wall material. The thermal conductivity for a given material is not constant with temperature and usually changes with a relation of the form:

$$k = B + \sum_{n=1}^{m} A_m \cdot T^m \tag{3.37}$$

For a wide variety of materials these equations are known and validated for specific temperature ranges. An overview of many such equations can be found in [44] and these equations were used where applicable. If materials were simulated for which such equations were not readily available the equations were created manually by fitting equation 3.37 to data available in manufacturer data sheets or scientific literature ([10, 26, 36, 44]) using a regression analysis. The resulting equations usually have a very high accuracy. For example in the case of the stainless steel alloy used within the PM200 the $R^2$ value of the fit obtained with equation 3.37 was found to be 0.9985 and the Standard Error of the Estimate (SEE) was found to be 0.0773.

In case the temperature of the wall material exceeds the validity range of the equations derived from equation 3.37 and the equations given in [44], the equations are evaluated at the maximum (or minimum) temperature for which the equation is still valid. This is obviously a source of error, however it is still more accurate than assuming a constant value. It is also possible to extrapolate the equations beyond the validity ranges given, this however may lead to nonphysical results so therefore this was not implemented in the model.

To evaluate the temperature fluxes over the boundary surfaces as stated in equation 3.29 a value for $\Gamma^{\phi}$ is required on the boundary surface. The thermal conductivity as calculated in equation 3.37 is however calculated at each of the cell centroids. Therefore a conversion needs to be performed to obtain the value for $\Gamma^{\phi}$ on the boundary surfaces at point f. The value of the diffusivity at this point can be calculated using equation 3.38.

$$\Gamma_f^{\phi} = (1 - g_c)\Gamma_C^{\phi} + g_c\Gamma_F^{\phi} \tag{3.38}$$

Where $\Gamma_C^{\phi}$ and $\Gamma_F^{\phi}$ are the diffusivity values at the cell centroids and where $g_c$ is the geometric interpolation factor as defined by equation 3.31.

As was briefly mentioned earlier, on the boundaries of the grid a von Neumann boundary condition was applied. This is essentially a heat flux specified boundary condition. For cells on the inside of the combustion chamber these boundary conditions are specified using the sum of the values calculated from equations 3.7 and 3.18. For the outside of the thruster these boundary conditions are specified using the radiation heat transfer to the environment as calculated using equation 3.20. The heat flux at the boundary at the front of the combustion chamber and the boundary at the nozzle exit are also calculated using equation 3.20.

### 3.2.2. Solution of the unsteady term (Finite Difference Method)

To solve the Diffusion equation (equation 3.22) in the time dimension a finite difference approach is used. This can be done because the grid in the time direction is one dimensional and structured. Because of this there are no non-orthogonal-like terms as were encountered in the spacial domain and the evaluation simplifies. In the following, the approach as detailed by [27] is again adopted.

Returning to diffusion equation as specified in equation 3.22 and changing the notation slightly, the following equation can be obtained:

$$\frac{\partial(\rho c_p \phi)}{\partial t} + \Lambda(\phi) = 0$$

Where $\Lambda(\phi)$ represents the sum of all the non-transient terms (i.e. the diffusion term in this case). Integrating this equation over an element C and discretizing about the volume centroid equation 3.39 can be obtained.

$$\frac{\partial(\rho_c c_p \phi_c)}{\partial t} V_c + L(\phi_c^t) = 0 \tag{3.39}$$

In equation 3.39 the term $L(\phi_c^t)$ represents the discretized version of $\Lambda(\phi)$, which is the result from equation 3.29 as described in the previous section. From this it follows that the only step left in order to solve equation 3.39 is to evaluate the term $\frac{\partial(\rho_c c_p \phi_c)}{\partial t}$. This term can be approximated by performing a Taylor series expansion of the term $(\rho_c c_p \phi_c)$ at point $t + \Delta t$ to obtain equation 3.40.

$$(\rho c_p \phi)_{t+\Delta t} = (\rho c_p \phi)_t + \left.\frac{\partial(\rho c_p \phi)}{\partial t}\right|_t \Delta t + \left.\frac{\partial^2(\rho c_p \phi)}{\partial t^2}\right|_t \frac{\Delta t^2}{2!} + \left.\frac{\partial^3(\rho c_p \phi)}{\partial t^3}\right|_t \frac{\Delta t^3}{3!} + \ldots \tag{3.40}$$

Rewriting equation 3.40 and truncating the series at $O^2$ terms an expression for $\frac{\partial(\rho_c c_p \phi_c)}{\partial t}$ can be obtained as seen in equation 3.41.

$$\frac{\partial(\rho_c c_p \phi_c)}{\partial t} = \frac{(\rho c_p \phi)_{t+\Delta t} - (\rho c_p \phi)_t}{\Delta t} \tag{3.41}$$

By substituting this result into equation 3.39 and rearranging terms an equation for the temperature at the next time step can be obtained as is seen in equation 3.42.

$$\phi_{t+\Delta t} = \phi_t - \frac{L(\phi_t)\Delta t}{V_c \rho c_p} \tag{3.42}$$

This scheme is called the Forward Euler scheme. The Forward Euler scheme is not unconditionally stable. It can be shown that for the Forward Euler scheme the time step $\Delta t$ has to satisfy the requirement outlined in equation 3.43 for stability.

$$\Delta t \leq \frac{\rho_{t-1} V_c c_p}{\sum_{f \, \epsilon \, C} \Gamma_f^{\phi} \frac{E_f}{d_{CF}}} \tag{3.43}$$

Starting at a certain start temperature, the temperature at the next time step can thus be calculated using equation 3.42. The next time step is governed by the criterion specified in equation 3.43. In the program for every mesh cell equation 3.43 is evaluated, the maximum allowed time step is then determined by comparing the values for every cell and the program proceeds to the next time step using this maximum time step.

### 3.2.3. Code implementation details

In this section the model implementation of the equations mentioned in the previous sections will be presented. In figure 3.6 a flow diagram can be seen which explains the program logic for a radiation cooled engine.

As can be seen from figure 3.6 the program consists of three main loops: the time loop, the x-loop and the y-loop. Each of these loops corresponds to a set of calculations being performed in a certain dimension/direction. In this case the time dimension, the axial direction, and the radial direction respectively. Within these three loops the following steps are performed:

- **Step 1:** Calculate the temperatures at the nodes for the current time step. (Equation 3.34)
- **Step 2:** Calculate the temperature gradient at every centroid. (Equations 3.36)

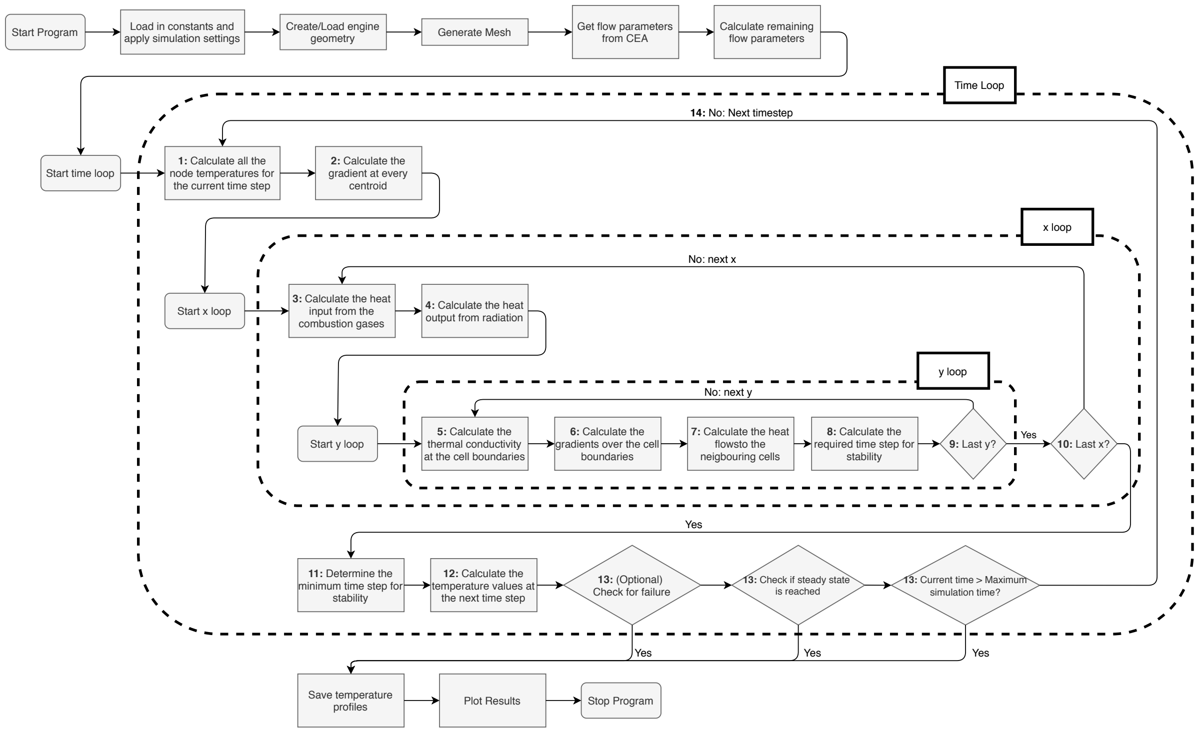


Figure 3.6: Flow diagram showing the program logic for the thruster temperature when radiation cooling is used.

- **Step 3:** Calculate the heat input from the combustion gases. (Equations 3.7 and 3.8 or 3.10)
- **Step 4:** Calculate the heat output from radiation. (Equation 3.20)
- **Step 5:** Calculate the thermal conductivity at the cell boundaries. (Equation 3.38)
- **Step 6:** Calculate the gradients over the cell boundaries. (Equation 3.30)
- **Step 7:** Calculate the heat flows between each cell. (Equation 3.29)
- **Step 8:** Calculate the required time step for stability (for the current cell). (Equation 3.43)
- **Step 9:** Return to step 5 for the next cell in the y-direction. If this is the last cell in the y-direction continue to step 10.
- **Step 10:** Return to step 3 for the next cell in the x-direction. If this is the last cell in the x-direction continue to step 11.
- **Step 11:** From all the time steps calculated in step 8, determine the minimum time step and increase the time by this time step.
- **Step 12:** Calculate the temperature at the next time step. (Equation 3.42)
- **Step 13:** Check if the stopping criteria is satisfied.
- **Step 14:** Return to step 1 for the next time step.

Looking at the flow diagram in figure 3.6 it can be seen that the code marches through the the mesh from the bottom left cell, which is designated with coordinates (1,1) to the top right cell (m,n). It does this by evaluating all parameters for the column of cells at a given x-coordinate before moving on to the next column of cells. One thing to note is that for neighbouring cells the flux between these two cells is equal in magnitude but opposite in sign when calculated for a certain cell (i.e. the flux from cell (1,1) to (1,2) is equal to the flux from cell (1,2) to (1,1) but opposite in sign). This is because they are physically the same flux but just calculated in a different reference frame (with respect to cell (1,1) or with respect to cell (1,2) ). To save memory and to simplify the program the choice was therefore made to only calculate the flux on the upper and right most boundaries of each cell. The fluxes from the lower and left boundaries of each cell are obtained by taking the flux calculated in the previous cell in either direction and applying the sign change. Only for the first layer of cells in the y-direction and the first layer in the x-direction the flux values of the left and bottom boundary are explicitly calculated. Using this strategy the amount of calculations can be halved, reducing the amount of computational time required. Graphically this can also be seen in figure 3.5, where it can be seen that the vectors used to calculate the flux are always pointing to the right and up, with the exception of the vectors on the bottom layer of cells. It can be seen that the vectors on the lower boundary of the bottom layer of cells point downwards.

After the 12 step process outlined above has been completed, three checks are performed to see if the code needs to keep running. First an (optional) failure analysis is performed, more details about this failure analysis can be found in Appendix B.2. Secondly a steady state check is performed, this check is performed by summing the change in the temperature values between the current and the previous pre-specified time step (so not the time step calculated in step 8, but usually a larger time step; in the simulation results presented in this report a value of 0.1s was used) and checking if the sum of the change of temperature is equal to 0.01 times the amount of cells. In other words, if the average change in temperature per cell is less than 0.01 K the model assumes that a steady state is achieved. This criterion can also be relaxed to speed up the program if required. The previously mentioned pre-specified time step is not only used for the steady state check, this time step is also used as the interval at which the temperature data is stored. The last check which is performed to check whether or not the code should still keep running is a check of the current simulation time. When running the program a maximum simulation time can be set, if this time is exceeded the simulation will also terminate.

Upon termination, the program outputs several datasets, a ".mat" file is created which contains all the simulation settings, as well as all data gathered during the simulation. Additionally a number of ".csv" files is created which contain the temperature distribution for a certain row of y-cells for every time step of the previously mentioned pre-specified time step. For example if a 50x5 mesh is used and the simulation is run for 10 seconds with a time step of 0.1s, 5 ".csv" files will be created each containing the temperature distribution at a certain y-location for 101 time steps (because the "zeroth" time step is also included).

## 3.3. Regenerative cooling

The second cooling case considered with in the model is Regenerative cooling. Two different cases for regenerative cooling were considered: the case were the cooling channels are oriented in the axial direction and the case were the cooling channels are oriented as a helix around the combustion chamber. Although a large overlap exists in the analysis of these two cases, the axial case is the most simple to evaluate and therefore this case will be discussed first. The case where the cooling channels are oriented in the tangential direction (i.e. oriented as a helix) will be discussed in section 3.3.3.

The analysis for the thermal distribution for the regeneratively cooled case is in a large part identical to the analysis performed for the radiation / heat-sink cooling model. The heat transfer between the combustion gases and the combustion chamber wall is the same and the conduction modelling within the walls is identical as well. In this case a cooling channel is however also present in the wall. The first step to model such a cooling channel is to calculate the cooling fluid properties.

### 3.3.1. Cooling Fluid Properties

In order to determine how much of the heat within the combustion chamber walls is transferred to the cooling channel the properties of the flow within the cooling channels need to be determined. In this section it is assumed that Nitrous Oxide is used as the coolant, but a similar analysis is possible for any other propellant/coolant.

The fluid properties of a given fluid are related to each other by an equation of state. Multiple equations of state have been developed over the years for Nitrous Oxide with varying degrees of accuracy and applicability. Within the model used in this study the equation of state by Lemmon and Span [21] was used. This equation of state is very accurate with an error below 0.1% for the calculation of the density and an error below 2% for the calculation of the heat capacity. The equation of state developed by Lemmon and Span uses the Helmholtz energy to calculate the fluid properties and can be seen in equation 3.44.

$$\alpha(\delta,\tau) = \alpha^0(\delta,\tau) + \alpha^r(\delta,\tau) \tag{3.44}$$

Where $\delta$ is defined as $\rho/\rho_{crit}$ with $\rho$ and $\rho_{crit}$ the density and critical density of the coolant fluid respectively. The factor $\tau$ is defined as $T/T_{crit}$ with $T$ and $T_{crit}$ being the temperature and critical temperature of the coolant fluid. $\alpha^0$ and $\alpha^r$ represent the Helmholtz energy of the ideal gas and real gas respectively. They can be calculated using equations 3.45 and 3.46.

$$\alpha^0 = a_1 + a_2 \cdot \tau + ln\delta + (c_0 - 1)ln\tau - \frac{c_1(T_{crit}/K)^{c_2}}{c_2(c_2+1)}\tau^{-c_2} + \sum_{k=1}^{5} v_k ln[1 - exp(-u_k\tau/T_{crit})] \tag{3.45}$$

The remaining parameters in equation 3.45 are the so called “Einstein” constants and these can be found for various gases including Nitrous Oxide in [21].

$$\begin{aligned}\alpha^r(\delta,\tau) = {} & n_1\delta\tau^{0.25} + n_2\delta\tau^{1.25} + n_3\delta\tau^{1.5} + n_4\delta^3\tau^{0.25} \\ & + n_5\delta^7\tau^{0.875} + n_6\delta\tau^{-\delta} + n_7\delta^2\tau^{2.0}e^{-\delta} + n_8\delta^5\tau^{2.125}e^{-\delta} \\ & + n_9\delta\tau^{3.5}e^{-\delta^2} + n_{10}\delta\tau^{6.5}e^{-\delta^2} + n_{11}\delta^4\tau^{4.75}e^{-\delta^2} + n_{12}\delta^2\tau^{12.5}e^{-\delta^3}\end{aligned} \tag{3.46}$$

The parameters $n_1$-$n_{12}$ in equation 3.46 are again constants which can be determined for a given fluid and which are listed in [21] for Nitrous Oxide.

Using the equation of state the density of the coolant at any cell can be calculated using equation 3.47.

$$\rho = \frac{p}{RT\left(1 + \frac{1}{\rho_c}\left(\frac{\partial\alpha^r}{\partial\delta}\right)_\tau\right)} \tag{3.47}$$

The (isobaric) heat capacity of the cooling fluid can be calculated in each cell using equation 3.48

$$c_p = \left(\frac{c_v}{R} + \frac{\left[1 + \delta\left(\frac{\partial\alpha^r}{\partial\delta}\right)_\tau - \delta\tau\left(\frac{\partial^2\alpha^r}{\partial\delta\partial\tau}\right)\right]^2}{\left[1 + 2\delta\left(\frac{\partial\alpha^r}{\partial\delta}\right)_\tau + \delta^2\left(\frac{\delta^2\alpha^r}{\partial\delta^2}\right)_\tau\right]}\right) \cdot R \tag{3.48}$$

With R the gas constant and $c_v$ the isochoric heat capacity equal to:

$$c_v = -R\tau^2\left[\left(\frac{\partial^2\alpha^0}{\partial\tau}\right)_\delta + \left(\frac{\partial^2\alpha^r}{\partial\tau^2}\right)_\delta\right] \tag{3.49}$$

Solving equations 3.47,3.48 and 3.49 is a relatively time intensive task due to the fact that the value of $\delta$ needs to be determined using an iterative approach. Using a numerical solver in Matlab a single evaluation of $\delta$ could take up to 1.36 seconds. This is obviously problematic since $\delta$ has to be evaluated millions of times during a single run of the program. Therefore a separate script was written which solved for $\delta$ using a numerical method after which the solution was tabulated for a large amount of combinations of densities and temperatures. Within the main program the correct value for $\delta$ was then found by bilinear interpolation of the values from this table. After obtaining the value for $\delta$ it was substituted into equations 3.47,3.48 and 3.49 which were then solved analytically. The resulting density and heat capacity values as calculated from the interpolated values of $\delta$ were found to be accurate within 0.15% as will be shown in section 3.7.3. The choice to solve equations 3.47,3.48 and 3.49 analytically was made because it was found that this was approximately 20 times faster than using the numerical solver in Matlab.

Using equations 3.47,3.48 and 3.49 the density and heat capacity of the cooling fluid were calculated at any cell for a given pressure and temperature at the cell.

The pressure at a given cell has to be calculated sequentially, in this case the pressure can simply be calculated by subtracting the total pressure drop at the current cell from the pressure in the previous cell. For the first cell the pressure is defined by the inlet pressure. The pressure drop in the cooling channels was calculated using the method presented by Naraghi et al. [28]. The total pressure drop per cell is described by equation 3.50 and consists of two terms: pressure drop due to friction (viscous pressure drop, $\Delta P_{v_{i,i-1}}$ ), and a pressure drop due to a change in cooling channel area ($\Delta P_{c-e_{i,i-1}}$).[2]

$$\Delta P_{i,i-1} = \Delta P_{v_{i,i-1}} + \Delta P_{c-e_{i,i-1}} \tag{3.50}$$

The viscous pressure drop can be calculated using the Darcy–Weisbach equation:

$$\Delta P_{v_{i,i-1}} = \frac{f_i \cdot \rho \cdot v_c^2 \cdot \Delta x_{i,i-1}}{2 \cdot D_h} \tag{3.51}$$

Where $f_i$ is a friction factor, $v_c$ the coolant velocity, $D_h$ the hydraulic diameter of the cooling channel, and $\Delta x_{i,i-1}$ the cell length. For low Reynolds numbers the friction factor is only dependent on Reynolds number, while for high Reynolds numbers the roughness of the cooling channel also plays a role (see equations 3.52 and 3.53). Naraghi [28] uses the Colebrook equation to calculate the friction factor, however this equation is implicit and requires an iterative approach to solve which is quite computationally intensive. An alternative equation is the equation presented by Chen [8] (equation 3.53). This equation gives very similar results to the Colebrook equation but is instead explicit and therefore requires less computing time to evaluate. Because of this advantage it was decided to implement the equation by Chen instead of the Colebrook equation. The friction factor is then calculated using equations 3.52 and 3.53 with the former being used if the Reynolds number is low and the latter being used for higher Reynolds number flows.

$$f_i = 64/Re \qquad \text{For } Re \leq 2300. \tag{3.52}$$

$$f_i = \left( \frac{1}{-2 \cdot log10\left(\frac{e_f}{3.7065}\right) - \left(\frac{5.0452}{Re}\right) \cdot log10(A)} \right)^2 \qquad \text{For } Re > 2300. \tag{3.53}$$

With A equal to:

$$A = \frac{e_f^{1.1098}}{2.8257} + \left(\frac{7.149}{Re}\right)^{0.8981} \tag{3.54}$$

With $e_f$ being the channel roughness of the cooling channel. Since the PM200 thruster is additively manufactured (i.e. 3D printed), the channel roughness is in this case equal to the

[2] For completeness, it is also possible to include a momentum pressure drop $\Delta P_{m_{i,i-1}}$ due to fluid acceleration. This term was however not included within the model because the calculation of this term requires an iterative approach which would slow down the model. In text books and other sources this term is usually also neglected [14, 32, 40].

surface finish accuracy of the 3D printer used.

The pressure drop due to a change in coolant channel area can be calculated using equation 3.55.

$$\Delta P_{c-e_{i,i-1}} = \frac{K \cdot \rho \cdot v_c^2}{2} \tag{3.55}$$

Where K is a geometrical factor dependent on the contraction or expansion of the channel between to subsequent cells. In the case expansion takes place between two cells K is calculated using equation 3.56.

$$K = \left[\left(\frac{D_{h_i}}{D_{h_{i-1}}}\right)^2 - 1\right]^2 \tag{3.56}$$

For the case when contraction takes place between two cells K is calculated using equation 3.57.

$$K = 0.5 - 0.167\frac{D_{h_{i-1}}}{D_{h_i}} - 0.125\left(\frac{D_{h_{i-1}}}{D_{h_i}}\right)^2 - 0.208\left(\frac{D_{h_{i-1}}}{D_{h_i}}\right)^3 \tag{3.57}$$

After calculating the pressure drop terms discussed above, the pressure in the next cell can be calculated by simply subtracting the sum of the pressure drop terms from the pressure in the current cell as can be seen in equation 3.58.

$$P_{i-1} = P_i - (\Delta P_{v_{i,i-1}} + \Delta P_{c-e_{i,i-1}}) \tag{3.58}$$

With the pressure in each cell known, only the temperature in each cell is required to evaluate equations 3.47,3.48 and 3.49. For the first time step this temperature is obviously equal to the inlet temperature or to the bulk temperature of the coolant in the tank. For the thrusters considered within this study this temperature is equal to the ambient temperature. To calculate the temperatures within the cooling channel for later time steps an approach similar to as discussed in section 3.2.2 is used.

The heat flux from the combustion chamber wall to the cooling fluid is calculated using equation 3.59.

$$q_{wc} = q_{conv,wc} + q_{rad,wc} \tag{3.59}$$

With $q_{conv,wc}$ the convective heat flux and $q_{rad,wc}$ the radiation heat flux. The convective heat flux is calculated in a similar way as the convective heat flux from the combustion gases to the chamber wall by rewriting equation 3.7 into equation 3.60.

$$q_{conv,wc} = h_c \cdot (T_w - T_b) \tag{3.60}$$

With $T_w$ the chamber wall temperature on the inner side of the coolant channel and $T_b$ the bulk temperature of the coolant in a given cell. $h_c$ is again the convective heat transfer coefficient. The subscript c indicates that this is the convective heat transfer coefficient for the coolant. This heat transfer coefficient can be calculated using a wide variety of equations. In the model presented here two were implemented, the first is the Sieder-tate relationship which can be seen in equation 3.61.

$$h_c = (0.025) \cdot \frac{k_c}{D_h} \cdot \left(Re_c^{0.8} \cdot Pr_c^{0.4}\right) \cdot (T_b/T_w)^{0.55} \tag{3.61}$$

The Sieder-tate relationship was not developed specifically for Nitrous Oxide but was instead developed for gaseous hydrogen and helium. Nevertheless it is commonly used to determine the coolant side convective heat transfer coefficient in rocket motors [3, 14]. There are several reasons for this: the Sieder Tate relationship has the advantage that it is valid for a wide range of coolant temperatures and pressures and it is also valid for a wide variety of coolant channel length to diameter ratios. Furthermore, it was found that the Sieder-tate relationship gave accurate results for a wide variety of different coolants used within rocket motors and that the equation gives accurate results in general for single phase fluids [3].

The second equation used is the Dittus-Boelter equation given by equation 3.62:

$$Nu = 0.023 \cdot Re_c^{0.8} Pr_c^n \tag{3.62}$$

Where n is a constant equal to 0.3 if the cooling fluid is being cooled and equal to 0.4 if the coolant fluid is being heated. The Dittus-Boelter equation doesn't directly give the coolant heat transfer coefficient. Instead it is used to calculate the Nusselt number Nu, which represents the ratio between the convective and conductive heat transfer at the boundary between the wall and the fluid. The Nusselt number can in turn be used to calculate the heat transfer coefficient using equation 3.63:

$$h_c = Nu \cdot \frac{k_c}{D_h} \tag{3.63}$$

The Reynolds number as used in equations 3.61 and 3.62 can be calculated using equation 3.64.

$$Re_c = \frac{\rho_c \cdot v_c \cdot D_h}{\mu_c} \tag{3.64}$$

With $\mu_c$ being the coolant viscosity. The coolant flow velocity $v_c$ is calculated using equation 3.65.

$$v_c = \frac{\dot{m}_c}{\rho_c \cdot A_c} \tag{3.65}$$

Here $\dot{m}_c$ represents the coolant mass flow and $A_c$ represents the local coolant channel cross sectional area. The Prandtl number of the coolant follows from equation 3.66.

$$Pr_c = \frac{c_p \cdot \mu_c}{k_c} \tag{3.66}$$

To calculate the heat transfer from the coolant fluid to the outer wall equations 3.60 and 3.61 were used again. It should be noted that in this case the coolant bulk temperature is higher than the wall temperature meaning that the heat flux calculated using equation 3.60 is negative. This indicates that energy is leaving the cooling fluid which is exactly what is to be expected. Any heat transferred to the outer wall of the thruster will spread out due to conduction in an identical manner as calculated earlier in section 3.2. As the cells located within the outermost layer heat up they will also radiate heat away.

Besides convective heat transfer between the thruster wall and the cooling fluid, part of the heat will also be transferred by radiation. An optional feature was therefore added to the program which simulates the radiation heat transfer from the wall to the coolant and from the coolant to the wall. The radiation heat transfer from the inner wall to the cooling fluid and from the cooling fluid to the outer wall was calculated using equation 3.20 where the temperature variables were swapped out for their relevant counterparts in this situation (i.e. the coolant fluid temperature and the wall temperature “below” and “above” the cooling channel). The main difficulty in evaluating equation 3.20 for the radiation heat transfer from the cooling fluid to the wall is to determine the value of emissivity of the coolant fluid. This is not straightforward as gases usually only absorb and emit radiation at certain wavelengths or so called radiation bands. This makes it difficult to get an accurate number for the overall emissivity of the gas. Nevertheless Tien et al. [41] studied the emissivity of nitrous oxide for a wide range of temperatures and pressures and provided a method for calculating the emissivity of nitrous oxide. In the work by Tien et al. it can be seen that the variation in emissivity is relatively small for a change in pressure or temperature and therefore determining the exact value of the emissivity for every temperature and pressure combination is not required. Furthermore, the method to calculate the exact value of the emissivity as provided by Tien et al. is relatively complex, so therefore it was instead chosen to take an average value for the emissivity based on their analysis. It should also be noted that the radiation heat transfer usually only comprises a small part of the total coolant heat transfer as the coolant temperature typically stays relatively low to prevent coolant decomposition.

With the equations to calculate the coolant flow properties established, the framework has been made to calculate the heat transfer between each of the coolant cells and wall material cells. One of the questions that remains is how to calculate the coolant temperature in each cell. For the wall cells equation 3.42 was applied to calculate the temperature in each cell. For the cooling channel some modifications need to be made however. This is because for the cooling channel there is coolant mass flowing through each of the cells and therefore there is also heat transfer due to advection. The general conservation equation established in equation 3.21 can be used to model the advective process. In this case instead of solving the diffusion term, the equation is solved for the convection term. Adding the heat capacity $c_p$, equation 3.67 is obtained.

$$\frac{\partial}{\partial t}(\rho c_p \phi) + \nabla \cdot (\rho \mathbf{v} c_p \phi) = 0 \tag{3.67}$$

Where $\mathbf{v}$ represents the (coolant) velocity vector. While the diffusion term was solved using a central difference-like scheme where the surrounding cell values were used to determine the properties at the cell boundaries, the convection term as presented in Equation 3.67 is solved using an upwind scheme. The reason for choosing this upwind scheme is that the advection process is highly directional. If discretization is performed using a linear symmetric profile as was done for the diffusion term, this will lead to nonphysical results [27]. Multiple different types of upwind schemes exist, here it was chosen to use one of the most basic ones which can be visually represented as seen in figure 3.7:

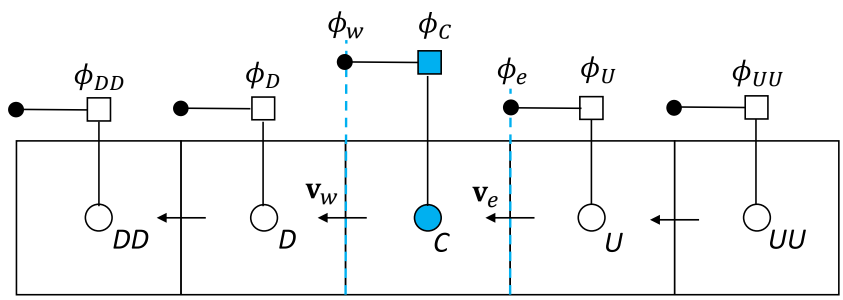


Figure 3.7: Visual representation of the upwind scheme as used for the coolant channel cells (adapted from [27]).

The subscripts indicated in figure 3.7 represent the following: C is the central node (i.e. the node at the cell being analysed), U is the upwind node, UU is the far upwind node, D is the downwind node, DD is the far downwind node and w and e represent the westward (left) and eastward (right) boundaries respectively. The upwind scheme works by using the temperature value of the upwind node to represent the temperature value at the boundary surface with the downwind cell (in this study this is always the westward boundary). The discretized advection flux for the westward boundary can then be calculated using equation 3.68:

$$(\rho c_p \mathbf{v} \cdot \mathbf{S})_w \cdot \phi_w = (\rho v A_{coolant} c_p)_w \phi_C = \dot{m}_{coolant} c_{p,w} \phi_C \tag{3.68}$$

The subscript “coolant” is used here for the coolant flow parameters to avoid confusion with the subscript “C” used for the central node. In a similar fashion the flux for the other boundaries can be calculated. For the first cell of the cooling channel an inlet boundary condition is imposed. The flux at the boundary is calculated in the same manner as the flux at the other boundaries, with the exception that a pre-specified temperature is used; in this case the ambient temperature. It should however be noted that even though the calculation of the inlet flux is similar, it should be treated as a boundary condition and not as a regular flux. This is an important distinction as this has an influence on how the system of equations should be solved, this will become clear in section 3.5.

One might wonder why such a basic upwind scheme was chosen. There are several reasons for this: the first reason is that this scheme is unconditionally stable for most cases presented in this report, or can be made to be stable quite easily. This is a big advantage, especially for some of the techniques that will be discussed in section 3.5. The second reason is that choosing a higher order scheme will cost more computational effort for little gain as the truncation error will be governed by the transient term (The term on the left hand side in equation 3.67). The reason for this will become clear in section 3.5. Lastly and most importantly, it will be shown in section 3.7 and chapter 4 that this basic upwind scheme is sufficient to get adequate results from the model.

Using equation 3.68 and the equations established earlier the heat flows to and from a cooling channel cell can be visualised as shown in figure 3.8 (here using the letter T to represent the temperature). An important note to make is that the heat flows in the j direction (the vertical arrows in the diagram) can reverse direction depending on the temperature of the coolant fluid and the temperature of the wall cells with index (i,j+1) and (i,j-1). The heat flows in the i direction (the horizontal arrows in the diagram) are however unidirectional and can only flow from right to left (in this case) due to the fact that these arrows represent a physical transfer of coolant mass which can only flow in one direction (towards the injector).

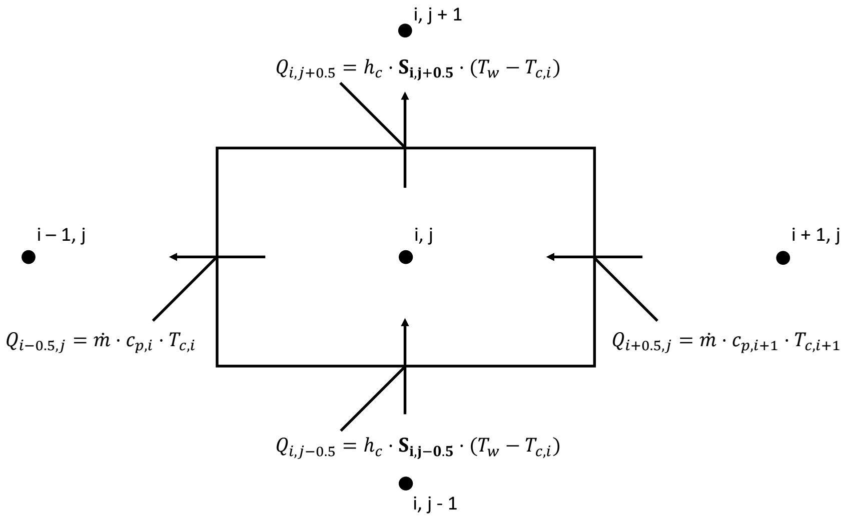


Figure 3.8: Heat flows for a coolant channel cell (i,j)

As was discussed in section 3.2 the time step in equation 3.42 was bound by the stability criterion given in equation 3.43. This criterion obviously does not hold for the cooling channel cells as this criterion is based on the properties of the wall material. Therefore, a different stability criterion had to be implemented for the cooling channel. It can be shown that for the advection equation, the criterion shown in equation 3.69 is required for stability [27].

$$\Delta t \leq \frac{\Delta x_c}{(v_c)_t} \tag{3.69}$$

### 3.3.2. The Addition of Ribs to the Cooling Channel

The steps described in section 3.3.1 are sufficient to describe the cooling fluid properties in a single cooling “sleeve” around the combustion chamber. In many cases however the cooling channel does not encompass the entire combustion chamber but instead consists of multiple channels with ribs in between (see figure 3.9). In this case some additional steps are required to calculate the wall temperature and cooling channel parameters accurately.

As a first step two parameters were defined. The parameter N and the parameter $\Re$. N is defined as the number of cooling channels and $\Re$ is defined as the ratio between the angular width of the cooling channels and the angular width of the ribs, or in equation form:

$$\Re = \frac{\alpha_c}{\alpha_{rib}}$$

With $\alpha_c$ and $\alpha_{rib}$ defined as shown in figure 3.9. Here it is assumed that the angular width of each of the ribs and cooling channels is constant for a given cell (i.e. each rib has the same width for a given axial position).

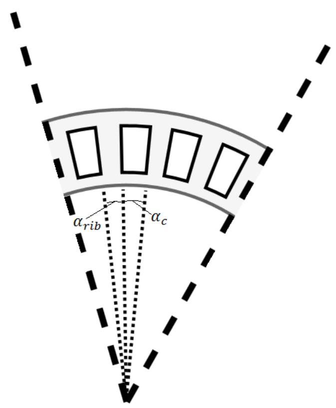


Figure 3.9: Cross section of the coolant channels with ribs present

Using these parameters the variables used in the equations mentioned in the previous section can be corrected. For example the cooling channel cross sectional area, the heat flow from the lower wall, and the heat flow to the upper wall can be corrected by multiplying these parameters as calculated for an annulus with the factor:

$$\frac{\Re}{1 + \Re}$$

The heat transfer from the lower wall to the ribs is calculated in similar way as the heat transfer between different wall elements, however a correction factor again needs to be applied to account for the “missing” mass which would be situated in the area occupied by the cooling channels. This correction is performed by applying the correction factor below:

$$\frac{1}{1 + \Re}$$

Using the factors described above two cases were pre-programmed into the model. A case were $\Re$ is constant for all values of x and a case were the channel width $\Delta z_{j-0.5}$ is constant for all values of x. This second case roughly corresponds to the case were the coolant channels have a constant cross sectional area although it should be noted that some variation is still present due to the change in the radius of curvature of the cooling channel with each cell.

For each cell there are six different heat flows to and from the cooling channels, the two heat flows from the lower and upper wall to the cooling channels, the two heat flows from each of the ribs to the cooling channels and the two heat flows resulting from the mass transfer within the coolant channels. Visually the heat flows for a coolant channel in a cell (i,j) are shown in figure 3.10.

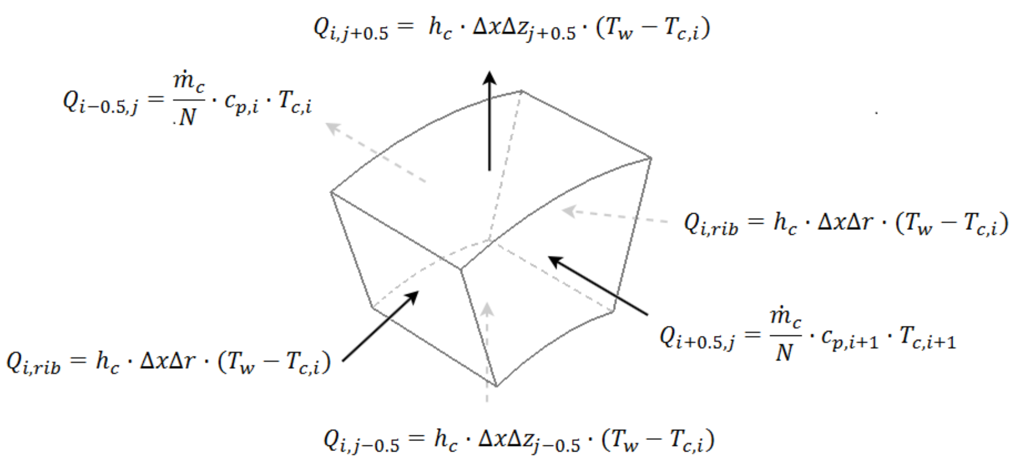


Figure 3.10: Heat flows for a coolant channel in a cell (i,j) with ribs present

Where $\Delta z_{j\pm0.5}$ is in this case defined as:

$$\Delta z_{j\pm0.5} = 2\pi\left(r_j \pm \frac{\Delta r}{2}\right) \cdot \begin{bmatrix} r_{i+0.5,j} - r_{i-0.5,j} \\ -x_{i+0.5,j\pm0.5} - x_{i-0.5,j\pm0.5} \end{bmatrix} \cdot \frac{\Re}{(1+\Re)\cdot N} \tag{3.70}$$

The vector present in equation 3.70 is the 2D representation of $\mathbf{S}_f$.

It should again be noted that the heat flows from the ribs as shown in figure 3.10 can reverse direction depending on the respective temperatures of the ribs and the coolant fluid.

To evaluate the heat transfer coefficient in equation 3.61 and some of the other coolant fluid parameters discussed earlier the hydraulic diameter is required. In figure 3.10 it can be seen that for the case were ribs are present the cooling channel cross sections take the shape of an annulus sector. Using the parameters defined earlier it can be shown that in this case the hydraulic diameter of the cooling channels can be calculated using equation 3.71.

$$D_h = \frac{\left(\pi \cdot r_{j+0.5}^2 - \pi r_{j-0.5}^2\right)}{(2\pi r_{j-0.5}) + (2\pi r_{j+0.5}) + \frac{2\Delta r \cdot N \cdot (1+\Re)}{\Re}} \tag{3.71}$$

### 3.3.3. Helical cooling channels

In many rocket engines, helical cooling channels are used (sometimes also referred to as circumferential or tangential cooling channels). Helical cooling channels increase the effective cooling channel length and therefore increase cooling effectiveness at the cost of a higher pressure drop. Because of the potential benefit of helical cooling channels and the fact that some of the engines used in the validation cases use helical cooling channels, helical cooling channels were also implemented in the model.

The helical cooling channel is defined by three parameters: the pitch of the helix, the width of the channel and the height of the channel. Using these three parameters, the centerline coordinates of the helical cooling channel can be calculated using equations 3.72 and 3.73.

$$y = (r_i + \frac{1}{2}\Delta r) \cdot sin\left(\pi\frac{w_c}{2} + \frac{x_i \cdot 2\pi}{\Lambda}\right) \tag{3.72}$$

$$z = (r_i + \frac{1}{2}\Delta r) \cdot cos\left(\pi\frac{w_c}{2} + \frac{x_i \cdot 2\pi}{\Lambda}\right) \tag{3.73}$$

With $\Lambda$ the pitch of the cooling channel helix and $w_c$ the width of the cooling channel. An example helical cooling channel as calculated using equations 3.72 and 3.73 as compared to a straight cooling channel can be seen in figure 3.11.

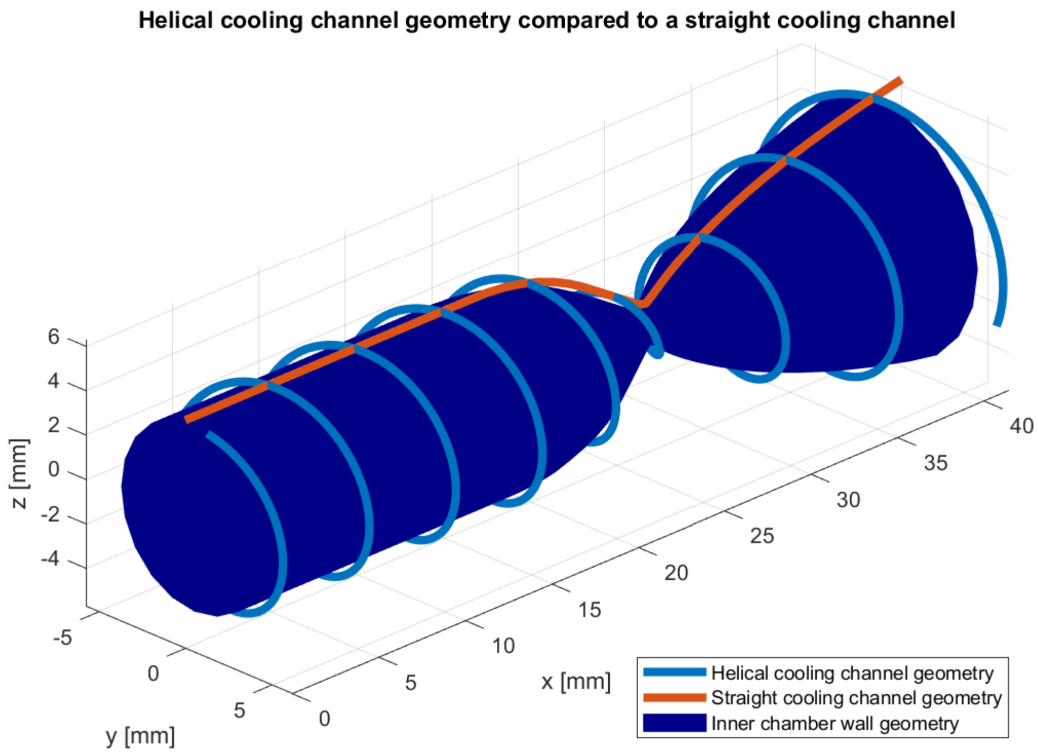


Figure 3.11: The geometry of a single helical cooling channel compared to a single straight channel

The calculation of the heat transfer and coolant fluid parameters is largely the same for both the helical and the straight channel. The main difference is that for the helical channels the coolant channel length is larger, and that consequently the surface/contact area between the coolant and the wall is also larger. The main problem to solve is how to calculate the difference in length of the helical cooling channel for each cell of the mesh. To determine the distance between two points in 3D space Pythagoras theorem (equation 3.74) can simply be used.

$$L_{helicalsection} = \sqrt{x^2 + y^2 + z^2} \tag{3.74}$$

It should be noted that equation 3.74 determines the straight distance between 2 points in 3D, so if one were to just use this formula to calculate the length of the cooling channel by taking the start and end point of the cooling channel it would not work. It is however possible to split the cooling channel up into a large amount of small sections. If the sections are small enough their curvature will also be small and therefore their length can be approximated using equation 3.74. The length of these sections can then be summed together to get the total length of the curve. This process is essentially a numerical integration of the curve to obtain the length.

A problem with this method is however that if few mesh cells are chosen in the x-direction (which can for example be done to speed up the program), the cooling channel will not be approximated properly anymore and could get “blocky”. To prevent this a secondary mesh was set up which is much more fine than the overall mesh. The only purpose of this mesh is to get an accurate description of the cooling channel so the overall length can be calculated accurately. An example of a cooling channel generated using this method can be seen in figure 3.11. In this example only 50 cells were used in the x-direction of the overall mesh, yet the cooling channel is still accurately described as 1000 cells were used to generate the cooling channel. Using this accurate mesh the difference in length between the the straight and helical version cooling channels can be calculated. For the example given above the result can be seen below in figure 3.12.

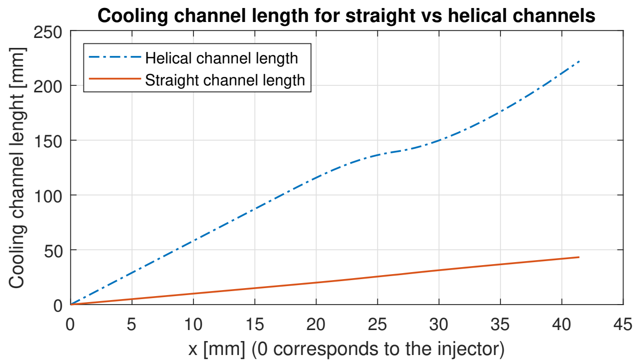


Figure 3.12: Comparison of the cooling channel length for a helical channel and a straight channel

It can be seen in figure 3.12 that for the example given above the cooling channel length of the helical channel is longer by a factor of almost five when compared to the straight channel. It can also be seen that the rate of increase in cooling channel length is not the same for the helical channel and the straight channel.

Once the length of the helical channel is obtained, the length of each of the cooling channel sections corresponding to the overall mesh (so the coarser mesh on which the actual thermal analysis is performed) can be determined. Based on this the ratio between the length of the straight channel and the length of the helical channel is determined for each cell. The analysis is then performed in exactly the same manner as for a straight channel, with the exception that the surface areas, cell lengths and all corresponding properties of the cooling channel are corrected for the larger cooling channel length using the ratio determined earlier.

### 3.3.4. Code implementation details

The code logic for the regenerative cooling part of the code is for a large part identical to that of the radiation cooled part of the code. In fact, many of the scripts and functions used in both codes are the exact same and changes are only made where ever necessary. For the regenerative cooling code the thruster is basically split up in three parts as can be seen in figure 3.13: the thruster wall below the cooling channel, the cooling channel, and the thruster wall above the cooling channel.

For the wall sections, the code is essentially solved exactly the same as for the radiation cooling code with the exception that the boundary conditions are changed. For the lower part of the wall the boundary condition for the top cells is specified as the heat transfer to the coolant channel for the cells which border a coolant channel cell (see the red arrows in figure 3.13). For cells in the top layer of the bottom part of the wall which do not border a cooling channel cell (this can happen when the cooling channel does not span the entire thruster), the boundary condition is specified using equation 3.20, similarly to how it was implemented for the radiation cooled case. For the upper part of the wall the boundary conditions at the bottom of the wall are changed from the heat transfer from the combustion gases to the heat transfer from the cooling channel.

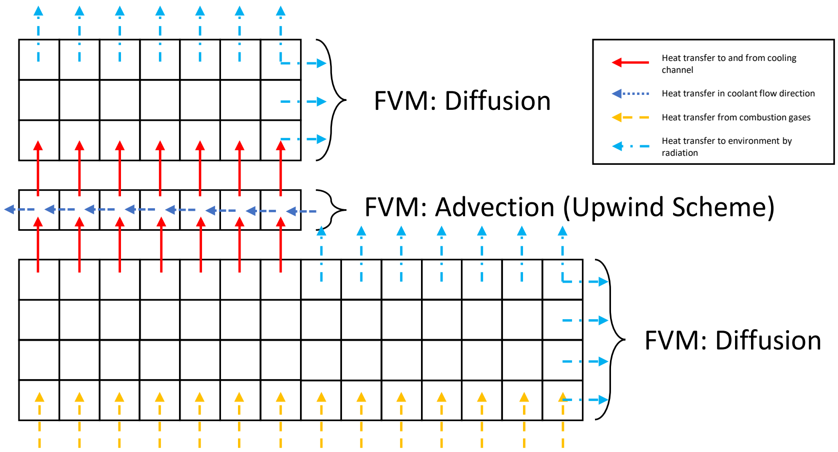


Figure 3.13: Simplified mesh showing the computation logic used by the program in the case regenerative cooling is used.

For the cooling channel, the heat transfer is calculated based on the temperature values in the neighbouring cells and the coolant fluid properties. This is done using an upwind scheme in the axial direction and by using the semi-empirical heat transfer equations (equations 3.60, 3.61,3.62, 3.63 and 3.68) in the radial direction. The time stepping is performed using a finite difference method approach. Since the coolant properties at the channel outlet are dependent on the cooling properties in the previous cells the mesh is solved from right to left (since the coolant is assumed to flow from right to left) for the regeneratively cooled case. This is the opposite direction as was used for the radiation cooled case, in this case the mesh was solved from left to right. This also includes the calculations for the bottom and upper part of the wall.

A flow diagram of the code logic can be seen figure 3.14. It can be seen that the program flow is largely the same as for the radiation cooled case, with the following exceptions:

- A cooling channel geometry is defined and generated during the creation of the mesh.
- The coolant flow parameters are calculated in the x loop (axial direction). (step 5 in figure 3.14)
- The coolant heat transfer in the radial direction is calculated for each x position. (step 6 in figure 3.14)

Within the model, three options were implemented for setting the cooling channel length: the first option was to just specify the cooling channel inlet position (this option is called the “specified” option within the program. In this case the program will find the nearest cell in the mesh to this position and create the cooling channel inlet here. This can be seen in figure 3.15. In figure 3.15 the band of larger cells spanning from the nozzle convergent to the injector is the cooling channel. If this case is selected, the amount of cells in the y-direction to the right of the cooling channel inlet will be equal to the amount of cells in the y-direction under the cooling channel. This was done to keep the problem split up into three parts as was shown in figure 3.13. For the cooling channel inlet, the lower cell boundary of the cooling channel inlet cell will be set equal to the outer wall radius. This is done because the real inlet can not start randomly somewhere in the middle of the wall material. In figure 3.15 it can be seen that just before the start of the nozzle convergent there is a little spike in the outer wall of the thruster. This is where the cooling channel inlet is located. Because there also needs to be some wall material on the outside of the cooling channel, the outer wall is also disrupted. A different and perhaps more clear representation of this phenomenon using colour is given in chapter 5 in figure 5.20 where the final simulation result is shown for a case with a cooling channel starting at a specified starting condition.

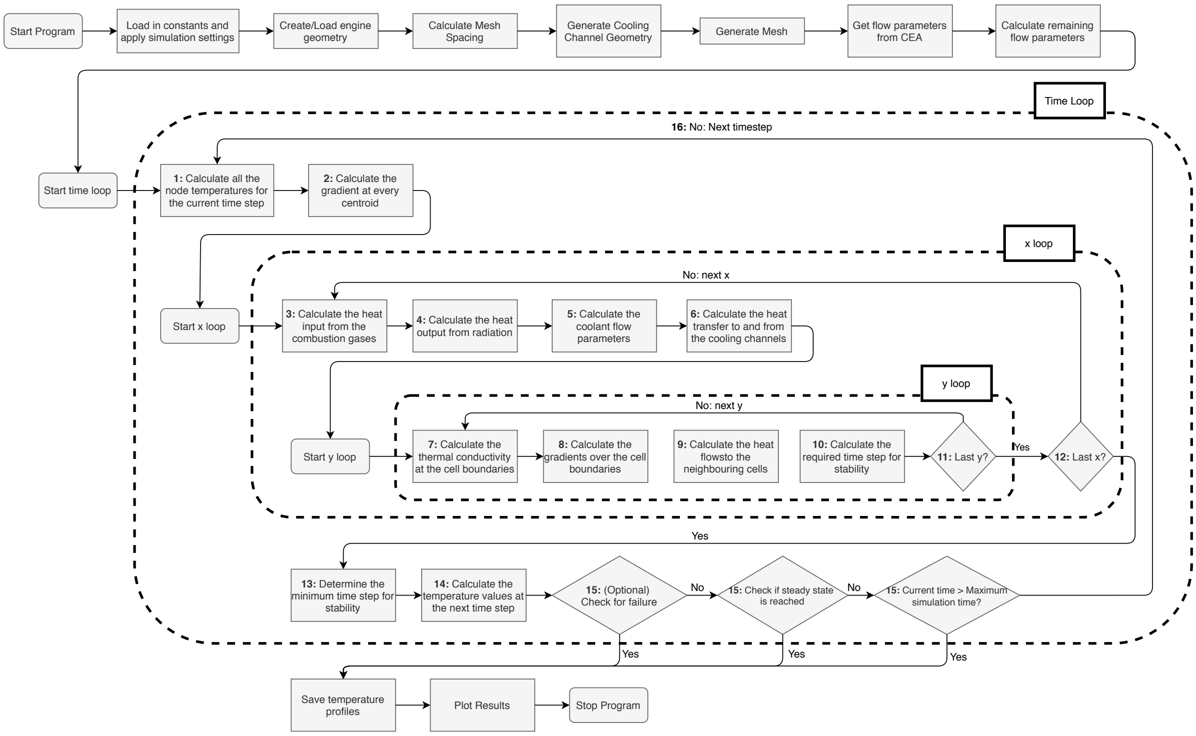


Figure 3.14: Flow diagram showing the program logic for the thruster temperature when regenerative cooling is used.

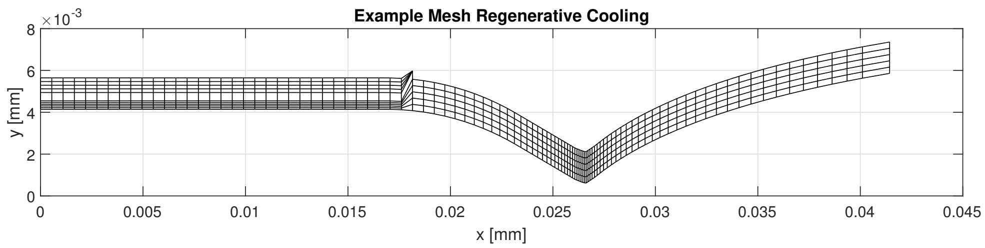


Figure 3.15: An example mesh for a reference thruster with 100 cells in the x direction and 10 cells in the radial direction with a cooling channel starting at a specified location.

The second option is to have a cooling channel which starts at the nozzle exit and which spans the entire thruster. The mesh for such a cooling channel can be seen in figure 3.16. In this case the amount of cells in the y-direction below and above the cooling channel remains constant for the entire thruster cross section.

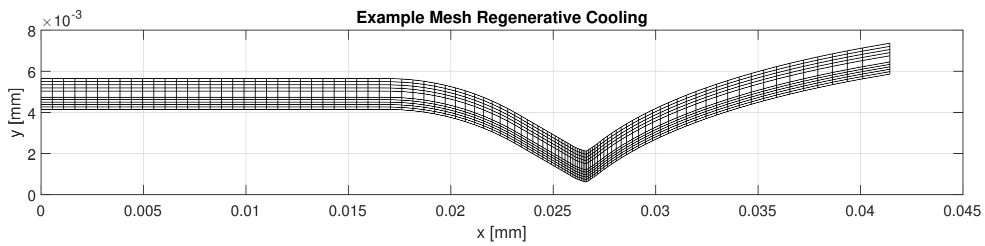


Figure 3.16: An example mesh for a reference thruster with 100 cells in the x direction and 10 cells in the radial direction with a cooling channel starting at the nozzle exit.

The last option which can be implemented occurs when the nozzle and the chamber have a different wall thickness. Within the program this option is called the 'joint' option and if this option is selected the cooling channel inlet will be placed at the transition point between the chamber and the nozzle. It is essentially a specialised version of the specified option.

It is also possible to modify the cooling channel shape in the program. Two options are implemented within the program. “Rectangular” channels (These take the shape of an annulus sector) and circular channels. By default the program assumes that rectangular channels are used. As was mentioned previously, for the rectangular channels option there are two options: either the width of the cooling channel is kept constant, or the ratio between the width of the cooling channel and the ribs is kept constant. If circular channels are selected a correction is applied for the channel surface area. The channel surface area is in this case multiplied by a factor of $\pi/4$ which is the ratio between the circumferences of a circle and a square with equal diameter and side lengths respectively. For a circular cooling channel the cooling channel area is also calculated accordingly, which in this case is simply equal to the area of the circle. Furthermore, for a circular cooling channel the hydraulic diameter is obviously just equal to the actual diameter of the cooling channel.

## 3.4. Thermal Barrier Coatings

For both the radiation cooled case and the regenerative cooled case an option was added to the program to add a Thermal Barrier Coating (TBC) to the inside of the thruster. The implementation of the TBC within the program is relatively simple as it is essentially a layer of material with a low thermal conductivity. Within the program the user can specify the thickness of the coating, the coating material, and the amount of mesh cells in the coating in the radial direction. The mesh cells in the radial direction are divided equally in the radial direction (each cell has the same thickness). In the axial direction the mesh cell boundaries are made to coincide with the normal wall cell boundaries. An example mesh including a TBC for a section of a radiation cooled nozzle can be seen in figure 3.17. The heat fluxes and temperatures within the coating can be calculated in the same way as was described in section 3.2, albeit taking into account the different values for the thermal conductivity, heat capacity and density of the coating.

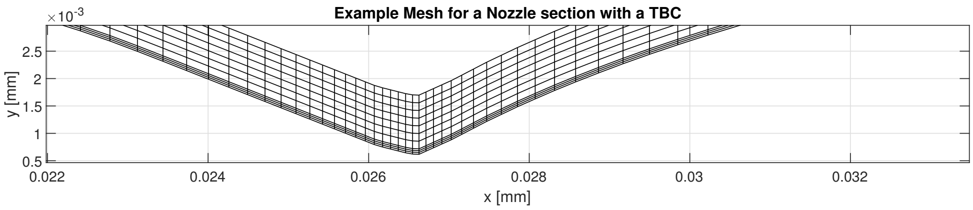


Figure 3.17: An example mesh for a radiation cooled nozzle section with a thermal barrier coating applied.

The approach as described above works for most of the cells in the TBC layer. However, for the boundary cells that interface with the wall material this approach does not work. The main reason for this is that using equation 3.38 to compute the thermal conductivity at the boundary between the two materials will lead to rather incorrect values which in turn will lead to nonphysical results for the heat flux and the cell temperatures [27]. An alternative equation was therefore implemented to compute an effective thermal conductivity for the boundary at the interface between the two different materials. It should be noted that the implementation of such an effective thermal conductivity does not actually lead to an accurate representation of the thermal conductivity at the interface between the two materials, but rather it leads to an accurate representation of the heat flux over the boundary such that the temperature values in the neighbouring cells can be computed accurately. Since the temperature distribution within the thruster is of primary interest, the fact that the thermal conductivity is not accurately represented at the boundary is not a problem. The effective thermal conductivity at the boundary was therefore calculated using equation 3.75 [27].

$$\frac{1}{\Gamma^{\phi}_{f_{eff}}} = \left(\frac{1-g_c}{\Gamma^{\phi}_{F}} + \frac{g_c}{\Gamma^{\phi}_{C}}\right) \quad \rightarrow \quad \Gamma^{\phi}_{f_{eff}} = \frac{1}{\left(\frac{1-g_c}{\Gamma^{\phi}_{F}} + \frac{g_c}{\Gamma^{\phi}_{C}}\right)} \tag{3.75}$$

Currently, only one thermal barrier coating was implemented within the model, the parameters for this coating can be seen in table 3.2. The program was however set up such that adding an additional thermal barrier coating is relatively simple. Within the program there is a wall material database Matlab file. Within this file all the wall material properties are stored as well as all the thermal barrier coatings. The coating is selected using a switch case structure. Therefore, adding in a new coating is as simple as adding in a new case, copying all the parameters from a different case and modifying them according to the needs of the user. If the user has the coating parameters available, this can be done in less than a minute.

Table 3.2: Available Thermal Barrier Coatings and their characteristics as used within the program

| Coating Material | Thermal Conductivity [W/mK] | Max. Operating Temperature [K] | Heat Capacity [J/kgK] | Density [kg/m$^3$] |
|---|---|---|---|---|
| Yttria-stabilized zirconia | 1.5 | 1473.15 | 450 | 5900 |

## 3.5. Alternative transient solution methods

In section 3.2.2 the Forward Euler time stepping method was introduced. Within the program this method can be used to simulate any of the cooling methods as described in previous sections. However this method is inefficient due to the limitations imposed by the condition in equations 3.43 and 3.69. Due to this limitation the time step which can be used to advance the simulation is limited per set of calculations. For small rocket engines in particular this is a large problem. Looking at equation 3.43 (reproduced below) it can be seen that the numerator consists of the thermal mass of the thruster while the denominator consists of the orthogonal component of the “effective” heat transfer coefficient (heat flux divided by the temperature difference). For bi-propellant rocket engines it is known that the heat flux is large, values in the order of several MW/m$^2$ are not uncommon [14, 40]. For small rocket engines the thermal mass is however small, meaning that equation 3.43 will lead to very small time step values.

$$\Delta t \leq \frac{\rho_{t-1} V_c c_p}{\sum_{f\,\epsilon\,C} \Gamma^{\phi}_{f} \frac{E_f}{d_{CF}}}$$

In some cases some manipulations can be performed to circumvent this problem. However, for the regeneratively cooled case in particular the time step decreases steeply even when these manipulations are performed. This makes the computational cost of the time stepping scheme presented in equation 3.42 too large for it to be used in a practical manner due to simulations taking hours if not days or weeks. An example of the required time step as function of simulated burn time for a thruster cooled using five axial cooling channels running from the nozzle exit to the injector can be seen in figure 3.18. It can be seen that for roughly the first eleven seconds the time step stays mostly constant. Between seven and eleven seconds fluctuations start to occur in the required time step due to an alternation in the dominance of the criteria set out by equations 3.43 and 3.69. After eleven seconds a steep decrease in time step can be seen, first by one order of magnitude and later even by two orders of magnitude to a number of order $10^{-6}$ s.
The main reason for the sudden drop in required time step is due to the fact that during the first seven seconds the stability criterion for conduction is the factor limiting the time step size. However as the coolant temperature becomes higher the criterion set out by equation 3.69 becomes dominant and quickly decreases the required time step. Predicting the behaviour of the time step is difficult as the behaviour appears to be quite chaotic, however a downward trend can clearly be observed.

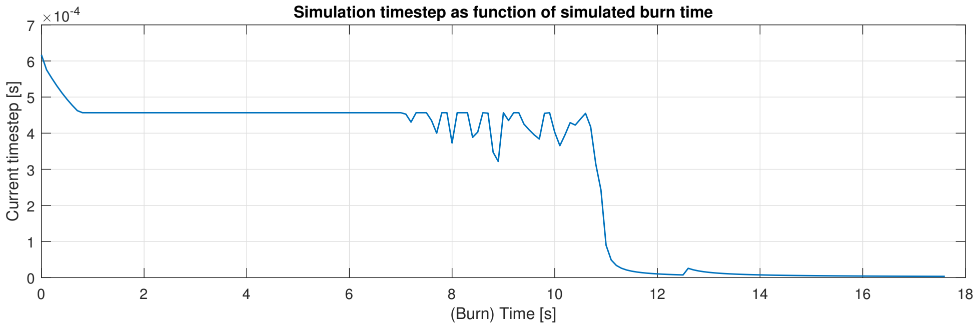


Figure 3.18: Simulation time step as function of the simulated burn time.

The problem outlined above is one of the main difficulties which was encountered in simulating the transients of small scale bi-propellant rocket engines because it not only limits the use of the time stepping scheme used in equation 3.18, it also limits the use of other higher order time stepping schemes such as the Crank-Nicolson scheme which is bound by a similar stability criterion [27].

An alternative solution for solving the unsteady term in equation 3.21 was therefore implemented in the program, which will be presented next. The method was again largely based on the methods presented in [27]. In order to implement this solution, the solution of the diffusion equation (equation 3.22) was first rewritten in an algebraic form. The diffusion term (equation 3.23) of the diffusion equation can be written as equation 3.76 using this algebraic form.

$$a_C \phi_C + \sum_{F \in C} a_F \phi_F = b_C \tag{3.76}$$

With $a_C$ and $a_F$ consisting of the orthogonal components of the diffusion flux as given by equations 3.77 and 3.78.

$$a_C = \sum_{f \in C} \Gamma_f^\phi \frac{E_f}{d_{CF}} \tag{3.77}$$

$$a_F = -\Gamma_f^\phi \frac{E_f}{d_{CF}} \tag{3.78}$$

The term $b_C$ consists of all the non-linear terms which in this case are the non-orthogonal terms and the flux from the boundary conditions as can be seen in equation 3.79.

$$b_C = \sum_{f \in C} \left(\Gamma_f^\phi \nabla \phi\right)_f \cdot \mathbf{T}_f + \sum_{f \in C} q_b \cdot \mathbf{S}_b \tag{3.79}$$

Using the algebraic form of the diffusion term as given in equation 3.76 the diffusion term for the entire mesh can be written as a system of equations as can be seen in equation 3.80. This property was exploited to implement two other solutions methods for solving the unsteady term.

$$\begin{bmatrix} a_{1,1} & a_{1,2} & \cdots & a_{1,n-1} & a_{1,n} \\ a_{2,1} & a_{2,2} & \cdots & a_{2,n-1} & a_{2,n} \\ \vdots & \cdots & \cdots & \cdots & \vdots \\ a_{m-1,1} & a_{m-1,2} & \cdots & a_{m-1,n-1} & a_{m-1,n} \\ a_{m,1} & a_{m,2} & \cdots & a_{m,n-1} & a_{m,n} \end{bmatrix} \cdot \begin{bmatrix} \phi_{1,1} \\ \phi_{1,2} \\ \vdots \\ \phi_{m,n-1} \\ \phi_{m,n} \end{bmatrix} = \begin{bmatrix} b_{1,1} \\ b_{1,2} \\ \vdots \\ b_{m,n-1} \\ b_{m,n} \end{bmatrix} \tag{3.80}$$

### 3.5.1. The implicit method

In section 3.2.2 an explicit method was derived for calculating the transient term of the diffusion equation by performing a taylor series expansion around the point t + Δt. As shown above, this method has the downside that in some cases it becomes incredibly slow. An alternative method can be derived by performing a taylor series expansion around the point t - Δt. The resulting taylor expansion can be seen in equation 3.81.

$$(\rho c_p \phi)_{t-\Delta t} = (\rho c_p \phi)_t - \left.\frac{\partial(\rho c_p \phi)}{\partial t}\right|_t \Delta t + \left.\frac{\partial^2(\rho c_p \phi)}{\partial t^2}\right|_t \frac{\Delta t^2}{2!} - \left.\frac{\partial^3(\rho c_p \phi)}{\partial t^3}\right|_t \frac{\Delta t^3}{3!} + \dots \tag{3.81}$$

Rewriting equation 3.81 to solve for $\frac{\partial(\rho c_p \phi)}{\partial t}$ and truncating the series at $\mathcal{O}^2$ terms, equation 3.82 can be obtained.

$$\frac{\partial(\rho c_p \phi)}{\partial t} = \frac{(\rho c_p \phi)_t - (\rho c_p \phi)_{t-\Delta t}}{\Delta t} \tag{3.82}$$

Substituting equation 3.82 back into equation 3.39, equation 3.83 can be obtained.

$$\phi_t = \phi_{t-\Delta t} - \frac{L(\phi_t)\Delta t}{V_c \rho c_p} \tag{3.83}$$

At first glance this equation may seem similar to equation 3.42. However the difference is that the diffusion term $L(\phi_t)$ is evaluated at the same time step as the newly calculated temperatures $\phi_t$. This method is therefore implicit as in this case a system of equations has to be solved. Solving this system of equations is obviously more computationally intensive as the method using equation 3.42, the implicit method however has the big advantage that it is stable for any time step. [27, 46] The time step can therefore be kept constant, eliminating the problem where the required time step for stability becomes increasingly smaller.

The system of equations can be set up by writing equation 3.83 into an algebraic form (similar to what was done with equation 3.76). The resulting equation becomes equation 3.84.

$$(a_C^t + a_C)\phi_C + \sum_{F\ \epsilon\ C} a_F \phi_F = b_C + a_C^{t-\Delta t}(\phi_C)^{t-\Delta t} \tag{3.84}$$

With $a_C^t$ and $a_C^{t-\Delta t}$ equal to:

$$a_C^t = \frac{\rho_c V_c}{\Delta t} \tag{3.85}$$

$$a_C^{t-\Delta t} = \frac{\rho_{t-\Delta t} V_c}{\Delta t} \tag{3.86}$$

Equation 3.84 can be set up for every cell in the mesh leading to a system of equations as can be seen in equation 3.87.

$$\begin{bmatrix} a_{1,1} & a_{1,2} & 0 & \dots & 0 \\ a_{2,1} & a_{2,2} & a_{2,3} & 0 & \dots \\ 0 & \dots & \dots & \dots & 0 \\ \dots & 0 & a_{m-1,n-2} & a_{m-1,n-1} & a_{m-1,n} \\ 0 & \dots & 0 & a_{m,n-1} & a_{m,n} \end{bmatrix} \cdot \begin{bmatrix} \phi_{1,1} \\ \phi_{1,2} \\ \vdots \\ \phi_{m,n-1} \\ \phi_{m,n} \end{bmatrix} = \begin{bmatrix} b_{1,1} \\ b_{1,2} \\ \vdots \\ b_{m,n-1} \\ b_{m,n} \end{bmatrix} + \begin{bmatrix} a_{1,1}^{t-\Delta t} & 0 & \dots & 0 & 0 \\ 0 & a_{2,2}^{t-\Delta t} & \dots & 0 & 0 \\ \vdots & \dots & \dots & \dots & \vdots \\ 0 & 0 & \dots & a_{m-1,n-1}^{t-\Delta t} & 0 \\ 0 & 0 & \dots & 0 & a_{m,n}^{t-\Delta t} \end{bmatrix} \cdot \begin{bmatrix} (\phi_{1,1})_{t-1} \\ (\phi_{1,2})_{t-1} \\ \vdots \\ (\phi_{m,n-1})_{t-1} \\ (\phi_{m,n})_{t-1} \end{bmatrix} \tag{3.87}$$

This can be written in a more concise form as:

$$\mathbf{A}\boldsymbol{\phi}^t = \mathbf{b} + \mathbf{C} \cdot \boldsymbol{\phi}^{t-\Delta t} \tag{3.88}$$

The A-matrix in equation 3.88 is a sparse matrix consisting of the sum of the orthogonal components of the diffusion flux and the transient components for time step t. If the original mesh was of size i × j then the A-matrix will have size (i × j) × (i × j). The $\boldsymbol{\phi}^t$ matrix has size (i × j) × 1 and consists of the (unknown) temperature values in every cell at the next time step.

The structure of the A matrix can be determined from equation 3.84. The diagonal elements consist of the a-coefficients which correspond to the flux of the cell in the current row while the elements with an offset of 1 from the diagonal correspond to the flux from the cells left and right of the current cell. The elements which are offset by a factor of "i" from the diagonal are also filled, these elements correspond to the flux from the cell above and below the current cell. As an example, the sparsity pattern for a 5 × 5 mesh is shown in figure 3.19.

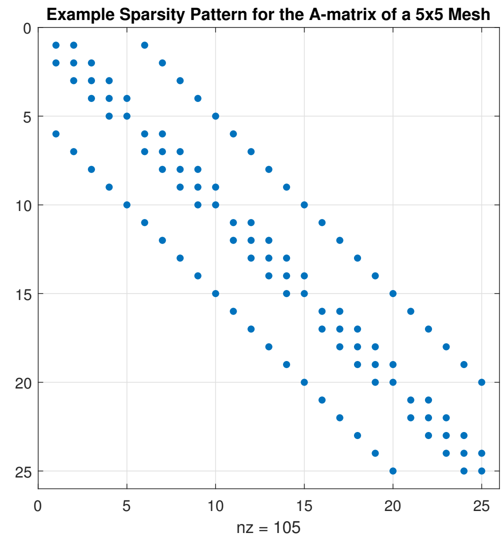


Figure 3.19: Shape of the A Matrix in equation 3.88 for a 5x5 system

From figure 3.19 it can be seen that in this case the A-matrix is a 25 × 25 matrix with all diagonal elements filled. The elements in the 5 and -5 diagonals are also all filled and the elements in the 1 and -1 diagonals are almost completely filled. There are five "gaps" in each of the 1 and -1 diagonals. The diagonal elements at these rows represent the boundary cells, therefore the $a_F$ coefficients for the i+1'th or i-1'th cell do not exist. Instead, for these rows a boundary condition is added to the **b** matrix. For larger meshes the sparsity pattern is essentially identical, except the A-matrix becomes larger and therefore the spacing between the filled-in elements is changed accordingly.

To solve the system in equation 3.88 a fixed-point iteration scheme is used. The procedure was set up as follows. First **A** is decomposed as: **A** = **M**-**N**, this is substituted in equation 3.88 and a fixed-point iteration is applied. From these steps equation 3.89 was obtained.

$$\mathbf{M}\boldsymbol{\phi}^n = \mathbf{N}\boldsymbol{\phi}^{n-1} + \left(\mathbf{b} + \mathbf{C}\boldsymbol{\phi}^{t-\Delta t}\right) \tag{3.89}$$

Defining $\mathbf{B} = \mathbf{M}^{-1}\mathbf{N}$, equation 3.89 can be written as equation 3.90 which gives the solution to the system.

$$\boldsymbol{\phi}^n = \mathbf{B}\boldsymbol{\phi}^{n-1} + \mathbf{M}^{-1}\left(\mathbf{b} + \mathbf{C}\boldsymbol{\phi}^{t-\Delta t}\right) \tag{3.90}$$

The Matrix **B** is called the iteration matrix. The choice of **B** is dependent on the problem and the iteration scheme. In order for the iteration method to converge it is required that the spectral radius of **B** is smaller than unity [27], or in equation form:

$$\rho(\mathbf{B}) < 1 \tag{3.91}$$

Furthermore, the closer the value $\rho(\mathbf{B})$ is to zero, the faster the method will converge. Because of this, a preconditioner matrix is used. A preconditioner matrix is essentially just a transformation matrix which transforms the original system into a system with an equivalent solution but with better spectral properties. In equation form, a preconditioner is a matrix $\mathbf{P}$ such that $\mathbf{P}^{-1}\mathbf{A}\boldsymbol{\phi} = \mathbf{P}^{-1}\mathbf{b}$ has the same solution as $\mathbf{A}\boldsymbol{\phi} = \mathbf{b}$ but with better spectral properties. In case a preconditioner is used, it is required that the condition in equation 3.92 holds for the method to be stable.

$$\rho\left(\mathbf{I} - \mathbf{P}^{-1}\mathbf{A}\right) < 1 \tag{3.92}$$

Within the program developed in this study a preconditioner is used which uses Incomplete LU factorisation with no fill in. This method is also known as the ILU(0) method. This method uses a preconditioner equal to $\bar{\mathbf{L}}\bar{\mathbf{U}}$, where $\bar{\mathbf{L}}$ and $\bar{\mathbf{U}}$ are approximations of the LU decomposition matrices $\mathbf{L}$ and $\mathbf{U}$ given by:

$$\mathbf{L} = \begin{bmatrix} 1 & 0 & \dots & 0 & 0 \\ l_{2,1} & 1 & \dots & 0 & 0 \\ \vdots & \dots & \dots & \dots & \vdots \\ l_{m-1,1} & l_{m-1,2} & \dots & 1 & 0 \\ l_{m,1} & l_{m,2} & \dots & l_{m,n-1} & 1 \end{bmatrix} \tag{3.93}$$

$$\mathbf{U} = \begin{bmatrix} u_{1,1} & u_{1,2} & \dots & u_{1,n-1} & u_{1,n} \\ 0 & u_{2,2} & \dots & u_{2,n-1} & u_{2,n} \\ \vdots & \dots & \dots & \dots & \vdots \\ 0 & 0 & \dots & u_{m-1,n-1} & u_{m-1,n} \\ 0 & 0 & \dots & 0 & u_{m,n} \end{bmatrix} \tag{3.94}$$

The matrices $\mathbf{L}$ and $\mathbf{U}$ are lower triangular and upper triangular respectively. The coefficients are such that $\mathbf{LU} = \mathbf{A}$. The coefficients can be found using the following set of equations [27]:

$$\begin{aligned} u_{1,j} &= a_{1,j} && j = 1 \to n \\ l_{i,1} &= \frac{a_{i,1}}{u_{1,1}} && i = 2 \to n \\ u_{i,j} &= a_{i,j} - \sum_{k=1}^{i-1} l_{i,k}u_{k,j} && j = i, i+1, \dots, n \\ l_{k,i} &= \frac{a_{k,i} - \sum_{j=1}^{i-1} l_{k,j}u_{j,i}}{u_i i} && k = i+1, i+2, n \\ u_{mn} &= a_{mn} - \sum_{i=1}^{n-1} l_{N,i}u_{i,N} \end{aligned} \tag{3.95}$$

The approximation of $\mathbf{L}$ and $\mathbf{U}$ by the matrices $\bar{\mathbf{L}}$ and $\bar{\mathbf{U}}$ depends on the amount of in-fill that is permitted. When using equations 3.95 to construct the $\mathbf{L}$ and $\mathbf{U}$ matrices the sparsity of the original $\mathbf{A}$ matrix is lost. In fact, if equations 3.95 were used to construct the full $\mathbf{L}$ and $\mathbf{U}$ matrices the system could be solved directly and no iteration would be required. Solving such a system becomes very computationally expensive and is often impractical, especially when non-linear terms are present in the $\mathbf{b}$-matrix [27]. Therefore instead of using the matrices $\mathbf{L}$ and $\mathbf{U}$ the approximations $\bar{\mathbf{L}}$ and $\bar{\mathbf{U}}$ are used. Within the program no fill-in was permitted, meaning that to obtain the $\bar{\mathbf{L}}$ and $\bar{\mathbf{U}}$ matrices, equations 3.95 are evaluated and any nonzero element arising from equations 3.95 is set to zero if it appears in a position where in the original system there was a zero. In this way the sparsity pattern of the original system is maintained.

Obviously the product of matrices $\bar{\mathbf{L}}$ and $\bar{\mathbf{U}}$ is not equal to the matrix $\mathbf{A}$, therefore multiple iterations are required before the program finds the right solution. If more fill-in is allowed the matrices $\bar{\mathbf{L}}$ and $\bar{\mathbf{U}}$ will become better approximations of $\mathbf{L}$ and $\mathbf{U}$ and therefore less iterations are required. However, the computational cost per iteration will also rise if more fill-in is permitted. In practise there is an optimum amount of fill-in for which the program will run the quickest. The optimum amount of fill-in depends on many factors, including the problem itself. There is no general rule for finding the optimum amount of fill-in and the optimum is often determined using trial and error [35]. In the program presented here, the choice was made to always use zero fill-in for simplicity.

With the $\bar{\mathbf{L}}$ and $\bar{\mathbf{U}}$ matrices known, the iteration scheme can be set up. Adding the preconditioner $\bar{\mathbf{L}}\bar{\mathbf{U}}$ and using equation 3.90, equation 3.96 can be obtained.

$$\boldsymbol{\phi}^{n} = \left(\mathbf{I} - \left(\bar{\mathbf{L}}\bar{\mathbf{U}}\right)^{-1}\mathbf{A}\right)\boldsymbol{\phi}^{n-1} + \left(\bar{\mathbf{L}}\bar{\mathbf{U}}\right)^{-1}\left(\mathbf{b} + \mathbf{C}\boldsymbol{\phi}^{t-\Delta t}\right) \tag{3.96}$$

The result from equation 3.96 is the input for the next iteration within the iteration cycle. The whole x and y loop (as discussed in section 3.2.3) has to be re-evaluated during every iteration. In turn every iteration cycle corresponds to a time-step (or a step in the time loop). This is obviously quite computationally intensive, however using this method the amount of evaluations of the time-loop (see section 3.2.3) can be decreased substantially, which leads to an overall faster algorithm in most cases. For a 0.01s time step the amount of iterations required per iteration cycle is usually less than 10 (without ribs) or 20 cycles (with ribs). Compare this to the time step required for the explicit method. As was shown in figure 3.18, in this case the time step was of order $10^{-6}$s and thus between 1,000 and 10,000 evaluations of the x and y loop were required for an increase of 0.01s in the time value. To show the benefit of the implicit method the simulations performed for the 1200N regeneratively cooled engine that will be introduced in section 3.7.4 can be taken as an example. For that case the time step required using the Forward Euler method was between $10^{-4}$ and $10^{-5}$s and reaching the steady state solution took almost 2.5 hours of simulation time. For the implicit method the same simulation was completed in less than 15 minutes. For smaller engines like the PM200 the difference in the required simulation time becomes even larger as the required time step for the Forward Euler method becomes smaller with a smaller engine size. The advantage of the implicit method is thus clear.

As a last step, for each iteration cycle a stopping criteria is required. In the model presented here the stopping criterion as specified in equation 3.97 is used.

$$Max\left|\frac{\phi_i^n - \phi_i^{n-1}}{\phi_i^n}\right| \cdot 100 \leq \epsilon \tag{3.97}$$

Where in this case $\epsilon$ was taken to be 0.1%.

### 3.5.2. The implicit method for regenerative cooling & flux limiting

With the implementation of the implicit method for a rocket engine with a regenerative cooling channel a number of unique problems arise which will be addressed in this section. The problems which arise can be divided into two main categories, the first problem which will be discussed is the general approach on how to implement the discretised advection equation into the system of matrix equations presented in the previous sections. Related to this problem is also the problem of how to implement the temperature values of the rib cells to the matrix equations for the case were ribs are present. The second problem to be discussed is related to some numerical instabilities which occur during the iterative process due to the small scale of the cooling channels studied within this report.

The advection equation used for the calculation of the heat transfer in the cooling channel can be implemented into the system of equations given in equation 3.87 by using the following coefficients:

$$a_C = \dot{m}_c \cdot c_p \tag{3.98}$$

$$a_{F,e} = -\dot{m}_c \cdot c_{p,i+1} \tag{3.99}$$

Note that for the cooling channel the only $a_F$ coefficient which is nonzero is the $a_F$ coefficient for the eastward (right) boundary. The $a_F$ coefficient for the westward (left) boundary is zero due to the upwind scheme used, the heat flow out of the westward boundary due to advection is therefore represented in the $a_C$ coefficient as can be seen in equation 3.98. The North (top) and South (bottom) $a_F$ coefficients are also zero because the heat flows through these boundaries are represented by a boundary condition in the **b**-matrix instead (specified by equation 3.59). For the cooling channel inlet a constant temperature equal to the ambient temperature was assumed. This is achieved using a Dirichlet boundary condition (a temperature specified boundary condition). In this case the $a_{F,e}$ coefficient is placed in the **b**-matrix and multiplied with the starting temperature of the cooling fluid.

An example sparsity pattern of the **A**-matrix for a 5x5 mesh for an engine with a regenerative cooling channel without ribs can be seen in figure 3.20. The a-coefficients corresponding to the cooling channel can be easily identified, they are the coefficients on the diagonal which only have a single coefficient one column to the right of them. It can also be seen that the North (top) and South (bottom) $a_F$ coefficients for the cells bordering the cooling channel are removed for the bottom and upper wall respectively, these are replaced by a boundary condition in the **b**-matrix instead.

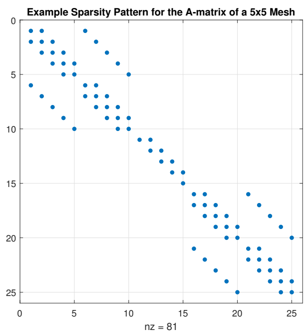


Figure 3.20: Sparsity pattern of the A Matrix for a 5x5 system with regenerative cooling.

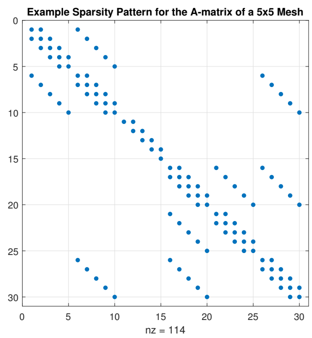


Figure 3.21: Sparsity pattern of the A Matrix for a 5x5 system with regenerative cooling with ribs.

If ribs are present within the cooling channel the question arises how to add the heat transfer from the ribs cells to the **A**-matrix. Within the system, the rib cells are located in parallel positions with the cooling channel cells so their positioning within the **A**-matrix is not obvious. The choice was made to add the rib cell temperatures at the bottom of the $\phi$ matrix, which corresponds to the cells in the bottom right corner of the **A**-matrix. As an example the sparsity pattern of the **A**-matrix for a 5x5 mesh for an engine with a regenerative cooling channel with ribs can be seen in figure 3.21. In this case the five cells on the lower right of the diagonal represent the $a_C$ coefficients of the rib cells. It can be seen that the $a_F$ coefficients of the North (top) and South (bottom) boundaries of the rib cells link back to the wall cells below and under the cooling channel.

With the modifications listed above the implicit method can be set up for Regeneratively cooled engines. For simulating large engines like the 1200 N engine used in the verification case the implicit method gave no problems, however when down scaling to the size of the PM200 several problems occurred. It was found that during the iterative process the model would often overestimate the coolant temperature during the first iteration steps, so much so that the coolant temperature would become higher than the maximum wall temperature. This is of course not possible as heat always flows from high to low temperatures. In the second iteration step the program therefore tried to compensate for the error by reversing the heat flow. In doing so the program would however again overcompensate leading to the coolant temperature to be underestimated and becoming even lower than the inlet temperature. This oscillatory behaviour would continue with the oscillations growing larger until the program would fail.

The cause of these oscillations can be attributed to the discretization in the time direction. The temperature in each cell is only known at the start of each time step. Based on these temperatures the heat flows are calculated. The convective heat transfer to the cooling channel is calculated using equation 3.60, which is reproduced below:

$$q_{conv,wc} = h_c \cdot (T_w - T_b)$$

As can be seen the heat flux is directly dependent on the temperature difference between the wall and the coolant. When a small thruster is simulated this temperature difference will be equal to zero during the first iteration step as the thruster starts at a temperature equal to the coolant temperature. The heat flux to the cooling channel is thus calculated to be zero in the first iteration, leading to a large increase in the wall temperature. In the second iteration step the coolant is still at the ambient temperature, while the wall temperature is already very high. This causes a relatively high temperature difference in equation 3.60 which in turn causes the program to overestimate the heat flux. For large engines this is not a problem as the coolant mass flow is relatively large, meaning that the coolant temperature does not overshoot the wall temperature. Because of this the error in the heat flux will be dampened in subsequent iteration steps. For small engines however the coolant mass flows are relatively low, which leads to an overshoot in the coolant temperature values. Because of this the heat flux will change sign as $T_b$ is now larger than $T_w$. This causes a large decrease in coolant temperature and the coolant temperature is now underestimated and the cycle thus starts again. The heat flux is overestimated again and in subsequent iterations the coolant temperature will oscillate between a too high and a too low temperature. For many cases these oscillations would continue to grow until the program fails. The main problem is that the temperature rise in the wall cells during the discrete time step is so large that the temperature difference between the wall cells and the coolant cells gets overestimated. On the other hand the wall temperature doesn't get hot enough so that the coolant temperature does not overshoot the value achieved by the wall temperature. An obvious solution to solve this problem would be to decrease the time step, this would lead to the temperature difference being smaller and would therefore reduce the overestimation of the heat flux. This is however undesirable as it will increase the simulation time and the whole point of implementing the implicit method was to decrease the simulation time. An alternative solution is to find a way to limit the heat flux calculated by equation 3.60 to realistic values such that the temperature values stay bounded and correct from a physical perspective. This second solution has the advantage that the time step does not need to be decreased and therefore it was decided to implement this second solution.

The question then becomes how to implement a method which limits the flux to a realistic value. The solution lies in realising that from a physical perspective no new maximum or minimum temperature can be created in a cooling channel cell with respect to its surrounding wall cells and the upwind cooling channel cell (see figure 3.22). For example: if the temperature in the upwind cooling channel cell is higher than the temperatures in both wall channel cells then the coolant temperature must decrease in cell C as no heat will be transferred from the wall into the coolant. Since the coolant starts out with the temperature of the upwind cell the coolant will transfer heat to the walls in cells $W_{j-1}$ and $W_{j+1}$. The amount of heat that is transferred from the coolant to the wall is limited by the temperature of the wall cells. The coolant temperature physically can not become lower than the wall temperature since heat is always transferred from high to low temperatures. Similarly if the lower wall temperature is higher than the upwind coolant channel cell temperature and the upper wall temperature the temperature will rise in cell C. This temperature rise can however not be such that the temperature in cell C becomes higher than the lower wall temperature because again, physically heat can only flow from high to low temperatures. Using similar logic it can be deduced that the temperature in cell C can never be a maximum or minimum for the four cells considered in figure 3.22. As an additional constraint, when the engine is burning it is also not possible for the temperature in cell C to become lower than the temperature of cell C in the previous time step (because the engine is heating up). The heat flux into the wall must thus be constrained such that the criteria mentioned above are met.

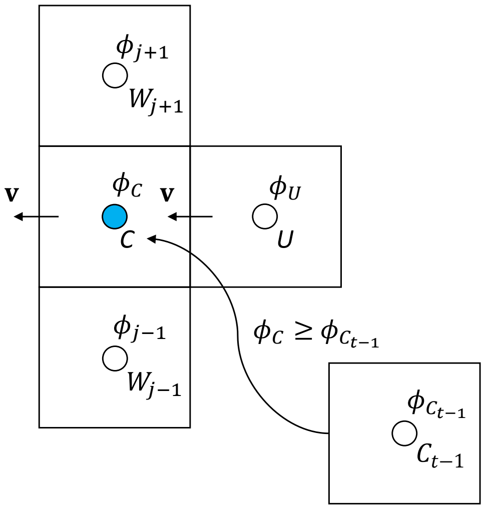


Figure 3.22: Temperature bounds on the temperature of the current cooling channel cell

To achieve this the following strategy was used. After calculation of the coolant temperature for a given iteration step the coolant temperature in every cell was compared to the lowest and highest surrounding temperature values. If the coolant temperature was a new maximum or minimum the cell would be flagged. For all cells that were flagged the temperature value was overwritten by a value equal to the average of the calculated value in the previous iteration and the maximum or minimum allowable value for that cell depending on whether or not the calculated value was too low high or too low respectively. By averaging the previously calculated value with the maximum or minimum allowable value the solution will automatically fall within the allowable range. If the value calculated in the following iteration is still above the maximum temperature, the same procedure is performed raising the temperature while still keeping it within the allowable range, using this methodology the method will always tend towards the correct value and once it is close enough to the real solution the over and undershoots will no longer occur. Additionally, if oscillations continue to be present for each of the flagged cells the heat flow in the next iteration is multiplied with a factor $\omega$ calculated using equation 3.100:

$$\omega = 0.95^{\frac{1000}{max(\phi)} \cdot n_T} \tag{3.100}$$

With $max(\phi)$ being the maximum temperature over the entire mesh and $n_T$ is the number of times the cell has been flagged in the current iteration cycle. By limiting the heat flux the oscillations between iterations are damped even further. Once the calculated coolant temperature value falls in between the maximum and minimum allowable value the factor $\omega$ is removed. At this point the temperature is however close enough to the actual solution that the over or underestimation of the heat flux is very small. Therefore overshoots and undershoots of the maximum and minimum temperature values will no longer occur and the scheme will convergence. It should be stressed that for the final calculation of the temperature the factor $\omega$ is not taken into account, it is strictly used to get the iterative scheme close to the true solution, once the outcome of the iteration is close enough to the true solution it is no longer required.

The values of 0.95, 1000 and $max(\phi)$ as used in equation 3.100 were selected such that they led to relatively fast convergence for the cases considered within this report. For different cases other values may be more suitable. The maximum temperature term in particular was included to ensure that the correction factor would decrease less fast when higher temperatures were reached. This is because for higher temperatures the over and undershoots are usually a lot smaller, so it doesn't make sense to immediately put a very large limitation on the heat flux. This is important as putting a too large limitation on the heat flux can lead to an underestimation of the heat flux which can cause the program to get stuck. This can for example happen when the estimated temperature is above the maximum allowable temperature but the absolute value heat flux has been lowered so much that the absolute value of the negative flux is not high enough to bring the temperature below the maximum heat flux value. To prevent the program from stalling in these cases a secondary equation was implemented which would raise the heat flux again slightly, but in smaller steps than the steps used in equation 3.100. This process is however requires additional steps, so ideally the parameters in equation 3.100 are chosen such that this scenario rarely occurs.

In general the instabilities described above occur only for the first few time steps (approx. t < 0.2s) and the corrections listed above are only required during the first few iterations. Once the cooling fluid has increased in temperature the corrections are no longer required and convergence usually occurs within a couple iterations without requiring any corrections.

One final problem that can occur is that the iteration scheme sometimes falls into a pattern where the iteration alternates between two or more values in a fixed order. If the error between none of these iterations is less than 0.1% this will cause the convergence criterion in equation 3.97 to not be met and the program will get stuck in an infinite loop. An additional feature was added to the program to detect when this problem occurs. In this case the program will calculate the temperature value for the next iteration as a weighted average of the temperature values in the previous iterations. This will break the pattern, allowing the iteration scheme to continue.

### 3.5.3. Direct Steady State solution

A similar approach as described above can also be used to directly solve for a steady state solution for a given thruster. In this case the system to be solved is the system given by equation 3.80. Applying the ILU(0) algorithm, the system of equations given in equation 3.80 can be solved using equation 3.101

$$\boldsymbol{\phi}^n = \left(\mathbf{I} - \left(\omega\bar{\mathbf{L}}\bar{\mathbf{U}}\right)^{-1}\mathbf{A}\right)\boldsymbol{\phi}^{n-1} + \left(\omega\bar{\mathbf{L}}\bar{\mathbf{U}}\right)^{-1}\mathbf{b} \tag{3.101}$$

Where $\omega$ is an under-relaxation factor which has a value between 1 and 0. This under-relaxation factor was implemented because during the implementation of the above mentioned method within the program it was noted that in many cases the spectral radius of the iteration matrix was equal to 1 or slightly above 1 for some iteration steps. In theory this can lead to a divergence in the solution although this was never observed during testing of the program. Nevertheless, in order to make sure that such a divergence could never occur an algorithm was added to the program which automatically applies under-relaxation to the iteration if the spectral radius becomes larger or equal to 1 during any given iteration step. In principle the factor $\omega$ is always set to 1 (no relaxation). However, if the algorithm detects that the spectral radius of the iteration matrix becomes equal or larger than unity, the program will decrease the value of $\omega$ until the spectral radius becomes smaller than 1.

## 3.6. Meshing strategy and grid convergence

In previous sections the mesh used within the program was discussed briefly. In this section the meshing will be discussed in more detail, explaining how the mesh is generated followed by a grid convergence study. Based on this grid convergence study some recommendations will be given to aid the user of the program in selecting a mesh. The results of the grid convergence study will also explain why certain mesh sizes were chosen in the analysis presented in chapter 5.

### 3.6.1. Mesh Generation

As was briefly mentioned before, the mesh generated within the program is a structured, non-orthogonal quadrilateral mesh. It was chosen to keep the “vertical” vertices of the mesh parallel to each other and perpendicular to the axis of symmetry, although this is not strictly required. In generating the mesh, the main question is how to distribute these “vertical” vertices in the best way. As will be shown in the next section, within the thruster the largest heat flux will be present at the sections with the smallest radius which is in this case the nozzle throat. Because of this, the largest temperature gradients as well as the largest temperatures will occur around these locations and these regions are therefore of the most interest. Therefore the choice was made to make the spacing in the axial direction of the vertical vertices proportional to the local radius. The following algorithm was used to generate the grid:

- **Step 1:** Divide the thruster into i equal elements Δx.
- **Step 2:** For each element determine the local radius of the thruster and determine the sum of the radius values for all elements.
- **Step 3:** Determine for each element what fraction the current radius value is of the total sum.
- **Step 4:** Multiply each of the Δx values by its corresponding fraction.
- **Step 5:** Using the new Δx values, determine the new start and end point of each element and the corresponding new radius value for each element.
- **Step 6:** Repeat this process until the Δx value for each element remains constant.

The iterations are required because otherwise in some cases the grid can become very skewed to one side depending on the geometry. Convergence of the grid is usually achieved relatively fast with less than ten iterations required.

### 3.6.2. Grid Convergence

A grid convergence study was performed to check what grid size is required for the program solution to become independent of the grid. This grid study was performed for two cases to rule out case dependency. The first case was using the Forward Euler time stepping method on a simplified version of the PM200 geometry. The second case was performed using the direct steady state solution on a reference thruster with design parameters which are different from those of the PM200 but still of roughly the same order of magnitude.

The result for the first case can be seen in figure 3.23. Pictured are the normalised temperature distributions for the outer wall of the thruster after a 3 second burn for different grid sizes. Seven different grid sizes were investigated with the most coarse grid being 30x5 and the most refined grid being 250x10. From figure 3.23 it becomes clear that the solutions are reasonably close. To illustrate this point, the percentage deviation between the solutions as compared to the 250x10 grid are plotted in figure 3.24. It can be seen that for all cases the solutions deviate less than 2% from each other.

The results for the second case can be seen in figure 3.25. Pictured are the normalised temperature distributions for the outer wall of the thruster in steady state. Six grid sizes are used with the most coarse grid being 20x5 and the most refined grid being 100x5. There is again a good agreement between the solutions. Looking at figure 3.26 it can be seen that the deviation between the solutions is less than 0.7% for all cases except for the 20x5 grid, which

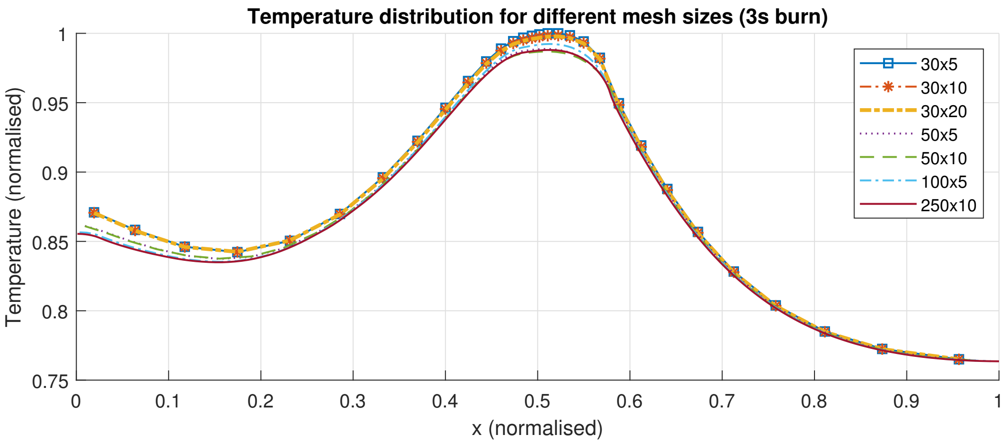


Figure 3.23: Normalised temperature distribution of the outer wall after 3 seconds of burn time for five different mesh sizes

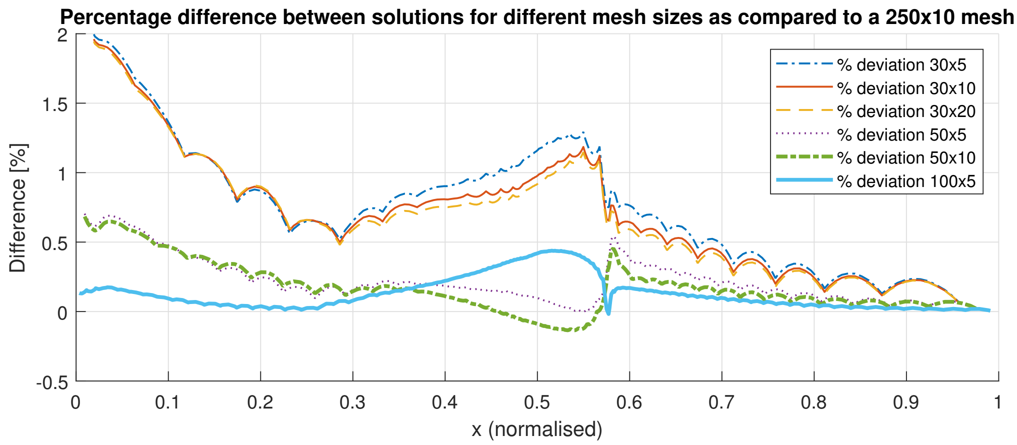


Figure 3.24: Difference between temperature distributions for four different mesh sizes as compared to a 250x10 mesh

has a maximum deviation of a little under 2%. This is most likely due to the fact that for coarser grids the thruster geometry is less accurately represented by the grid (see figure 3.27).

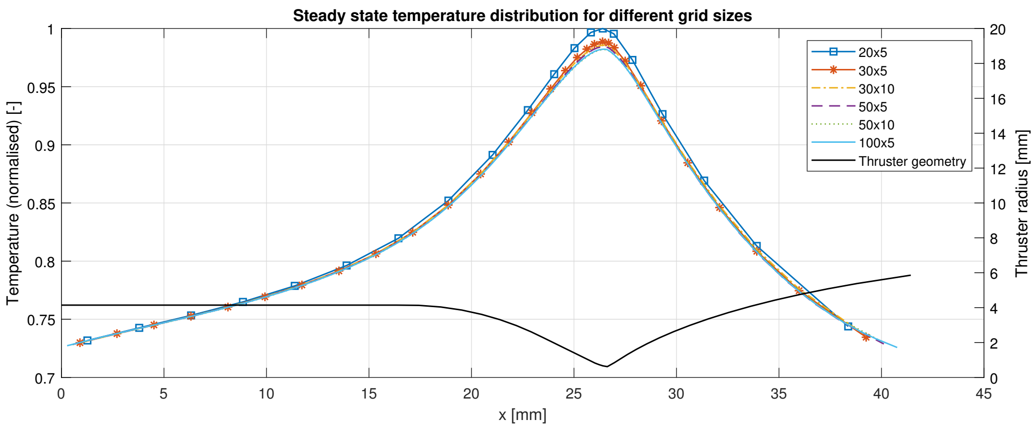


Figure 3.25: Normalised steady state temperature distribution of the outer wall for different mesh sizes

From the results shown above several conclusions can be drawn. It can be seen that grid convergence is achieved for a relatively coarse grid already as the solution is almost identical for all different grid sizes. The main factor determining the amount of grid points required

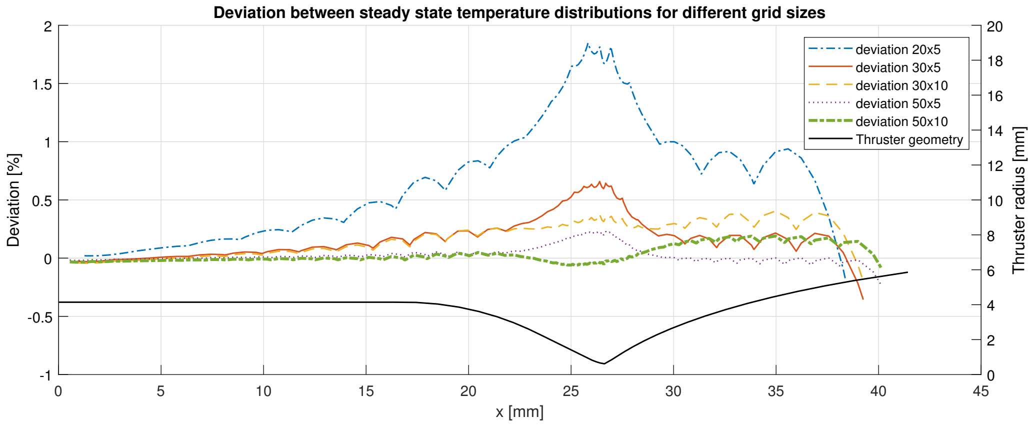


Figure 3.26: Deviation between the steady state temperature distribution of the outer wall for different mesh sizes as compared to a 100x5 mesh

is the minimum amount of grid points that are required to accurately represent the thruster geometry. This effect can be seen in figure 3.27. It can be seen that the 10x5 grid models the overall thruster geometry less accurately than the 100x5 grid, which causes a deviation in the solution. It can be seen that for the 20x5 grid the geometry is already represented more reasonably, although it can still be seen that the "curved" parts of the thruster are still quite "blocky". This also explains why the differences in the model results are largest near the nozzle throat (see figure 3.26 and 3.24); this is where the most curvature is present. For the PM200 a relatively large difference is also present near the injector, this is because for the PM200 design the wall is also curved near the injector. With a coarse grid this part of the geometry is not represented well, leading to a relatively large error at this point. For the 30x5 grid this "blockyness" is already reduced quite a bit, and this also translates into a more accurate solution as can be seen in figures 3.25 and 3.26.

From figures 3.23, 3.24, 3.25 and 3.26 it can also be seen that changing the grid size in the axial direction has a larger effect than changing the grid size in the radial direction. Adding more cells in the radial direction does however have a much larger impact on the required simulation time because adding a row of cells to the radial direction in general leads to more cells being added than adding a column in the axial direction. The wall thickness is also usually a lot smaller than the size of the thruster in the axial direction, so adding additional cells in the radial direction also more rapidly decreases the cell size, which leads to a decrease in the required time step (see equation 3.43), at least for the Forward Euler solution method.

Based on the above, it can be concluded that it is beneficial to add as little cells as possible in the radial direction, as this has relatively little effect on the outcome of the program but a large effect on the required simulation time. For radiation cooling a minimum of 3 cells are required in the radial direction. The mesh size in the axial direction can be larger, but a very large grid is not required based on the results presented above. It can be concluded that a 30x5 or a 50x5 grid is more than sufficient to get an accurate solution.

In the case a regenerative cooling channel or a Thermal Barrier Coating is added a slightly larger grid is required. This is to ensure that enough cell layers are present to represent each of the physical boundaries within the model. For the case where the thruster has a regenerative cooling channel a minimum of 5 cells are required in the radial direction, while for a thruster with a thermal barrier coating a minimum of 4 cells are required.

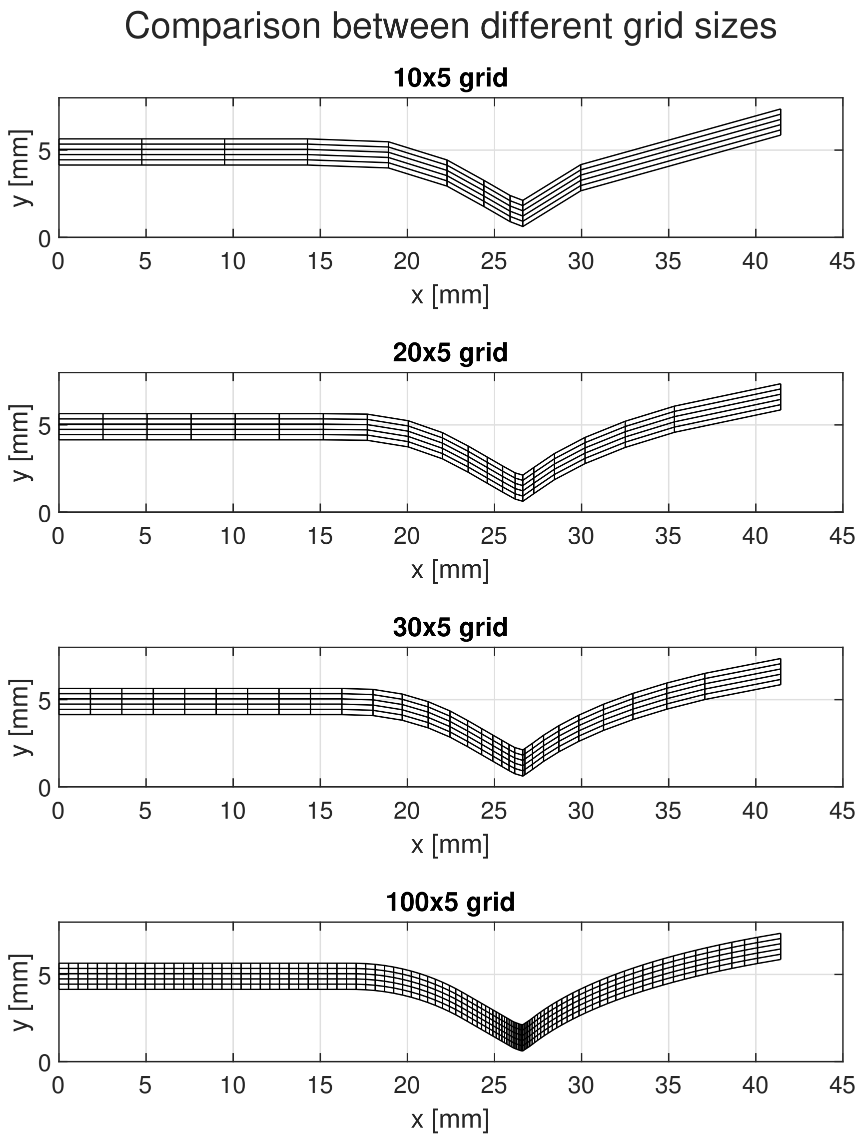


Figure 3.27: Comparison between different grid sizes for coarse meshes and more refined meshes

## 3.7. Model verification

To ensure correct implementation of the numerical model the model was extensively verified. The results from various pieces of code were compared to several different already available models which have been verified and validated before. In this way it was checked if every individual piece of code was implemented correctly. All calculations related to the verification of the model will be done using the reference thruster introduced in section 2.1.4. For convenience, a summary of the design parameters of this reference thruster is reproduced below in table 3.3.

The different aspects of the model were verified using several different software packages. The heat transfer from the combustion gases, the heat conduction model and the coolant temperature was verified using Rocket Propulsion Analysis v.2.3.2 (RPA), the cooling fluid properties were verified using the National Institute of Standards and Technology's (NIST) Reference Fluid Thermodynamic and Transport Properties Database (REFPROP).

Table 3.3: Verification case parameters

| Parameter | Parameter value [unit] |
|---|---|
| Thrust | 0.7 [N] |
| Chamber Pressure | 3 [bar] |
| Area Ratio (Supersonic) | 90 [-] |
| Area Ratio (Subsonic) | 45 [-] |
| Wall thickness | 1.5 [mm] |
| Fuel | Propylene [-] |
| Oxidizer | Nitrous Oxide [-] |
| O/F Ratio | 8 [-] |
| Material Thermal Conductivity | 15 [W/mK] (kept constant) |

### 3.7.1. Verification of the heat transfer coefficient and heat flux

To verify the heat transfer coefficient and heat flux the reference thruster was put into RPA, a commonly used computer tool for the design of rocket engines which is based on NASA CEA.[3] RPA has been extensively verified and validated and this is documented in various scientific papers and technical reports which are publicly available.[4]

RPA has the ability to perform a 1D steady state thermal analysis. While the approach used in RPA is simpler than the approach of the model presented in this report, it can still be used to verify the outcome of various parts of the model such as the calculation of the heat transfer from the combustion gases to the wall as will be discussed in this section. The conduction model and the calculation of the temperature distribution of the inner and outer thruster wall can also be verified by making some simplifications, this will be discussed in section 3.7.2.

The verification of the model using RPA was done in two steps: first the calculation of the convective heat transfer coefficient and the calculation of the heat flux were checked. Secondly the temperature distribution within the thruster was checked.

Because RPA can only perform a steady state analysis compared to the transient analysis performed by the model presented here the temperature profile of the wall was pre-specified within the model and it was set equal to the temperature distribution as given by RPA. This way the input parameters for calculating the convective heat transfer coefficient and the heat flux should be (nearly) identical which allows for the verification of these models. The result of this analysis can be seen in figures 3.28 and 3.29 where the convective heat transfer coefficient and heat flux as calculated by RPA and the current model are plotted. It should be noted that RPA calculated the convective heat transfer coefficient using the Bartz equation, nevertheless the results from the equation by Cornelisse et al. ([14]) are also shown in figure 3.28 for comparison.

From figures 3.28 and 3.29 it can be seen that the the outcome of the current model agrees excellently with the outcome from RPA. Some very small variations between the solutions can still be seen near the throat of the thruster were the convective heat transfer coefficient and heat flux are highest. There is however a simple explanation for this: RPA calculates the heat transfer coefficients and heat flux at several nodes (50 in this case) and then performs a 1D heat transfer analysis from these nodes to determine the temperature at each node. The finite volume model however calculates the heat transfer at the boundaries of every cell and uses this to calculate an average temperature at the center of each cell. This means that there is a slight offset in the temperature distributions calculated in RPA and the temperature

[3] RPA: When Computational Science meets Engineering - Computational simulation and design applications for research and development in the field of Chemical Rocket Propulsion and Combustion, A Ponomarenko, 2020, Available online at: http://propulsion-analysis.com/index.htm

[4] RP Software+Engineering UG - Publications, A Ponomarenko, 2020, Available online at: http://propulsion-analysis.com/publications.htm

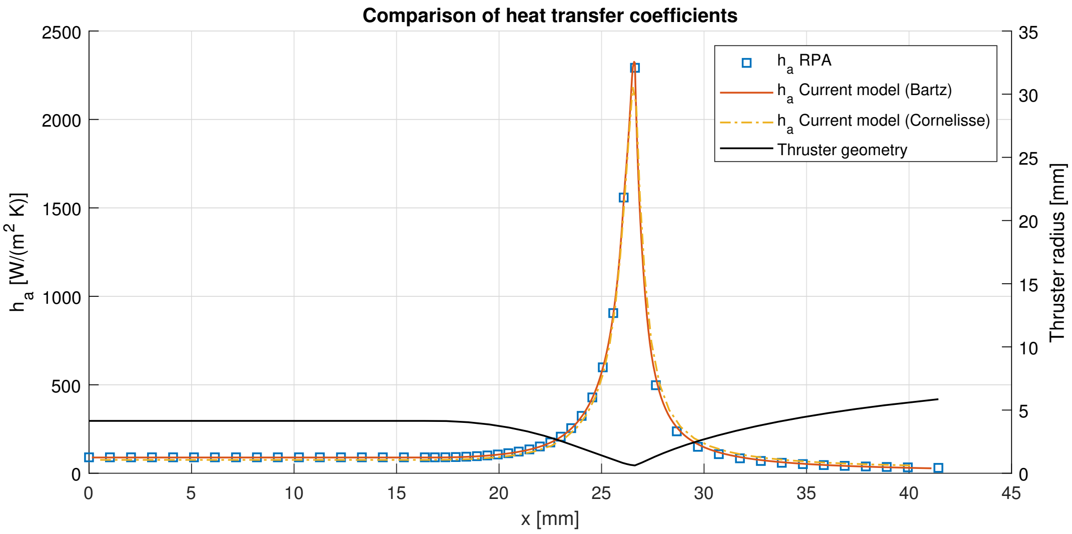


Figure 3.28: Comparison of the heat transfer coefficient as calculated by RPA and the current model

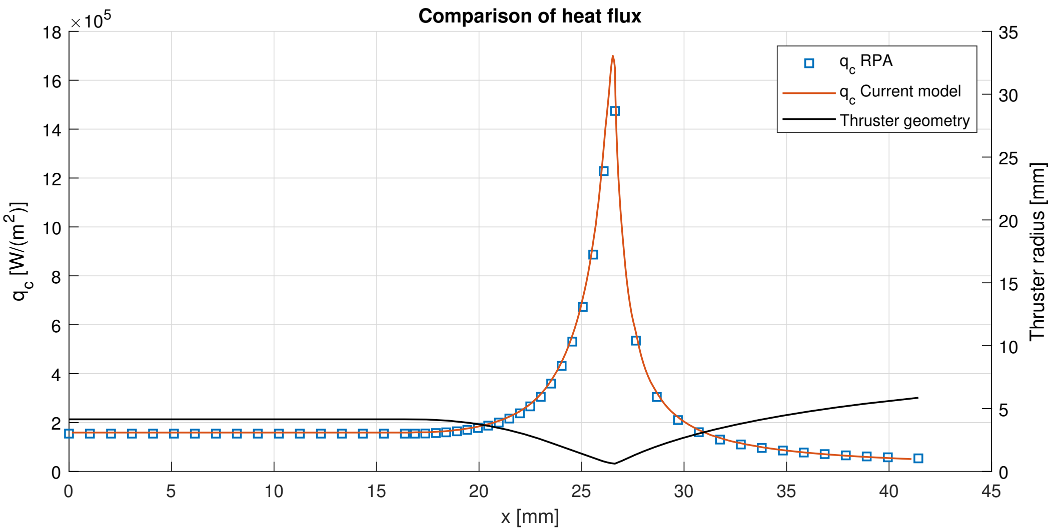


Figure 3.29: Comparison of the convective heat flux from the combustion gases as calculated using RPA and using the current model.

distribution within the finite volume model. This is displayed graphically for the nodes at the nozzle throat in figure 3.30. In figure 3.30 the temperatures T1 and T2 which are displayed in boldface are temperatures and their corresponding locations as calculated by the finite volume model while the temperatures T1, T2 and T3 displayed in italic are the temperatures and their corresponding locations as calculated by RPA. The grid spacing for the RPA model and the finite volume are not identical either meaning that the evaluation points may be even further apart. To create figure 3.28 and 3.29 the convective heat transfer coefficient and the convective heat flux were determined at several evaluation points and the graph was created by interpolating between these points. Since there is a slight offset between the points used in both models it is therefore not surprising that some points have a slight offset. This can also be confirmed by looking at the left side of the graphs were the solution is constant, in this case the solutions match exactly because the temperature profile is constant, eliminating the mismatch. In conclusion it can thus be said that the solutions practically identical which means that the models for calculating the heat transfer coefficient and the heat flux are implemented correctly.

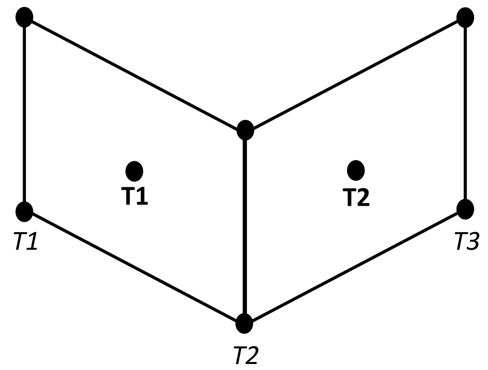


Figure 3.30: Difference in evaluation points for RPA and the current model.

The result from the method by Cornelisse et al. also agrees well with the results obtained using the Bartz method as can be seen in figure 3.28. The equation by Cornelisse et al. however predicts a slightly lower heat transfer coefficient in the combustion chamber and the nozzle throat, while predicting a slightly higher heat transfer coefficient in the divergent part of the nozzle. While these results look promising, it does not necessarily verify the correct implementation of the equation by Cornelisse et al. as this equation does not necessarily have to give similar results to the Bartz equation. In literature no verification data for the method by Cornelisse et al. could be found. Some example calculations using the method by Cornelisse et al. were however found in lecture notes[5] which were used to verify the correct implementation of the method. It was found that the equations by Cornelisse et al. as implemented in the model agreed with the example calculations (within 1%), verifying the correct implementation of the equations.

### 3.7.2. Verification of the conduction model

As mentioned earlier RPA has the ability to perform a 1D steady state thermal analysis. Because the model presented in this report is in 2D some alterations had to be made to verify the conduction model. To compare the two solutions an adaptation to the code was made which overwrote all the heat flux values in the axial direction and set them equal to zero. This way only the heat flux in the radial direction would be used for calculating the temperatures and a 1D model similar to the model RPA uses was obtained. It should be noted that the code which calculates the heat flux in the axial direction is identical to the code which calculates the heat flux in the radial direction, the only difference is the input parameters used. Therefore if the code is shown to be correct in the radial direction, it can also be assumed to be correct in the axial direction. Another adaptation that was made to the model was that curvature of the wall was neglected. This was done because RPA does not take into account the curvature of the thruster for its conduction model (i.e. a linear conduction profile is assumed). This has a slight effect on the model outcome and will be discussed in more detail at the end of this section.

To compare the numerical model with RPA, the code was run until a steady state was reached, this steady state solution was then compared to the steady state solution given by RPA. By comparing the solutions in this way not only the conduction model is checked, but it is also checked if the transient solution actually converges to the steady state solution for a sufficiently large simulation duration. In this way the time stepping algorithm can also checked at the same time. The results from the analysis described above can be seen below in figure 3.31 and 3.32 where a solution from RPA is compared to two solutions from the presented model with different mesh sizes.

[5] Thermal Rocket Propulsion (Lecture notes version 2.07), pages 173-175, B.T.C. Zandbergen, August 2018, Delft University of Technology, Faculty of Aerospace Engineering. Copy available at the TU Delft Library.

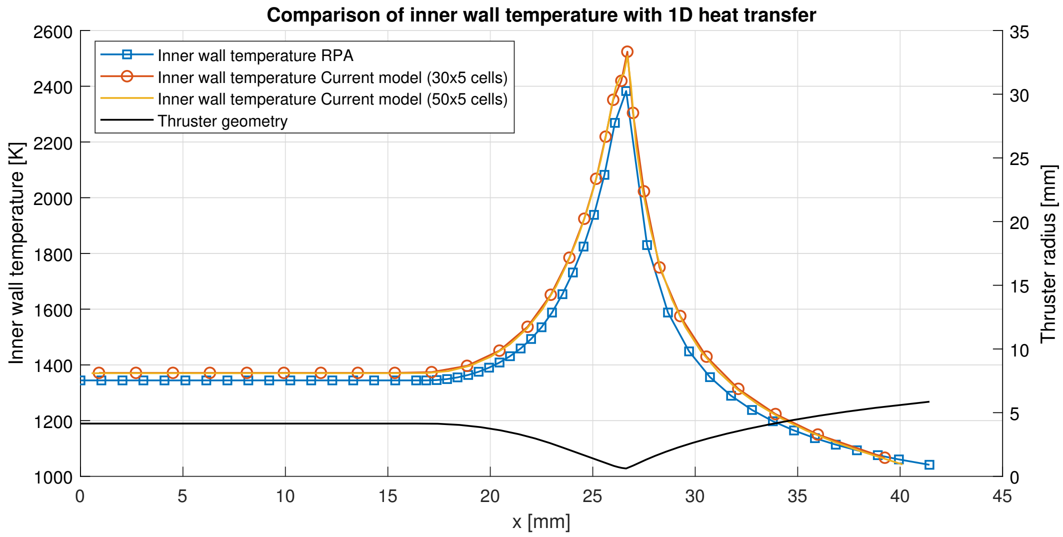


Figure 3.31: Comparison of the inner wall temperature as calculated using RPA and using the current model.

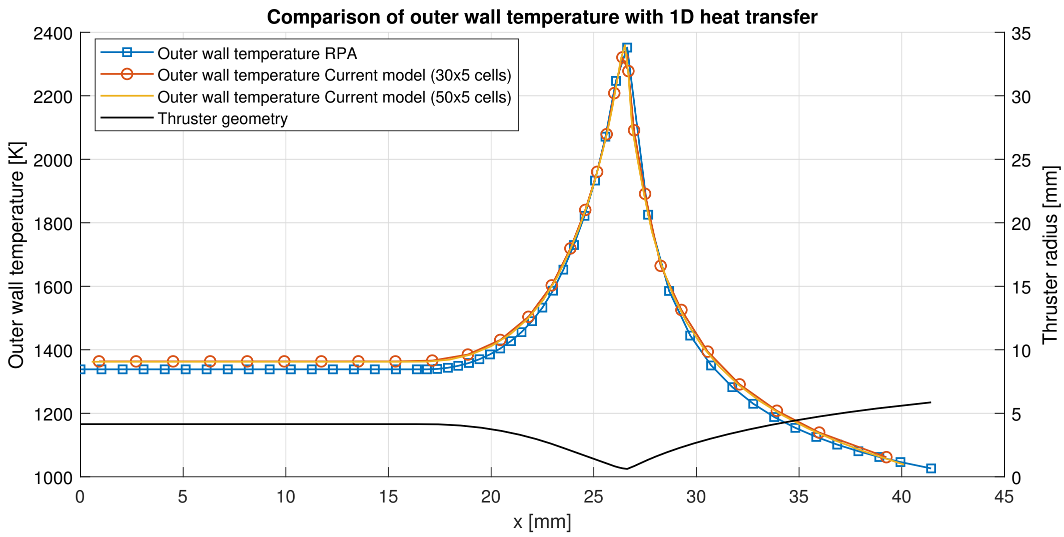


Figure 3.32: Comparison of the outer wall temperature as calculated using RPA and using the current model.

From figures 3.31 and 3.32 it can be seen that for the most part the solutions provided by RPA and the current model agree. Especially the outer wall temperature is very similar. For the inner wall temperature the current model gets slightly higher values than RPA. The difference between the two models as a function of axial coordinate can be seen below in figure 3.33.

It can be seen that for the majority of the axial coordinates the solutions of the model agree within 2% of each other. In the nozzle throat the solutions differ more, up to 7.6% for the inner wall temperature and up to 4% for the outer wall temperature. It should be noted that the graph presented here is an interpolation of the solutions given by both models and that it is therefore slightly misleading. However looking at figures 3.31 and 3.32 it can be seen that even at similar x-coordinates or at locations were the solution is constant there is some difference, so the difference isn't entirely caused by the interpolation error. There are multiple potential reasons for the differences in the two solutions, some more likely ones are listed below:

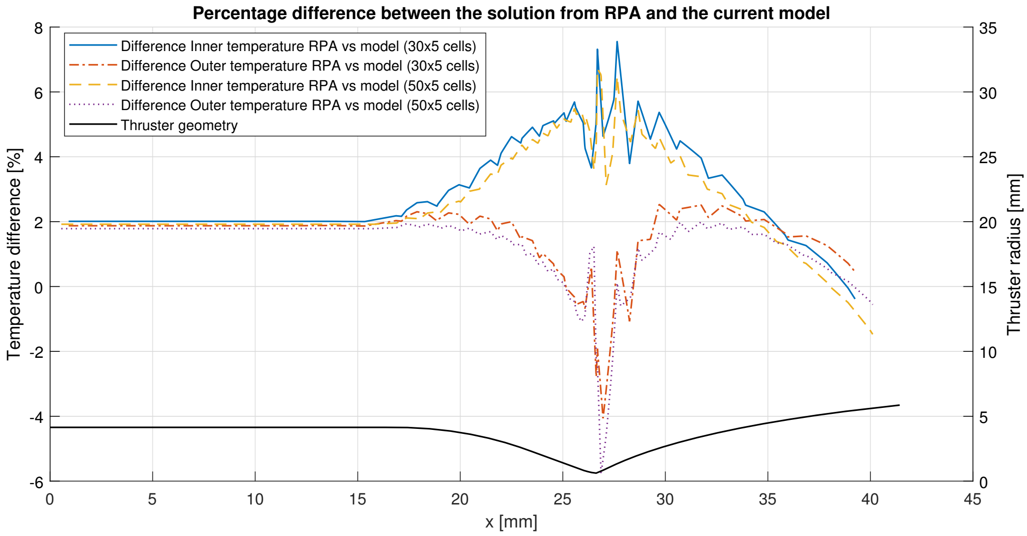


Figure 3.33: Difference between the inner and outer wall temperature as calculated using RPA and using the current model.

- The presented model arrived at the steady state solution using a transient calculation until steady state was reached while RPA directly solves for the steady state solution. The convergence criteria used in both models are therefore not the same and as a result the solutions could vary slightly. In the documentation of RPA [31] it can be seen that the RPA program considers the solution to have converged if the error between subsequent iterations is 5% or less, meaning that the potential error in the solution given by RPA could be up to 5%. For the outer wall the current model is always in agreement within this 5% error margin. For the inner wall the model is also in agreement within this 5% margin for the majority of the thruster cross section, only going beyond the 5% margin during some small sections within the nozzle throat.

- As mentioned in the previous section, part of the error is likely caused by the misalignment of the nodes at which RPA calculates the temperature values and the cell centroids at which the current model evaluated the temperature.

- The time stepping scheme used in the presented model has a finite accuracy, which could explain some of the differences observed.

- As was seen in section 3.6 the inner wall temperature as predicted by the current model decreases slightly as the amount of mesh cells is increased, since the verification case used a rather course mesh this could also explain part of the mismatch. It can also be seen in figure 3.33 that the mismatch for the case with more mesh cells is smaller than for the case with less mesh cells.

- It is unclear how many nodes RPA uses for its calculations in the radial direction, it could be that the amount of nodes used slightly alters the solution.

Besides the small differences, it can be said that overall the model agrees well with the solution from RPA. Especially considering the fact that the error margin of the RPA program is 5% as explained above. Therefore it can be assumed that the conduction model is implemented correctly.

As a final step the output from the model using the 1D restriction on the conduction model was compared to the output from the model where conduction was calculated in 2D. The steady state temperature distribution for the 1D conduction case as calculated by the model can be seen below in figure 3.34.

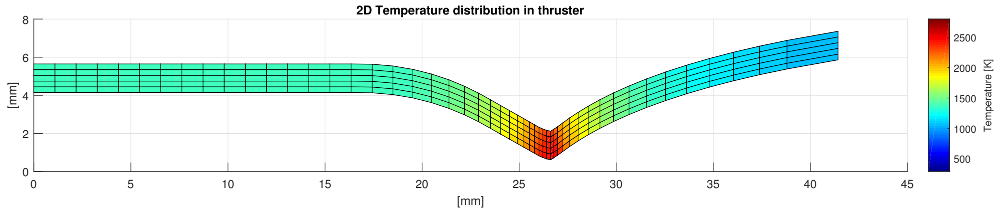


Figure 3.34: Steady state temperature distribution within the thruster body as calculated using conduction in 1 dimension (radial).

The steady state temperature distribution for 2D conduction as calculated by the model can be seen below in figure 3.35.

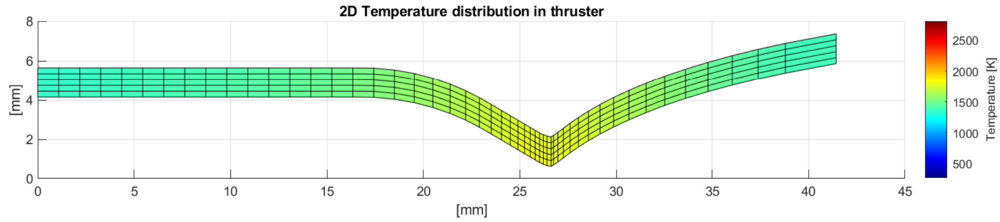


Figure 3.35: Steady state temperature distribution within the thruster body as calculated using conduction in 2 dimensions (radial and axial).

It can be seen that a 1D or a 2D evaluation of the conduction has a large effect on the final outcome of the temperature profile. Overall the behaviour is as expected, it can be seen that in the 2D case the wall temperature in the throat is lower when compared to the 1D case since the heat in this case can also be dissipated to cells on the side as compared to only in the radial direction. It can also be seen that the wall temperature in the combustion chamber and near the nozzle exit is higher in the 2D case when compared to the 1D case. This of course also makes sense as part of the heat from the nozzle throat is transferred to these regions. The results are also quite promising as in the 2D case the predicted temperature values of the wall are below 2000 K which allows for a wider range of materials which could be selected for a radiation cooled design when compared to the 1D case where the predicted maximum temperature is almost 2600 K.

As mentioned at the start of this section, RPA assumes a linear conduction profile for the calculation of the radiation cooled thruster. This is possible because in most cases the combustion chamber inner diameter is large compared to the wall thickness. In this case the difference between the circumference of the inside and outside of the combustion chamber wall is negligible and the curvature of the thruster can be neglected (i.e. the thruster is modelled as a flat plate which leads to a linear conduction profile). The PM200 and the reference case presented above however have a relatively high wall thickness compared to the combustion chamber inner diameter. For the 1D case the linear conduction profile only has a small effect on the outcome. However if 2D conduction is taken into account the curvature can no longer be neglected as the ratios between the side surfaces and the upper and lower surfaces of each cell no longer stay constant. Especially where there are large differences in the local diameter this gives issues (for example at the nozzle). The model presented here therefore takes the curvature of the thruster into account, the resulting steady state temperature distribution for the 2D conduction case while taking the curvature of the thruster into account can be seen in figure 3.36.
It can be seen that the main differences in the temperature distribution are located near the nozzle. A significant reduction in temperature is seen near the nozzle throat and the nozzle exit. The nozzle exit becomes colder because the vertical surfaces at the nozzle exit become larger when curvature is taken into account. This results in an increase in radiative heat

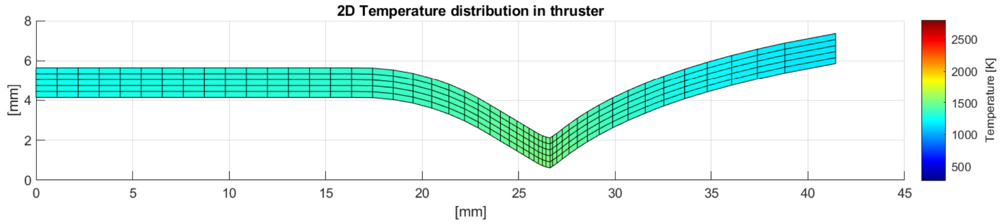


Figure 3.36: Steady state temperature distribution within the thruster body as calculated using conduction in 2 dimensions (radial and axial) and curvature effects included.

transfer to the environment explaining the reduction in temperature. As a result, the nozzle throat also becomes colder because more heat can now be conducted towards the nozzle exit since the wall temperature is now lower here. By taking curvature effects into account the overall temperature in the nozzle throat decreases by almost 250K. For the combustion chamber itself there is almost no change in the temperature, this is because a different boundary condition is used at the injector interface. This boundary condition is not affected by curvature effects and therefore the difference in the solution is small at this location.

### 3.7.3. Verification of coolant fluid properties

The calculation of the coolant fluid properties within the model was verified by comparing the results to results from REFPROP. The primary equations to be verified were the equations of state used to calculate the density and the heat capacity of the coolant fluid, furthermore the thermal conductivity and the viscosity of the fluid were also verified. In figures 3.37 and 3.38 the calculated densities and heat capacities for a range of temperatures and pressures can be seen as calculated by the current model compared to the values obtained from REFPROP.

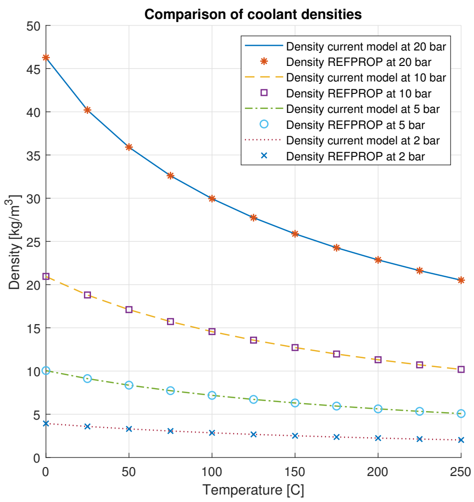


Figure 3.37: Density as calculated by the current model compared to REFPROP

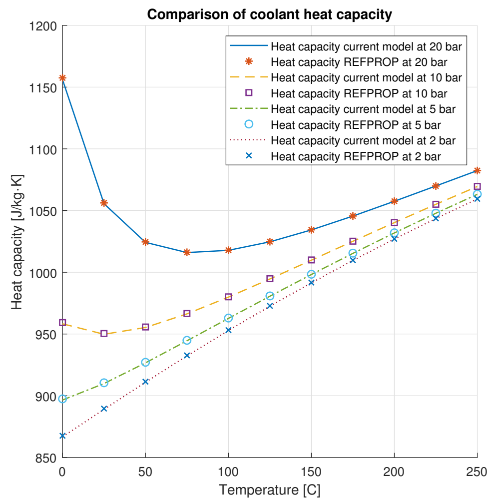


Figure 3.38: Heat capacity as calculated by the current model compared to REFPROP

From figures 3.37 and 3.38 it can be seen that there is a good agreement between the two models. The exact error for the 10 and 20 bar cases is also plotted below in figure 3.39, it can be seen that the largest differences occur within the calculation of the heat capacity and that the differences mostly occur at low temperatures. Nevertheless the differences are less than 0.15% which can easily be explained by rounding errors. Similar results were obtained for the other two cases presented in figures 3.37 and 3.38. Overall it can be said that there is an excellent agreement between the current model and REFPROP, meaning that the calculations for the density and heat capacity were correctly implemented.

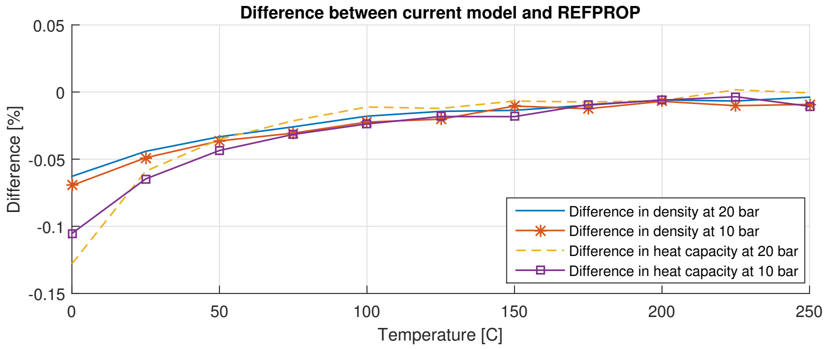


Figure 3.39: Difference between density and heat capacity as calculated using the current model and using REFPROP

In figures 3.40 and 3.41 the thermal conductivity and viscosity of the fluid as calculated by the model can be seen compared to the values given by REFPROP. Again it can be seen that there is an excellent agreement between the model and REFPROP. Although the error graphs will not be presented here, it is noted that the errors observed were similar in magnitude to the errors shown in figure 3.39. It can therefore also be concluded that the calculations for the thermal conductivity and viscosity of the fluid are implemented correctly.

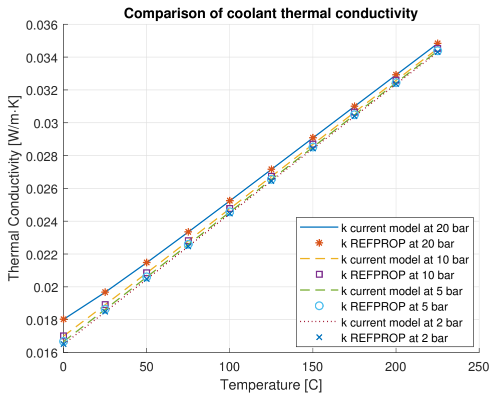


Figure 3.40: Thermal conductivity as calculated by the current model compared to REFPROP

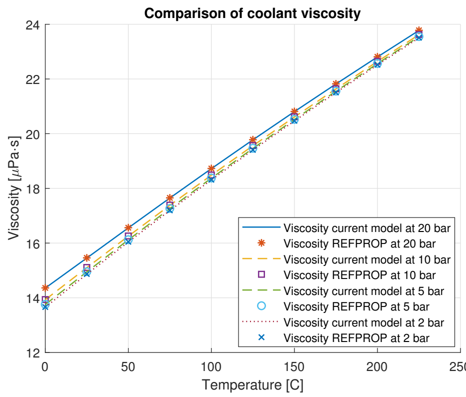


Figure 3.41: Viscosity as calculated by the current model compared to REFPROP

### 3.7.4. Verification of coolant fluid properties within the cooling channel

As shown in the previous section, the coolant density and heat capacity are correctly calculated by the model for a given pressure and temperature. To verify that the coolant fluid properties are also correctly calculated in the model while in a coolant channel the program output was compared with outputs from RPA.

As mentioned before, while RPA is a useful tool it has certain limitations. One of these limitations is that for engines within the thrust ranges considered in this report certain functions of the RPA program simply don't work. One of these was the regenerative cooling analysis. Therefore to verify the current model and to compare it with RPA a different, larger reference engine was used. The parameters for this engine were roughly based on Dawn Aerospace's NP120 engine [48] (but the thrust was scaled up by a factor of 10) and can be seen below in table 3.4.

RPA does not have nitrous oxide pre-programmed as a coolant. RPA does however allow one to add coolants by providing a table which gives the heat capacity, density, viscosity and thermal conductivity for a given coolant temperature and pressure. Since these coolant

Table 3.4: Verification case parameters for the regeneratively cooled case.

| Parameter | Parameter value [unit] |
|---|---|
| Thrust | 1200 [N] |
| Chamber Pressure | 3 [bar] |
| Area Ratio (Supersonic) | 2.4 [-] |
| Area Ratio (Subsonic) | 3.5 [-] |
| Inner wall thickness | 1.5 [mm] |
| Fuel | Propylene [-] |
| Oxidizer | Nitrous Oxide [-] |
| O/F Ratio | 6.5 [-] |
| Material Thermal Conductivity | 15 [W/mK] (kept constant) |
| Cooling using | Oxidiser [-] |
| Cooling channel type | Singular Sleeve [-] |

properties were shown to be accurately modelled in section 3.7.3, such a table could easily be generated. This table was then imported into RPA and the coolant properties are then determined by interpolating between the points specified in the table. Due to the nature of the importing process in RPA, only a limited amount of points could be imported. The fluid properties were therefore imported for the pressures 2, 5, 10 and 20 bar and for steps of 25K for the temperatures ranges between 273.15-523.15 K and with steps of 175K for the temperature ranges between 523.15-2273.15 K. This was done because below temperatures of 250 °C the coolant properties are highly non-linear (see figures 3.37 and 3.38 for example) so more data points are needed to get an accurate interpolation while for temperatures above 250 °C the coolant properties behave almost linearly so less data points are required. Nevertheless it should be noted that because the amount of data points within the table is relatively small, the solution given by RPA can be expected to be somewhat off due to interpolation errors.

The verification of the coolant fluid properties within the coolant channel was performed in a similar manner as the verification of the heat transfer coefficient. The temperature distribution as given by RPA was directly substituted in the model to ensure that input parameters for determining the coolant fluid properties were identical. The program outputs were then compared to the outputs from RPA. The following parameters were verified: the coolant flow velocity, the coolant density distribution and the coolant pressure distribution. The results can be seen below in figures 3.42, 3.43 and 3.44.

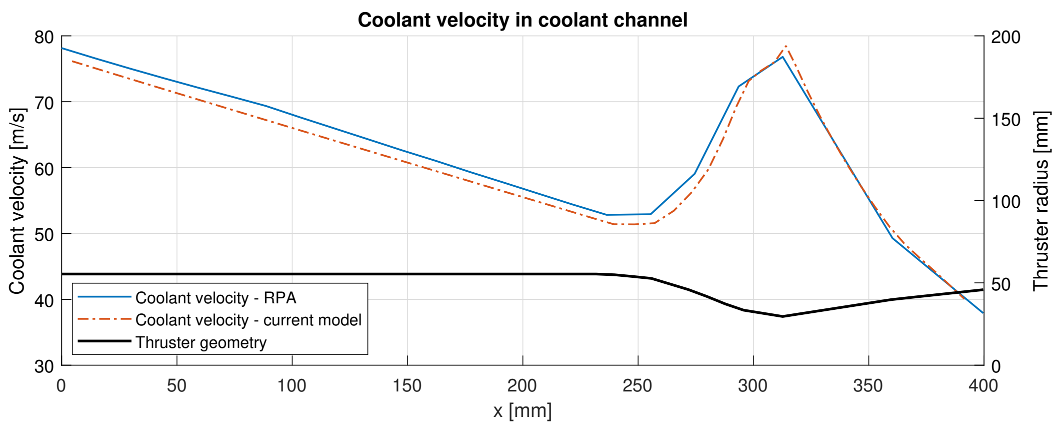


Figure 3.42: Coolant velocity as calculated by the current model compared to RPA

Overall it can be seen that there is a good agreement between the current model and RPA. For the coolant pressure distribution there still is a relatively large error of up to 5%. This is because RPA uses a different equation to calculate the friction factor within the coolant

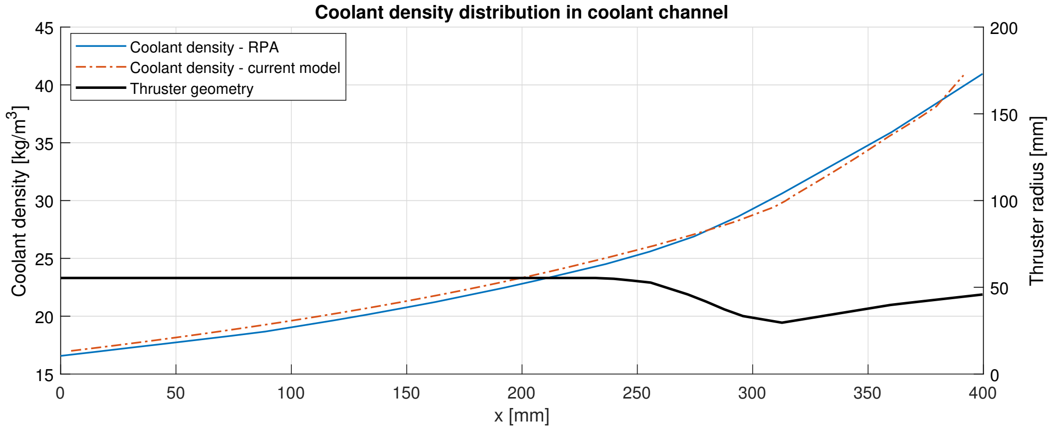


Figure 3.43: Density distribution within the cooling channel as calculated by the current model compared to RPA.

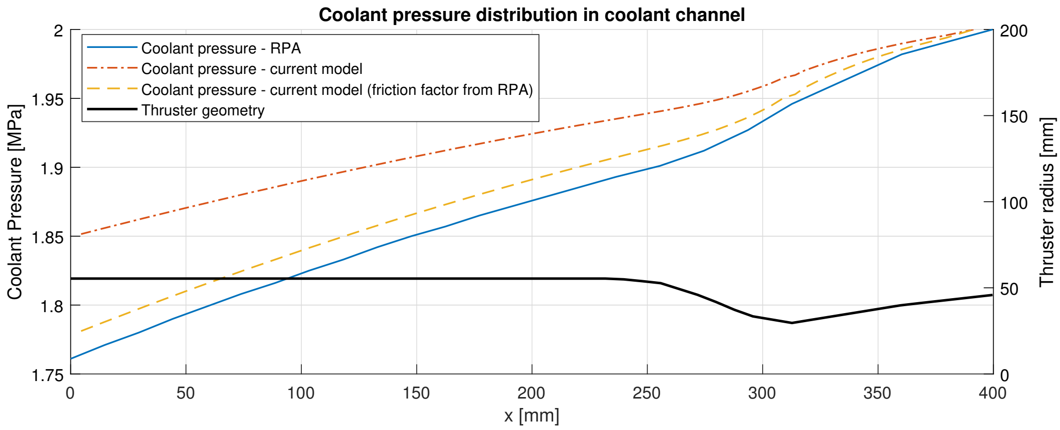


Figure 3.44: Coolant pressure distribution within the cooling channel as calculated by the current model compared to RPA.

channel [31]. This equation is given by equation 3.102.

$$f_i = \frac{0.3164}{Re^{1/4}} \cdot 1.5 \tag{3.102}$$

In this equation an extra factor of 1.5 is added, which increases the pressure drop. A source in Russian is given for this factor. However since this source could not be independently verified it was decided to not adopt this different equation. To check whether this different friction factor equation was the source of the error, the alternative equation was implemented within the presented model. In figure 3.45 it can be seen in this case the error between the solution from RPA and the model is less than 1%. It can therefore be concluded that the main difference between the two models is due to the usage of a different friction factor equation. Overall both models are still within an agreement of 5% for all coolant fluid parameters, verifying the correctness of the presented model.

Looking at figure 3.45 it can be seen that the coolant velocity, coolant density and coolant pressure match within 5.5%. Overall this is a good match, especially considering the fact that the amount of input data points for the fluid properties was rather limited which decreased the accuracy of the RPA model somewhat. It can thus be concluded that the coolant properties are also correctly simulated within the cooling channel.

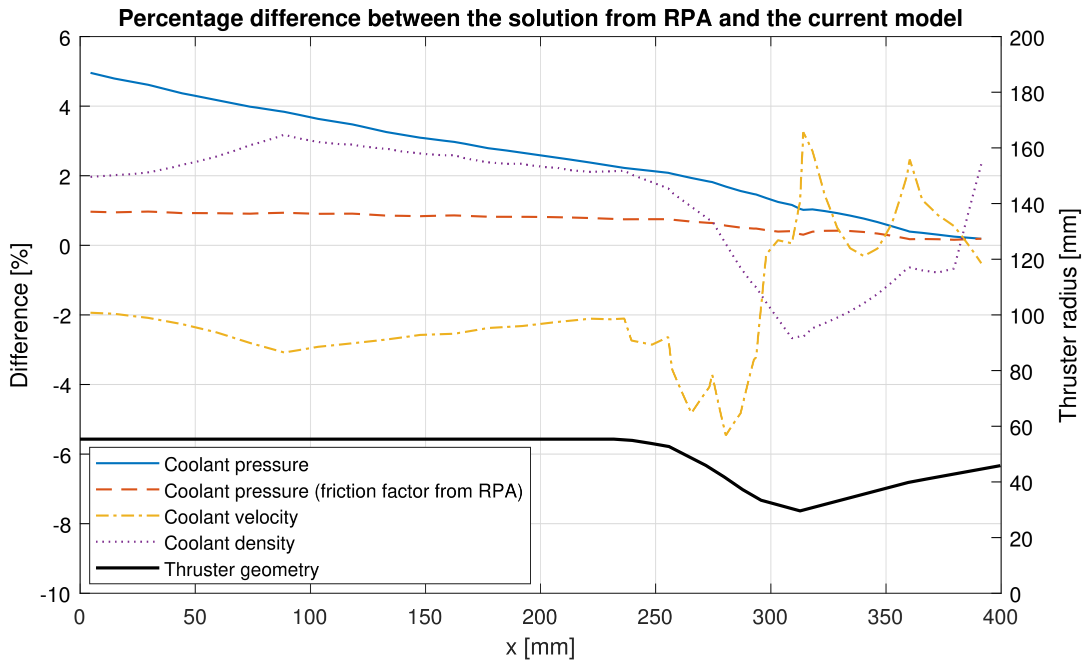


Figure 3.45: Difference between the coolant properties in the coolant channel as calculated using RPA and the current model.

### 3.7.5. Verification of coolant heat transfer and coolant temperature

With the coolant properties verified, the final step is to verify the heat transfer from the combustion chamber walls to the coolant fluid and the coolant temperature. Because the RPA program is much simpler than the model presented here, several simplifications had to be made, these were:

- The Wall thermal conductivity was set to be constant at 15 W/mK.
- Heat transfer due to conduction was limited to 1 dimension (in the radial direction).
- No heat transfer from the coolant to the outer wall elements was allowed.
- The heat transfer was set such that the heat transfer could only be from the wall to the coolant, not the other way around.
- Only the viscous pressure drop was taken into account, the pressure drop due to expansion and contraction of the cooling channel was neglected.
- Heat transfer due to radiation was neglected, both for the heat transfer from the combustion gases to the wall as well as for the heat transfer from the wall to the coolant channel.
- The friction factor was calculated using the method from RPA (equation 3.102)
- Heat capacity was kept constant (not in all cases, see clarification below)

To verify the heat transfer coefficient and heat flux from the wall to the coolant, the temperature profiles obtained from RPA were put into the program in a similar manner as was done for the verification of the heat flux from the combustion gases. Again, this was done to ensure that the input parameters for the calculation of the heat transfer coefficient would be (nearly) identical so a proper comparison could be made.

According to the technical documentation of RPA [31], RPA has four different methods for calculating the heat transfer coefficient to the cooling fluid. The method chosen depends on the cooling fluid. Methods are available for Kerosene, Liquid Hydrogen, Methane and “other coolants” [31]. Since Nitrous Oxide is used in this case, the equation for “other coolants” was used, which is the Dittus-Boelter equation which was given in equation 3.62 and which is also used in the current model.

In figure 3.46 it can be seen that the result of the current model does not match up well with the result for RPA when the Dittus-Boelter equation is used. However, upon further investigation it appears that this is not a mistake in the presented model, but rather it appears to be an error in the documentation of RPA. It can quite simply be proven that the heat transfer coefficient distribution as plotted in figure 3.46 using the Dittus-Boelter equation is correct for the input parameters in RPA. The Dittus-Boelter equation is only dependent on the Reynolds number and the Prandtl number, thus if it can be shown that these two parameters were implemented correctly the heat transfer coefficient distribution must also be correct.

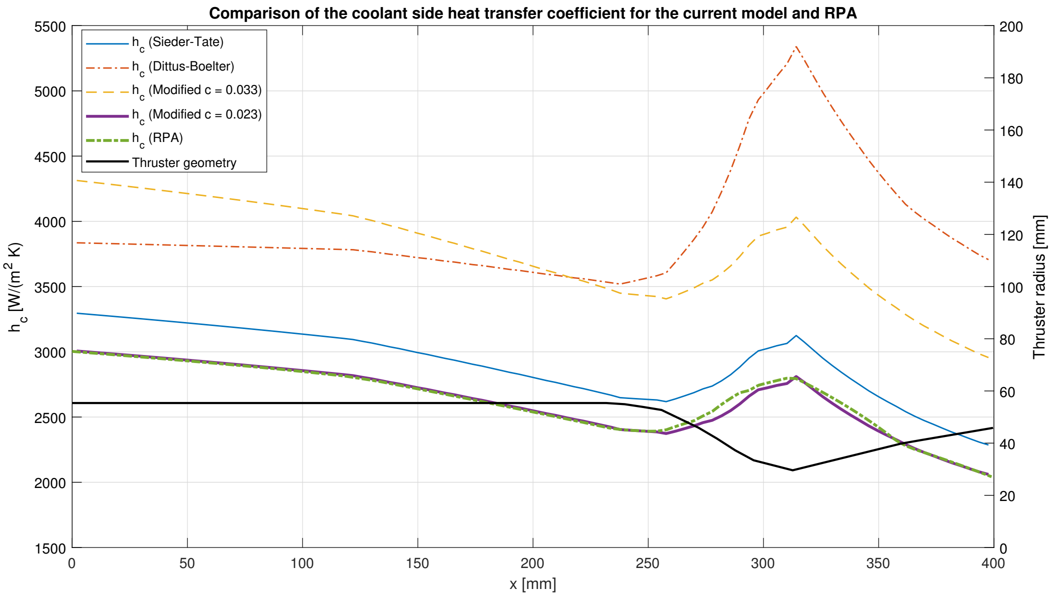


Figure 3.46: Comparison of the coolant heat transfer coefficient as calculated using RPA and using the current model.

As was shown in section 3.7.4, the pressure drop as calculated by the current model and by RPA agree within 1% when equation 3.102 was implemented. This equation is solely dependent on the Reynolds number. Therefore, it can be assumed that the Reynolds number is implemented correctly since the two results match within 1%. The only difference could thus be in the Prandtl number, which is given by equation 3.66. This equation is however dependent only on the specific heat capacity, viscosity and thermal conductivity of the fluid, which were input values for RPA. By comparing the heat capacity, viscosity and thermal conductivity of the cooling fluid for the temperature and pressure distribution with the table of input values, it was checked whether or not there were differences between any of the values and it was found that there were none. This means that the Prandtl number was also calculated correctly. As a result, it must be concluded that the heat transfer coefficient distribution as plotted in figure 3.46 using the Dittus-Boelter equation is correct. It is mathematically impossible to arrive at the same result as given by RPA using the Dittus-Boelter equation.

In an attempt to understand where the result from RPA came from, the other equations given in the documentation of RPA ([31]) for different cooling fluids were implemented within the model. It was found that the equation which supposedly is used for liquid hydrogen by the RPA program (equation 3.103) matches the shape of the heat transfer coefficient distribution as given by RPA well, except the curve is about a factor of 30% larger in magnitude. In figure 3.46 this curve is indicated as "$h_c$ (Modified c = 0.033)".

$$Nu = 0.033 \cdot Re_c^{0.8} \cdot Pr_c^{0.4} \cdot \left(\frac{T_c}{T_w}\right)^{0.57} \tag{3.103}$$

Note that equation 3.103 is essentially the same as the Sieder-Tate relationship (equation 3.61) when rewriting this equation into the Nusselt number form (using equation 3.63) and as the Dittus-Boelter equation (equation 3.62). The only differences between equation 3.103 and the Dittus-Boelter equation are the temperature dependent term at the end and the fact that the constant at the start of the equation is changed from 0.023 to 0.033. The difference between the 0.033 and 0.023 is almost exactly 30%. Replacing the value of 0.033 in equation 3.103 by a value of 0.023 the curve labelled by "$h_c$ (Modified c = 0.023)" was obtained. It can be seen that this curve matches almost exactly with the distribution given by RPA. The small difference is easily explained by rounding errors and discretization errors. It thus appears that RPA uses equation 3.103 but with the constant modified to be 0.023 in its calculations.

There are several options for what could potentially have caused this discrepancy. It could be that the factor 0.033 is a typo in the documentation of RPA. However, looking at the original source of the equation ([20]) it appears that the equation as given by 3.103 is correct. This option thus seems unlikely.

It could be that RPA scales the factor of 0.033 based on the cooling fluid parameters and that this is not documented within the technical documentation. Or it could be that there is a mistake in the RPA program.

For verification of the temperature distribution the modified equation ("$h_c$ (Modified c = 0.023)") was used. Furthermore a comparison was also made for the the Sieder-Tate relationship since this equation is very similar to the modified equation discussed previously. For the modified equation, two different cases were simulated, one were the coolant heat capacity was kept constant at the mean value and one where the coolant heat capacity was allowed to vary. This was because the documentation of RPA states that an average coolant heat capacity is used [31], however it is not exactly clear whether this refers to an average coolant heat capacity over the entire cooling channel or an average coolant heat capacity per station. In any case, the difference between the two solutions is minor as can be seen in figure 3.47 and for both cases the results match well with the solution give by RPA.

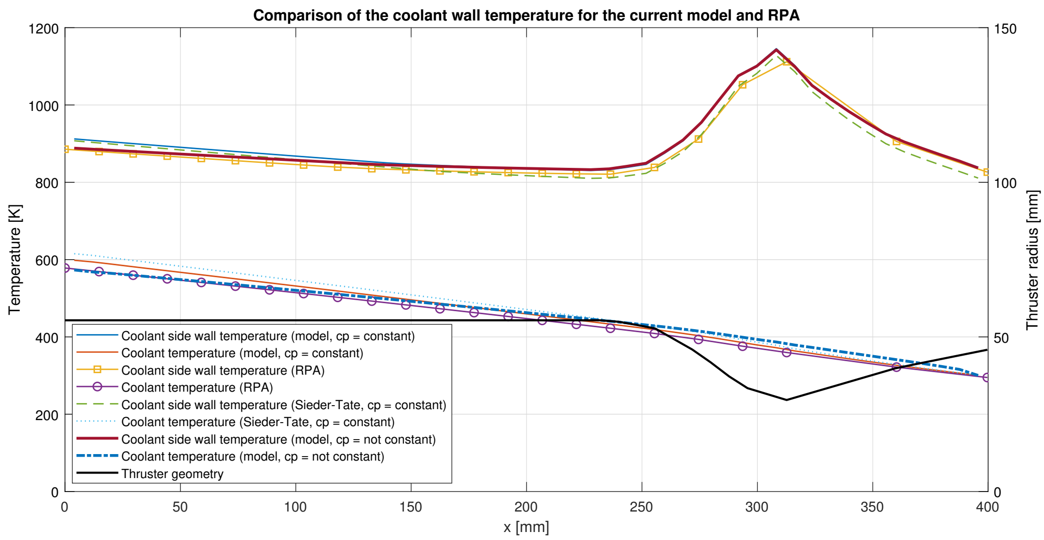


Figure 3.47: Comparison of the coolant and coolant side wall temperature as calculated using RPA and using the current model.

In figure 3.48 the percentage difference between the solution from RPA and the current model can be seen. Somewhat surprisingly it can be seen that the wall temperature achieves the best match when the Sieder-Tate relationship is used. For the modified equation the result for the constant and non constant coolant heat capacity are close although for the wall temperature the case with non constant heat capacity matches somewhat better. For both cases the difference is within the 5% error margin that RPA uses as its convergence criterion. For the coolant temperatures a good agreement is reached for all cases. It can be seen that for the case where the heat capacity is kept constant the difference between the solution of the model and RPA seems to be slightly larger at the end of the cooling channel with a maximum deviation of below 4.1%. For the case where the heat capacity is not kept constant the difference at the end of the channel is less than 1%, however a larger error of almost 6.5% is seen near the start of the cooling channel. Overall the differences are similar as were observed for the radiation cooled case and they are in good agreement with the results from RPA. It can thus be concluded that implementation of the regenerative cooling model is correct, verifying the model.

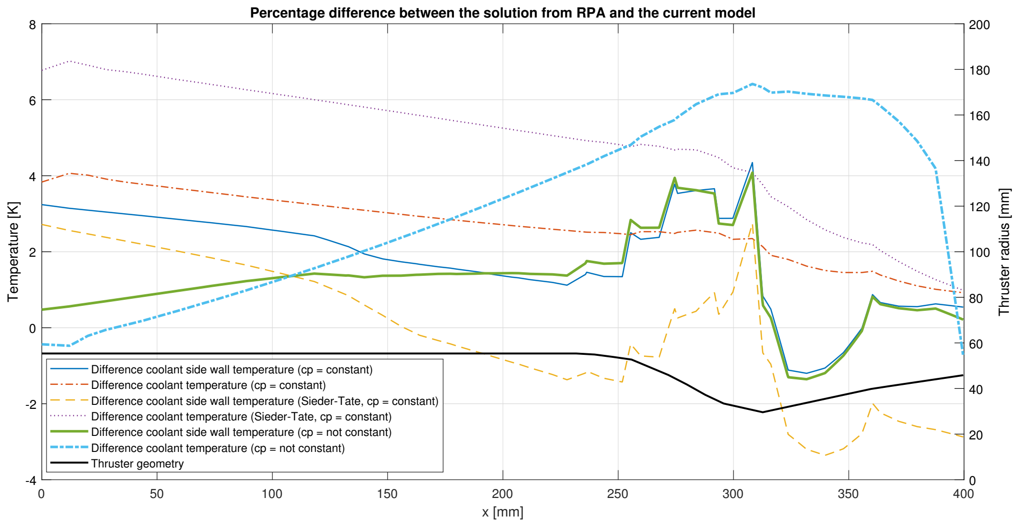


Figure 3.48: Difference between the coolant and coolant side wall temperature as calculated using RPA and the current model.

As a final step, the output from the model using the 1D restriction on the conduction model and the other restrictions as specified above was compared to the output from the model where conduction was calculated in 2D without any of the restrictions mentioned above. The steady state temperature distribution for the 1D conduction case as calculated by the model can be seen below in figure 3.49. Note that the top layer of cells above the cooling channel cells are still at 295K because no heat transfer was permitted to these cells. Also note that the mesh lines are turned off in this plot to make the plot more readable.

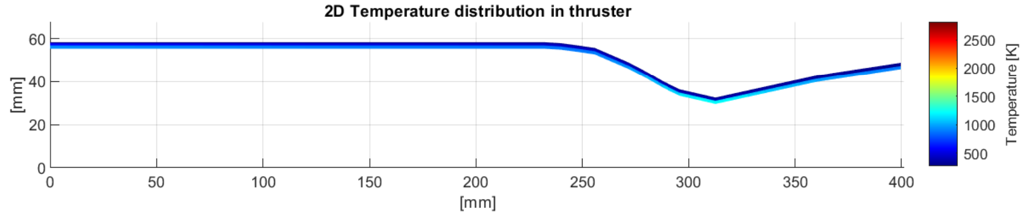


Figure 3.49: Steady state temperature distribution for the Regeneratively cooled case performing heat transfer calculations in 1 dimension (radial).

In figure 3.50 the temperature distribution within the thruster can be seen with conduction in 2 dimensions (radial and axial). It can be seen that the solution for the 2D conduction case is very close to the solution for the 1D conduction case. This is because the coolant channel is the main factor in determining the heat transfer distribution in this case and the equilibrium condition is roughly the same. The top wall cells reach approximately the same temperature as the coolant fluid.

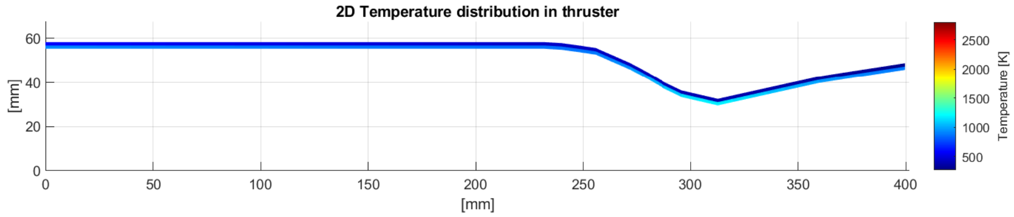


Figure 3.50: Steady state temperature distribution for the Regeneratively cooled case performing heat transfer calculations in 2 dimension (radial and axial).

### 3.7.6. Verification of implicit solution method & direct steady state solution method

In section 3.7.2 it was verified that the Forward Euler time stepping scheme converges to the correct solution. To verify whether or not the implicit method and the direct steady state approach as introduced in section 3.5 were implemented correctly in the model the solution obtained through these methods was checked against the solution obtained from the Forward Euler Method. A comparison of the 2D temperature distribution[6] of the thruster in steady state as calculated by the three different methods can be seen in figure 3.51.

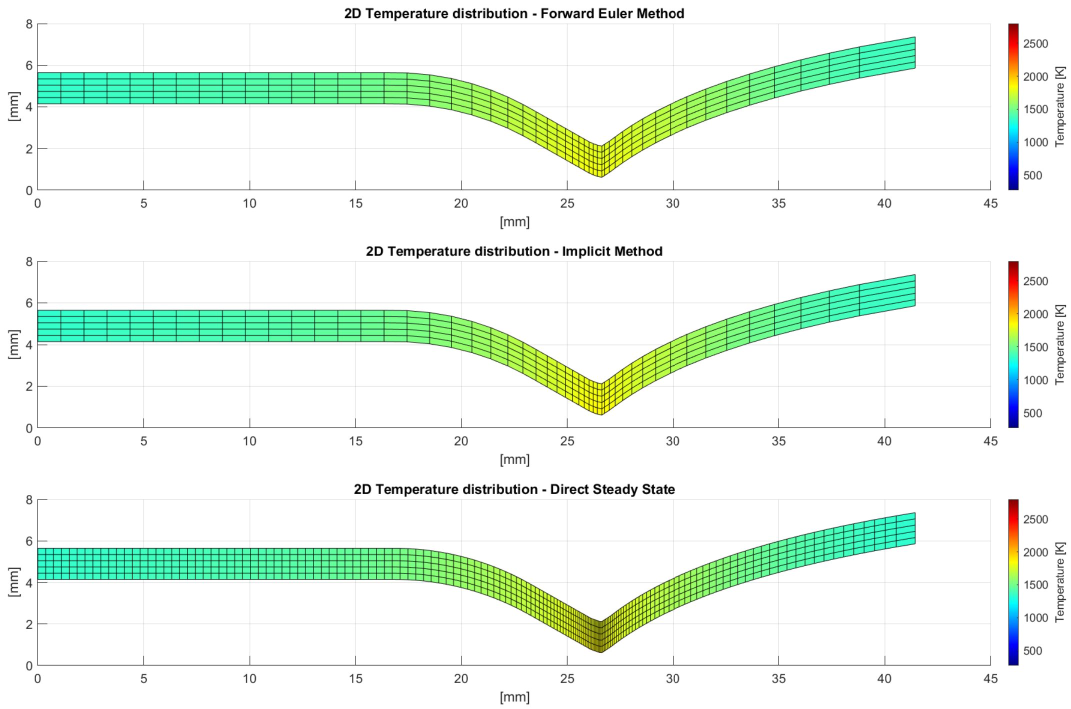


Figure 3.51: Comparison of the Steady State solution as calculated using the Forward Euler, Implicit and Direct Steady State method

[6]For the simulations presented here curvature effects were not included. This was done to reduce the computational time required for the Forward Euler Method.

From figure 3.51 it can be seen that overall there is a good agreement between the three models. Looking closely it can be seen that there are some small differences. This becomes more clear when plotting the temperature distribution for the outer layer of cells for each of the methods as can be seen in figure 3.53. It can be seen that the implicit method and the direct steady state method both predict a slightly higher temperature at the nozzle throat and that the temperature profile is also slightly different. The maximum deviation between the three methods is less than 1.5%, so they are still in good agreement with each other. Looking at literature [46], it can be seen that deviations of this magnitude are not atypical for the solution methods presented. It can therefore be assumed that each of the three methods is implemented correctly and that the deviations are due to minor numerical errors introduced in the solution process.

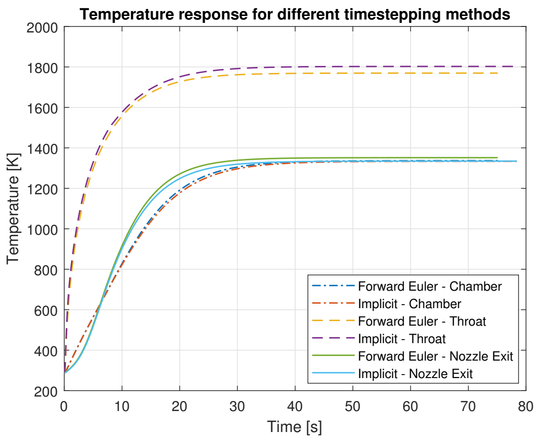


Figure 3.52: Temperature response as function of time for the Forward Euler and Implicit methods

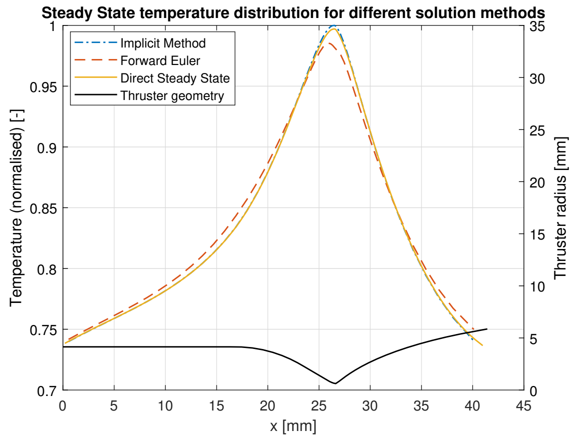


Figure 3.53: Steady State Temperature Distribution for the outer layer of the wall as calculated using the Forward Euler, Implicit and Direct Steady State Methods

In figure 3.52 the temperature response as a function of time can be seen as calculated using the Forward Euler time stepping scheme and the implicit time stepping scheme. The temperature is plotted for three points on the outer wall of the thruster: at the combustion chamber (first cell), at the throat (cell 33) and at the last cell near the nozzle exit (cell 50). It can be seen that overall there is a good agreement between the two different solution methods. It can also be seen that during the start of the simulation (in the transient regime), the two solutions are closer together when compared to the steady state part of the solution. This further confirms that the deviations between the two solutions are mostly caused by numerical errors in the solution process.

As a final note, it can be seen looking at figure 3.51 that the solution obtained using the direct steady state method uses a finer grid than the solutions from the other two methods. This is due to the fact that for the direct steady state method only one iteration cycle has to be performed, so larger mesh sizes can still easily be solved without requiring a very large computational time. It is interesting to see however that even for a more refined mesh the solution is still essentially identical, this confirms the findings of section 3.6 where it was found that mesh convergence is achieved already for relatively coarse meshes.

## 3.8. Model sensitivity analysis

As mentioned previously, during the development of the model, some of the input parameters such as empirical constants were largely unknown, other parameters such as the chamber pressure or the O/F ratio were assumed based on measurement data. During the model calibration, an attempt was made to find the right parameter values for each of these unknown inputs. These values are however not perfect and there will always be some error.

In this section the sensitivity of the model to these errors will be investigated. Additionally, some other parameters will also be varied to determine if changing these parameters would be useful in reducing the wall temperature reached. This will be done using a One-at-a-time (OAT/OFAT) approach. In this approach one input variable is allowed to be changed while the other input variables are kept constant. This is then done for all the unknown input variables. The obtained solution for each variable is compared to the baseline solution to get an estimate for the sensitivity of each input variable.

### 3.8.1. Wall material emissivity

The wall material emissivity of the materials used in the PM200 is unknown. In literature a value of 0.8 is often used for the emissivity of wall materials in rocket engines [50]. For the stainless steel, the material used within the PM200, different values for emissivity can be found in a variety of sources depending on the type of stainless steel used, its manufacturing method, and its surface finish. Even if all these parameters are kept constant, different emissivity values ranging from 0.1 on the low end to 0.98 on the high end can be found depending on the source. It is therefore not straightforward to select the correct emissivity value for the model presented here. To investigate the effect of a potential error in the selection of the emissivity value the model was run for different emissivity values. As a baseline an emissivity value of 0.8 was used. Simulations where then run for an emissivity value of ± 10%, ± 20% and -50%, it was not possible to simulate an emissivity value of +50% as this value would exceed a value of 1 (the maximum possible emissivity value), therefore instead an emissivity value of 1 (+25%) was also simulated. In Figure 3.54 the resulting temperature graphs can be seen. In these graphs the maximum temperature of the thruster wall is plotted. The differences in temperature are also shown in figure 3.55.

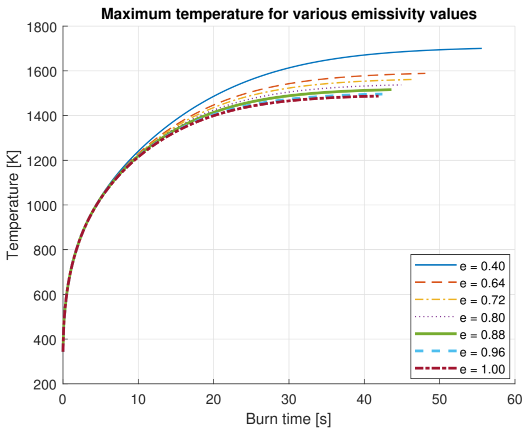


Figure 3.54: Temperature difference for several different emissivity values

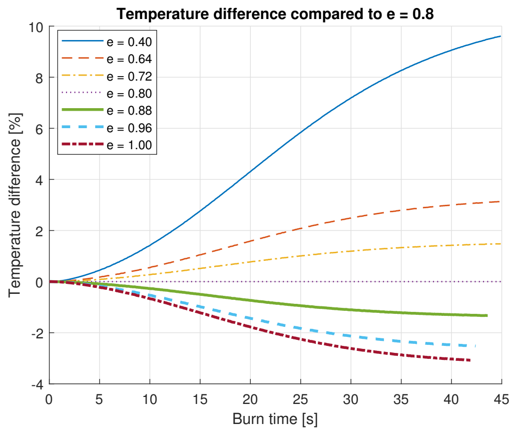


Figure 3.55: Percentage difference in temperature values for several different emissivity values

From the results in figures 3.54 and 3.55 it can be seen that there is not a large difference in wall temperature for different values of emissivity. If the emissivity is decreased by 50%, the maximum deviation in the final result is less than 10%. This result is valuable as it implies that uncertainty in the unknown wall emissivity value only has a relatively small effect on the outcome of the model. Similarly, it can be seen that by increasing the emissivity to the theoretical maximum value of 1, only a roughly 3% decrease in maximum temperature can be achieved.

### 3.8.2. Chamber Pressure

The second parameter to be investigated is the chamber pressure. The chamber pressure was measured during each burn so this parameter was well known for every test. Even though the chamber pressure was well known for every test, the chamber pressure can not be controlled very easily due to it being dependent on the ambient temperature. It is therefore still interesting to see what the effect of chamber pressure is on the heat transfer. The following cases were run: a nominal chamber pressure of 3 bar, $P_c$±10%, $P_c$±20% and $P_c$+50%. The case $P_c$-50% was not run because in this case the chamber pressure would be only 1.5 bar, which would be too low for the motor to operate. To compare the results, the maximum wall temperature as function of time for each case was used. The results can be seen in figure 3.56. The percentage difference between the results and the baseline case with a chamber pressure of 3 bar can be seen in figure 3.57.

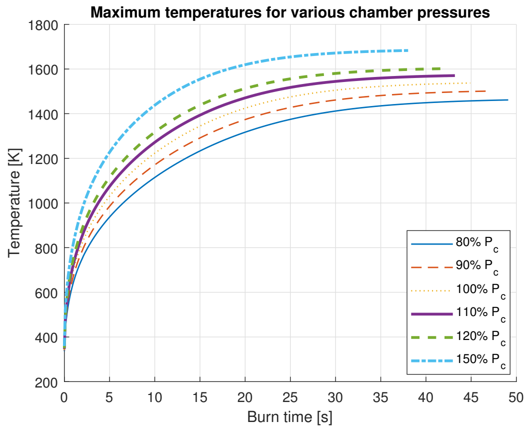


Figure 3.56: Throat temperature as a function of time for several different chamber pressures

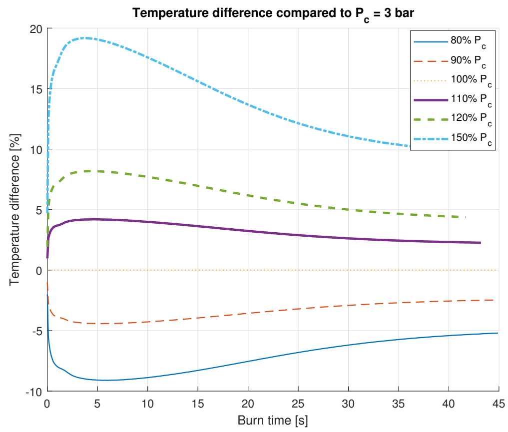


Figure 3.57: Percentage difference in throat temperature as function of time for several different chamber pressures

What is interesting to see is that unlike what was seen for a change in emissivity, for a change in chamber pressure the largest differences occur in the transient phase of the model. During the steady state the results are somewhat close, with an increase in chamber pressure of 50% resulting in a change of approximately 10% in the final result. During the transient phase however this difference can reach almost 19%, almost twice as much. While the overall difference of 10% in chamber pressure is not that large, it should be noted that for many engines theoretically much higher chamber pressures than 4.5 bar can be reached. For such engines the heat transfer could thus be significantly higher. For the PM200 the chamber pressure is however unlikely to exceed approximately 6 bar in any realistic scenario. This is because for the PM200 the chamber pressure is dependent on the ambient temperature and a chamber pressure above 6 bar would only be reached at an ambient temperature outside of the operational envelope of the PM200.

### 3.8.3. O/F Ratio

While the O/F ratio was determined for research thruster 2 as discussed in appendix C, it was observed that some small differences in O/F ratio occurred based on a variety of conditions. For example if the fuel tank was heated slightly more than the oxidiser tank, the O/F ratio could shift a little bit. Because of this the sensitivity of the O/F ratio to the model output was determined. A nominal O/F ratio of 8 was taken as the baseline case and cases for $O/F$±10%, $O/F$±20%, and $O/F$±50% were simulated. Again the maximum wall temperature was taken as the reference point. The resulting transient temperature distributions can be seen in figure 3.58 and the percentage difference between the results can be seen in figure 3.59.

From figures 3.58 and 3.59 it becomes clear that the O/F ratio does not have a large influence on the final throat temperature achieved, at least for O/F ratios close to the optimum O/F ratio of 8.223. Even for combustion that is relatively oxidiser rich (OF = 12) the model result only differs by a maximum of less than 5%. It can again be seen that the maximum differences occur in the transient regime. If the O/F ratio would be changed even more than 50% it could theoretically be the case that even larger differences in temperature would be observed.

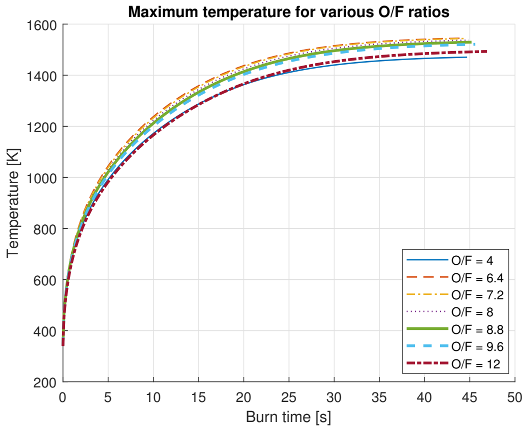


Figure 3.58: Temperature difference for several different O/F ratios

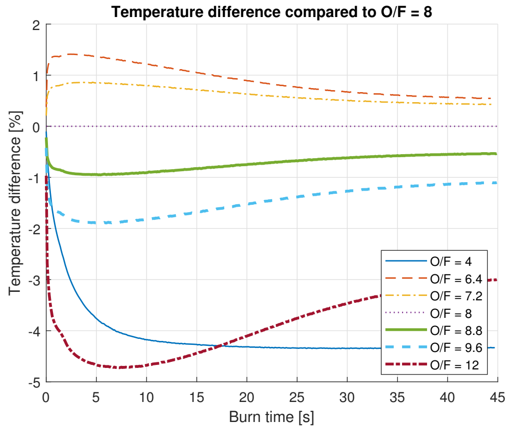


Figure 3.59: Percentage difference in temperature values for several different O/F ratios

However, it is unlikely that the motor would ignite at these conditions. These scenarios are therefore not considered to be realistic and will not be discussed here.

### 3.8.4. Wall thermal conductivity

As was mentioned in section 3.2 the thermal conductivity of the wall material was calculated based on empirical relations from literature or from data sheets. While these relationships appeared to be relatively accurate, they may still be subject to error. It is thus interesting to look at how sensitive the model would be to such errors. Furthermore, investigating the wall thermal conductivity is interesting as it can indicate if switching to a different material with a higher or lower thermal conductivity would be beneficial in reaching a lower final wall temperature. Simulations were again performed for thermal conductivity values (here indicated with the letter “k”) of ± 10%, ± 20% and ± 50%. Since the wall thermal conductivity values are not assumed to be constant within the model, these percentages are added or subtracted to the calculated thermal conductivity values. The maximum temperature as function of burn time can be seen in figure 3.60, the temperature differences for each case can be seen in figure 3.61.

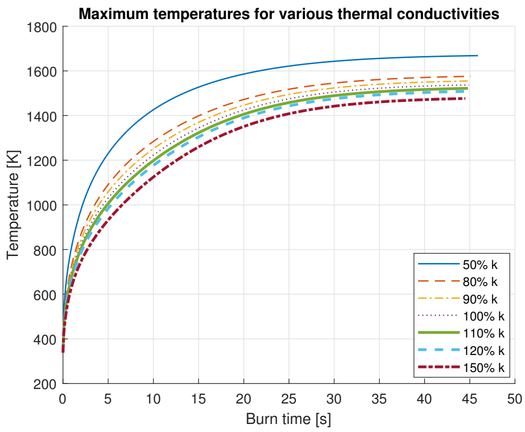


Figure 3.60: Temperature difference for several different values of wall thermal conductivity (k)

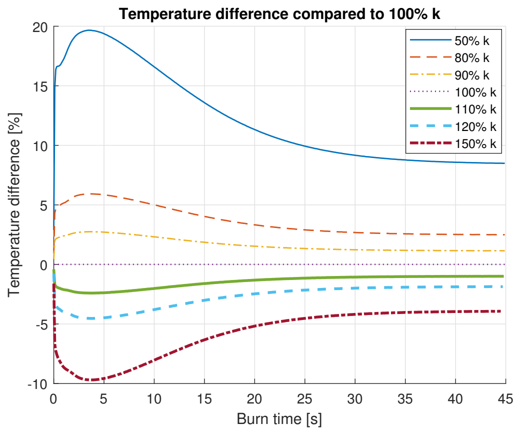


Figure 3.61: Percentage difference in temperature values for several different values of wall thermal conductivity (k)

From figure 3.61 it can be seen that the higher the thermal conductivity of the wall material, the lower the maximum wall temperature. Upon inspection it can also be seen that the differences are not symmetric around the 100% k value. Lower values for the thermal conductivity lead to a relatively higher increase in maximum temperature when compared to the decrease in temperature reached for higher values of thermal conductivity. A linear increase in thermal conductivity thus does not lead to a linear decrease in maximum temperature.

### 3.8.5. Coolant heat capacity

The last parameter for which the sensitivity will be determined is the coolant heat capacity. As was shown in section 3.7.3, the coolant heat capacity was calculated very accurately within the model (results were in agreement within 0.15% with the results from the REFPROP program). It is however interesting to look at the effect of the coolant heat capacity to determine whether or not it would be beneficial to switch to a coolant with a lower or higher heat capacity. Simulations were performed for coolant heat capacity values of $\pm$ 10%, $\pm$ 20% and $\pm$ 50% the nominal calculated value. The resulting maximum wall temperature as function of burn time can be seen in figure 3.62, the temperature difference between the different cases can be seen in figure 3.63.

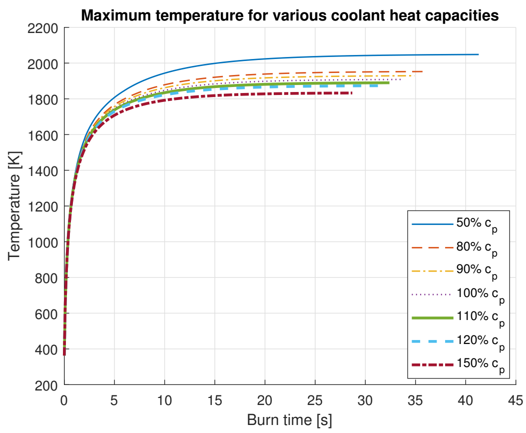


Figure 3.62: Temperature difference for several different coolant heat capacity values

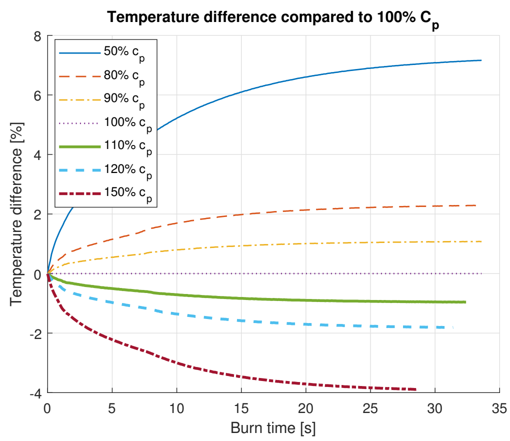


Figure 3.63: Percentage difference in temperature values for several different coolant heat capacity values

From figure 3.63 it can be seen that for different heat capacities the largest differences occur at the steady state point. Higher coolant heat capacities result in lower wall temperatures and lower coolant heat capacities result in higher wall temperatures. Intuitively these results make sense. If the heat capacity is increased by 50% a decrease in wall temperature of 4% can be achieved. This is a modest decrease in temperature. However, propellants may be available which have much higher heat capacities than 150% the heat capacity of nitrous oxide. Hydrogen for example has a heat capacity nearly 14 times the heat capacity of nitrous oxide. Although hydrogen is not suitable for a thruster like the PM200, this does show that potentially coolants could exist with much higher heat capacities. If such a suitable coolant could be found, large cooling performance gains could thus potentially be achieved. For this report, the focus will however remain on nitrous oxide and the option of other coolants will not be explored further.

# 4

# Model Validation and Validation Tests

In section 3.7 it was shown that the model was extensively verified and that the methods used within the numerical model were implemented correctly and in accordance with scientific theory. Verification does however not answer the question of whether or not the model correctly reflects reality and for this model validation is required. In this chapter the validation approach and the corresponding tests which were performed to validate the model will be presented.

## 4.1. Model Calibration and Validation Strategy

As discussed in section 3.7 the model was verified and shown to be implemented correctly. However if one were to run this model and compare it to test data it is still likely that there would be disagreements. The main reason for this is that equations 3.8, 3.10, and 3.61 rely on empirical coefficients. In the discussion that follows in this section the coefficient in equations 3.8 and 3.10 will be referred to as the "a"-coefficients while the coefficient in equation 3.61 will be referred to as the "c"-coefficient. While the original sources of these equations ([2],[14]) do give values for these empirical coefficients, these coefficients were based on different rocket engine designs and on different experimental set ups. Therefore, these coefficients are not necessarily valid for the PM200 or similar thrusters. One of the main problems with the original coefficients is that they are usually tailored towards larger rocket engine designs with high chamber pressures and that they don't scale very well to smaller rocket engine designs. Several examples of this can be seen in literature. For example, in research by Schoenman and Block [38] it was found that for small thrusters with low chamber pressures (thrust levels of around 440 N and 100 N) the original "a"-coefficient given in the Bartz equation (equation 3.8) overestimates the heat flux by more than a factor of two and in some cases even by a factor of more than four. Similar observations were also reported in research by Kirchberger (in [17, 18]) who noted that for small (hydrocarbon based) rocket engines the Bartz equation significantly over predicts the heat transfer for low chamber pressures and for low O/F ratios. If it is assumed that this trend continues as rocket engines get even smaller it can be expected that the original "a"-coefficient in the Bartz equation overestimates the heat transfer for the PM200 even more. In order to get accurate predictions from the model it is therefore required to get an estimate of these empirical coefficients for the PM200.

The main difficulty of estimating the empirical coefficients is that there are multiple unknown coefficients or other unknown factors that need to be determined simultaneously and given the amount of resources available it was not possible to measure each of these coefficients separately. It therefore becomes difficult to determine what each coefficient or factor should be as they all contribute to the error of the program, but their contributions relative to each other are unknown. The following coefficients or parameters were unknown:

- The "a"-coefficients in equation 3.8 or 3.10 for the convective heat transfer from the combustion gases.

- The coefficients in the radiative heat transfer equations for the combustion gases.
- The “c”-coefficient in the Sieder-Tate relationship.
- The emissivity of the wall material.

As stated before, determining these four parameters separately was not possible with the resources available within this study. However this is also not strictly required as long as the error introduced into the model by an error in one of the parameters above is small. In section 3.8 it was shown that for a 50% input error in the emissivity value the outcome of the model is changed by less than 11%. In other words, getting a 100% correct value for the emissivity is not required as the emissivity only has a small impact on the model outcome. The radiative heat transfer from the combustion gases typically accounts for only a small percentage of the total heat transfer from the combustion gases, meaning it can often be neglected or that an error in these coefficients only has a small impact on the result. The main two coefficients that need to be determined are therefore the “a”-coefficients in equations 3.8 or 3.10 and the “c”-coefficient in equations 3.61 and 3.62.

Determining these last two coefficients proved quite the challenge for the PM200. While the temperature of the thruster was measured at several locations during testing, it proved difficult to determine the “a” and “c” coefficients simultaneously as both coefficients simultaneously introduced an error and the ratio between the error in both coefficients was not known. Therefore a new “research thruster” design was made which did not feature a cooling channel. This way the “a”-coefficients for equations 3.8 or 3.10 could be determined without interference from the error caused by the “c”-coefficient. As part of this new thruster design several other improvements were also made to aid data acquisition. The design of the research thrusters is discussed further in section 4.2.

After the “a”-coefficient was determined this could be substituted into the model making the “c”-coefficient the only unknown. This made it possible to determine the “c”-coefficient. To determine the “c”-coefficient temperature data from the cooling channel was required. For the PM200 this data was difficult to obtain as the small dimensions made it almost impossible to place temperature sensors within the cooling channel. Because the B20 thruster is larger than the PM200 it was easier to measure the coolant temperature for the B20. During initial testing it was found that the thermal response of the PM200 and the B20 were very similar and therefore it was decided to use the coolant temperature data from the B20 thruster for calibrating the “c”-coefficient.

After the “a” and “c” coefficients were determined the model can be validated by testing it for accuracy on the PM200 thruster.

## 4.2. Design of research thrusters

As mentioned previously, several research thrusters were designed to gather data on the thermal behaviour of the PM200. Internally, these research thrusters were for the most part identical to the regular PM200 thruster, but some differences were present. In this section the design of these research thrusters will be discussed with a focus on the goal of these thrusters and what their main differences were with respect to the regular PM200 thrusters.

The research thrusters were designed with three primary goals:

- To determine the “a”-coefficient as discussed in the previous section without the interference of the cooling channel.
- To obtain better quality/more precise thermal data by adding better mounting points for the thermocouples.
- To be able to compare thermal data from a thruster with and without cooling channel to determine the effectiveness of the current cooling channel design as implemented on the PM200.

Below in figures 4.1 and 4.2 Research Thruster 1 (RT1) and Research Thruster 2 (RT2) can be seen. These thrusters were identical to each other with the exception of the thermocouple mounting points. For research thruster 1 the mounting points consist of slots which can be used to clamp in the thermocouples. The thermocouples would be clamped in the slots and afterwards tightened down using steel wire. Since it was unsure how well the slots would print on the 3D printer it was decided to also make a second version which had simpler slots. This version (Research Thruster 2) had slots which were only used to keep the steel wire in place which in turn kept the thermocouples in place.

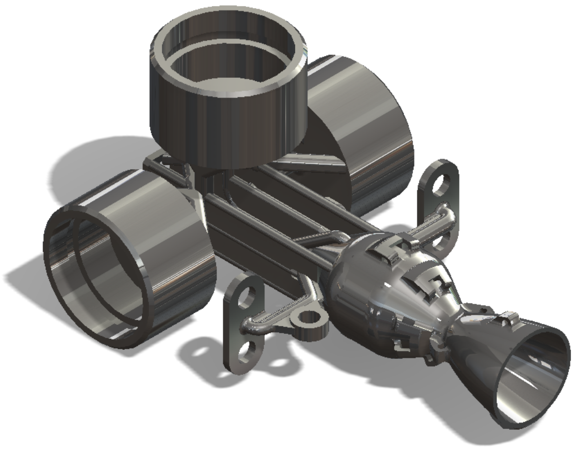

Figure 4.1: Version 1 of the radiation cooled version of the PM200 used in testing.

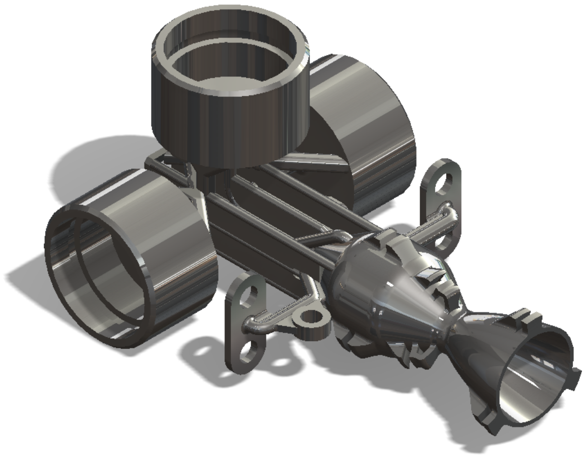

Figure 4.2: Version 2 of the radiation cooled version of the PM200 used in testing.

In the end, both mounting methods worked and both mounting methods had some advantages and disadvantages. The mounting points for Research Thruster 1 had the advantage that by design the thermocouples would always be clamped in properly. Which meant that there could be no doubt about whether or not the thermocouple was attached at the right location and whether or not it was properly in contact with the thruster wall material. As a downside this method restricted the locations were the thermocouples could be placed to a couple of fixed azimuth angles. The mounting points for Research Thruster 2 allowed the thermocouples to be placed at any azimuth angle. The downside of these mounting points was however that it was relatively difficult to ensure that there was a proper connection between the thermocouple and the wall material. It was very easy to accidentally disconnect a thermocouple by simply handling the module and preparing for a test, which made this mounting method especially challenging from an operational point of view.

Compared to the regular PM200, the Research thrusters had several differences. These are listed below:

- RT1 and RT2 did not have a cooling channel, as a consequence the supply lines were also shorter and the injector geometry was modified slightly due to the inlet point being at a different location.
- The pressure sensor ports for RT1 and RT2 were moved further away from the combustion chamber to limit the heat loading on the pressure sensors, they were also rotated 180 degrees with respect to the original PM200 module.
- For RT1 and RT2 mounting points were added to the thrusters to mount thermocouples.
- For RT1 and RT2 the external geometry of the thruster was slightly modified to better correspond to the geometry in the thermal model discussed in the previous chapter.
- For RT1 and RT2 the igniter was mounted on the opposite side of the thruster compared to the PM200, it was also mounted at a slightly different position.

- For RT1 and RT2 the thrust vector control system and associated mechanical systems/geometries were removed.
- For RT1 and RT2 the thruster was mounted higher on the module. This allowed for easier access and inspection without having to dismount the thruster from the module.

Even though research thrusters 1 and 2 were largely similar to the regular version of the PM200, getting them to ignite properly proved to be a significant challenge and a lot of debugging was required. During this debugging RT1 was unfortunately damaged beyond repair and therefore no successful tests have been performed using this thruster. RT2 was however fired successfully over one-hundred times.

To replace RT1, a third research thruster was designed which improved on some of the flaws present in RT1 and RT2. The design of research thruster 3 can be seen below in figure 4.3. This design had the following changes compared to RT1:

- The igniter position was changed to be identical to the regular PM200 design.
- The pressure sensor ports were rotated 180 degrees to match with the regular PM200 design.
- The propellant feed lines were increased in diameter (where possible) to prevent clogging of the lines.
- Additional material was added to increase the strength at some fragile parts of the thruster.
- Several design changes were made to improve post-processing and post-machining
- RT3 was printed out of an inconel alloy compared to a stainless steel alloy as used in the regular PM200, RT1 and RT2.

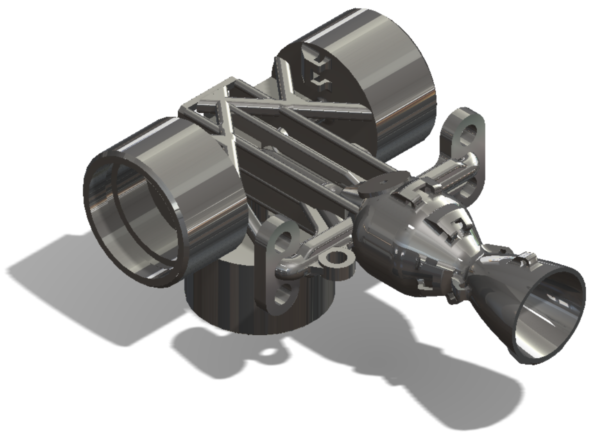

Figure 4.3: Version 3 of the radiation cooled version of the PM200 used in testing.

## 4.3. Experimental set-up

As mentioned previously, several tests were performed to experimentally validate the results from the model and to gain more insight into the thermal behaviour of the PM200 thruster. In this section the experimental test set-up will be described. Tests were performed at several different locations using different test set ups. Tests with the PM200 thruster were performed using the test set-up in the Dawn Aerospace Netherlands office in Delft/Delfgauw. Tests with the B20 were performed using the test set-up at Dawn Aerospace New Zealand in Christchurch, New Zealand. The tests performed in New Zealand were performed independently of this thesis study, but data from these tests were used for the calibration and validation of the model presented within this report. Therefore, this section will focus on the test set-up at the Dawn Aerospace Netherlands, which was used for testing the PM200. The tests performed at this test set-up were specifically performed for this thesis study and the author was also involved in setting up this test set-up.

### 4.3.1. Test set-up PM200 static fire tests

The test set-up for the PM200 was relatively simple and consisted of the following components: a vacuum chamber, several sensors and a system for data acquisition. A picture of the test set up used can be seen in figure 4.4.

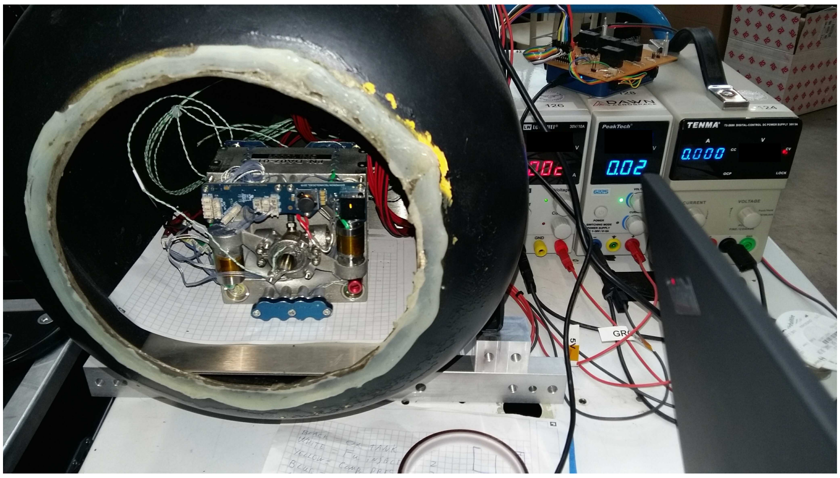


Figure 4.4: The test set-up at Dawn Aerospace

The vacuum chamber consisted of a cylindrical metal tube with an access point on one side. The access point was used to load and unload the PM200 plus any sensors that were required. The access point was covered using a transparent lid which is held in place by the vacuum inside the chamber itself. A vacuum pump was used to maintain a vacuum during operations. Pressures as low as 2 mbar could be achieved. Most tests were however performed at pressures between 80-200 mbar because it was found to be easier to ignite the thruster at these pressure ranges.[1] The pressure in the chamber was constantly monitored during the tests using a pressure sensor. During a test the vacuum pump was turned on and a small valve on top of the vacuum chamber was opened to supply fresh air. A continuous airflow was thus created in the chamber. This was done so that the exhaust gases of the thruster could be cleared while keeping the vacuum chamber at a constant pressure level. The small valve thus effectively acted as a “throttle setting” for the vacuum pump. Pumping out the combustion gases was required for two reasons: the first reason was to maintain a roughly

[1] Tests at lower pressures than 80 mbar were attempted but were (mostly) unsuccessful. The reason for this was that at lower pressures electric arcs interfered with the igniter of the thruster or the thermocouples used to perform the temperature measurements. This is because the breakdown voltage reaches a minimum at these pressures according to Paschen’s Law. In space this is not a problem because in space the pressure is sufficiently low that the breakdown voltage goes up again. In other words: the minimum pressure that the vacuum chamber could reach was not low enough to test the thruster at the lowest vacuum setting while also being able to collect data reliably.

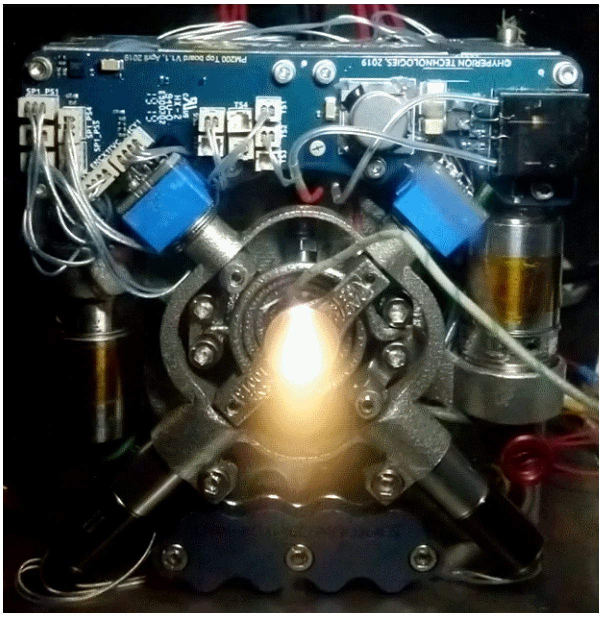

Figure 4.5: Static Fire test of the PM200

constant pressure level and the second reason was that the pressure sensor measuring the pressure inside the vacuum chamber would not display the correct pressure if gases other than air were present within the vacuum chamber.

To perform a test the PM200 was simply placed inside the vacuum chamber and the thruster was fired. A picture of such a firing can be seen in figure 4.5.

The chamber had a 25 pin RS232 feed-through which could be used to transfer data from sensors inside the chamber to a data acquisition module which was in turn connected to a computer were the data was collected using a custom made Labview program. For every test the following parameters were measured:

- Oxidiser tank pressure (Typical values between 40-65 bar)
- Fuel tank pressure (Typical values between 7.8 and 14 bar)
- Oxidiser injector pressure (before injector orifices) (Typical values between 7 and 12 bar)
- Fuel injector pressure (before injector orifices) (Typical values between 6 and 10 bar)
- Combustion Chamber pressure (Typical values between 2-5 bar)
- Vacuum chamber pressure (rough measurement only) (Typical values between 50-250 mbar)
- Temperature data at four different points

Temperature data was collected using K-type thermocouples. Initially, data collection was performed using a custom made Arduino board, however this method proved to be relatively unreliable as the Arduino electronics and the igniter of the thruster interfered with each other which often lead to a loss of data. For later tests the temperature data was collected using a National Instruments NI-9211 module which was more reliable.

Attaching the thermocouples to the thrusters proved to be a challenge due to the small thruster dimensions and the high temperatures which were encountered. In the end the most reliable method was found to be to attach the thermocouples using steel wires. This attachment method was tested on a known temperature source (a soldering iron) and was found to give a very accurate temperature reading (within 1°C at a temperature of 200°C equalling an error of less than 0.5%). As an example, in figure 4.6 the attachment of three thermocouples to Research Thruster 2 can be seen.

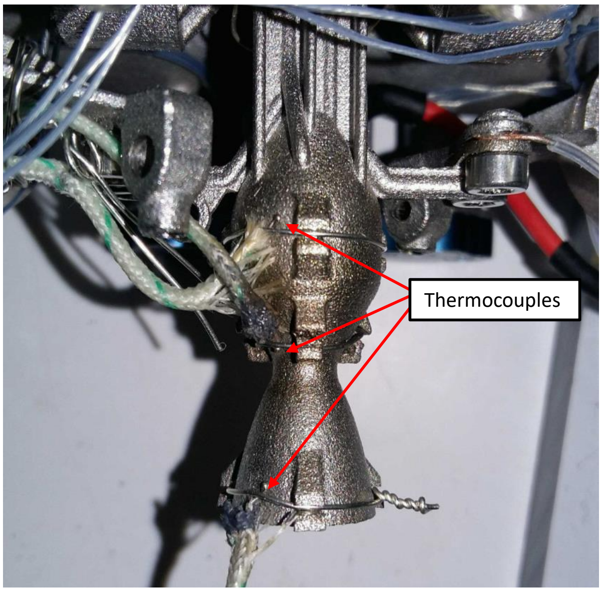


Figure 4.6: Attachment of the thermocouples to the research thruster 2

Tests were performed using several different versions of the PM200. This was done for two reasons: the first reason was to get more insight into what the effect of certain design parameters were and the second reason was that some thruster configurations were tested to validate specific parts of the numerical model. In total 325 tests were performed for the thesis study, an overview of the amount of tests per thruster is given in table 4.1.

Table 4.1: Overview of thrusters used for testing

| Thruster Identifier | Cooling method | Material properties | Number of tests[2] | Note |
|---|---|---|---|---|
| SN10016 | Regenerative Cooling | Stainless Steel | 54 | Standard version |
| Unmarked | Regenerative Cooling | Stainless Steel, No surface finish in nozzle | 88 | |
| Inconel | Regenerative Cooling | Inconel | 43 | |
| Research Thruster 1 | No cooling/Radiation Cooling | Stainless Steel | 38 | See section 4.2 |
| Research Thruster 2 | No cooling/Radiation Cooling | Stainless Steel | 102 | See section 4.2 |
| Research Thruster 3 | No cooling/Radiation Cooling | Inconel | 0 | See section 4.2 |

The temperature data gathered varied per thruster. For the original PM200 designs (the first three thrusters listed in table 4.1), the temperature data that was gathered was limited. This was mainly due to the fact that it was difficult to mount thermocouples correctly for this design as there were no dedicated mounting points. An additional factor which made the mounting of the thermocouples difficult is that for these designs many additional features were present (such as the pressure sensor ports and the spiral for the thrust vector control mechanism) which effectively blocked access to many parts of the thruster (see figure 2.2). Most of the tests performed with the original PM200 designs were also performed using early iterations of the test set-up and earlier iterations of the PM200 module. The combination of these factors resulted in only a small data-set being available for these thrusters. The research thrusters were specifically designed to aid the gathering of temperature data and had dedicated mounting points for thermocouples, so for these thrusters temperature data could be collected more easily at multiple locations. In figure 4.7 an overview of the measurement

[2]The number of tests given here represents the total amount of tests attempted and also includes unsuccessful tests.

locations present for research thruster 1 can be seen.

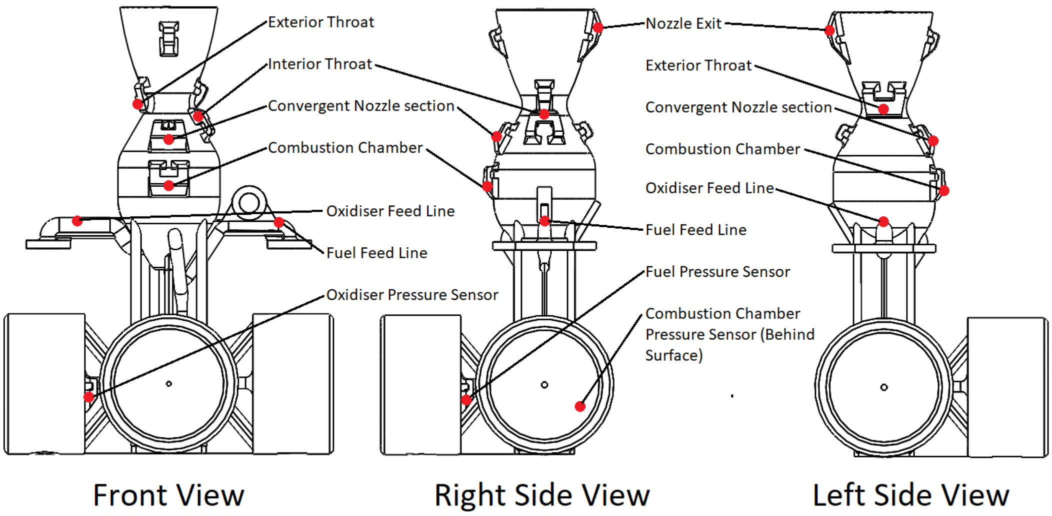


Figure 4.7: Thermocouple locations as used on Research Thruster 1

As can be seen in 4.7, multiple mounting points were added across the combustion chamber and nozzle. For research thruster 1 these mounting points included a “clamp”, meaning that the thermocouple was mounted at a fixed radial/azimuth angle. For research thruster 2 the mounting points were identical except that the clamps were not present and instead only brackets were present to hold the steel wire in place (see also figures 4.2 and 4.6). This meant that for research thruster 2 the thermocouples could be mounted at any azimuth angle.

## 4.4. Discussion of experimental results

In this section some general observations from the experimental results will be discussed. This discussion is required to gain a better understanding of how to interpret the measurement data which is in turn required to understand the analysis performed in the remainder of the sections within this chapter. During the entire thesis project more than 200 static fire tests were performed in various configurations, therefore not all data obtained will be presented and discussed in this section. Instead, in this section a couple phenomena of interest will be discussed which were observed from the tests and test data. This will be done in two steps: first a random data set was chosen which will serve as an example to show what a typical data set looks like. The example case selected was Test 14 performed with Research Thruster 2 on 22-06-2020. There is no particular reason for using this particular data set other than that this data set is a fairly typical and representative data set obtained from a fairly typical test. In the remainder of this section this particular test will simply be referred to as test 14. Secondly, it was assumed within the model that the temperature distribution was symmetrical around the x-axis. It is however unknown whether or not this assumption is valid. If this assumption is not valid the results would be dependent on the azimuth angle at which the thermocouples would be mounted. To see whether or not there is a dependence on the mounting angle of the thermocouple the test data will be compared based on the azimuth angles of the thermocouples in section 4.4.3.

### 4.4.1. Discussion of a typical data set obtained from a test

In this section a typical data set will be discussed to give the reader insight in what data was collected during a given test, and what this data looked like. As was mentioned before, test 14 performed with Research Thruster 2 will be used for this. The test was a 3 second burn performed in the Dawn Aerospace vacuum chamber under a pressure of approximately 200 mbar. Eight sensors were used to record data during the test: three pressure sensors located on the thruster measuring the chamber pressure, oxidiser injection pressure and fuel injection pressure, one pressure sensor measuring the vacuum chamber pressure (only read out once before the start of the burn) and four thermocouples measuring the temperature at the exterior throat, chamber, nozzle exit and internal throat respectively (see figure 4.7).

Below in figure 4.9 the pressure data is plotted. The data is normalised to a standard reference chamber pressure which will be used for the analysis in the following sections of this chapter. This standard reference chamber pressure was selected to be equal to 3.5 bar, which was roughly equal to the average chamber pressure observed during testing. The zero point in time on the x-axis is set at the point where the rise in chamber pressure reaches a maximum, it is assumed that this point is close to the ignition point of the thruster.

Comparing figure 4.9 to figure 2.3 a couple things can be noted:

It can be seen that the chamber pressure and injection pressures seem to rise substantially slower when compared to the baseline PM200 design. It is suspected that the behaviour in the combustion chamber and in the injector is not actually different but that this is an artefact due to the placement of the pressure sensors. In the research thrusters, the pressure sensors were placed further away from the chamber to limit the heat transfer to the pressure sensor bodies. However this also means that the lines connecting the pressure sensors to the injector and combustion chamber have a relatively large volume, which means they take longer to “fill up”.

The above mentioned phenomenon explains why the initial start-up of the pressure curve is slower than that of the baseline PM200, but it does not explain why the oxidiser injector curve lags behind the fuel injector and combustion chamber pressure curves. It was hypothesised that this behaviour was caused by the oxidiser line being clogged with debris. An X-ray scan (see figure 4.8) was performed of the thruster at the faculty of Civil Engineering and Geosciences at TU Delft and this scan confirmed the hypothesis that there was debris present in the line. It is suspected that this debris came partially from the printing process: part of the metal printing powder remained inside the line. The remainder of the debris was likely sealant which was applied during debugging. This sealant was added because there were some suspected leaks observed during the initial testing. The presence of the sealant and the printing powder caused a blockage in the line which in turn causes a longer delay until the correct measurement is obtained. An attempt was made to clear out the line to get more reliable measurements, but this was unsuccessful.

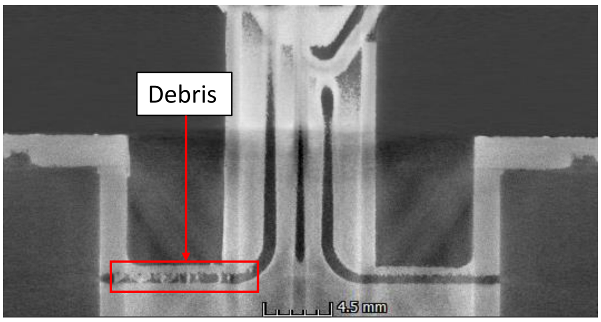


Figure 4.8: Debris visible inside the oxidiser pressure sensor channel

It can be seen that the effect is particularly visible for the oxidiser injector measurement, which gives a lower pressure value than the combustion chamber pressure at the start of the burn; something which is physically impossible. The same behaviour is also visible for the shutdown transient, which appears to be much longer compared to the baseline PM200 design. In figure 4.8, from left to right oxidiser, fuel, and combustion chamber pressure sensor lines can be seen, it can clearly be seen that the oxidiser injector line has the most debris out of the three channels, explaining why the pressure increase in this line is slower compared to the pressure increase in the other two lines.

It can thus be concluded that the transients of the pressure measurements are not accurate for the pressure sensors attached to the thruster. This is however not a big problem as for the model only the steady state chamber pressure is required. Once the steady state is reached the measurements can be considered accurate. This is mostly based on the fact that the measured pressures agree very well to the baseline version of the PM200, which did not suffer any of the issues mentioned above.

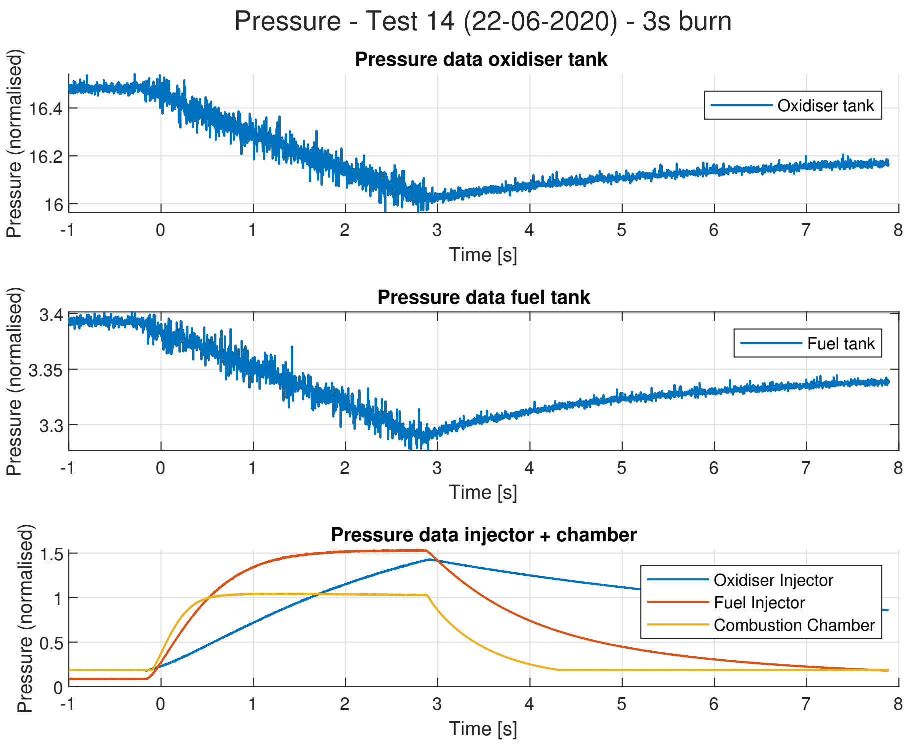


Figure 4.9: Pressures as recorded during test 14 on 22-06-2020

In figure 4.10 the temperature profile can be seen as measured at the four locations mentioned previously. The data is normalised to the maximum temperature measured during the burn, which in this case occurred at the nozzle throat as expected. The cooling down of the thruster is also measured and shown.

In figure 4.11 a zoomed in version of figure 4.10 can be seen which focuses just on the heating up part of the thruster. It can be seen that different parts of the thruster heat up at different rates, and also that they reach their maximum temperatures at different times. This can be explained by the fact that the thruster does not heat up evenly everywhere; the nozzle throat and the combustion chamber generally heat up faster than the injector and the nozzle divergent. As a result, after engine shutdown heat will be conducted away from the hotter parts of the thruster towards the colder parts of the thruster until an even temperature distribution is achieved. This can also be seen in figures 4.10 and 4.11 where it can be seen that all temperatures measured tend to converge to a common curve after shutdown of the thruster.

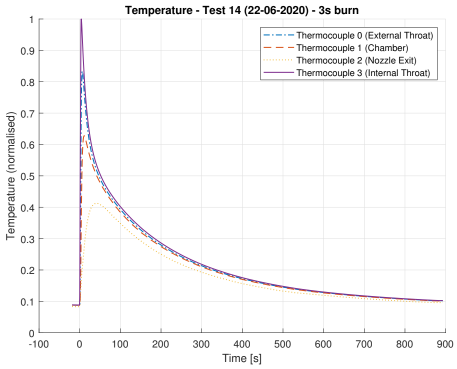


Figure 4.10: Temperatures as recorded during test 14 on 22-06-2020

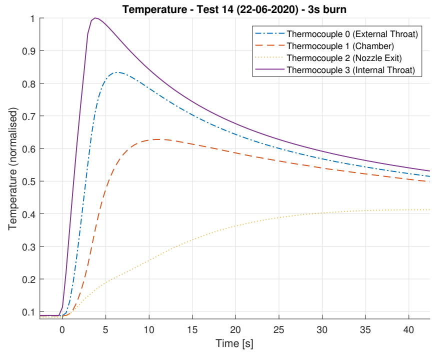


Figure 4.11: Temperatures as recorded during test 14 on 22-06-2020 refocused on the temperature rise during the burn

### 4.4.2. Measurement errors & uncertainty

During the testing of the thrusters and during the post test data analyse several phenomena were observed which contribute to the measurement error or uncertainty in the measurements performed. In this section these phenomena will be discussed.

It was observed that the achieved sampling rate of the thermocouples was lower than expected. Samples were taken every 414 ms even though the LabVIEW program used was programmed to take a sample every 100 ms. Since the burns performed for this study were all below 10s this introduced a large uncertainty for determining the exact start and end time of a test. It also introduced an error in the measured temperature profile; if the program performed a measurement right after start-up of the engine the first data point would give a relatively low temperature compared to if the program performed a measurement 414 ms after start-up of the engine. Because of this issue, determining the temperature at the supposed shutdown time of the engine gave inconsistent results. Because the temperature at shutdown was required for the calibration of the program this was problematic. To solve this issue it was decided to determine the temperatures for the shutdown condition at a fixed reference point. This fixed reference point was set equal to the data point where the interior throat value reaches a maximum, the interior throat temperature is thus used as a reference.

The main reason for using the interior throat as a reference point is as follows: It was observed that for short burn times (all tests performed with RT1 and RT2 were below 4s) the interior throat was always the point where the maximum temperature was reached. This means that after shutdown, the interior throat sees the least amount of temperature rise due to conduction as heat is not conducted to the interior throat but instead it is conducted away from the interior throat to other parts of the thruster. In turn this means that the interior throat will reach its maximum temperature shortly after shutdown of the thruster. This was indeed also observed; the maximum temperature in the interior throat would always be reached within approximately 0.5-1s of the expected shut-down time of the engine.

The advantage of using this reference point to determine the temperature value was that the results became more consistent; tests performed at similar starting conditions gave similar outcomes, tests with higher starting temperatures gave higher final temperatures and tests with higher chamber pressures gave higher final temperatures. The downside of using this approach is that the values determined using this method likely overestimate the actual temperature slightly. This means that if these values are used for calibration of the model, the model will also overestimate the temperatures slightly. In the end it was decided that this was an acceptable compromise because of three main reasons: Firstly because it was seen during validation of the model (see section 4.6) that the model in general underestimates the temperature rise in the throat after shutdown of the thruster. This means that by calibrating the model to a somewhat higher temperature value, the model predicts the maximum observed temperature better. Secondly, it was found that by calibrating the model to a slightly higher temperature value, the temperature gradient as a function of burn time was predicted better, leading to a better prediction of the temperature value when different burn times were simulated. The third reason is related to a different phenomenon which was observed during testing which will be explained below.

It was observed that the temperature rise at the start of the burn was always a bit slower than the model predicted. Part of this can be explained due to the fact that the model assumes a step change in chamber pressure at the ignition point while in reality there is a short start up transient. Because of this, the heat transfer is overestimated at the start of the burn. This start up transient (in the pressure) has a duration of approximately 25 ms and it was observed that the measured temperature values lagged the model values by more than this 25 ms. There must thus be another cause which causes the test data to lag the model prediction. It was suspected that the lag can be attributed to the thermal response time of the thermocouples themselves; it takes a little bit of time for the thermocouple itself to heat up and to register a temperature response. Because of this the temperature measured by the thermocouple lags the real temperature value slightly. To confirm this suspicion a test was performed: a thermocouple was held to a soldering iron which was set at a constant temperature of 200 °C. This created a step input change in the temperature value. The thermal response of the thermocouple was measured. The results can be seen below in figure 4.12.

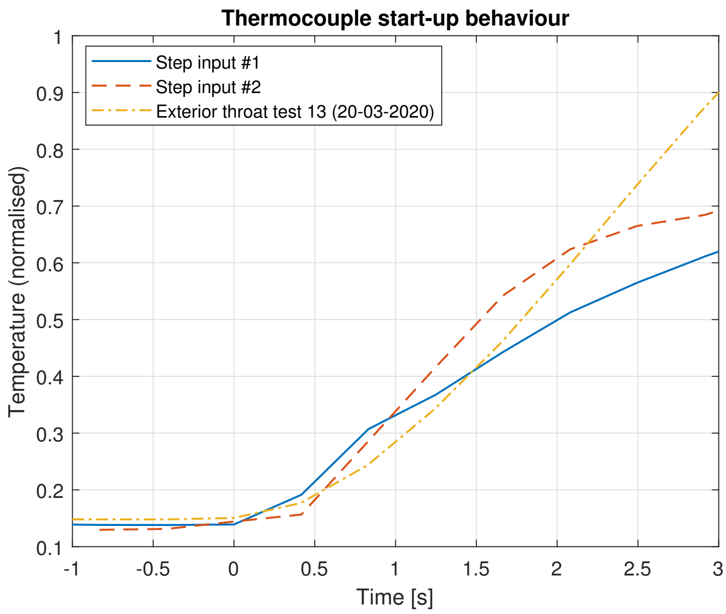


Figure 4.12: Thermocouple response to a step input versus the response to the thruster (Temperature is normalised to a value of 200 °C)

It can be seen that the thermocouple response to a step input change in temperature is similar to the response as observed for the thruster firing, at least for the first 1-1.5s. This indicates that the initial part of the measurement is heavily influenced by the properties of the thermocouple rather than the thermal behaviour of the thruster. The thermocouple measurement data thus somewhat lags the real temperature data, which explains the discrepancy between the thermocouple data and the model results. Because of this effect, comparing the (transient) curve of the model and the measurement data isn't completely fair as there is an unknown lag in the measurement data. Some sort of translation is required to make a fair comparison. In order to do this, the reference point discussed earlier was used. This was done by comparing the measured temperature values at the same time step as the time step where the maximum value of the interior throat was achieved with the temperature values predicted by the model. It was found that by using this approach the model consistently would predict the correct values at the reference point even for different burn times and starting conditions as will be shown in section 4.6.

In conclusion it can be said that by calibrating the model to these slightly higher temperature values the model overestimates the temperature somewhat during the burn. The maximum temperature reached after shutdown is however predicted better using this approach. From a design perspective the prediction of this maximum temperature reached is more critical, because the maximum temperature reached will determine whether or not the wall material will fail. Because of these reasons, the approach outlined above was considered the best approach.

### 4.4.3. Azimuthal variation in temperature distribution

In section 3.2 it was discussed that in the developed model it was assumed that the temperature distribution within the thruster was axisymmetric. To confirm this assumption, for RT2 the test results were plotted for each of the measurements positions as a function of azimuth angle at which the thermocouple was mounted. Below in Figures 4.13 to 4.18 the measured temperature for 56 tests performed using RT2 is plotted as function of the azimuth angle at which the thermocouple was located. The following observations can be made:

- For the injector, only measurements were performed at the top side of the combustion chamber. For all tests performed the measured data seemed relatively consistent.
- For the combustion chamber, measurement data was taken at at least four different azimuthal angles. It can be seen that the thermocouples mounted to the bottom of the engine recorded lower temperatures than those mounted at the top. As an additional note, some data points are shown at an azimuth angle of zero degrees. For these data points the azimuth angle of the thermocouple was unknown.
- For the nozzle convergent relatively few tests were performed. All tests were also performed at a different angle as used in the calibration case (as will be explained in section 4.5). The main reason for the lack of data at this location was because it was relatively difficult to mount a thermocouple at this position while at the same time also having a thermocouple attached at the interior throat. Since the interior throat was used as a reference point, it was preferred to have a thermocouple at the interior throat and consequently only little data was collected at the nozzle convergent.
- For the interior throat data was collected for two different angles. Looking at figure 4.16 the data seems relatively consistent for the interior throat although slightly higher temperatures are observed for the measurement point near the top of the nozzle.
- For the exterior throat and the nozzle exit the temperatures seem relatively consistent independent of the azimuth angle.

While for most axial positions most of the measurements were performed in the top quadrant of the thruster, it can still be said that relatively little variation was present overall between measurement points at different mounting angles. The only axial position for which substantial differences were noted between different mounting angles was at the chamber. It is suspected that this might be because the igniter was mounted near the chamber measurement point, which may have had an impact on the heat transfer as the measurements performed on the lower half of the thruster (the half were the igniter was mounted) all showed lower values than the measurements performed on the upper half of the thruster.

Ideally more measurements would be performed for each axial position at a wider variety of azimuth angles to completely rule out any azimuthal variation in the temperature distribution within the thruster. However, this was not feasible given the scope and time available within this study. Overall, based on the data collected so far it looks like the temperature distribution is mostly axisymmetric confirming the validity of the assumption made in section 3.2.

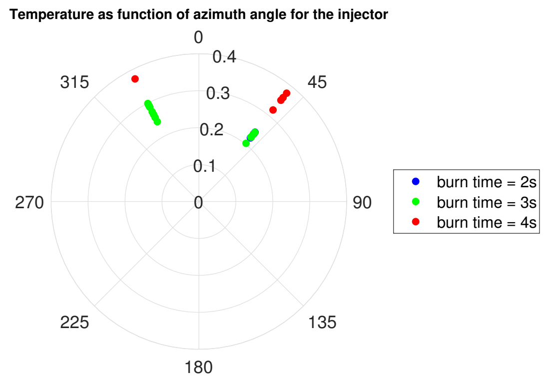


Figure 4.13: Normalised temperatures as recorded at the injector for RT2 as function of azimuth angle. (22 data points)

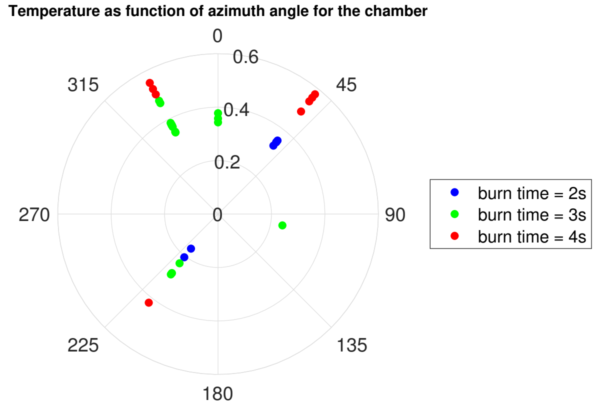


Figure 4.14: Normalised temperatures as recorded at the chamber for RT2 as function of azimuth angle. (32 data points)

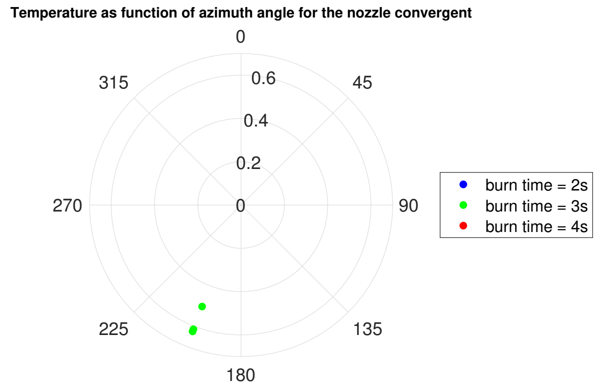


Figure 4.15: Normalised temperatures as recorded at the nozzle convergent for RT2 as function of azimuth angle. (3 data points)

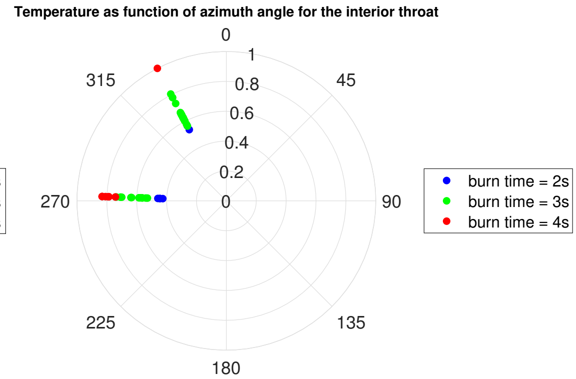


Figure 4.16: Normalised temperatures as recorded at the internal throat for RT2 as function of azimuth angle. (51 data points)

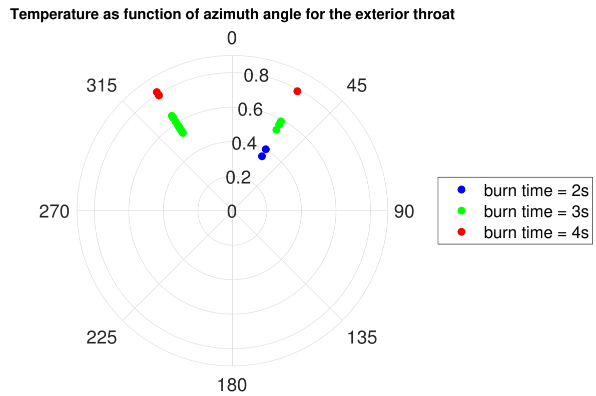


Figure 4.17: Normalised temperatures as recorded at the external throat for RT2 as function of azimuth angle. (27 data points)

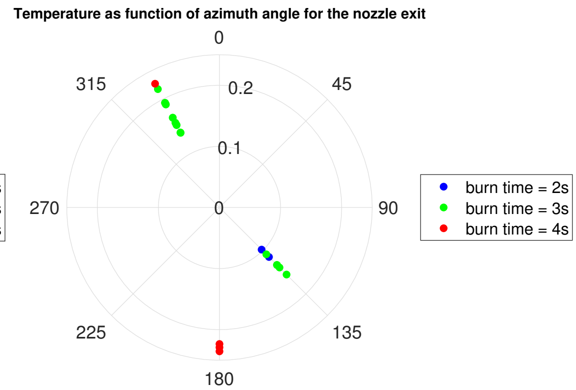


Figure 4.18: Normalised temperatures as recorded at the nozzle exit for RT2 as function of azimuth angle. (24 data points)

## 4.5. Model calibration

In this section the calibration of the model will be discussed. This will be split up into two parts, first the methodology for the determination of the a-coefficient will be discussed followed by the methodology used for the c-coefficient. Both were determined in a slightly different fashion, this was mainly because a different amount of test data was available for both cases. The a-coefficient was determined using the radiation/heat-sink cooled version of the PM200 for which there was more data available. For the determination of the a-coefficient a more elaborate (and more accurate) calibration scheme could therefore be used.

### 4.5.1. Generating the calibration case

To calibrate the model a calibration case was required which could be used to adjust the empirical parameters within the model. This of course raises the question of how such a calibration case could be best selected or generated. Using data from a single test may not be ideal as in this case any measurement error present within the data could throw off the results of the model. Therefore, it was decided to create a theoretical reference case based on the data obtained from multiple tests. In order to do this a data set of 55 tests performed with RT2 was used.

As was discussed in the previous section, from the test data it appeared that the temperature distribution did not vary as a function of the azimuthal position with the exception for the chamber. However, in order to rule out any 3D effects it was chosen to calibrate the model for one specific 2D cross section of the thruster (i.e. only data from one specific azimuth angle was used to generate the calibration case). It was chosen to take this 2D cross section at an angle of 332.5 degrees. This specific angle was selected because at this angle the highest temperatures were recorded during the initial tests and because the worst case temperatures are of most interest for the thermal design of the thruster.

Multiple measurements were performed for each axial position at the given cross section (i.e. at the same angular position) with the exception of the nozzle convergent (again this was because it was difficult to put a thermocouple at this location while at the same time also mounting a thermocouple at the interior throat). Based on these measurements a calibration case for the temperature distribution was made. It should be noted that during each test there were always some small variations between the starting conditions due to uncontrollable circumstances. For example, if the ambient temperature was higher, the tank pressure would also be higher, leading to a higher chamber pressure. If more tests were performed in sequence, the heat generated by the thruster also heated up the tank, leading to higher chamber pressures for tests which were performed later on in the sequence. The starting temperature of the thruster was also always slightly different.

Because of these factors, making the calibration case was not just as simple as taking the test data from a single test or the average from multiple tests. Instead it was chosen to plot the measured temperatures as recorded after 3 seconds for each test as a function of the measured starting temperature of the thruster and the chamber pressure. These starting temperatures were determined for each measurement position independently, because usually there was some variation between the starting temperatures at each measurement location. The results can be seen in Figures 4.19 to 4.24. The data in this figure is normalised in the following way: the measured temperature is normalised to the maximum temperature recorded during the entire test series. Note that this maximum temperature occurred during a 4s burn and that only results from 3s burns are indicated here, this means that there is no data point with a value of 1. The start temperature was normalised to the start temperature which was used for the calibration case, which was equal to 30 °C. The chamber pressure was normalised to the chamber pressure used in the calibration case, which was chosen to be 3.5 bar. This chamber pressure was chosen because it was roughly equal to the average chamber pressure observed during testing.

Based on the data, planes of best fit could be created which predict the temperature for a given chamber pressure and starting temperature. The equations for these planes are given in table 4.2 together with their $R^2$ values and their error Sum of Squares (SSE) given by:

$$SSE = \sum_{n}^{i=1} (x_i - \bar{x})^2 \tag{4.1}$$

With $x_i$ being the values of the data points and $\bar{x}$ being the value predicted using the equation for the plane of best fit at the corresponding location.

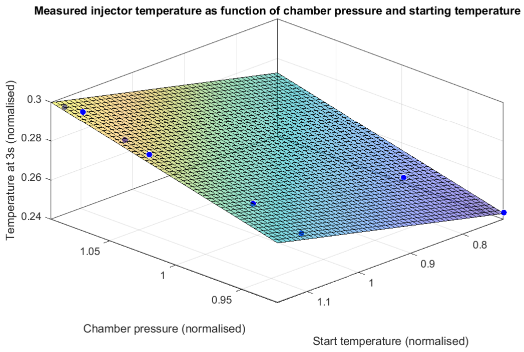


Figure 4.19: Normalised temperatures as recorded at the injector for RT2 as function of chamber pressure and starting temperature.

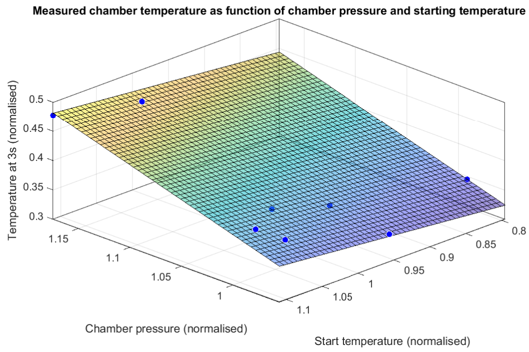


Figure 4.20: Normalised temperatures as recorded at the chamber for RT2 as function of chamber pressure and starting temperature.

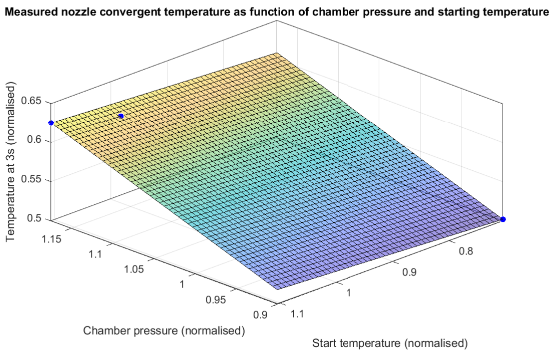


Figure 4.21: Normalised temperatures as recorded at the nozzle convergent for RT2 as function of chamber pressure and starting temperature.

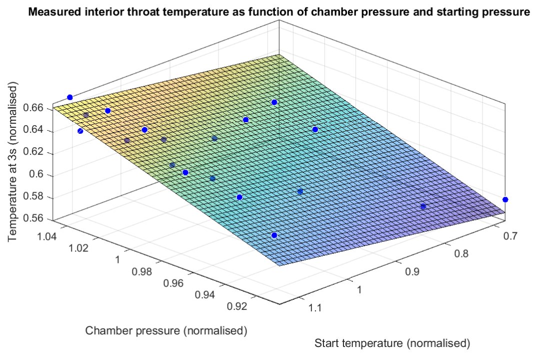


Figure 4.22: Normalised temperatures as recorded at the interior throat for RT2 as function of chamber pressure and starting temperature.

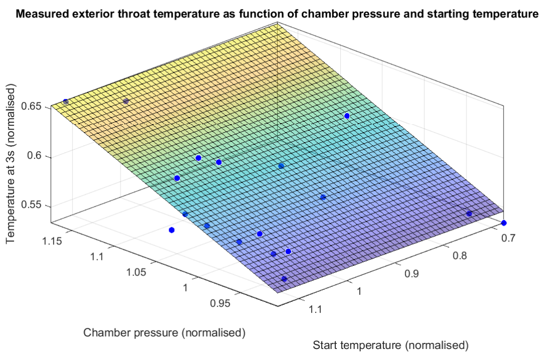


Figure 4.23: Normalised temperatures as recorded at the exterior throat for RT2 as function of chamber pressure and starting temperature.

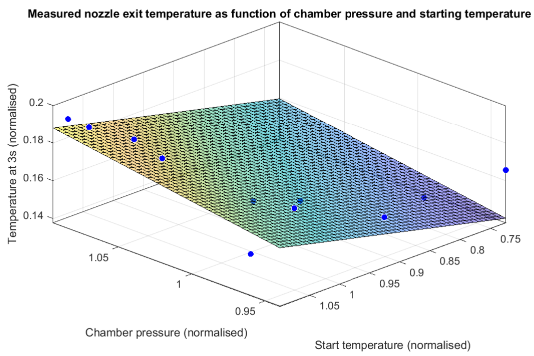


Figure 4.24: Normalised temperatures as recorded at the nozzle exit for RT2 as function of chamber pressure and starting temperature.

From Figures 4.19 to 4.24 some interesting trends can be observed. It can be seen that for higher chamber pressures, the measured temperature is higher. This is also as expected when looking at equations 3.8 and 3.10. It can also be seen that for a higher starting temperature the measured final temperature is also higher, which makes sense. Something which can be seen is that the slope on the starting temperature axis is different for each plane. It can for example be seen that for figure 4.21, 4.22 and 4.23 the slope on the starting temperature axis is less steep than for figures 4.19, 4.20 and 4.24. This is due to the fact for areas which get hotter, a small difference in starting temperature is a much smaller percentage of the final temperature reached. So percentage-wise the starting temperature has a smaller influence. This can also be seen in the test data, although it is likely that part of the reason for the shallow slope is also due to measurement error. This becomes evident due to the fact that the internal throat has a larger gradient (as function of the starting temperature) compared to the gradients at some other locations, despite the final temperature being higher in the internal throat.

In table 4.2 the equations for the plane of best fit are shown. Overall it can be seen that most equations fit well with a high $R^2$ value and a low SSE. For the exterior throat and the nozzle exit the fit was initially quite poor. To mediate this, three outliers were excluded for the exterior throat and two outliers were excluded for the nozzle exit. The new resulting equations clearly show a better fit, so these equations were used to generate the calibration case.

Table 4.2: Equations of the planes of best fit for each measurement location

| **Location** | **Equation** | **$R^2$** | **SSE** | **# Data points** |
|---|---|---|---|---|
| Injector | $0.0386 + 0.1724 \cdot P_c + 0.06282 \cdot T_{start}$ | 0.9812 | $5.3591 \cdot 10^{-5}$ | 8 |
| Chamber | $-0.2902 + 0.5445 \cdot P_c + 0.1191 \cdot T_{start}$ | 0.9887 | $2.0980 \cdot 10^{-4}$ | 8 |
| Nozzle Convergent | $0.1237 + 0.3882 \cdot P_c + 0.04117 \cdot T_{start}$ | 1 | $1.2326 \cdot 10^{-32}$ | 3 |
| Interior Throat | $0.09641 + 0.4765 \cdot P_c + 0.05852 \cdot T_{start}$ | 0.8602 | 0.0017 | 19 |
| Exterior Throat | $0.1867 + 0.3943 \cdot P_c + 0.003365 \cdot T_{start}$ | 0.5837 | 0.0102 | 18 |
| Exterior Throat* | $0.1807 + 0.3775 \cdot P_c + 0.01675 \cdot T_{start}$ | 0.8847 | 0.0018 | 15 |
| Nozzle Exit | $-0.0327 + 0.1253 \cdot P_c + 0.07594 \cdot T_{start}$ | 0.4875 | 0.0024 | 11 |
| Nozzle Exit* | $-0.05012 + 0.06915 \cdot P_c + 0.153 \cdot T_{start}$ | 0.9165 | $3.1421 \cdot 10^{-4}$ | 9 |

### 4.5.2. The calibration algorithm and calibration results

Below in figure 4.25 the temperature curve as predicted by the model before calibration can be seen compared to the temperature of the calibration case derived from the measured temperature data. In this figure, the zero point on the x-axis corresponds to the axial position of the injector and axial value of one corresponds to the nozzle exit. The temperature is normalised with respect to the maximum temperature of the calibration case.

It can be seen that the model overestimates the temperature by a large margin. In the throat by almost a factor of three and near the injector/chamber and nozzle exit by almost a factor of two. This is not very surprising, as it was already found in literature that the Bartz equation with the standard empirical coefficient of 0.026 severely overestimates the heat transfer in small rocket engines [18, 38]. What is more important is to look at the trend. It can be seen that while the model predicts much higher temperatures overall, the shape of the temperature distribution is in good agreement with the measurement data. One difference that can be observed is that the result from the model predicts a rise in temperature near the injector while this is not the case according to the measurement data. There is a simple explanation for this: as can be seen in figure 4.27 the combustion chamber of the PM200 has a smaller internal radius near the injector. The Bartz equation was not specifically developed to handle such geometries. Since the heat transfer coefficient as predicted by Bartz equation is a function of the inverse of the local internal chamber diameter, the Bartz equation overestimates the heat transfer by a large margin in this area which causes the rise in temperature near the injector.

It is clear that a calibration is needed. This was done by considering the problem an inverse heat conduction problem. In an inverse heat conduction problem the outer wall temperature is considered known and the heat transfer distribution to inside of the wall is to be deter-

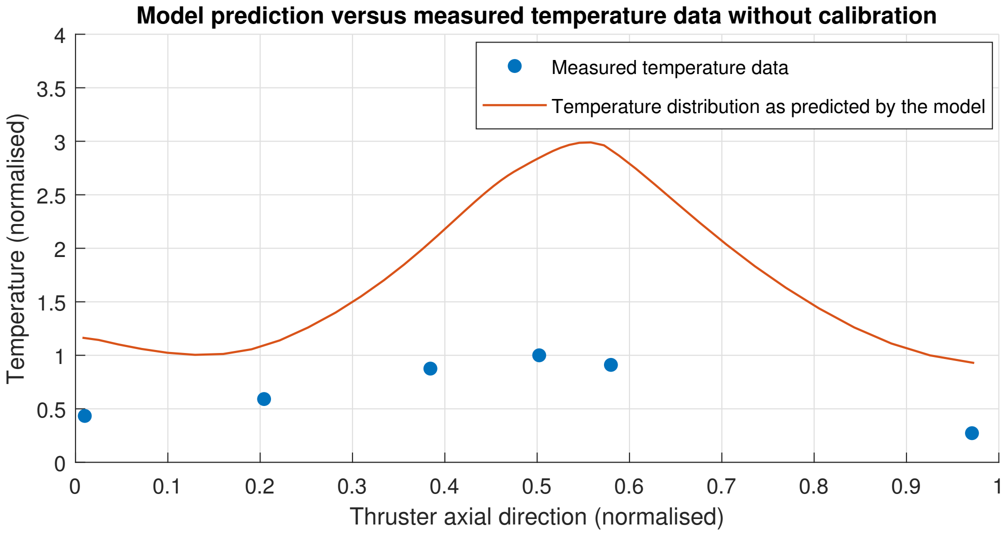


Figure 4.25: Model prediction versus measured temperature data without calibration.

mined. Such techniques have been used before to determine the heat flux distribution and temperature profiles in rocket engines, see for example: [9, 19, 30]. One of the main difficulties in these types of problems is that they are ill-posed (i.e. the solution is often unstable for different input parameters). In the case here the problem is slightly modified as the primary interest is not to determine the internal heat flux distribution, but instead the goal is to find correction factors for the empirical parameters in the Bartz equation.

The way this is done is by running the program with the empirical factor in the Bartz equation set to 0.026, from this figure 4.25 was obtained. The program then tries to readjust the empirical parameter of the Bartz equation for each measurement point by dividing the measured temperature by the model output and multiplying the empirical factor in the Bartz equation by this number. This cycle is repeated until the SSE value of the program falls below a certain threshold, in this case 0.1 $K^2$. The result of the model after completing this calibration procedure for the calibration case can be seen below in figure 4.26.

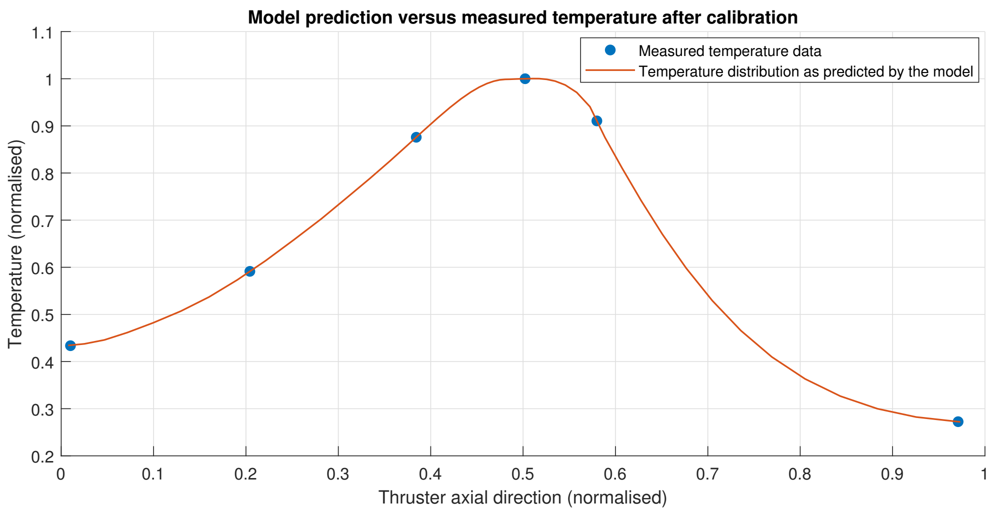


Figure 4.26: Model prediction versus measured temperature data after calibration.

As can be seen in figure 4.26 the model result now matches the test data closely, at least for the calibration case. The question remains how well the model will predict the temperature distribution for different cases. This will be discussed in section 4.6.

The distribution of the correction factor for the empirical constant for the Bartz equation resulting from the calibration can be seen below in figure 4.28 (blue uninterrupted line). From this figure some interesting information can be gained. It can be seen that based on the model results it appears that the Bartz equation overestimates the heat transfer coefficient by a factor of between 1.79 and 10.83 at the nozzle convergent, the interior throat, the exterior throat and the nozzle exit. In the combustion chamber some strange behaviour is seen. At the widest part of the chamber the model seems to suggest that the Bartz equation underestimates the heat flux while at the injector the model suggests that the Bartz equation severely overestimates the heat flux by more than a factor of 30. Part of this strange behaviour can be explained by the internal shape of the thruster. Because the thruster has a smaller diameter at the injector when compared to the chamber (see figure 4.27), the Bartz equation overestimates the heat flux by a large margin in this area. This causes the calibration algorithm to lower the empirical coefficient for the Bartz equation near the injector.

An explanation for the high correction factor value of 1.5 in the chamber could be due to way the Bartz equation was set up in the model. As explained in section 3.1 the input values of the Bartz equation were evaluated at frozen flow conditions because this was in agreement with literature [2, 32]. In reality the flow is likely not yet frozen in the chamber as combustion is occurring here, this causes an increase in heat transfer which is not accounted for when frozen flow is assumed. A study by Herbertz and Selzer [11] suggests that assuming a shifting equilibrium flow of 33% may be more appropriate. They note that the ratio of the shifting equilibrium flow changes with chamber pressure, with the ratio for lower chamber pressures tending more towards frozen flow. Furthermore, this study also found that the heat transfer coefficient near the injector is overestimated by the Bartz equation, even when the combustion chamber diameter is kept constant. This further explains the low value of the correction factor observed near the injector.

A second possible explanation for the high correction factor value of 1.5 in the chamber can be found in the original paper by Bartz [2], in this paper it is stated that the Bartz equation usually underestimates the value of the heat flux in the chamber itself. In the paper it is stated that this is because convection is not the only important phenomenon contributing to the heat transfer inside the combustion chamber.

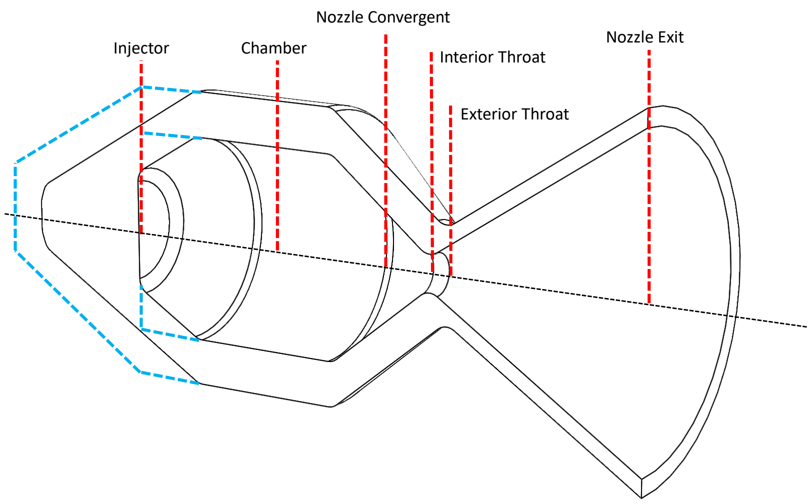


Figure 4.27: Simplified internal geometry of the PM200 with thermocouple locations indicated.

While the distribution obtained for the PM200 as shown in figure 4.28 leads to accurate

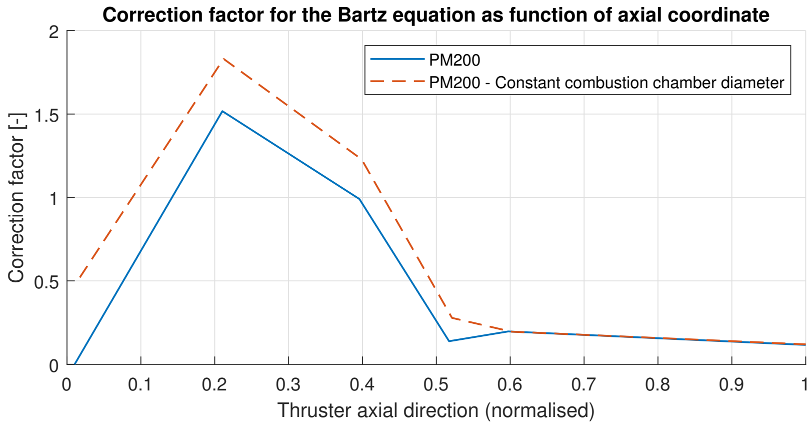


Figure 4.28: Distribution of the correction factor for the Bartz equation as function of the axial coordinate within the thruster.

results for the PM200 as will be shown in section 4.6, this distribution is problematic for other geometries such as the reference thruster introduced in table 3.3 or the B20 thruster introduced in section 2.1.3. These thrusters have a constant internal diameter throughout the entire combustion chamber and therefore applying the correction factor distribution as obtained for the PM200 would lead to a severe underestimation of the heat flux near the injector. A second correction to the curve is therefore needed for thrusters which have a constant combustion chamber diameter. To create this curve the calibration was run again, but in this case the diameter inside the combustion chamber was assumed to be constant throughout the chamber as shown in figure 4.27 using the dotted light blue lines. Based on this the red dotted curve as shown in figure 4.28 was obtained. This curve, but scaled to the appropriate dimensions will be used for the calculations performed on the B20 thruster and for the result obtained for the reference thruster which will be presented in chapter 5.

In figure 4.29 the heat flux distribution obtained when applying the correction factors plotted in figure 4.28 can be seen for the reference thruster design. Note that the heat flux plotted in figure 4.29 is the heat flux at the start of the burn (so with the thruster wall still at the ambient temperature). It can be seen that in general the heat flux distribution looks similar to the uncalibrated distribution (seen in figure 3.29) with a large peak in heat flux visible near the nozzle throat. In the chamber some different behaviour can be seen however, for the uncalibrated case the heat flux was predicted to remain constant within the combustion chamber. After calibration it can be seen that a slight peak is seen at roughly 60% of the chamber length. It can also be seen that near the injector there is a decrease in heat flux. This result is in good agreement with experimental results presented by Herbertz and Selzer [11] who found a similar trend; near the injector they also measured a lower heat flux and at roughly the halfway point of the chamber they also measured a small peak in heat flux.

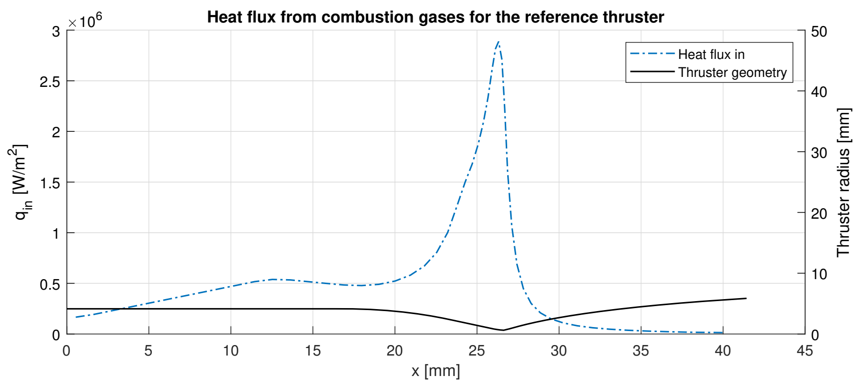


Figure 4.29: Heat flux from the combustion gases to the thruster wall for the reference thruster design after calibration

### 4.5.3. Regenerative cooling calibration

For determining the "c"-coefficient for the regenerative cooling channel, data from Dawn Aerospace's B20 thruster was used. Since dedicated tests to characterise the thermal behaviour of this thruster had not yet been performed on this thruster at the time of this study, the amount of thermal data for this thruster available to the author was limited. Because of this, it was decided to take the data from only one test for the calibration instead of using data from multiple tests as was done for the PM200. This is not ideal as this means that measurement errors will not be cancelled out, however as will be shown in the next few sections it is still sufficiently accurate to make good predictions.

As was observed in figure 2.3 in section 2.1, for the regeneratively cooled version of the PM200 the chamber pressure does not stay constant as the chamber pressure increases. For the B20 thruster a similar behaviour can be observed, except in this case the chamber pressure decreases with burn time. This is due to the fact that the mass flows for the B20 thruster are so high that the self-pressurising effect of the propellants is not sufficient to maintain the chamber pressure at a constant level. Since this effect is rather large, the pressure curve as obtained from test data was used in the calculation of the convective heat transfer coefficient (equation 3.8) instead of assuming a constant chamber pressure. For all other calculations which require NASA CEA to run, a constant chamber pressure was still used. This was done to prevent having to run NASA CEA for every loop, which would slow down the program to an unacceptable level. As input for NASA CEA the average chamber pressure was used.

For calibration test 3 performed on 19-09-2018 was used. This test consisted of a 8 second burn of the B20 thruster. Temperature measurements were performed using K-type thermocouples at the following locations: The nozzle throat, the combustion chamber, the cooling channel inlet and the cooling channel outlet.

The determination of the c-coefficient was split up into two parts: a correction was determined for the heating of the fluid, and a separate correction was determined for the cooling of the fluid. This was inspired by the fact that the Dittus-Boelter equation (equation 3.62) also uses different coefficients for heating and cooling of the flow. It was found that a correction factor of 5.5 for the heating of the cooling fluid gave a good match to the test data. For the cooling of the cooling fluid no correction factor was required and the empirical coefficient was kept unchanged. The results can be seen in figure 4.30.

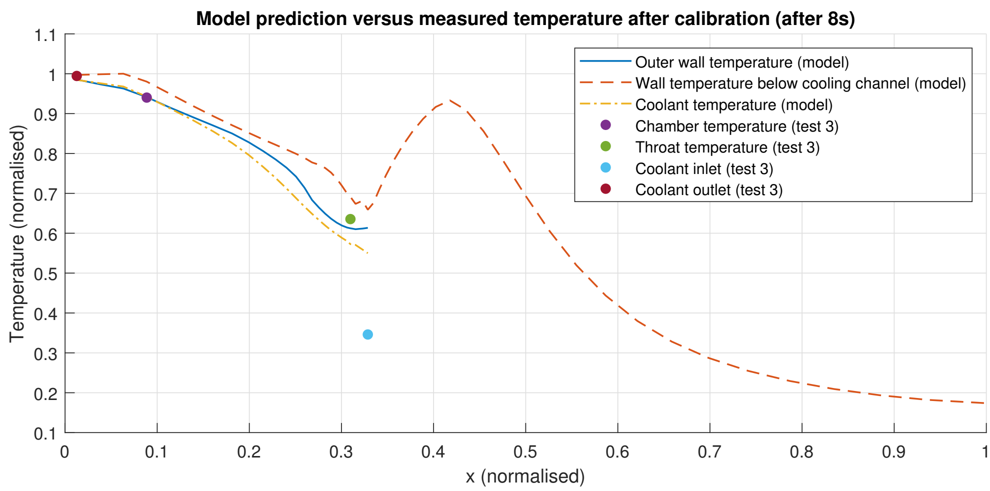


Figure 4.30: Model prediction versus measured temperature data after calibration for the B20 test data. Results shown are at t = 8s.

From figure 4.30 some interesting observations can be made. The temperatures are well predicted for the coolant outlet, the chamber and for the nozzle throat. For the coolant inlet the temperature is however overestimated substantially. This is likely because of the geometry of the cooling channel inlet. The cooling channel inlet for the B20 thruster consists of a annulus wrapping around the throat, this annulus has a relatively complex shape which is not well represented within the model. An attempt was made to model this annulus by removing the ribs from the first cooling channel cell and the resulting solution is the solution that was shown in figure 4.30. It appears that this simplified representation of the inlet is simply not adequate. In the end this is not a large issue as the wall temperature is still predicted correctly. In section 4.6.2 it will be shown that this is also the case for the PM200.

While the final temperatures of the model match well with the final temperatures observed in the test, the transient results do not appear to match. This can be seen in figures 4.31 and 4.32. It can be seen that trends predicted by the model do not match up well with the test measurements, except for the trend seen at the nozzle throat. This behaviour is rather strange and may be related to the fact that the internal geometry of the B20 thruster is not an exact scaled value of the PM200. Therefore the a-coefficients determined earlier may not be valid for the B20 thruster. The fact that the temperatures of the model and the test match at the eight second mark for the B20 thruster may therefore just be a coincidence. Nevertheless, a relatively good agreement was reached with the current c-values for the PM200, even the trends in the transient regime are predicted reasonably well as will be shown in section 4.6.2.

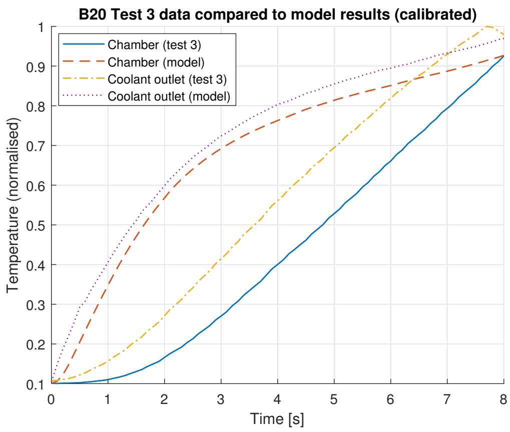


Figure 4.31: Calibrated transient temperature profile for a 8s test for the front half of the B20 thruster compared to the test data.

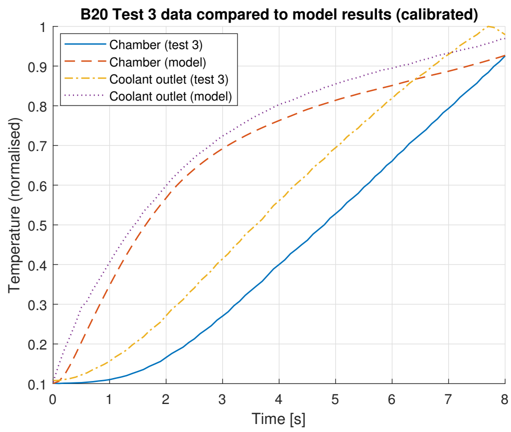


Figure 4.32: Calibrated transient temperature profile for a 8s test for the back half of the B20 thruster compared to the test data.

Lastly, it can be observed in figure 4.30 that after an 8 second burn the maximum temperature in the thruster occurs at the combustion chamber and not at the nozzle throat. This is somewhat surprising as for all prior cases the highest temperatures were always in the nozzle throat where the highest heat flux is expected. It appears that the regenerative cooling channel is successful in keeping the nozzle temperature down. As the coolant fluid moves towards the combustion chamber it heats up and the cooling becomes less effective, causing the temperature to rise. This was also physically visible during real life tests as can be seen in figure 4.33. It can be seen that the combustion chamber started to glow from the high temperatures while the nozzle throat remained relatively cool. It can also be seen that the model predicts this behaviour as well, with the model results matching the test data closely.

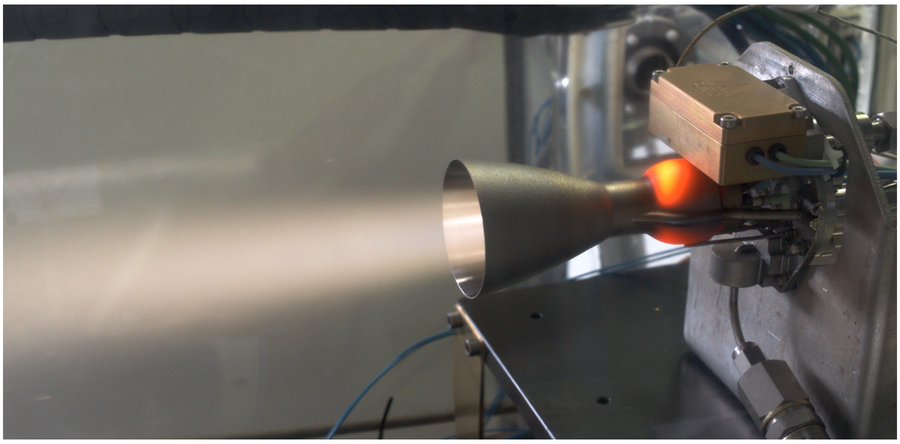

Figure 4.33: Heating pattern visible on the B20 thruster during a static hot fire test.

## 4.6. Model validation

With the model calibrated, it now becomes possible to validate the model to the test results and to determine the accuracy of the model. This was done in several steps. First the Radiation/Heat-sink cooled case will be validated. The Radiation/Heat-sink cooled case is the same case as the one which was used for calibration, so obviously the model will be very close to the test data for the calibration case. The question however remains how close the model results will be to the test data if the burn parameters are varied. Therefore the chamber pressure, starting temperature and burn time were varied and the model results were compared to experimental data. The full transient behaviour including the cool down behaviour of the thruster will also be validated. Secondly, the regenerative cooling code will be validated by comparing the model outcome with data from tests performed with a regeneratively cooled version of the PM200. In this section the model results for two different wall materials will also be compared to tests data from two thrusters with a different wall material.

### 4.6.1. Radiation/Heat-sink cooled

The validation of the Radiation/Heat-sink cooled case will be split up in three parts, first the model results will be validated for different chamber pressures and different starting temperatures for a three second burn time. Afterwards, the model results will be validated for a two and a four second burn time using experimental data. Lastly, the model results will be validated over the entire transient range for a three second burn time and a 97 second cooldown of the thruster.

**Validation results for different chamber pressures and starting temperatures**

As a first step in validating the model. The model was executed for different starting temperatures and chamber pressures for a 3s burn time. The results were compared to the test data. The result of this comparison can be seen in table 4.3. In this table the difference between the model results and the best fit of the test data is shown. The results are also shown graphically in Figures 4.34 to 4.39. In table 4.3 the red numbers indicate an error larger than 15%. A cell with a light red background indicates that the case fell outside of the validity range of the equation of best fit of the test data (i.e. no tests were performed which had similar starting conditions, so the error is based upon an extrapolation of the test data. This extrapolation may not be accurate). Validation cases were executed with starting temperatures ranging from 0.8 times the nominal starting temperature of 30 degrees up to 1.1 times the nominal starting temperature and with chamber pressures ranging from from 0.9 times the nominal chamber pressure up to 1.1 times the nominal chamber pressure. These ranges were selected because these were also the ranges which were observed during testing. By staying within the ranges observed during testing the error could be calculated by interpolation of test data points rather than by extrapolation. Especially for the chamber pressure this 10% range provided a rather representative boundary of typical operating conditions, as chamber pressures lower or higher than 10% of the nominal chamber pressure were rarely observed. As an additional step, some highly extrapolated cases were also executed where the chamber pressure and starting temperature were varied by 50%. This was mostly done to see how the program would perform in these cases.

Table 4.3: Difference between model results and the results from the best fit of the test data for a 3s burn

| $P_c$ | $T_{start}$ | Burntime | Error Injector [%] | Error Chamber [%] | Error NC [%] | Error IT [%] | Error ET [%] | Error NE [%] |
|---|---|---|---|---|---|---|---|---|
| 1 | 1 | 3 | -0.24 | 0.01 | 0.00 | 0.00 | 0.00 | 0.00 |
| 0.9 | 0.8 | 3 | -0.30 | -13.87 | 0.56 | -0.82 | 1.82 | -12.07 |
| 0.9 | 0.9 | 3 | -0.25 | -11.43 | 0.24 | -0.75 | 1.08 | -4.74 |
| 0.9 | 1 | 3 | -0.20 | -9.16 | -0.08 | -0.69 | 0.34 | 1.24 |
| 0.9 | 1.1 | 3 | -0.15 | -7.06 | -0.39 | -0.63 | -0.39 | 6.21 |
| 0.95 | 1 | 3 | -0.24 | -4.24 | -0.07 | -0.36 | 0.13 | 0.60 |
| 1 | 0.8 | 3 | -0.36 | -3.37 | 0.57 | -0.12 | 1.35 | -12.96 |
| 1 | 0.9 | 3 | -0.29 | -1.62 | 0.28 | -0.06 | 0.68 | -5.85 |
| 1 | 1.1 | 3 | -0.18 | 1.54 | -0.27 | 0.07 | -0.67 | 4.91 |
| 1.05 | 1 | 3 | -0.20 | 3.72 | 0.12 | 0.41 | -0.07 | -0.52 |
| 1.1 | 0.8 | 3 | -0.28 | 4.44 | 0.77 | 0.68 | 1.14 | -13.65 |
| 1.1 | 0.9 | 3 | -0.22 | 5.74 | 0.51 | 0.75 | 0.51 | -6.76 |
| 1.1 | 1 | 3 | -0.15 | 6.97 | 0.26 | 0.81 | -0.10 | -1.03 |
| 1.1 | 1.1 | 3 | -0.10 | 8.13 | 0.00 | 0.87 | -0.73 | 3.78 |
| 0.5 | 0.5 | 3 | 2.78 | -403.51 | 6.15 | -0.80 | 12.01 | -53.89 |
| 0.5 | 1 | 3 | 2.46 | -137.45 | 3.26 | -0.69 | 6.32 | 9.11 |
| 0.5 | 1.5 | 3 | 2.21 | -68.60 | 0.67 | -0.61 | 0.86 | 27.05 |
| 1 | 0.5 | 3 | -0.57 | -9.40 | 1.45 | -0.33 | 3.41 | -48.04 |
| 1 | 1.5 | 3 | 0.04 | 6.85 | -1.33 | 0.33 | -3.30 | 18.48 |
| 1.5 | 0.5 | 3 | 0.60 | 21.05 | 3.17 | 4.23 | 3.27 | -41.70 |
| 1.5 | 1 | 3 | 0.85 | 23.77 | 2.20 | 4.48 | 0.88 | -3.83 |
| 1.5 | 1.5 | 3 | 1.06 | 26.03 | 1.29 | 4.74 | -1.46 | 13.57 |

From table 4.3 the following observations can be made:

- It can be seen that for all cases which fall inside the validity range of the equations of the planes of best fit the error is always less than 15%. Furthermore, the error for the cases outside of the validity range of the planes of best fit is also within 15% for all cases, excluding the highly extrapolated cases. If the measurements at the chamber and nozzle are excluded the maximum error is even less than 1.35% for all cases.

- The model performs less well for the Chamber and the Nozzle exit, although the error is still within 15%. For the chamber, part of this error might be explained due to the fact that the thruster is not exactly axisymmetric due to the presence of the igniter at this location. Because of this the temperature distribution may not be perfectly axisymmetric either (as was shown in section 4.4.3), which could lead to 3D effects which influence the measured temperature.

- In general, the model performs a bit worse for the combination of a low starting temperature and a low chamber pressure.

- For the highly extrapolated cases, the model performs very poorly at the chamber and the nozzle exit for cases with a low chamber pressure. It is however likely that this is not due to the model being incorrect, but rather due to the extrapolation being incorrect as these cases fall far outside of the validity range of the equations of best fit. It should be noted that a linear extrapolation was performed. In reality the heat flux likely does not decrease linearly with chamber pressure (see equation 3.8, so this introduces an additional error.

- For the highly extrapolated cased the model also performs relatively poor at the chamber and nozzle exit for cases with a higher chamber pressure. This is likely also due to the fact that the extrapolation was done using a linear profile while the heat flux does not increase linearly with chamber pressure (see equation 3.8).

- For the highly extrapolated case where only the starting temperatures are varied, the model performs relatively well. For the injector and interior throat the error is less than 1% in both cases, for the nozzle convergent the error is less than 2%, for the exterior throat the error is lower than 4%. The chamber has a relatively large error but still below 10%, which is only slightly more than 1% higher than the highest error case which still falls in the validity range. For the nozzle exit the error is however quite large, with the largest error being more than 48%.

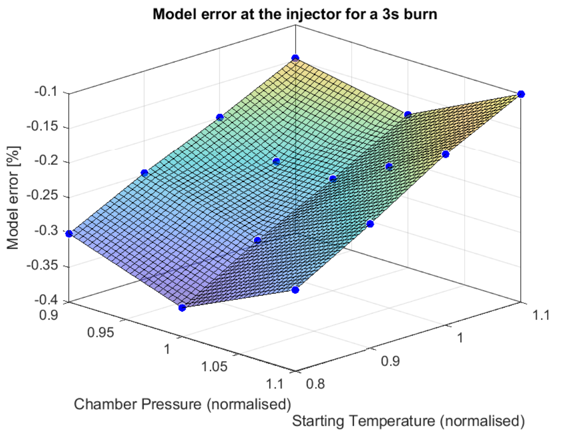


Figure 4.34: Model error at the injector compared to test data as function of chamber pressure and starting temperature (NOTE: Starting temperature axis is inverted for readability).

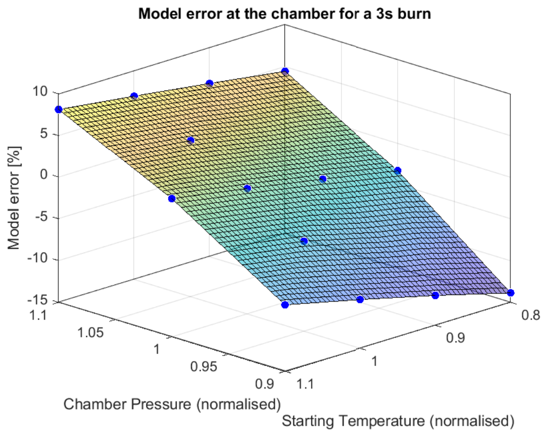


Figure 4.35: Model error at the chamber compared to test data as function of chamber pressure and starting temperature.

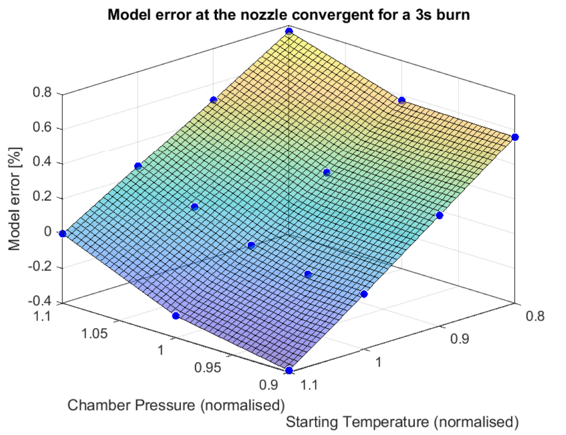


Figure 4.36: Model error at the nozzle convergent compared to test data as function of chamber pressure and starting temperature.

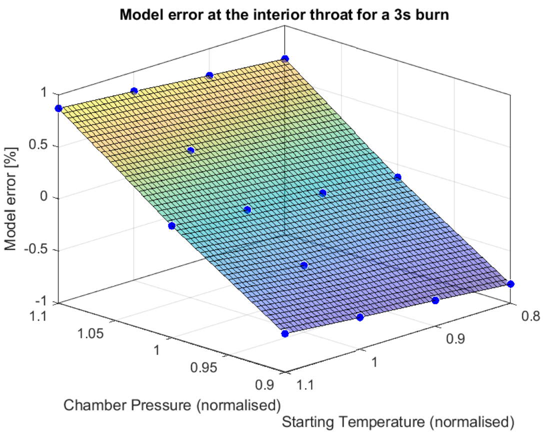


Figure 4.37: Model error at the interior throat compared to test data as function of chamber pressure and starting temperature.

It should be noted that the results presented above in table 4.3. and Figures 4.34 to 4.39 show the error of the model with respect to a bi-linear fit of the data. In reality, it is likely the case that the temperature variation with chamber pressure is not exactly linear. The errors presented here thus do not represent the exact errors, but rather a close approximation of the real errors.

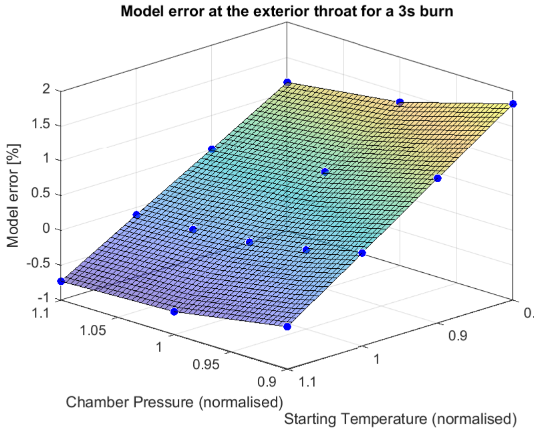


Figure 4.38: Model error at the exterior throat compared to test data as function of chamber pressure and starting temperature.

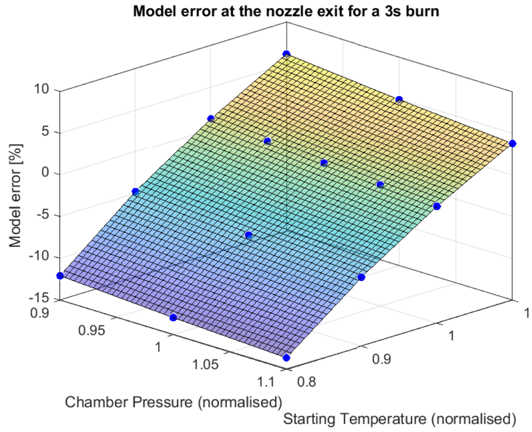


Figure 4.39: Model error at the nozzle exit compared to test data as function of chamber pressure and starting temperature (NOTE: Starting temperature axis is inverted for readability).

**Validation results for different burn times**

As shown in the previous section, the temperature of the thruster is predicted well by the model even if different chamber pressures or starting temperatures are used than the calibration case. Perhaps even more important is to see how the model behaves when the burn time is changed. In this section this will be investigated. Relatively little data was available for other burn times, only data for 2 and 4 second tests was available, and most of this data was recorded at different azimuth angles when compared to the calibration case. Initially the plan was to gather more data at other burn times also, however the amount of time required to do this proved excessive and unfeasible within the scope of this study. Using the same technique as was used for generating the calibration case as described in section 4.5, several planes of best fit could be generated for the data obtained at 2s and 4s. As relatively little data was available at other burn times, some things should be noted:

- For the 2s and 4s burns, a good fit was only obtained for the Injector, Chamber and the Interior Throat, the validity range of these fits was however very small compared to the validity ranges obtained for the 3s burns. For the 4s burns this was mainly because the 4s burns were usually performed later on in a sequence of tests, so the thruster and tank were hotter at this point due to all the heat from previous burns. This meant that for the 4s burns generally a higher chamber pressure and starting temperature were observed. The obtained planes of best fit can be seen in appendix D.1. For the 2s burns it just happened to be the case that there was very little spread in the measured chamber pressures, which was made worse by a lack of data points.

- Besides a good fit only being obtained for the Injector, Chamber and the Interior throat. Generally these fits were made using less data points and they also had a lower accuracy (lower $R^2$ value and higher SSE, see table 4.4). Because of this, it can be expected that the observed error is somewhat higher.

- The data for the 2s and 4s burns was mostly measured at different azimuth angles compared to the data which was used for the calibration case. In order to have sufficient data points to get a somewhat decent fit, data from multiple azimuth angles was used (see appendix D.1 for the raw data and the exact location at which the measurement was performed). However, as seen in section 4.4 this is not necessarily a problem, as for the axial positions mentioned above the test data was relatively consistent independent of azimuth angle.

- Even though data from 1s burns and shorter burns was available, this data was not used because for this data it was unclear what the chamber pressure was. This was due to the fact that it took approximately 1.5 seconds before the chamber pressure sensor read the right pressure value due to the relatively long line in between the combustion chamber and the pressure sensor.

Table 4.4: Equations of the planes of best fit for each measurement location for 2s and 4s burns

| Burntime | Location | Equation | $R^2$ | SSE | # Data points |
|---|---|---|---|---|---|
| 4 | Injector | $-0.07243 + 0.4006 \cdot P_c + 0.01183 \cdot T_{start}$ | 0.8018 | $4.3709 \cdot 10^{-4}$ | 5 |
| 4 | Chamber | $-0.2151 + 0.4412 \cdot P_c + 0.2779 \cdot T_{start}$ | 0.7648 | 0.0013 | 7 |
| 4 | Interior Throat | $-0.3299 + 0.8844 \cdot P_c + 0.2178 \cdot T_{start}$ | 0.3142 | 0.0249 | 8 |
| 4 | Interior Throat* | $-1.438 + 1.588 \cdot P_c + 0.6166 \cdot T_{start}$ | 0.8153 | 0.0059 | 5 |
| 2 | Injector | $-0.008414 + 0.1655 \cdot P_c + 0.0654 \cdot T_{start}$ | 0.9993 | $1.4571 \cdot 10^{-7}$ | 4 |
| 2 | Chamber | $0.03502 + 0.2175 \cdot P_c + 0.07695 \cdot T_{start}$ | 0.9999 | $4.6717 \cdot 10^{-8}$ | 4 |
| 2 | Interior Throat | $-0.07071 + 0.3962 \cdot P_c + 0.09393 \cdot T_{start}$ | 0.9998 | $9.5938 \cdot 10^{-8}$ | 4 |

Using the equations listed in table 4.4 the model results were compared for a variety of starting parameters. The results for the 4s burns can be seen in table 4.5. For the 2s burns the results can be seen in table 4.6.

Table 4.5: Difference between model results and the results from the test data for a 4s burn

| $P_c$ | $T_{start}$ | Burntime | Error Injector [%] | Error Chamber [%] | Error Interior Throat [%] |
|---|---|---|---|---|---|
| 1 | 1 | 4 | -7.93 | 3.18 | -0.77 |
| 0.9 | 0.8 | 4 | -10.87 | -9.34 | -46.35 |
| 0.9 | 0.9 | 4 | -12.47 | -3.67 | -30.79 |
| 0.9 | 1 | 4 | -14.06 | 1.31 | -18.40 |
| 0.9 | 1.1 | 4 | -15.60 | 5.74 | -8.26 |
| 0.95 | 1 | 4 | -10.82 | 2.26 | -8.61 |
| 1 | 0.8 | 4 | -5.10 | -6.21 | -18.48 |
| 1 | 0.9 | 4 | -6.52 | -1.24 | -8.85 |
| 1 | 1.1 | 4 | -9.32 | 7.14 | 6.11 |
| 1.05 | 1 | 4 | -5.33 | 4.05 | 5.64 |
| 1.1 | 0.8 | 4 | -0.41 | -3.47 | -1.40 |
| 1.1 | 0.9 | 4 | -1.68 | 0.94 | 5.25 |
| 1.1 | 1 | 4 | -2.97 | 4.89 | 11.01 |
| 1.1 | 1.1 | 4 | -4.23 | 8.46 | 16.05 |

The first thing that stands out is that for the 4s burns, almost all data falls outside of the range of validity of the planes of best fit (data outside of the range of validity of the plane of best fit is indicated with a red cell background in table 4.4). Furthermore, the following observations can be made per measurement point:

- For the injector: Although definite conclusions are hard to draw since all but two data points fall outside of the validity range of the plane of best fit, in general the error increased by up to 15.6%. For lower chamber pressures the error is generally worse than for higher chamber pressures. For higher chamber pressures the maximum error observed was 5.33% while for lower chamber pressures a maximum error of 15.6% was reached. For cases which fell within the validity range of the plane of best fit the maximum observed error was 9.32%. In all cases the model underestimates the temperature.
- For the chamber: For the 4s burns the maximum error is decreased. A maximum error of 13.87% was observed for the 3s burns while for the 4s burn the maximum error was 9.34%, it is interesting to note that the maximum error occurred for the same case for both the 3s and 4s burn, which is a case with a low chamber pressure and a low starting temperature. For the other cases the errors stayed comparable to the errors observed in the 3s tests. For cases which fell within the validity range of the plane of best fit the maximum observed error was 8.46%. In most cases the model slightly overestimated the temperature.

- For the interior throat: For the 4s burns the performance of the model generally deteriorated by a large margin. While for the calibration case the error was only 0.77% (which is comparable to the errors which were seen for the 3s burns), for other cases the error increased substantially. The maximum error observed was 46.35% for a case with a low chamber pressure and starting temperature (although this error did occur outside of the validity range of the plane of best fit). For the cases which fall within the validity range of the plane of best fit the maximum observed error was 8.85%. In absolute terms this is not a huge error, however it still is an error more than 10 times larger than the worst error seen for the internal throat for the 3s burns.
- For the chamber and interior throat it can be seen that in general the model performs worse for a lower chamber pressure and a lower starting temperature. This can also be seen in figures 4.41 and 4.42. However, this may also just be because all the 4s burns were performed at higher starting temperatures and higher chamber pressures, which lead to all the cases with low chamber pressures and low starting temperatures falling outside of the validity range of the planes of best fit.

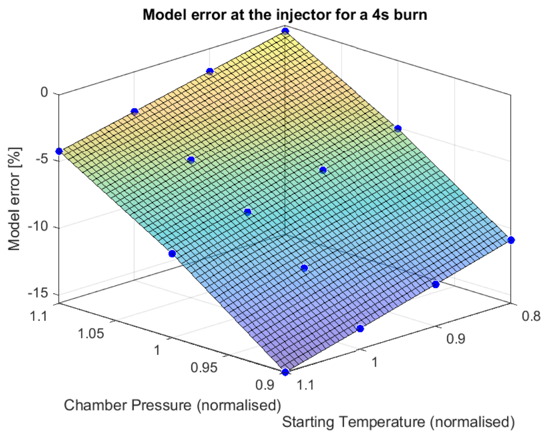


Figure 4.40: Model error at the injector compared to test data for a 4s burn as function of chamber pressure and starting temperature.

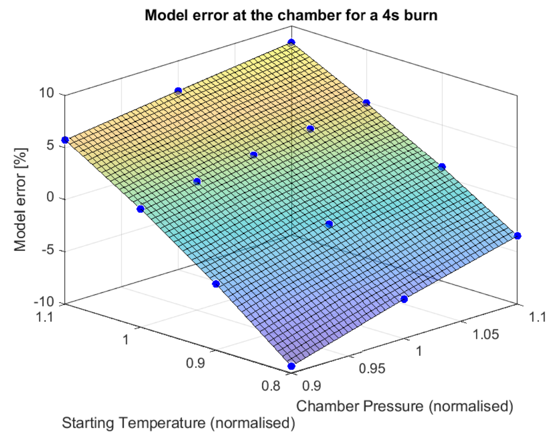


Figure 4.41: Model error at the nozzle exit compared to test data for a 4s burn as function of chamber pressure and starting temperature (NOTE: Starting temperature and chamber pressure axes are switched around for readability).

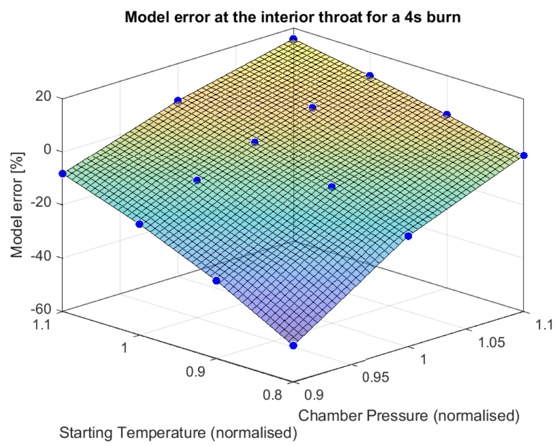


Figure 4.42: Model error at the interior throat compared to test data for a 4s burn as function of chamber pressure and starting temperature. (NOTE: Starting temperature and chamber pressure axes are switched around for readability)

Overall it can be seen that for the injector and the interior throat the error increases, while for the chamber the error remained roughly the same or even decreased a little bit. It is not exactly clear what causes this increase in error as there are several potential causes:

- For the 4s burns the planes of best fit were less accurate: less data points were used, the $R^2$ value was higher and the SSE values were also higher in all cases. It may therefore just be the case that the test data was represented less accurately and that therefore larger errors were observed.
- Almost all of the test cases fell outside of the validity range of the planes of best fit. It can also be seen in table 4.5 that in general the cases which fell within the validity range of the planes of best fit had a lower error than the cases which fell outside of the validity range. So it might be the case that the larger errors are just because the test data was collected over a smaller range of starting temperatures and chamber pressures and that the fit through the data was less accurate.
- Due to the fact that little data was available for the 4s burns, data from thermocouples mounted at different azimuth angles than the 3s calibration case were used. This was done because it was seen that the temperatures measured at these locations were roughly the same as the temperatures measured at the azimuth angle used in the calibration case. However, it may be the case that this temperature data is not representative at the azimuth angle used in the calibration case, which could explain the larger errors observed.
- The last option could be that errors are introduced within the model while performing the time step calculations. In this case the error can be expected to grow even further as the simulation times goes even further beyond the burn time of the calibration case. However, it will be shown in section 4.6.2 that this is most likely not the case. In this section it will be shown that the model also provides accurate results for longer burn times of up to 10 seconds.

For the 2 second burns, the results from comparing the test data with the model data can be seen in table 4.6. It can be seen that all cases except for one case fall outside of the validity range of the equations of the planes of best fit. Furthermore, it can be seen that in general the error is relatively large for the 2s burns.

Table 4.6: Difference between model results and the results from the test data for a 2s burn

| $P_c$ | $T_{start}$ | Burntime | Error Injector [%] | Error Chamber [%] | Error Interior Throat [%] |
|---|---|---|---|---|---|
| 1 | 1 | 2 | 14.38 | 21.24 | -11.87 |
| 0.9 | 0.8 | 2 | 13.13 | 20.94 | -17.93 |
| 0.9 | 0.9 | 2 | 12.86 | 20.93 | -16.48 |
| 0.9 | 1 | 2 | 12.61 | 20.92 | -15.10 |
| 0.9 | 1.1 | 2 | 12.38 | 20.91 | -13.79 |
| 0.95 | 1 | 2 | 13.53 | 21.09 | -13.41 |
| 1 | 0.8 | 2 | 14.94 | 21.26 | -14.29 |
| 1 | 0.9 | 2 | 14.65 | 21.25 | -13.05 |
| 1 | 1 | 2 | 14.38 | 21.24 | -11.87 |
| 1 | 1.1 | 2 | 14.12 | 21.24 | -10.73 |
| 1.05 | 1 | 2 | 15.22 | 21.45 | -10.36 |
| 1.1 | 0.8 | 2 | 16.59 | 21.65 | -11.10 |
| 1.1 | 0.9 | 2 | 16.28 | 21.64 | -10.02 |
| 1.1 | 1 | 2 | 15.99 | 21.63 | -8.99 |
| 1.1 | 1.1 | 2 | 15.72 | 21.63 | -7.99 |

The error for the 2s burns is relatively high. Although it is hard to draw any hard conclusions from table 4.6 as most data points fall outside of the testing range. Furthermore, while for the 2s burns the $R^2$ values of the planes of best fit were high and the SSE values were low, very few data points were used (only 4 for each case). Therefore, it is questionable whether or not these fits are really accurate. There is also very little variance between the test data points which makes it even more questionable if the fits are really accurate for a larger range of starting conditions. It can also be seen that the error is relatively constant for all cases (i.e. there is very little variance between the results for different input parameters). This seems to point at a bias somewhere, either in the test data, the plane of best fit, or in the model.

**Validation results of transient and cooldown behaviour**

As a last step, the transient behaviour over the full range of a test as predicted by the model will be compared to the test results for the radiation/heat-sink cooled thruster to see if the model predicts the overall trends observed not only in a quantitative matter but also in a qualitative matter. This will include the cooldown behaviour as predicted by the model.

In Figures 4.43 and 4.44 the test data and model results can be seen for a 3s burn and a cooldown time of 97 seconds. In these figures the results for the model correspond to the calibration case (i.e. normalised chamber pressure = 1 and normalised starting temperature = 1). Each of the curves representing the test data is taken from single tests only and not an average of multiple tests. This means that the test data plots may be subject to measurement errors. Furthermore, because none of tests had the exact same starting conditions as the calibration case, the starting conditions are slightly different (both in between tests and in between the test and the model), this causes an additional mismatch between the model and test results. To correct this the temperature data from the tests was raised or lowered so that the starting temperature matched the starting temperature of the model case, for all cases this correction amounted to a change of less than 7 K.

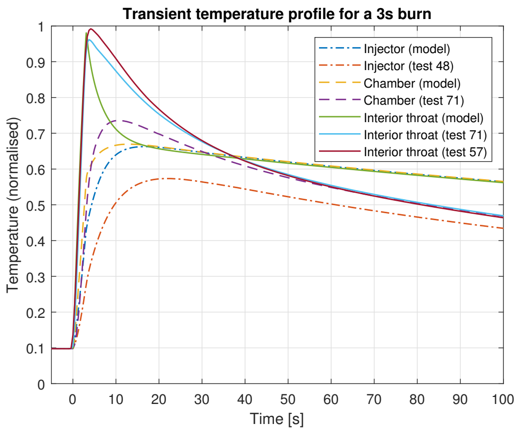


Figure 4.43: Transient temperature profile for a 3s test for the front half of the thruster compared to the test data.

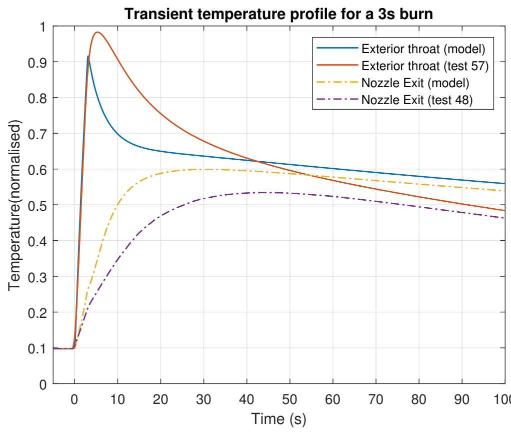


Figure 4.44: Transient temperature profile for a 3s test for the back half of the thruster compared to the test data.

Starting from the injector and moving towards the nozzle exit, the following observations can be made for each measurement point:

- For the injector, in general the model over predicts the temperature. It is suspected that this is because in the model the boundary cells at the injector cells do not have any other cells to conduct heat to. In reality the injector dome is present here, as well as the connection to the pressure sensors and the feed lines. These parts act as a heat-sink, causing a reduction in temperature near the injector when compared to the model results.

- For the chamber, the model result is in general very close, but the additional heating due to conduction is underestimated right after shutdown of the engine and overestimated later on.

- For the internal throat and the external throat the temperature is predicted well during the burn. However, the cooling down of the thruster is severely overestimated right after shut down. Similar as to what was observed for the chamber, later on after shutdown the cooling is underestimated again. It is suspected that this cooldown is overestimated due to the fact that the model assumes that heat radiated away from the thruster is not reabsorbed on other parts of the thruster. In reality this is however the case, causing the thruster to “hold on” to the heat for longer. Because the interior and exterior throat are relatively enclosed compared to other parts of the thruster, it is not surprising to see that this effect would be largest here. It is possible to model this behaviour using so called transfer functions [5]. However, implementing such equations within the model presented here would be relatively complex. Therefore, given the time constraints of the thesis study it was decided to not implement such transfer functions within the model.

- For the nozzle exit the temperature is generally over predicted slightly. During testing it was observed that flow separation occurred within the nozzle due to the relatively high ambient pressures the tests were performed at. It is suspected that this flow separation may have limited the heat transfer, resulting in the lower temperature values observed during testing. In addition, it could also be that the temperature at the nozzle is overestimated because radiation heat transfer to the environment from the inside of the nozzle is not taken into account.

Besides the reasons mentioned above, several other reasons were identified which can explain some of the behaviour seen above:

- It could be that the emissivity constant is overestimated or underestimated for the model. The emissivity constant used within the model was 0.8, this value was taken from literature [50] and was purely theoretical. The actual emissivity value of the thruster was not determined. If the emissivity was overestimated or underestimated this could explain some of the differences. While it was shown in section 3.8 that the emissivity behaviour has a small effect on the final temperature reached by the thruster, for the cooldown behaviour the emissivity constant can have a large effect.
- In the model it was assumed that heat transfer from the thruster to the environment was only through radiation. Since the tests with RT2 were performed at roughly 200 mbar it may be that cooling due to natural convection was also occurring. Especially during cooldown this could explain why after the 42s mark the thruster appears to cool down faster according to the test data when compared to the model data.
- In the model only the combustion chamber is modelled, while in reality the thruster is also connected to the feed lines and the lines/mounts connecting to the pressure sensors. This has two consequences: more of the heat is conducted away from the combustion chamber, and the thruster has a larger total radiating surface area. This means that it can be expected that the thruster cools down faster in real life when compared to the model, and this can indeed be seen in figures 4.43 and 4.44.

In general summarising all of the results above, the difference in the cooldown behaviour between the model and test results is suspected to be because of the following phenomena: Right after shutdown the temperature is underestimated near the throat because reabsorption of the heat radiated away is not taken into account. For the injector the temperature is overestimated because the pressure sensor ports, feed lines and the injector dome act as a heat-sink in real life which is not taken into account in the model. After approximately 40 seconds the model is again quite close to the test result, but now the model starts to overestimate the temperature. Possible reasons for this could be due to a difference in the emissivity constant and due to the fact that the real life thruster has a larger radiating surface area and thermal mass. It could also be that some natural convection is present in real life which is not taken into account in the model.

Overall it can still be said that the model captures the trends well. During the burn the model results are close to the measurement data. After shutdown, the general shape of the cooldown curve for the injector, chamber and nozzle exit is almost exactly the same as the shape obtained from the tests although the temperatures predicted do differ. The fact that at least the shape is correct confirms that the (conduction) model is implemented correctly.

In conclusion, it can be said that the model predicts the thermal behaviour well during the burn, during the cooldown behaviour the model can qualitatively predict the thermal behaviour of the thruster and indicate trends. Quantitatively the error is however relatively large for the cooldown behaviour. The model can thus not be used to determine the exact temperature after a given cooldown time.

### 4.6.2. Regeneratively cooled

The validation of the regeneratively cooled case will be subdivided into three different sections: first the validation for different chamber pressures, starting temperatures and burn times will be performed. Afterwards validation of the full transient curve and the cooldown behaviour will be investigated. Lastly, for the regeneratively cooled case the model will also be validated for a thruster with a different wall material.

**Validation results for different chamber pressures, starting temperatures and burn times**

With the radiation/heat-sink part of the model validated, the next step is to validate the model for a thruster with a regenerative cooling channel. The test data from the regular PM200 will be used for this. While a large amount of tests was performed using the regular PM200, most of these tests were performed early on during the thesis project. Because of this, these tests were mostly performed using an older iteration of the test set-up and an older iteration of the PM200 module resulting in only a limited amount of use-able data being gathered. Therefore, for the regeneratively cooled case the validation will not be done by creating planes of best fit through data points and comparing the model results to these planes. Instead several individual cases with different starting parameters and burn times were simulated. The results can be seen in table 4.7. For the cases presented in table 4.7 the chamber pressure and starting temperature were set to match the values from the test data in order to make a fair comparison. Measurements were obtained only at the Chamber, Exterior throat and at the Nozzle exit, the reason for this is because there were no good mounting points to obtain measurements at the interior throat, the nozzle convergent or at the injector. Nevertheless a good comparison can still be made for the other points.

Table 4.7: Difference between model results and the results from the test data for the regeneratively cooled case

| $\mathbf{P_c}$ (average) | $\mathbf{T_{start}}$ | Burntime | Error Chamber [%] | Error Exterior Throat [%] | Error Nozzle Exit [%] |
|---|---|---|---|---|---|
| 0.98 | 1.31 | 2 | -2.86 | -3.37 | -4.08 |
| 1.31 | 0.75 | 3 | 4.27 | -0.74 | -0.90 |
| 0.99 | 0.93 | 5 | -8.03 | -9.87 | -8.56 |
| 1.45 | 1 | 10 | -0.19 | 0.12 | 6.68 |

From the results shown in table 4.7 it can be seen that the model predicts the temperatures at the reference points accurately. All results are within 10% of the values observed during testing. It can also be seen that the model results are accurate for a wide variety of starting conditions and burn times. Even for longer burn times (t>4s), which were not studied for the radiation cooled/heat-sink cooled case, the model gives accurate results. The fact that the model is still accurate for long burn times (t>4s) is important, as it shows that even though the model was calibrated using a 3s burn time, the error does not grow without bounds if longer burn times are simulated. The results from table 4.7 are shown graphically in figure 4.45.

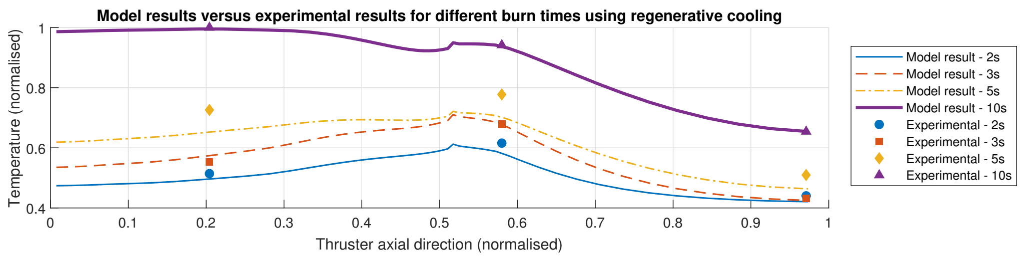


Figure 4.45: Model results versus experimental results for different burn times for the regeneratively cooled case

**Validation results of transient and cooldown behaviour**

Just as for the radiation/heat-sink cooled case, the transient and cooldown behaviour of the model was compared to the measurement data to see if the overall trends are predicted well by the model rather than only comparing the temperature values at certain given reference points. The result for a 10s burn time with a 90s cooldown can be seen in figure 4.46.

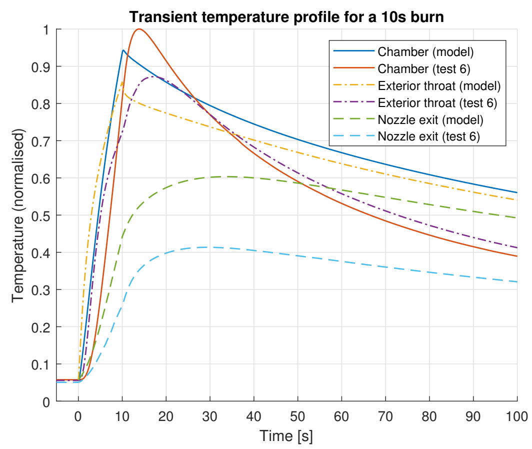


Figure 4.46: Transient temperature profile for a 10s burn using regenerative cooling compared to the test data

Looking at figure 4.46 similar trends are visible as were observed for the radiation/heat-sink cooled case: it can be seen that the model overestimates the conduction heat transfer to the nozzle after shutdown. The trend is however predicted quite well and the predicted cooldown slope is almost identical to the measurement data, just translated to a higher temperature. For the chamber and the exterior throat the cooldown curve is again not estimated well. Interesting to note is that while for the radiation/heat-sink cooled case the cooldown was first overestimated and then underestimated, for the regeneratively cooled case the cooldown is underestimated for the entire cooldown curve. This may be related to three factors: Firstly, it may be that this is because a longer burn time was simulated; it may be that the cooldown behaviour changes depending on the burn time. Secondly, it may be that the cooldown behaviour is not well modelled with the presence of cooling channels. In the model it is assumed that there was no heat transfer within the cooling channels during cooldown. In reality there is however still radiation heat transfer through the cooling channel which is not taken into account in the model presented here. Finally, it may be that the cooldown behaviour is different simply because the temperature is distributed differently due to the presence of the cooling channel.

Some other observations can also be made from figure 4.46. It can be seen that the highest temperature occurs in the combustion chamber rather than in the nozzle throat even though the highest heat flux is expected to occur in the nozzle throat. This behaviour was also seen for the B20 thruster during the calibration of the model in section 4.5.3. While at the start of the burn the temperature is highest in the nozzle throat, near the end of the burn the highest temperature occurs in the combustion chamber. This can be explained by the fact that the coolant channel runs from the nozzle towards the injector. Heat is thus transferred from the nozzle throat to the combustion chamber. As the coolant heats up the cooling becomes less effective leading to a higher overall wall temperature in the combustion chamber even though the heat flux is lower at this position.

As a consequence of the fact that the highest temperature occurs in the combustion chamber instead of in the nozzle throat, it can be seen that the error observed for the overall maximum temperature reached in the combustion chamber (after shutdown) is higher than the error at the reference point (which was -0.19%, see table 4.7). From figure 4.46 it can be determined that this error is still less than 5.5%, which is considered sufficient for the purposes of this study.

**Validation of wall material properties**
Besides the stainless steel version of the PM200, an inconel version of the PM200 thruster was also tested. A limited amount of thermal measurements was performed during these tests and these results can be used to validate the efficacy of the model for different wall materials. There are two reasons that there is only a limited amount of data available for the inconel thruster: The first reason was that due to the lack of mounting points on the inconel thruster, it was difficult to mount thermocouples on the thruster body itself. The only location where measurements could be obtained somewhat easily was at the exterior throat. The second reason is that for this thruster there was an excessive amount of soot formation on the igniter. Because of this only a limited amount of successful tests was performed with this thruster. Most of these tests were short in duration with burn times of 1s or less, which makes them not very suitable for testing the model. For the inconel thruster the thermocouples were located at the exterior throat, the igniter, the spiral (which is used for the oxidiser line) and on one of the pressure sensor ports. For comparison with the model, only the exterior throat data can be used. The data gathered at the other points was however not useless as the data from the other points was required to check other points of interest. This will be discussed in more detail in chapter 5.

Table 4.8: Difference between model results and the results from the test data for the regeneratively cooled case

| Test number | $\mathbf{P_c}$ (average) | $\mathbf{T_{start}}$ | Burntime | Error Exterior Throat [%] |
|---|---|---|---|---|
| 7 (21-04-2020) | 0.92 | 0.96 | 1 | 0.80 |
| 10 (21-04-2020) | 0.94 | 1.17 | 1 | 0.47 |
| 13 (21-04-2020) | 0.97 | 0.95 | 3 | -1.46 |
| 17 (21-04-2020) | 0.98 | 1.2 | 5 | -6.03 |

From table 4.8 it becomes clear that also for the inconel thruster the model is accurate, at least at the exterior throat. It is also interesting to note that for the 1s burn times the model tends to overestimate the temperature slightly, while for the longer burn times the model underestimates the temperature. The overestimation at the start could perhaps be related to the delayed thermal response at the start of the burn as discussed in section 4.4.2. It could also be that the model error becomes more and more negative as burn time is increased, however this seems rather unlikely as this trend was not visible for the stainless steel case.

### 4.6.3. Summary of results & concluding remarks

In the previous sections validation of the model was performed. It was found that overall the model provides accurate results. For the radiation/heat-sink cooled case the model was accurate within 15% for all chamber pressures and starting temperatures which were investigated within the testing envelope for a 3 second burn time. For a burn time of 4 seconds the model results were also within a 15% agreement with the experimental data. For the 2s burn times a maximum error of 21.45% was found. However, the amount of test data available for comparison was limited for the 2s case, meaning that the fit to the data was less accurate. Most of the cases investigated also fell outside of the testing envelope. It is thus suspected that the larger error observed for the 2s burns is due to insufficient experimental data rather than a model error.

For the regenerative cooling case less test data was available. Nevertheless, cases were investigated with burn times ranging between 1 and 10 seconds, chamber pressures between 3.2 and 5.1 bar and starting temperatures between 22 and 39 °C. The model was also compared to the results from thrusters with two different wall materials: Stainless Steel and Inconel. For all cases investigated the error observed was within 10%.

It was seen that the transient thermal behaviour was predicted well during the burn. After shutdown of the thruster the transient behaviour was predicted well qualitatively, but not quantitatively: the trends were in agreement with the experimental data but the temperature values showed large differences. It was also shown that the maximum temperature rise after shutdown was usually underestimated for the hottest parts of the thruster, while it was overestimated for the colder parts of the thruster. This was compensated by using a reference temperature during the model calibration.

Overall the model was in good agreement with the experimental results. The model is therefore considered to be validated to a sufficient degree for the purposes of this study.

# 5
# Model Results and Discussion

With the model validated using experimental results, it now becomes possible to use the model to predict the thermal behaviour of the PM200 for extended burn times (>10s). In this chapter, the results from the model will be discussed. First the model results per cooling method will be discussed in section 5.1. Afterwards, in section 5.2 the different cooling methods will be compared based on the results found in section 5.1 and based on the experimental results from the tests described in chapter 4. In section 5.3 some additional considerations with respect to the model results will be discussed. In section 5.4 the implications of the results for the PM200 design will be explained. Furthermore, some additional observations that were made during testing that may impact the thermal design of the PM200 will also be discussed in this section. Lastly, in section 5.5 the results and conclusions from this chapter will be used to answer the research questions posed in chapter 2.

## 5.1. Results per cooling method

In this section the results calculated from the model for different cooling methods will be presented. The different cooling methods will be applied to the reference thruster design introduced in section 2.1.4. All cases presented were run on a 50x5 grid. For each case the simulation was executed for a burn time of 100s or until the steady state criterion was triggered, whichever came first. The steady state criterion was set at an average change in temperature over each cell of 0.1 K per 0.1s.

The final goal is to compare the different cooling methods. To make this comparison fair, a somewhat optimum design must be selected for each cooling method. Since these optimums are not known several different cases were simulated for each cooling method. For each case the input parameters were varied slightly. From this a rough estimate of the optimum design for each cooling method can be made. Furthermore, by simulating multiple different cases the influence of several design parameters can be determined. For the final comparison of all cooling methods the best case result for each cooling method is compared. It should be noted that for all regeneratively cooled cases presented stainless steel is used as the wall material unless explicitly stated otherwise.

It should be noted that in this section and in section 5.2 the program outcomes will be given in a large amount of significant digits (5), this is mainly done to illustrate small differences in outcomes for different designs and to show the effect of different design parameters. It should be noted that the program is not expected to provide values with an accuracy of 5 digits, therefore in the discussion following section 5.1 and 5.2 the numbers will be rounded off except in the case where direct comparisons are made.

Since the PM200 is constructed using additive manufacturing for the cases presented in this chapter some limitations of additive manufacturing were taken into account. Mainly the minimum print sizes that can be achieved. Modern additive manufacturing techniques allow for a printing accuracy between approximately 0.3 and 0.5 mm. Because of this, for all cases presented here the following minimum requirements were adhered to:

- **DA-PM200-MAN-001:** The minimum wall thickness shall be larger than or equal to 0.4 mm in all directions with the exception of the wall thickness for the ribs.
- **DA-PM200-MAN-002:** The minimum wall thickness of the ribs shall be larger than or equal to 0.3 mm in all directions.
- **DA-PM200-MAN-003:** The minimum coolant channel dimensions (diameter / height / width / length) shall be larger than or equal to 0.3 mm.

For the results presented below, the following format will be used: First all the results for the full length cooling channels will be given (i.e. cooling channels which run from the nozzle outlet to the injector), based on the observations from these results some results will be given for non-full length cooling channels (i.e. cooling channels which do not start at the nozzle, but at other axial positions along the thruster). For each of the cases a table with all simulated sub-cases will be given, within this table the maximum attained temperature within the thruster will be given as well as the maximum coolant temperature (if applicable). In some cases additional notes are also given. Besides these tables, five figures will be given: the first figure will show the maximum temperature obtained as a function of burn time for each case. This plot will be used as the main point of comparison between the different cases. Besides the maximum temperature plot, a plot will be given which displays the axial position were the maximum temperature occurs as a function of burn time. Ideally the maximum temperature occurs at a position where the thruster diameter is smaller or at a position near the nozzle outlet. This is because at these locations the hoop stress in the thruster is smallest. The maximum temperature location also gives information about how to improve the cooling channel design for the non full length cooling channels. Besides showing the maximum temperature obtained within the thruster, for the regeneratively cooled thrusters two plots are given which display the maximum obtained cooling temperature and the axial position within the cooling channel were this maximum temperature is obtained. Finally, for each group of simulated cases, a 2D temperature profile for the best case solution will be presented. For clarity, for the 2D temperature profiles the grid will be turned off with the exception of the grid lines which indicate the inner and outer contour of the engine and the grid lines indicating the cooling channel contour.

### 5.1.1. Radiation cooling/Heat-sink cooling

Four radiation cooled/heat-sink cooled cases were simulated. The main differences between the cases were the wall materials used. Two “regular” metal alloys were simulated and two refractory metals were simulated. The two “regular” metal alloys simulated were stainless steel and inconel, these two materials were selected because Dawn Aerospace has experience with these materials and because thrusters using these materials were also tested as discussed in chapter 4. For the refractory metals two materials were selected: Tantalum and Niobium. These materials were selected because they have favourable thermal properties: a high melting point and a relatively high thermal conductivity. They are also commonly used in aerospace applications. Typically Tantalum and Niobium are not used in their pure form, instead they are used in the form of an alloy comprised of either Tantalum or Niobium in combination with some other metal, for example Zirconium. These alloys have relatively similar thermal properties to the base materials (see for example [26]) and therefore the properties of the base materials were used for the simulations presented here. The results can be seen in table 5.1 and figure 5.1.

From figure 5.1 it can be seen that the temperature for all cases are relatively close. The refractory metals perform a little bit better overall, this can be explained by the fact that both of the refractory metals have a higher thermal conductivity compared to Stainless steel and

Table 5.1: Results Radiation cooled cases

| Wall material | Max temperature [K] |
|---|---|
| Stainless Steel | 1416.1 |
| Inconel | 1434.7 |
| Tantalum | 1358.2 |
| Niobium | 1355.1 |

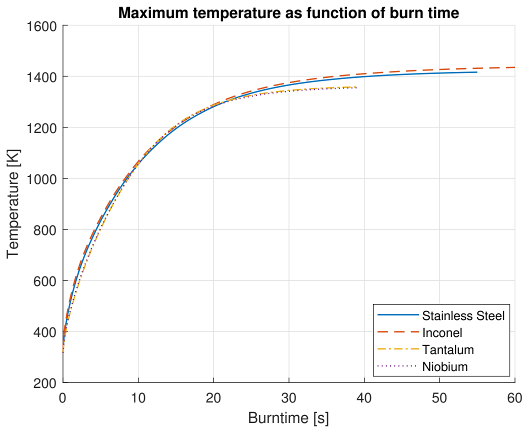


Figure 5.1: Maximum temperature as function of burn time. Radiation/Heat-sink cooled

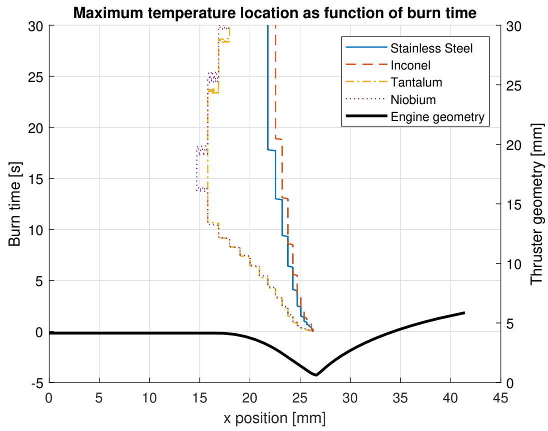


Figure 5.2: Location of the maximum temperature as function of burn time. Radiation/Heat-sink cooled

Inconel. The final temperatures are however still relatively close because Stainless steel and Inconel have a higher heat capacity compared to the refractory metals.

While the final temperatures are relatively close, it can be seen in figure 5.2 that the axial position of the maximum temperature is quite different for the refractory metals when compared to the non-refractory metals. For all cases the maximum temperature starts out at the nozzle throat, this is to be expected as at this location the heat transfer to the wall is highest. For the non-refractory metals the maximum temperature remains mostly close to the nozzle throat as the engine burns while for the refractory metals the maximum temperature location moves towards the entrance of the nozzle convergent. This can be explained by the fact that for the refractory metals the thermal conductivity is between two to three times higher. Because of this heat is conducted away more efficiently in the axial direction for the refractory metals. Since the nozzle divergent remains relatively cool, heat is conducted away from the throat towards the nozzle divergent, which causes the location of the maximum temperature point to shift more towards the combustion chamber. For the non-refractory metals this effect is smaller because the thermal conduction is less efficient in the axial direction.

The best result was obtained using the Niobium wall material, the 2D steady state temperature distribution for this case can be seen in figure 5.3. Note that the temperature scale here was reduced to a range of 270K-1600K compared to the temperature scale used for the results presented in chapter 3 which ran from 270K-2800K. This was done to allow for more contrast in the solution to ensure that trends can be identified more easily. In the remainder of this chapter this same reduced temperature scale will be used to allow for easy comparison between solutions. Even with the reduced temperature scale, at a first glance it appears that the temperature profile is constant in the radial direction, this is however not the case but is a result of the fact that the temperature difference in the wall is relatively small and therefore close to the resolution of the temperature scale used.

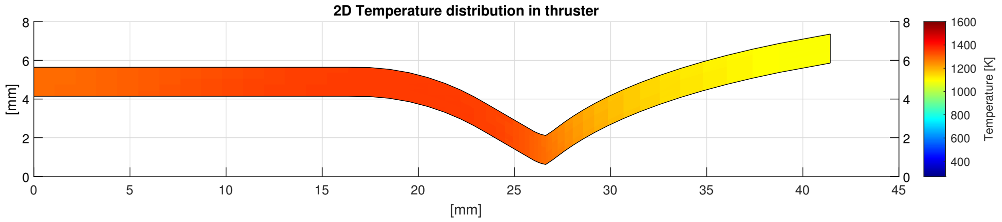


Figure 5.3: Steady state temperature distribution for the best Radiation/Heat-sink cooled case.

### 5.1.2. Regenerative - Cooling Sleeve

The first regeneratively cooled case that will be investigated is the case for an engine with a regenerative cooling sleeve. Initially three cases were simulated: a sleeve with a height “h” of 0.3 mm (the minimum sleeve height), 0.5 mm and 0.7 mm (maximum allowable sleeve height). These sizes were chosen because they represent the minimum and maximum printable sleeve heights while taking into account the requirements specified at the beginning of this chapter. An overview of the cases simulated can be seen in table 5.2.

Table 5.2: Results Regenerative Cooling - Sleeve

| h [mm] | Max temperature [K] | Max cooling fluid temperature [K] |
|---|---|---|
| 0.3 | 1228.4 | 1142.2 |
| 0.5 | 1274.6 | 1108.9 |
| 0.7 | 1344.8 | 1069.6 |

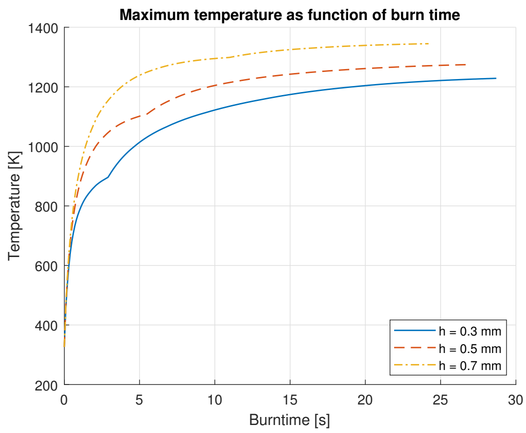


Figure 5.4: Maximum temperature as function of burn time. Regeneratively cooled - Sleeve

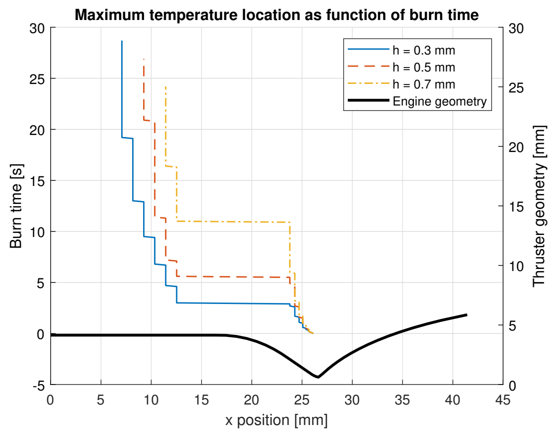


Figure 5.5: Location of the maximum temperature as function of burn time. Regeneratively cooled - Sleeve

From table 5.2 and figure 5.4 it can be seen that the case with a sleeve height of 0.3 mm performs best, reaching the lowest maximum temperature of 1228.4 K. This is perhaps not unexpected as for this design the coolant channel cross sectional area is lowest, leading to the highest flow velocity out of the cases simulated. This highest flow velocity leads to a high Reynolds number, which in turn leads to a high amount of heat transfer. This can also be seen in figure 5.6 where it can be seen that while the case with h = 0.3 mm has the lowest overall maximum temperature, it has the highest maximum coolant temperature.
The 2D steady state temperature distribution for the best case result (h = 0.3 mm) can be seen in figure 5.8. It can be seen that overall the temperatures are relatively low near the nozzle, indicating effective cooling. Furthermore, it can be seen that the highest temperatures occur near the injector. This is because near the injector the cooling fluid has heated up the most and therefore cooling is least effective here. It can also be seen that there is a relatively

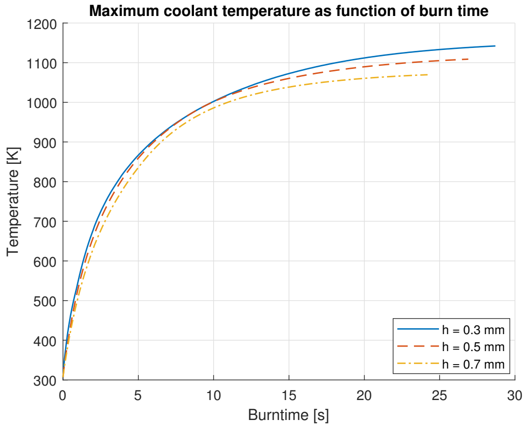


Figure 5.6: Maximum coolant temperature as function of burn time. Regeneratively cooled - Sleeve

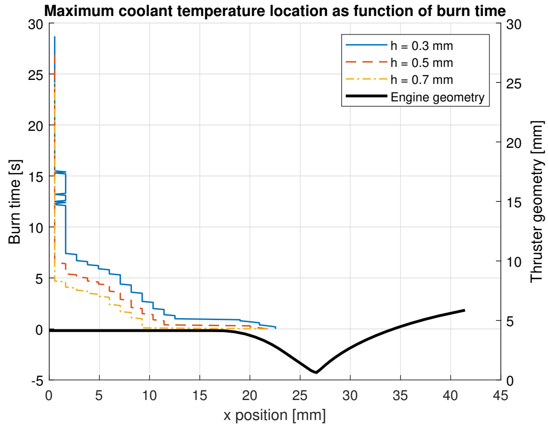


Figure 5.7: Location of the maximum coolant temperature as function of burn time. Regeneratively cooled - Sleeve

large temperature difference between the inner and outer wall, especially near the injector. Near the injector this temperature difference amounts to almost 290 K. It may be somewhat questionable whether or not this temperature drop is realistic over such a small distance. In reality there would likely be a significant amount of radiation heat transfer between the inner and outer wall. This effect was however not included in the model. In reality the inner wall would thus likely become somewhat colder and the outer wall would become somewhat hotter.

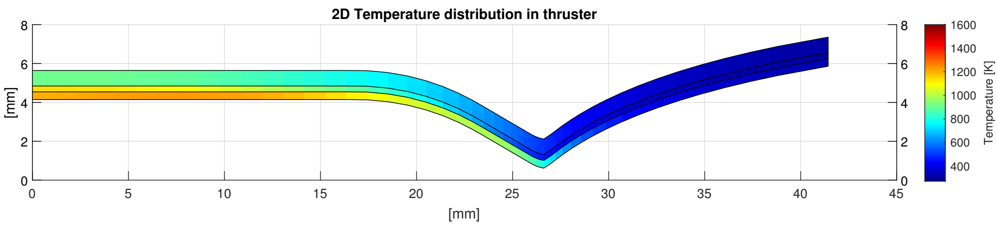


Figure 5.8: Steady state temperature distribution for a Regenerative cooling sleeve with h = 0.3 mm

From figures 5.6 and 5.8 it can be seen that the temperature of the coolant and the wall material near the injector is relatively high. According to Karabeyoglu et al. [16] at high pressures (40 bar and above) Nitrous Oxide decomposition starts occurring at roughly 850 K. At first these reactions occur slowly with typical decomposition times of around $10^4$ s. The typical decomposition time decreases exponentially as temperatures increase. At around 1100 K (at 40 bar) the typical decomposition time is in the order of seconds and at a temperature of around 1500 K (at 40 bar) the typical decomposition time is in the order of milliseconds [16]. Typical residence times for the coolant in the coolant channel are approximately between 12 and 30 milliseconds for the coolant sleeve designs considered here. At lower pressures, such as those which are likely to occur inside the cooling channel, reaction rates are even lower [16]. Temperatures are thus not necessarily high enough for coolant decomposition to occur at appreciable rates high enough to cause problems for the thruster. The temperatures observed are however somewhat close to the limit. Ideally the coolant temperature and the wall temperature would be decreased somewhat further.

Since the divergent part of the nozzle is still relatively cool, the cooling channel design could be improved by moving the cooling channel inlet closer towards the injector. This way the coolant temperature will be lower near the injector leading to better cooling. The nozzle temperature will increase in this case, however this is not necessarily a large problem as the heat transfer to the nozzle is relatively small.

Four different cases were simulated with the cooling channel inlet located at 29 mm, 26.5 mm, 24.5 mm and 22 mm respectively. These locations were selected using the following reasoning: the 29 mm case was selected because looking at figure 5.8 it can be seen that this is the first location were a large increase in temperature can be seen, by placing the cooling channel inlet at this location all of the parts which see a large amount of heat transfer are still cooled. The 26.5 mm case was selected because in this case the cooling channel starts at the throat. In this case the region which sees the highest heat transfer thus has optimal cooling. The last cases at 24.5 and 22 mm were selected because for these cases the coolant doesn't have to cool the throat, this results in a lower amount of heat transfer to the coolant meaning that better cooling is achieved in the chamber and at the injector. The nozzle throat is not cooled in this case even though the highest heat flux occurs here. The idea behind this approach is however that, because the chamber is better cooled in this case, the heat at the nozzle throat can be transferred in the axial direction more easily by conduction, which will still lead to a reduction in temperature in the nozzle throat. In this case the average temperature over the entire thruster body will rise, but the maximum temperature may decrease; the temperature is just spread out more evenly over the entire thruster body.

The results of the simulations with a shorter length cooling channel are shown in table 5.3, with the parameter L indicating the axial coordinate of the coolant inlet. The best case for the full length channel is also included.

Table 5.3: Results Regenerative Cooling - Sleeve - Variable inlet conditions

| h [mm] | L [mm] | Max temperature [K] | Max cooling fluid temperature [K] |
|---|---|---|---|
| 0.3 | 41.43 (full length) | 1228.4 | 1142.2 |
| 0.3 | 29 | 1213.1 | 1129.1 |
| 0.3 | 26.5 | 1157.5 | 1075.1 |
| 0.3 | 24.5 | 1149.4 | 1067.2 |
| 0.3 | 22 | 1185.8 | 1026 |

The results presented in table 5.3 indicate that the sleeve with the inlet coordinate at L = 24.5 gives the best cooling performance. This design reduces the maximum wall temperature by 79 K compared to the full length cooling sleeve running all the way from the nozzle. In reality the true optimum design likely lies somewhere in between L = 24.5 and L = 22 mm. This becomes clear when looking at figures 5.9 and 5.10. It can be seen that the results for the L = 24.5 and L = 22 mm are relatively close, for approximately the first 30 seconds the L = 22 mm design even performs better. What is most interesting to note is that for the L = 22 mm design the location of the maximum temperature shifts from the throat to somewhere in the chamber and eventually back to the throat again. This indicates that the cooling channel is just a little bit too close towards the injector as the nozzle throat becomes warmer than the chamber again after some time. The optimal design would be if the maximum temperature in the nozzle throat would be exactly equal to the maximum temperature in the chamber. This can be seen more clearly in figure 5.11 where the wall temperature profile at steady state is plotted for the inner wall for the cases with L = 24.5 and L = 22 mm.

Another observation that can be made is that by changing the cooling channel inlet position, the transient can be extended by approximately 15 seconds. For the case where the sleeve ran all the way from the nozzle to the injector all cases reached the steady state within 30 seconds, while for the cases with the modified cooling inlets some cases take almost 45 seconds to reach the steady state.

In figure 5.11 it can be seen that the optimum case is in between the cases for L = 24.5 and L = 22 mm. It can be seen that for the L = 24.5 mm case the chamber temperature is higher than it has to be while it can also be seen that for the L = 22 mm case the throat temperature is higher than it has to be. Both solutions are however relatively close to the optimum, so the case for L = 24.5 mm will be taken as the optimum case for comparison of all cooling methods.

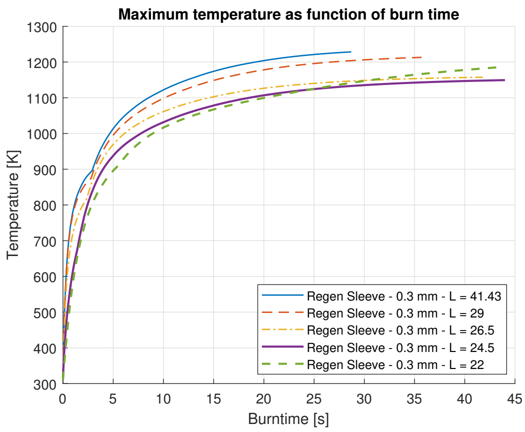


Figure 5.9: Maximum temperature as function of burn time. Regeneratively cooled - Sleeve - Variable inlet condition

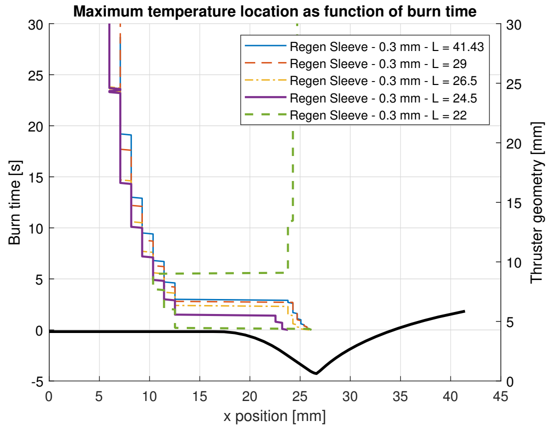


Figure 5.10: Location of the maximum temperature as function of burn time. Regeneratively cooled - Sleeve - Variable inlet condition

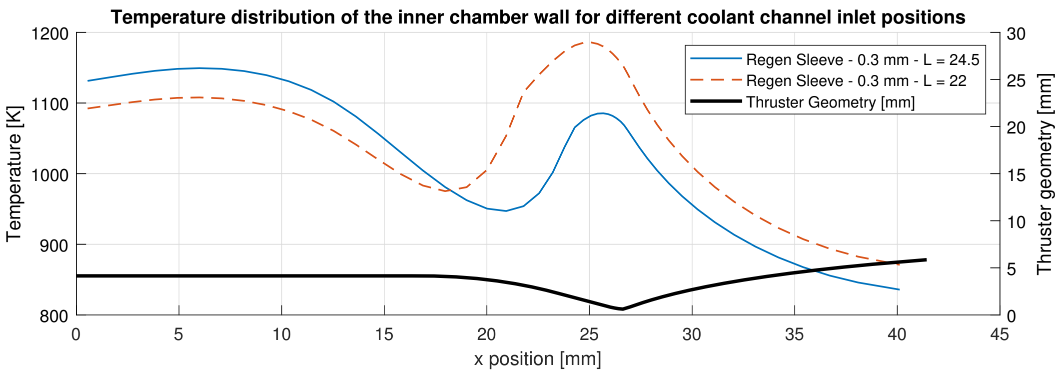


Figure 5.11: Steady state temperature distribution of the inner wall for different cooling sleeve lengths

The best case temperature distribution for the cases with variable cooling inlets is plotted in figure 5.12. It becomes clear that the temperature near the chamber and the injector is reduced while the temperature in the nozzle has increased.

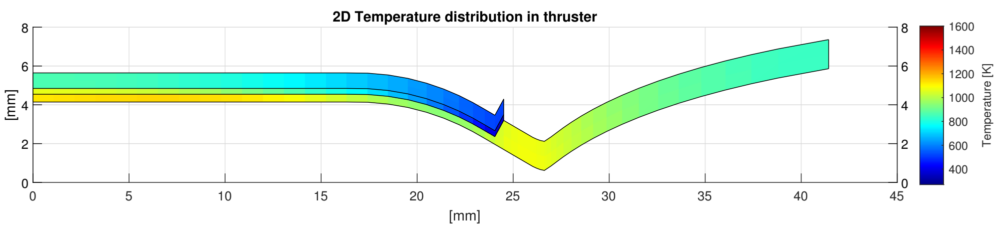


Figure 5.12: Steady state temperature distribution for a Regenerative cooling sleeve with h = 0.3 mm and L = 24.5 mm

### 5.1.3. Regenerative - Multiple channels Axial

For the regenerative cooling case with axial channels 12 cases were simulated. The cases simulated had the following characteristics: channel heights (indicated by h in table 5.4) were varied between 0.3, 0.5 and 0.7 mm. The amount of cooling channels was varied between 3, 5, 8 and 10 cooling channels (indicated by N in table 5.4). The channel cross sections were taken to be square except for some cases where this would not fit. This occurred for the cases where the height was between 0.5 and 0.7 mm and where 8 or more channels were used. For these cases the channel width (indicated by $w_c$ in table 5.4) was set to 0.3 mm in order to not violate requirement DA-PM200-MAN-002. It may be that having non-square channels would result in better cooling performance, such cases will however not be considered here to keep the amount of cases to be simulated somewhat manageable. The results can be seen in table 5.4.

Table 5.4: Results Regenerative Cooling - Axial (multiple channels)

| h [mm] | $w_c$ [mm] | N [-] | Max temperature [K] | Max cooling fluid temperature [K] |
|---|---|---|---|---|
| 0.3 | 0.3 | 3 | 1105.3 | 1098.8 |
| 0.3 | 0.3 | 5 | 1106.5 | 1100.5 |
| 0.3 | 0.3 | 8 | 1108.2 | 1102.1 |
| 0.3 | 0.3 | 10 | 1108.6 | 1101.5 |
| 0.5 | 0.5 | 3 | 1098.8 | 1088.9 |
| 0.5 | 0.5 | 5 | 1101.2 | 1092.1 |
| 0.5 | 0.5 | 8 | 1102.4 | 1093.9 |
| 0.5 | 0.3 | 10 | 1107 | 1100.2 |
| 0.7 | 0.7 | 3 | 1094 | 1080.1 |
| 0.7 | 0.7 | 5 | 1096.6 | 1084.2 |
| 0.7 | 0.3 | 8 | 1105.6 | 1097.8 |
| 0.7 | 0.3 | 10 | 1108 | 1091.1 |

From table 5.4 it can be seen that there is little difference between the results from each case. Contrary to what was the case for the sleeve design, for the axial cooling channels the best performing design is the design with the largest cooling channel cross sectional areas: 0.7x0.7 mm. It can also be seen that for each given cooling channel cross sectional area the case with the least amount of cooling channels (3) performs best. To keep the graphs somewhat readable, only the best cases for each given cooling channel cross sectional area are compared in figure 5.13. Again it can be seen in figure 5.14 that the maximum temperature occurs close to the injector; a little bit before the middle of the combustion chamber.

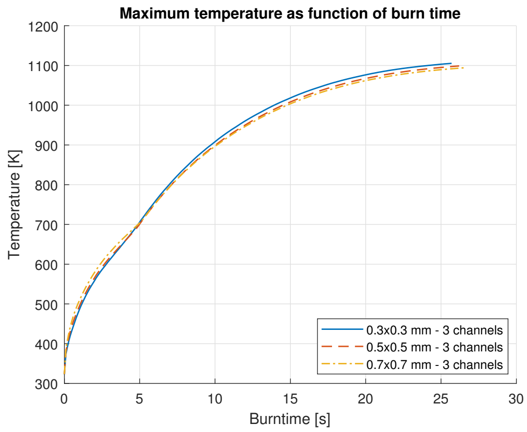


Figure 5.13: Maximum temperature as function of burn time. Regeneratively cooled - Axial (best cases)

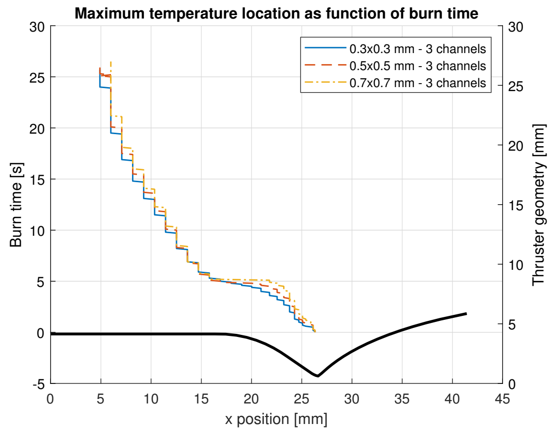


Figure 5.14: Location of the maximum temperature as function of burn time. Regeneratively cooled - Axial (best cases)

Also contrary to what was the case for the sleeve design, in figure 5.15 it can be seen that for the best axial case, the coolant temperature is the lowest out of the compared temperatures. The maximum coolant temperature also occurs closest to the injector as can be seen in figure 5.16.

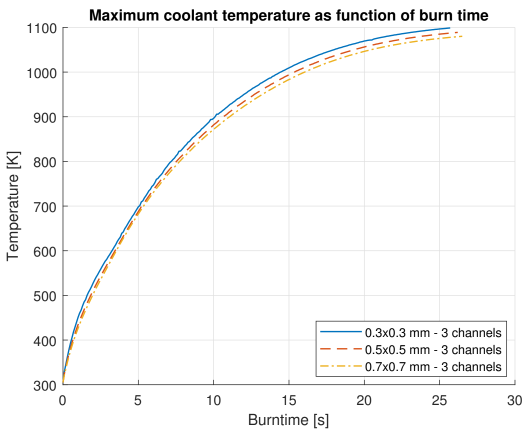


Figure 5.15: Maximum coolant temperature as function of burn time. Regeneratively cooled - Axial (best cases)

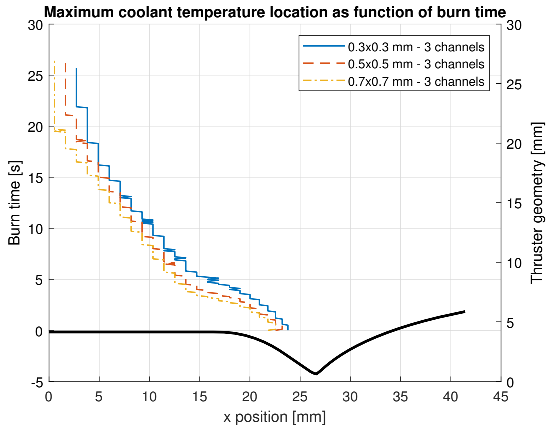


Figure 5.16: Location of the maximum coolant temperature as function of burn time. Regeneratively cooled - Axial (best cases)

The results discussed previously at first seem somewhat counter intuitive. However there is a relatively simple explanation for them. There are several effects going on: If more channels are present, the coolant velocity decreases, leading to less heat transfer to the coolant. At the same time, when more channels are present the total surface area in contact with the coolant increases, leading to an increase in heat transfer to the coolant. This second effect appears to be dominant, with more channels leading to an increase in coolant temperature (see table 5.4). Furthermore, for cases with smaller coolant channel cross sectional areas the coolant surface area is smaller leading to a reduction in heat transfer, however due to the smaller cross sectional area the coolant also has a higher flow velocity. This also leads to a net increase in heat transfer. Normally an increase in heat transfer to the coolant is beneficial. However in this case the coolant temperature is already so high that increasing the heat transfer to the coolant only reduces the cooling ability of the coolant near the end of the cooling channel. Since the highest wall temperatures are observed near the end of the channel, the best performing case is thus the one where the coolant heats up the least amount, as this leads to the best cooling performance near the injector and combustion chamber.

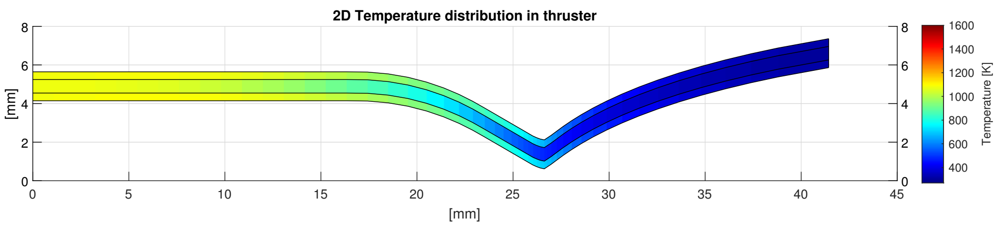


Figure 5.17: Steady state temperature distribution for the best case engine with Regenerative cooling - Axial, 0.7x0.7mm - 3 channels

Again it is possible to change the location of the cooling channel inlet. The same inlet positions as for the regenerative cooling sleeve were simulated. The results can be seen below in table 5.5.

It can be seen that the case with the coolant inlet at L = 24.5 mm performs best. It however does not perform better than the case with a cooling channel along the full length of the combustion chamber and nozzle (although the results are close). Although the case with L = 24.5 mm does not achieve a maximum temperature lower than the case with the cooling channel along the full length of the thruster, it can be seen in figure 5.18 that the L = 24.5 mm case

Table 5.5: Results Regenerative Cooling - Axial (multiple channels) - Variable inlet conditions

| h [mm] | $w_c$ [mm] | N [-] | L [mm] | Max temperature [K] | Max cooling fluid temperature [K] |
|---|---|---|---|---|---|
| 0.7 | 0.7 | 3 | 41.43 (full length) | 1094 | 1080.1 |
| 0.7 | 0.7 | 3 | 29 | 1109.6 | 1095.9 |
| 0.7 | 0.7 | 3 | 26.5 | 1114.6 | 1100.9 |
| 0.7 | 0.7 | 3 | 24.5 | 1095.1 | 1081.1 |
| 0.7 | 0.7 | 3 | 22 | 1172.3 | 1055.4 |

does heat up slower. The L = 24.5 mm case takes approximately 18 seconds longer to reach steady state compared to the case with a cooling channel running along the full length of the nozzle.

It should be noted that the L = 24.5 mm case does not have the most optimum cooling inlet position possible. It is therefore possible that by shifting the cooling inlet somewhat a better case could be found which has both a lower final maximum temperature and a slower start up transient when compared to the case with the full length cooling channel. Furthermore, it should be noted that the cases presented here were based on the optimum case for the full length of the nozzle with h = 0.7, $w_c$ = 0.7 and N = 3. These parameters were however only considered the optimal ones because they lead to the least amount of heating of the cooling fluid which in turn lead to low temperatures near the injector and the combustion chamber. If the cooling channel inlet is moved beyond the nozzle throat, this may not be the most optimal configuration anymore. It could be that for this case it is more beneficial to have better heat transfer to the cooling fluid. Further optimisation may thus be possible. Such optimisation is however beyond the scope of this study and therefore in this report the case with L = 24.5 mm presented above and the full length case will be taken as the two best cases. The steady state temperature distribution for the case with L = 24.5 mm can be seen in figure 5.20.

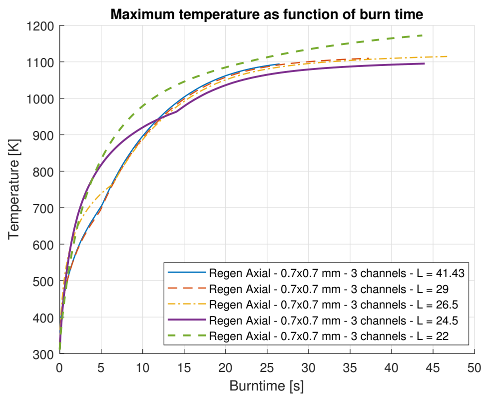


Figure 5.18: Maximum temperature as function of burn time. Regeneratively cooled - Axial - Variable inlet condition

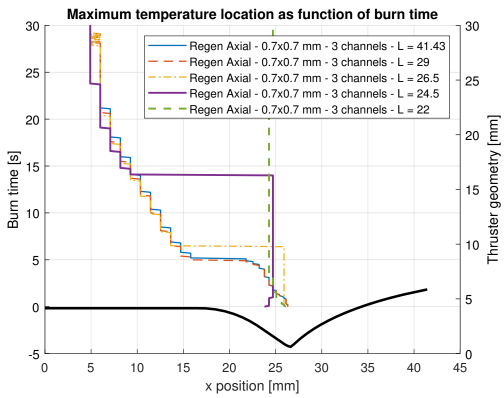


Figure 5.19: Location of the maximum temperature as function of burn time. Regeneratively cooled - Axial - Variable inlet condition

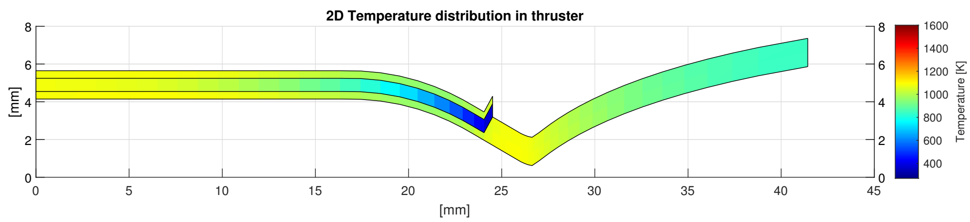


Figure 5.20: Steady state temperature distribution for the best case engine with Regenerative cooling - Axial, 0.7x0.7mm - 3 channels - L = 24.5 mm

### 5.1.4. Regenerative - Helical channels

For the regenerative cooling channel design with helical channels, 35 different cases were simulated. The following parameters were varied: two different channel cross sectional areas were simulated; 0.5x0.5 mm and 0.7x0.7 mm. Channels with a cross sectional area of 0.3x0.3 mm were not simulated as it was found that for these cases the pressure drop was too high for the motor to operate. The number of channels (N) was varied between 1, 3, 5 and 8 channels, and the amount of helices ($N_\Lambda$) was varied between 1, 2, 4, 6 and 8 helices. The results can be seen below in table 5.6. For designs with four or more helices it can be seen that for the cases with a single 0.5x0.5 mm cooling channel the pressure drop was too high for the engine to run until steady state. Although intermediate results were obtained (before the steady state was reached), these results were not included to avoid confusion.

Table 5.6: Results Regenerative Cooling - Helical

| **h [mm]** | **$w_c$ [mm]** | **N [-]** | **$N_\Lambda$ [-]** | **Max temperature [K]** | **Max cooling fluid temperature [K]** | **Notes** |
|---|---|---|---|---|---|---|
| 0.5 | 0.5 | 1 | 1 | 1096.1 | 1086.1 | |
| 0.5 | 0.5 | 1 | 2 | 1101.3 | 1094 | |
| 0.5 | 0.5 | 1 | 4 | N/A | N/A | Pressure drop too high. |
| 0.5 | 0.5 | 1 | 6 | N/A | N/A | Pressure drop too high. |
| 0.5 | 0.5 | 1 | 8 | N/A | N/A | Pressure drop too high. |
| 0.5 | 0.5 | 3 | 1 | 1101.6 | 1093.3 | |
| 0.5 | 0.5 | 3 | 2 | 1107.5 | 1099.4 | |
| 0.5 | 0.5 | 3 | 4 | 1110.8 | 1106.1 | |
| 0.5 | 0.5 | 3 | 6 | 1112.3 | 1107.9 | |
| 0.5 | 0.5 | 3 | 8 | 1116.9 | 1110.8 | |
| 0.5 | 0.5 | 5 | 1 | 1104 | 1096.4 | |
| 0.5 | 0.5 | 5 | 2 | 1108.7 | 1102.5 | |
| 0.5 | 0.5 | 5 | 4 | 1115.5 | 1110.5 | |
| 0.5 | 0.5 | 5 | 6 | 1117.4 | 1112.8 | |
| 0.5 | 0.5 | 5 | 8 | 1119.6 | 1114.3 | |
| 0.5 | 0.5 | 8 | 1 | 1105.3 | 1097.9 | |
| 0.5 | 0.5 | 8 | 2 | 1109.8 | 1103.8 | |
| 0.5 | 0.5 | 8 | 4 | 1116.2 | 1111.1 | |
| 0.5 | 0.5 | 8 | 6 | 1121.4 | 1116.3 | |
| 0.5 | 0.5 | 8 | 8 | 1125.2 | 1119.9 | |
| 0.7 | 0.7 | 1 | 1 | 1090.3 | 1076.7 | |
| 0.7 | 0.7 | 1 | 2 | 1096.8 | 1087.6 | |
| 0.7 | 0.7 | 1 | 4 | 1107.7 | 1101.6 | |
| 0.7 | 0.7 | 1 | 6 | 1112.4 | 1107.2 | |
| 0.7 | 0.7 | 1 | 8 | 1113.7 | 1108.9 | |
| 0.7 | 0.7 | 3 | 1 | 1097.1 | 1086.2 | |
| 0.7 | 0.7 | 3 | 2 | 1103.3 | 1095.2 | |
| 0.7 | 0.7 | 3 | 4 | 1112.5 | 1106.2 | |
| 0.7 | 0.7 | 3 | 6 | 1122.3 | 1113.8 | |
| 0.7 | 0.7 | 3 | 8 | 1123.6 | 1118 | |
| 0.7 | 0.7 | 5 | 1 | 1100 | 1089.9 | |
| 0.7 | 0.7 | 5 | 2 | 1106.3 | 1098.4 | |

| | | | | | | |
|---|---|---|---|---|---|---|
| 0.7 | 0.7 | 5 | 4 | 1115.4 | 1109 | |
| 0.7 | 0.7 | 5 | 6 | 1127 | 1117.4 | |
| 0.7 | 0.7 | 5 | 8 | 1125.2 | 1118.9 | |

In figure 5.21 the maximum temperatures can be seen for several different cases. Due to the large number of simulations performed, only the best cases are shown for each given cross sectional area and for each number of cooling channels. The cases which are plotted are highlighted in light green in table 5.6. It can be seen that the cases with a single helix give the best results for every number of cooling channels and for all coolant channel cross sections. The explanation for this result is similar to the explanation for why less cooling channels perform better than having more cooling channels. The heat transfer to the coolant is simply so high that the coolant becomes too hot near the end of the cooling channel near the injector where the maximum wall temperature occurs (see figure 5.22). It would therefore actually be beneficial to reduce the heat transfer to the coolant so that better cooling is achieved near the end of the channel. Counter intuitively, the design which is the worst in transferring heat to the coolant is thus the best design in terms of overall maximum temperature reached. In such a design an increase in temperature at the nozzle (throat) and start of the combustion chamber is allowed in favour of reducing the temperature near the injector.

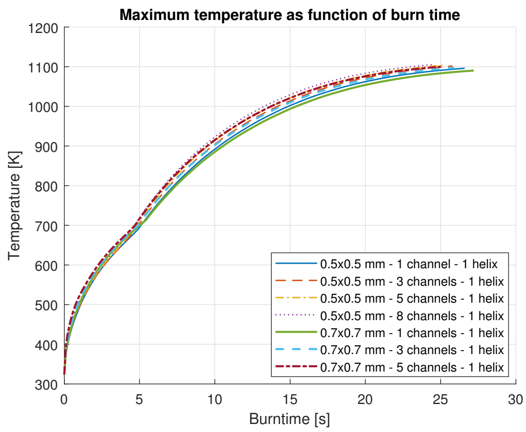


Figure 5.21: Maximum temperature as function of burn time. Regeneratively cooled - Helical (best cases)

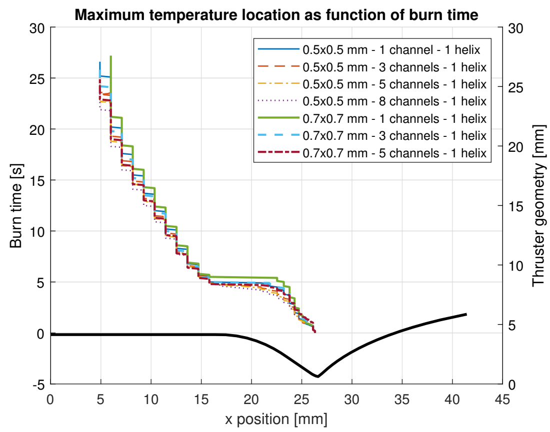


Figure 5.22: Location of the maximum temperature as function of burn time. Regeneratively cooled - Helical(best cases)

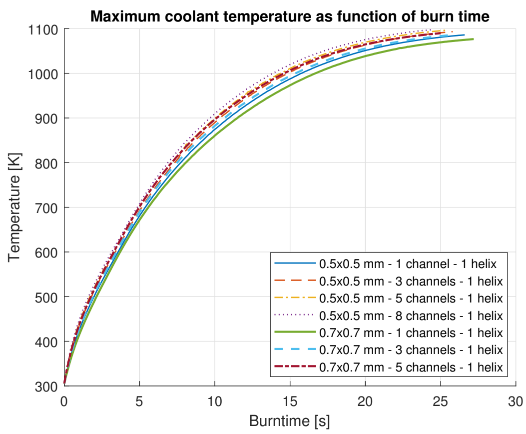


Figure 5.23: Maximum coolant temperature as function of burn time. Regeneratively cooled - Helical (best cases)

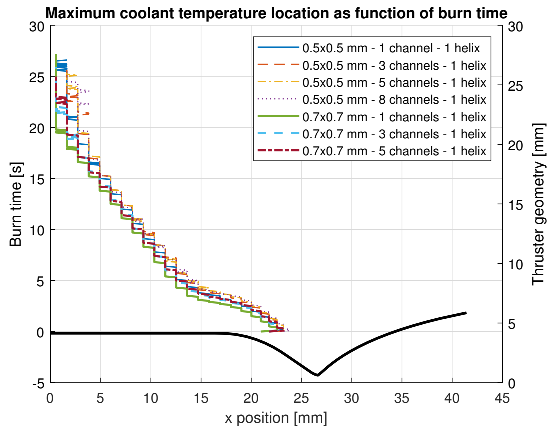


Figure 5.24: Location of the maximum coolant temperature as function of burn time. Regeneratively cooled - Helical (best cases)

In figure 5.25 the best case result for the helical channels can be seen. Note that in this plot a 2D projection of the helical channel is shown, in reality the channel wraps around the thruster. This design consists of a single cooling channel with a cross section of 0.7x0.7 mm, the cooling channel has a single helix. The similarities between figure 5.25 and figure 5.17 are immediately clear. This is perhaps also not surprising as both designs are quite similar. The extra heat transfer which is present in the axial case due to 3 channels being present is compensated by the additional cooling channel length present in the helical channel case.

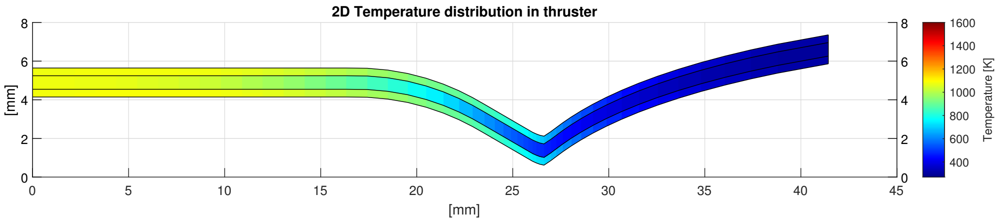


Figure 5.25: Steady state temperature distribution for the best case engine with Regenerative cooling - Helical, 0.7x0.7mm - 1 channel - 1 helix

For the optimal channel design it was again investigated if varying the inlet position would be beneficial. The results can be seen below in table 5.7. It should be noted that for each of the cases presented here the helix pitch $\Lambda$ was modified such that exactly one helix was completed between the cooling channel inlet and the injector.

Table 5.7: Results Regenerative Cooling - Axial (multiple channels) - Variable inlet conditions

| h [mm] | $w_c$ [mm] | N [-] | $N_\Lambda$ [-] | L [mm] | Max temperature [K] | Max cooling fluid temperature [K] |
|---|---|---|---|---|---|---|
| 0.7 | 0.7 | 1 | 1 | 41.43 (full length) | 1090.3 | 1076.7 |
| 0.7 | 0.7 | 1 | 1 | 29 | 1107.1 | 1095.9 |
| 0.7 | 0.7 | 1 | 1 | 26.5 | 1106 | 1100 |
| 0.7 | 0.7 | 1 | 1 | 24.5 | 1096.2 | 1086.4 |
| 0.7 | 0.7 | 1 | 1 | 22 | 1152.6 | 1071.9 |

From table 5.7 and figure 5.26 it can be seen that for the helical channel case the results and the trends observed are similar to the results for the axial case. Again none of the solutions are better than the full length channel although the case for L = 24.5 mm comes close. Furthermore just as was the case for the axial channels it can be seen that while the case for L=24.5 has a slightly higher maximum temperature, the time to reach the steady state is almost 25 seconds longer. It can also be seen in figure 5.27 that the behaviour of the location of the maximum temperature is almost identical to the behaviour observed for the axial cooling channel case.

The steady state temperature distribution for the best case result with L = 24.5 can be seen in figure 5.28. Again the similarities with the axial case are clear (see figure 5.20).

### 5.1.5. Radiation cooling/Heat-sink cooling & TBC

Both Radiation/Heat-sink cooling and Regenerative cooling performance can be enhanced by adding a TBC. In this section the simulation results for a Radiation/Heat-sink cooled engine with a TBC will be presented. Three different coating thicknesses were simulated: 0.1 mm, 0.2 mm and 0.3 mm. The coating simulated was Yttria-stabilized zirconia (YSZ). The results are shown in table 5.8. The parameter $t_{TBC}$ indicates the coating thickness.

As can be seen in table 5.8 and figure 5.29 the thickest coating leads to the lowest wall temperature as expected. However for the thick coatings the maximum TBC temperature is also higher. For YSZ, the maximum operating temperature is approximately 1473 K (1200°C). All

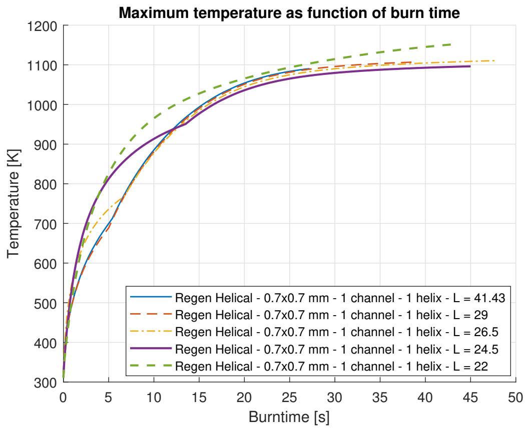


Figure 5.26: Maximum temperature as function of burn time. Regeneratively cooled - Helical - Variable inlet condition

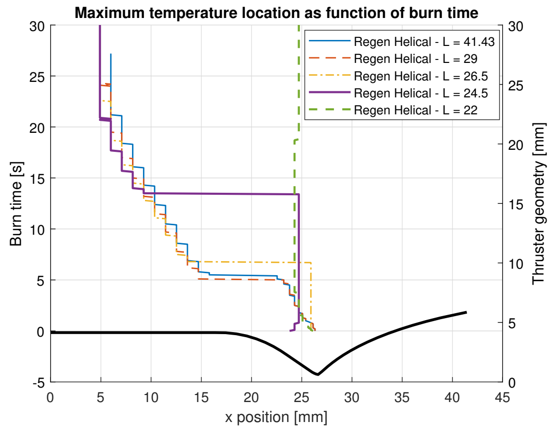


Figure 5.27: Location of the maximum temperature as function of burn time. Regeneratively cooled - Helical - Variable inlet condition

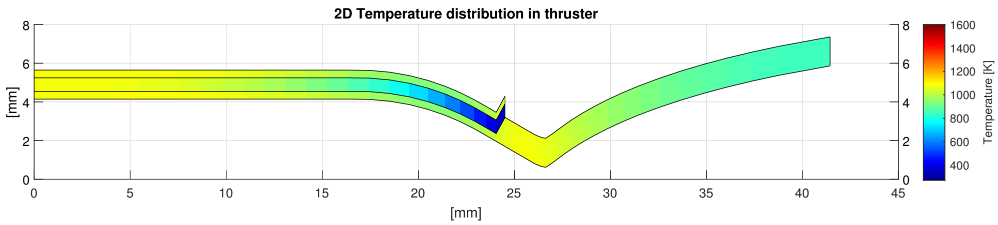


Figure 5.28: Steady state temperature distribution for the best case engine with Regenerative cooling - Helical, 0.7x0.7mm - 1 channel - 1 helix - L = 24.5 mm

Table 5.8: Results TBC + Radiation/Heat-sink cooling

| $t_{TBC}$ [mm] | Max wall temperature [K] | Max TBC temperature [K] |
|---|---|---|
| 0.1 | 1381.7 | 1463.8 |
| 0.2 | 1368.1 | 1481.9 |
| 0.3 | 1355.8 | 1493.9 |

cases are close to this value with the maximum difference being less than 21 K. The only case that falls below the limit of 1473 K is the case with a 0.1 mm coating thickness.

Looking at the locations where the maximum temperatures occurred in the wall and the coating in figures 5.30 and 5.32 some interesting observations can be made. It can be seen that for the TBC the maximum temperature always occurs in the nozzle throat. This makes sense as the heat flux in the nozzle throat is highest. Because the thermal conductivity of the TBC is very low (1.5 W/mK), there is almost no heat transfer in the axial direction. Because of this, the location of the maximum temperature in the TBC does not shift in the axial direction and stays in the nozzle throat. For the wall material a bigger shift is seen in the location of the maximum temperature. This is because due to the TBC the divergent part of the nozzle stays relatively cool. This allows for more heat to be conducted away from the nozzle throat, shifting the maximum temperature point more towards the combustion chamber. This can also be seen in figure 5.33.

Since the case with the 0.1 mm coating was the only case which didn't exceed the maximum operating temperature of the TBC (although barely), this case will be taken as the best case. The result can be seen in figure 5.33.

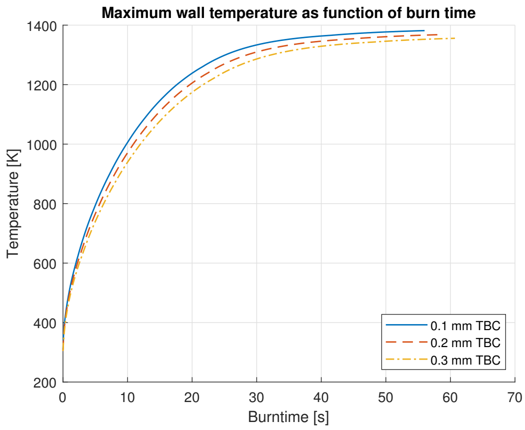


Figure 5.29: Maximum coolant temperature as function of burn time. Regeneratively cooled - Axial (best cases)

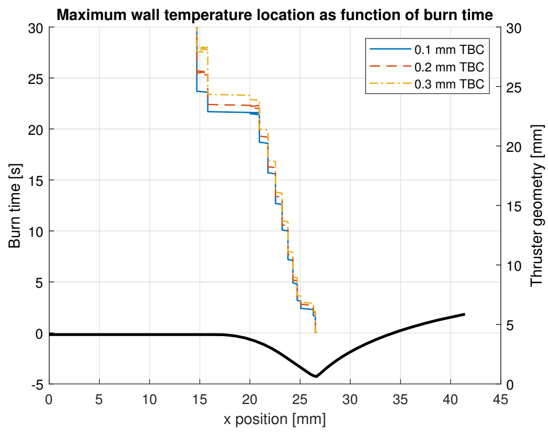


Figure 5.30: Location of the maximum coolant temperature as function of burn time. Regeneratively cooled - Axial (best cases)

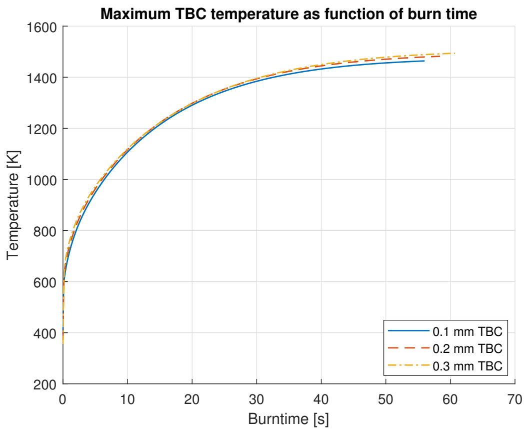


Figure 5.31: Maximum TBC temperature as function of burn time

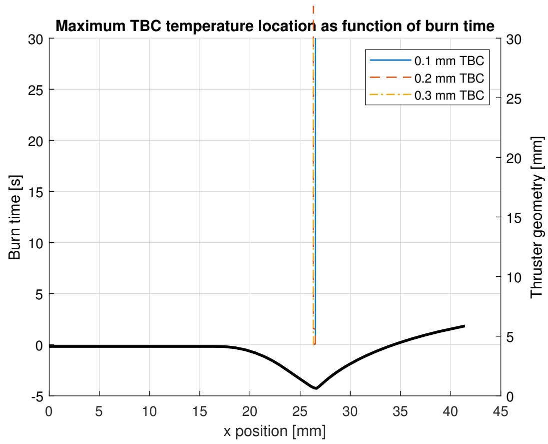


Figure 5.32: Location of the maximum TBC temperature as function of burn time

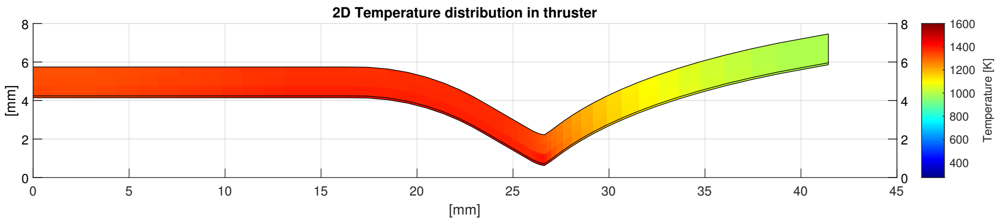


Figure 5.33: Steady state temperature distribution for the best case engine with Radiation/Heat-sink cooling and a TBC

### 5.1.6. Regenerative cooling & TBC

The last case considered is the case with Regenerative cooling in combination with a Thermal Barrier Coating. The best cases for each of the different regenerative cooling cases were selected and a 0.1 mm YSZ TBC was added. The simulation results can be seen below in table 5.9.

Table 5.9: Results TBC + Regenerative cooling

| h [mm] | $w_c$ [mm] | N [-] | $N_\Lambda$ [-] | $t_{TBC}$ [mm] | Max wall temp [K] | Max TBC temp [K] | Max coolant temp [K] |
|---|---|---|---|---|---|---|---|
| 0.3 | (Sleeve) | (Sleeve) | (Sleeve) | 0.1 | 1222.5 | 1235.2 | 1137 |
| 0.7 | 0.7 | 3 | (Axial) | 0.1 | 1095.9 | 1107.4 | 1081.1 |
| 0.7 | 0.7 | 1 | 1 | 0.1 | 1092.9 | 1104.1 | 1078.4 |

It can be seen from table 5.9 and figure 5.34 that for the regeneratively cooled case the TBC seems to have little effect. The maximum temperature is decreased only slightly for the regenerative cooling sleeve and for the other cases the temperature is even slightly higher. This second result is somewhat strange and is a result of the way the model was set-up. For all previous cases presented in this chapter a 50x5 mesh was used. For the regenerative cooling + TBC case 5 mesh cells in the radial direction were however insufficient to model both a TBC and a cooling channel. Therefore a 50x8 mesh was used for the simulations results presented here. Due to this change in mesh the centroid locations changed slightly resulting in the temperatures being evaluated at slightly different locations. Because of this the final results gave a slightly higher temperature result as the case without a TBC although in reality this is likely not the case. These results do however show that the reduction in temperature achieved by using the TBC is only small as it is even smaller than the model error. Combining this with the fact that the transient also has approximately the same duration as for the case without the coating it can be concluded that there is little benefit of adding a TBC. It can be seen that when a TBC is added the maximum temperature also occurs at approximately the same location as for the case without a TBC as can be seen in figure 5.35. It appears that the effect of the cooling channel is just much more influential than the effect of the TBC. While the heat flux into the inner wall and the coolant fluid is reduced due to the TBC, the heat transfer through the cooling fluid is a more dominant factor resulting in only a small reduction of the maximum observed temperature.

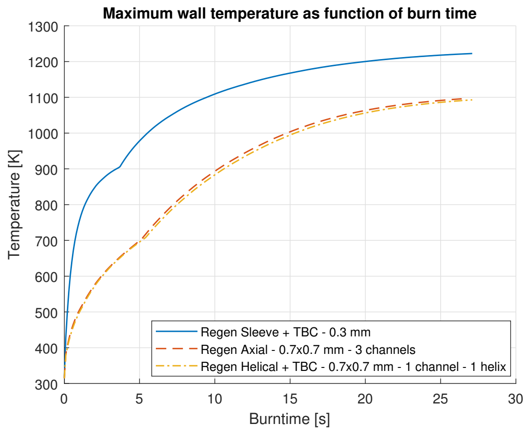


Figure 5.34: Maximum wall temperature as function of burn time. Regeneratively cooled + TBC

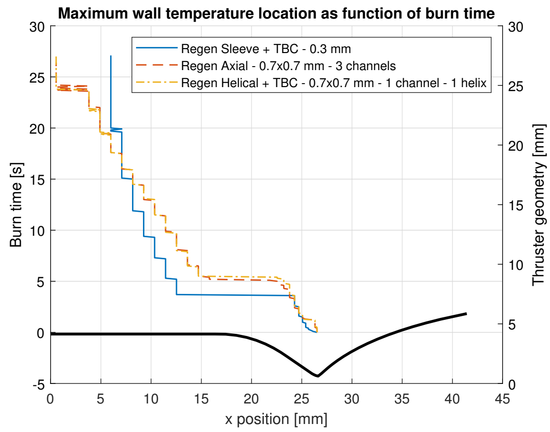


Figure 5.35: Location of the maximum wall temperature as function of burn time. Regeneratively cooled + TBC

The best case result for the combination of Regenerative cooling and a TBC can be seen below in figure 5.36. The similarities with the result from the case without the TBC are immediately noticeable when comparing figure 5.36 to figure 5.25.

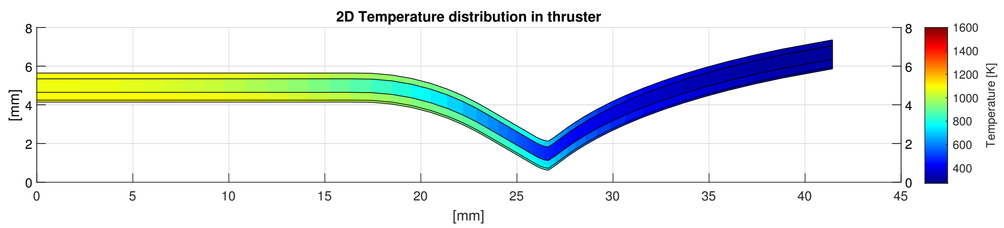


Figure 5.36: Steady state temperature distribution for the best case engine with Regenerative cooling and a TBC

## 5.2. Comparison of cooling methods

In this section each of the different cooling methods will be compared. Two different methods will be used for comparing the cooling methods. First, the results from the model will be compared for the reference engine. Secondly, the results from the tests described in chapter 4 will also be compared.

### 5.2.1. Model comparison

To compare the different cooling methods, the best case results for each of the cooling methods will be used to represent that particular cooling method. One exception to this is the Radiation/Heat-sink case. Although the lowest temperatures for this case were achieved by the thruster with a Niobium wall material, for the radiation/heat-sink cooled case the stainless steel case will be used. This is because for all other cooling methods stainless steel was taken as the wall material. To allow for a fair comparison and to determine how effective the other cooling methods are it is thus required that they are compared to the stainless steel radiation/heat-sink cooled case. This case will also serve as the baseline case to which the other cooling methods will be compared.

The different cooling methods will be compared in two different ways: first the maximum temperatures reached for each of the cooling methods will be compared. The difference in the transient will also be compared here. Afterwards, the steady state temperature distributions will be compared over the entire axial range of the thruster (i.e. from injector to nozzle exit).

Table 5.10: Results comparison - Maximum temperatures

| Case | Max temperature [K] | Difference to baseline [%] |
|---|---|---|
| Radiation/Heat-sink cooled (baseline) | 1416.1 | 0 |
| Regenerative - Sleeve - 0.3mm | 1228.4 | -13.25 |
| Regenerative - Axial - 0.7x0.7mm - 3 channels | 1094 | -22.75 |
| Regenerative - Helical - 0.7x0.7mm - 1 channel - 1 helix | 1090.3 | -23.01 |
| TBC + Radiation/Heat-sink cooling | 1381.7 | -2.43 |
| TBC + Regenerative - Helical | 1092.9 | -22.82 |
| Regenerative - Sleeve - 0.3mm - L=24.5 | 1149.4 | -18.83 |
| Regenerative - Axial - 0.7x0.7mm - 3 channels - L=24.5 | 1095.1 | -22.67 |
| Regenerative - Helical - 0.7x0.7mm - 1 channel - 1 helix - L=24.5 | 1096.2 | -22.59 |

From table 5.10 it can be seen that in terms of maximum temperature achieved the Regenerative cooling case with a single helical channel performs best, achieving a reduction in the final maximum temperature of 23.01%. It can also be seen that the performance of most designs is similar with temperature reductions of around 20%. This indicates that, at the small scales investigated within this study, the cooling channel design has only a limited effect on the maximum steady state temperature which is achieved. The maximum temperature as a function of burn time for the best cases can be seen in figures 5.37 and 5.38.
In figures 5.37 and 5.38 it can be seen that besides a reduction in overall temperature the transient curve of the maximum temperature is also changed depending on the cooling method used. To quantify this effect a factor $\Psi$ is introduced here, which will be referred to as the “burn time extension factor”. This factor indicates, for a given cooling method and a given failure temperature of the thruster, the additional burn time which can be achieved compared to the case where no cooling is present. For example: If a thruster would have a maximum operating temperature of 1100K and the value of $\Psi$ corresponding to this temperature is 6 seconds for a given cooling method, this means that the maximum attainable burn time would be 6 seconds longer when using this cooling method compared to the case where no cooling would be used.

$\Psi$ is thus a function of wall temperature, this is because it is not exactly sure at which temperature the chamber wall will fail. For stainless steel the melting point is between 1677-1713 K. None of the cases presented here reach this temperature. However, the maximum operating

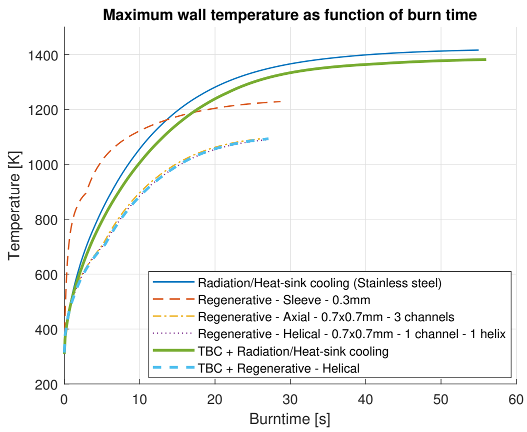


Figure 5.37: Comparison of maximum wall temperatures as function of burn time - Full length channels

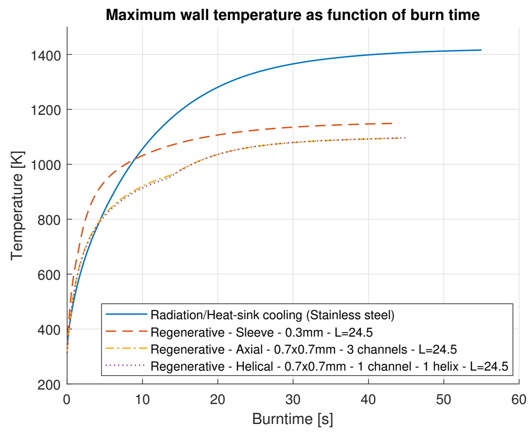


Figure 5.38: Comparison of maximum wall temperatures as function of burn time - Shortened channels

temperature of the chamber wall is likely lower than the melting point, this is because the yield strength of the material decreases as a function of temperature. This is discussed in more details in appendix B.2. Internal material tests performed at Dawn Aerospace indicate that a failure point of 1150 K is likely a good conservative estimate for the failure point. Nevertheless, the exact failure point remains difficult to determine without performing an actual test with the thruster itself.

In figures 5.39 and 5.40 the $\Psi$ factors for all cooling methods can be seen. It can be seen that, even if steady state operations can not be achieved, the burn time can still be extended by 33.6s in the most favourable scenario (yellow line in figure 5.40). This maximum burn time extension is achieved for the shortened helical cooling channel. If the failure temperature is above 1090.3 K then steady state operations can be achieved with regenerative cooling. This can be seen by looking at the positions of the dots at the end of each of the curves. These dots indicate that for a failure temperature higher than these points the cooling method can be used in steady state.

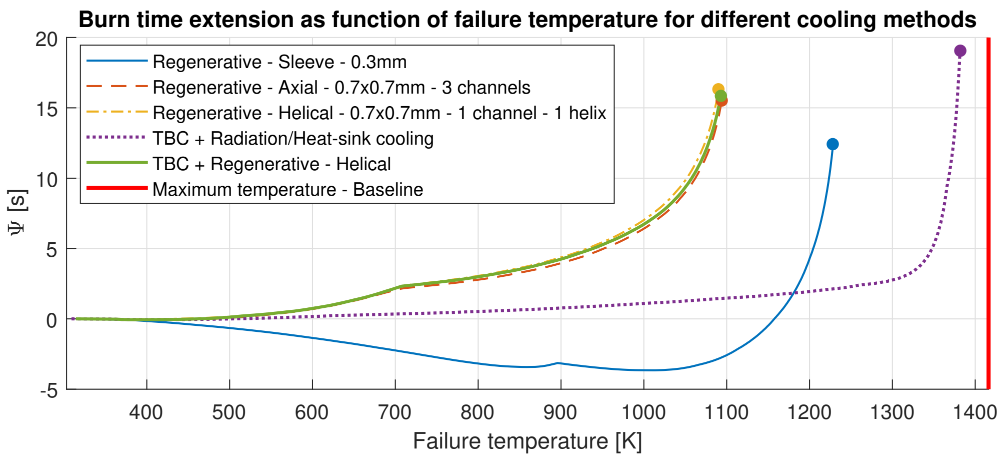


Figure 5.39: Burn time extension as function of failure temperature for different cooling methods

From figures 5.39 and 5.40 it can also be determined what the maximum burn time extension is for each given cooling method and with which cooling method this can be achieved. This is shown in figure 5.41. The blue line indicates the maximum burn time extension that can be achieved in seconds for a given failure temperature. The red lines indicate the boundaries between which a certain cooling method is best with the numbers in the top indicating which

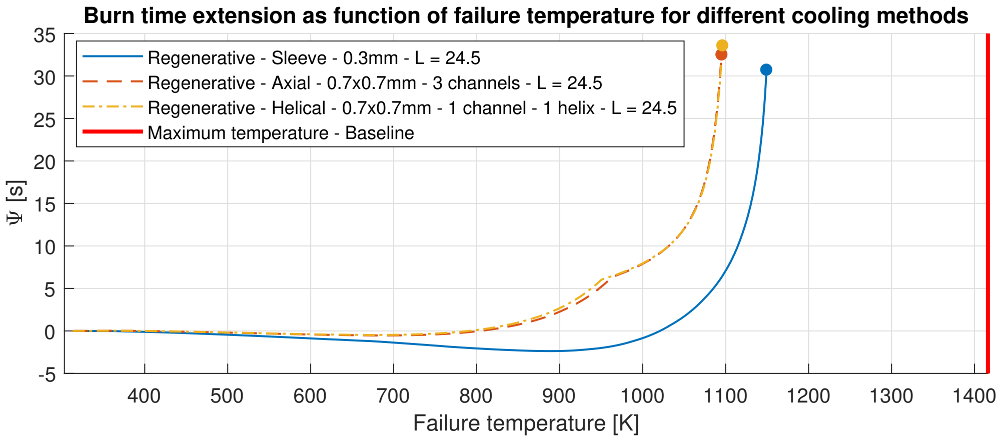


Figure 5.40: Burn time extension as function of failure temperature for different cooling methods - Shortened channels)

cooling method is best. Each of the numbers corresponds to a cooling method, an overview of which number corresponds to which cooling method and for which scenarios this cooling method is best can be seen in table 5.11. The failure temperature is indicated by $T_F$ in this table.

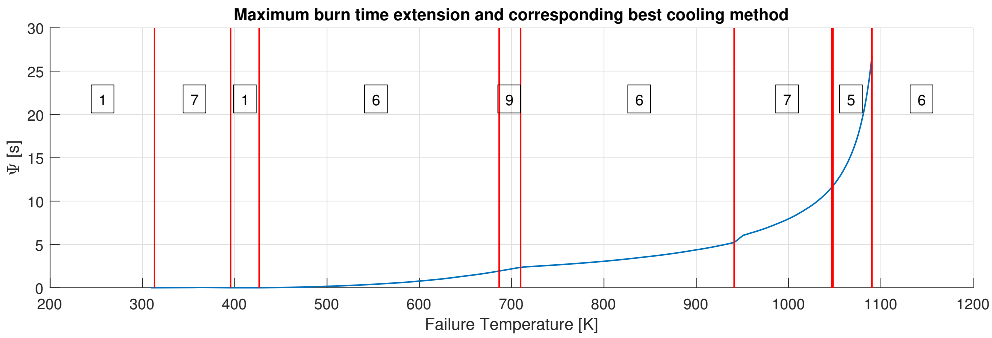


Figure 5.41: Maximum burn time extension as function of failure temperature and corresponding best cooling method

Table 5.11: Cooling methods and the scenarios for which they are best

| Case number | Cooling method | Best case for following conditions |
|---|---|---|
| 1 | Radiation/Heat-sink cooling | $T_F \leq 313.1K$ & $395.6K \leq T_F \leq 426.5K$ |
| 2 | Regen Sleeve - 0.3mm | Never |
| 3 | Regen Sleeve - 0.3mm - L=24.5 | Never |
| 4 | Regen Axial - 0.7x0.7 mm - 3 channels | Never |
| 5 | Regen Axial - 0.7x0.7 mm - 3 channels - L=24.5 | $1048K \leq T_F \leq 1090K$ |
| 6 | Regen Helical - 0.7x0.7 mm - 1 channel - 1 helix | $426.5K \leq T_F \leq 686.4K$ & $709.7K \leq T_F \leq 941.1K$ & $T_F \geq 1090.3$ |
| 7 | Regen Helical - 0.7x0.7 mm - 1 channel - 1 helix - L=24.5 | $313.1K \leq T_F \leq 395.6K$ & $941.1 \leq T_F \leq 1048K$ |
| 8 | TBC + Radiation/Heat-sink cooling | Never |
| 9 | TBC + Regen Helical - 0.7x0.7 mm - 1 channel - 1 helix | $686.4K \leq T_F \leq 709.7K$ |

From table 5.11 and figure 5.41 it can be seen that for most failure temperatures case 6 is the best case. For a large majority of the failure temperatures this case will fail last and it is also the case which reaches the lowest steady state temperature.

Interesting to note is that the regenerative sleeve designs never perform best. In fact, looking at figure 5.39 and figure 5.40 it can be seen that for most failure temperatures the sleeve designs perform even worse than the case with no cooling. Only for failure temperatures above approximately 1040 and 1158 K do they start to perform better than the case with no cooling. This result seems counter intuitive, however it can be explained by the fact that for the sleeve design there are no ribs to transfer heat to the outer wall of the engine. Because of this, the amount of heat that can be emitted by the thruster is limited by the amount of heat that can be transferred to the coolant. At the same time, the effective thermal mass of the thruster is also reduced since the outer wall is no longer able to directly store heat energy through the ribs. These two factors combined make it so that if the coolant is efficient at absorbing and transferring away heat the thruster will be cooler than the non-cooled case, however if the coolant is not efficient at absorbing and transferring heat the thruster will become warmer than the non-cooled case as the coolant will act as an insulator in this case. During the first part of the burn and at lower failure temperatures it appears that the second scenario is occurring. The coolant is not efficient enough at absorbing and transferring away heat. This in combination with the reduced effective thermal mass of the system causes a reduction in achievable burn times for failure temperatures below approximately 1040 K. However, above approximately 1158 K the effect reverses and the sleeve design becomes effective. In this case the burn time can be extended.

Looking at the results in table 5.10 it was seen that the maximum temperature could be reduced by 23.01% using regenerative cooling. Locally the maximum temperature reached can be reduced even further when regenerative cooling is used. This is shown in figure 5.42 where the steady state temperature reduction for different regeneratively cooled designs is shown as a function of axial position. The reduction shown is with respect to the case where no cooling is present. It can be seen that in the nozzle larger temperature reductions can be achieved of up to 67.87%. In the nozzle throat temperature reductions of between 40-50% can be achieved.

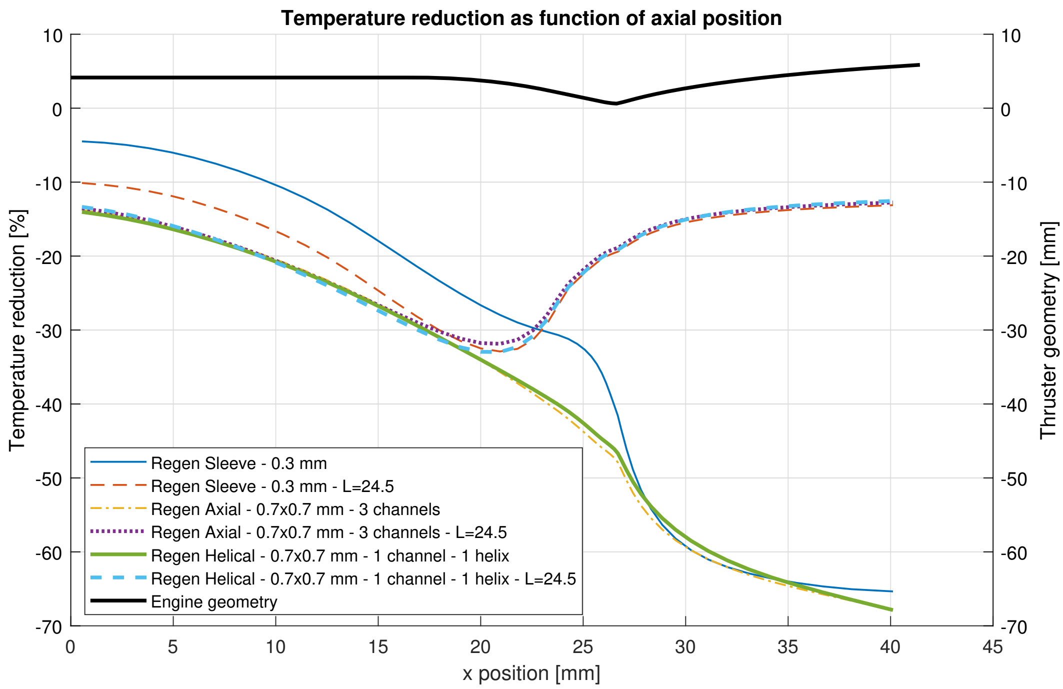


Figure 5.42: Percentage temperature reduction as function of axial position for different cooling methods

From figure 5.42 it can also be seen that, with the exception of the cases with the shortened channels, the results are similar for all other cooling channel designs. This indicates that there is little difference between the performance of the cooling channel designs. This was also seen earlier in table 5.10 where it was seen that most cases performed similar. It thus appears that the cooling achieved is not very sensitive to the cooling channel design and that little can be gained by optimising the cooling channel design.

As mentioned before, under the conditions seen in the PM200 and similar thrusters, the stainless steel wall material is expected to fail when it reaches a temperature of 1150 K.[1] Under this assumption, the effectiveness of each cooling method can be determined. The results are shown below in table 5.12.

Table 5.12: Burn time extension for each cooling method based on a failure temperature of 1150K

| Case | Max temperature [K] | Burn time extension [s] |
|---|---|---|
| Radiation/Heat-sink cooled (baseline) | 1416.1 | 0 |
| Regenerative - Sleeve - 0.3mm | 1228.4 | -0.36 |
| Regenerative - Axial - 0.7x0.7mm - 3 channels | 1094 | Steady State |
| Regenerative - Helical - 0.7x0.7mm - 1 channel - 1 helix | 1090.3 | Steady State |
| TBC + Radiation/Heat-sink cooling | 1381.7 | +1.69 |
| TBC + Regenerative - Helical | 1092.9 | Steady state |
| Regenerative - Sleeve - 0.3mm - L=24.5 | 1149.4 | Steady state |
| Regenerative - Axial - 0.7x0.7mm - 3 channels - L=24.5 | 1095.1 | Steady state |
| Regenerative - Helical - 0.7x0.7mm - 1 channel - 1 helix - L=24.5 | 1096.2 | Steady state |

From table 5.12 it can be seen that, with the exception of the full regenerative cooling sleeved design, all regeneratively cooled designs allow for a steady state burn time to be reached. For the regeneratively cooled sleeve with the cooling channel inlet at 24.5mm the margin is only 0.6 K, which is within the margin of error of the program. Out of all the regeneratively cooled designs, the cooling sleeve designs perform the worst, with the full length regenerative cooling sleeve even leading to a reduction in maximum achievable burn time according to the simulation results.

For all radiation/heat-sink cooled designs it is not possible to reach the steady state with a stainless steel wall material, even if a thermal barrier coating is added. To make radiation cooling work there are two possible options: A different wall material can be used which performs better at higher temperatures. This strategy is likely to be effective but will also come at an increase in cost as temperature resistant metals are generally more costly to 3D print.[2] A second option is to change the geometry and/or surface finish of the thruster to increase the heat rejection of the thruster. By changing the geometry of the thruster its effective shape factor [3] can be increased, leading to a higher heat rejection. This can for example be done by adding radiation fins. A study by Batha et al. [4] found that based on experimental data temperature decreases of up to 111K can be achieved within the thruster wall using radiation fins. For the reference thruster design used in this study such a temperature decrease would not be sufficient to make radiation cooling feasible without requiring a different wall material. However, the use of radiation fins may be beneficial for different thruster designs where the margins are closer. It should also be noted that the radiation fins used in the study by Batha et al. [4] were not optimised and that even larger temperature decreases may be possible. Additionally, it should also be noted that due to the low thermal conductivity of stainless steel adding radiation fins may be an inefficient solution.

### 5.2.2. Experimental comparison

As discussed in chapter 4, several tests were performed with the PM200 for a radiation/heat-sink cooled engine and a regeneratively cooled engine. Using the data from these tests, both

[1] This value is a conservative estimate based on material tests performed at Dawn Aerospace.
[2] Based on data from Dawn Aerospace suppliers.
[3] The effective shape factor is the effective surface area of the thruster that can radiate away heat.

cooling methods can also be compared using the experimental data. It should be noted that for the experimental results, the thermocouples were not necessarily located at the positions where the highest temperatures occurred within the thruster. Because of this the absolute maximum temperatures occurring within the thrusters can not be compared. It is however still possible to compare the temperatures at the measurement points. The temperature at three points were compared: at the chamber, at the exterior throat and at the nozzle exit. Especially the temperatures at the chamber and at the exterior throat are of interest, as these points are likely close to the point where the maximum temperature occurs based on the model results.

The burn time extension for the current cooling channel design of the PM200 as function of the failure temperature is shown in figure 5.43. Because test data was only available for particular burn times, it was not possible to use test data for the entire curve. For the radiation/heat-sink cooled engine only test data of up to four seconds was available. During the first four seconds of the burn, the burn time extension can thus be plotted purely as a function of experimental results (uninterrupted lines in figure 5.43). For burn times beyond four seconds, but below ten seconds, experimental data is only available for the regeneratively cooled version of the PM200. For this portion of the curve the experimental data from the regeneratively cooled version of the PM200 is thus compared to the model results from the radiation cooled/heat-sink cooled version of the PM200 (interrupted dashed lines in figure 5.43). For burn times beyond ten seconds, no experimental data is available. To construct this part of the curve, only model results were used (dashed line interrupted by dots in figure 5.43).

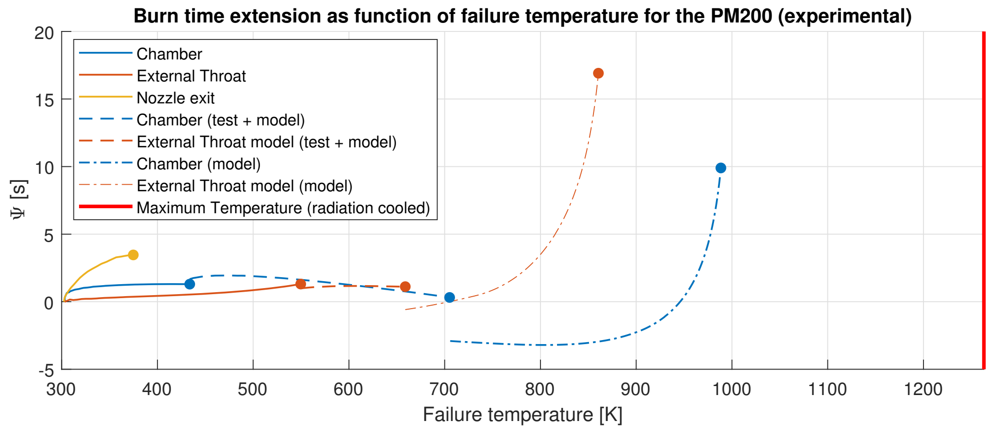


Figure 5.43: Burn time extension as fnction of failure temperature for the PM200 (using experimental + model data points)

Several observations can be made from figure 5.43: Looking at the curves, it can be seen that there are discontinuities at the locations where the curve switches from being based purely on experimental data to being based on a combination of model and experimental data. Even larger discontinuities are present for the second switch where the curve switches from the combined results to the purely model based results. These discontinuities are to be expected as the model results can not be expected to precisely match the experimental data. For the first set of discontinuities, where the curve switches from the experimental results to the combined results, the discontinuities are relatively small, indicating a good match between the model and the test results. For the second set of discontinuities, where the curve switches from the combined results to purely model based results, the discontinuities are relatively large, especially for the measurements at the chamber. This means that the model is rather pessimistic, at least for the chamber measurement point. The burn time extensions presented in figure 5.43 are therefore likely conservative estimates.

Furthermore, it can be seen that at low temperatures the extension in burn time is relatively low; between 1 and 2 seconds. This means that for low failure temperatures in the transient regime the cooling is not very effective in delaying the temperature rise. It can also be seen that for the chamber measurement point the burn time extension starts to decrease and even becomes negative during the middle range of the failure temperatures. This can be explained partially by the fact that the model is somewhat conservative. However, the downwards trend is also clearly visible for the combined results and upon closer inspection it can be seen that it is also visible for the purely experimental result. It can thus not be attributed purely to the conservative nature of the model. From a physical perspective it also makes sense that the burn time extension factor decreases for the combustion chamber as it was seen in section 5.1 that for regeneratively cooled thrusters the maximum temperature location shifts more towards the combustion chamber. It is therefore reasonable to assume that the combustion chamber wall temperature at some point becomes higher for the regeneratively cooled case when compared to the combustion chamber wall temperature for the purely radiation/heat-sink cooled case.

Additionally it can be seen that based on the results for the measurement points shown in figure 5.43, the maximum burn time extension for the transient case is 9.9 s. It should however be noted that the temperatures for the points indicated in figure 5.43 are likely not the maximum temperatures occurring within the thruster, so the actual maximum burn time extension may be different. It can also be seen that for the steady state temperature, a relatively large reduction in temperature is achieved. The red line on the right indicates the maximum steady state temperature as predicted for the combustion chamber for the radiation cooled case. It can be seen that by implementing regenerative cooling the final steady state temperature is decreased by approximately 275 K.

In figure 5.44 the steady state temperature distribution of the outer wall as predicted by the model for both the radiation cooled and regeneratively cooled version of the PM200 can be seen. For the regeneratively cooled case the current cooling channel design was used. It can be seen that the current cooling channel design achieves a maximum reduction in the final temperature of 35.94%. This reduction occurs right after the cooling channel inlet. At the location where the maximum temperature is predicted for the radiation cooled case a reduction of 34.28% is achieved using the regenerative cooling channel. The reduction in the maximum temperature overall is 21.97% which is comparable to the decrease in maximum temperature seen for the reference engine. It should be noted that the current cooling channel design was not optimised, so further reductions in the temperature may be achieved. It is however unlikely that such an optimisation of the cooling channel design would lead to substantially higher reductions in the final temperature as was seen in section 5.1.

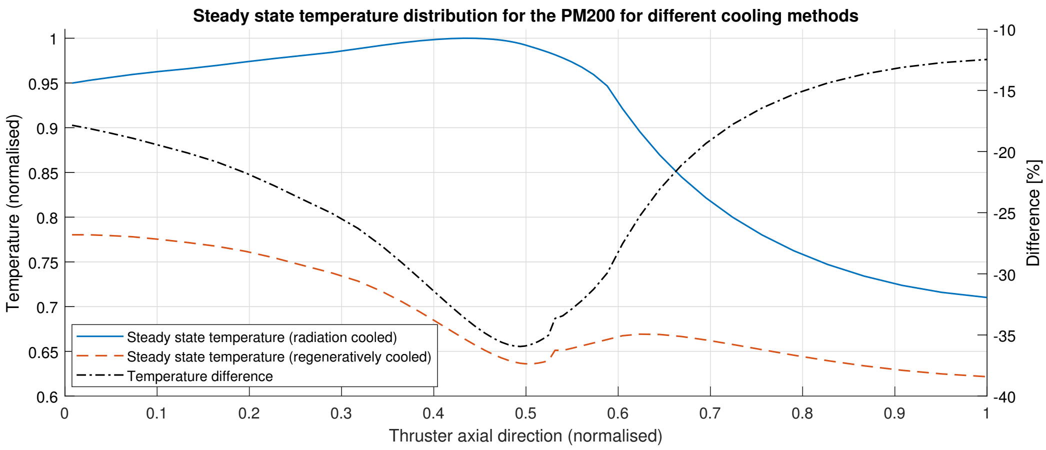


Figure 5.44: Comparison of the steady state temperature distributions for the regeneratively cooled and radiation cooled version of the PM200.

Changes to the cooling channel design could however be made to raise the burn time extension factor curve seen in figure 5.43 so that the downwards trend seen between approximately 400-850 K does no longer occur or is reduced. This would however only be beneficial if the steady state can not be reached.

In figure 5.44 it can also be seen that the smallest temperature decrease it achieved at the nozzle exit. This is not surprising as no cooling channel is present here. For the PM200 the cooling channel inlet is located at approximately the 0.65 point on the x-axis.

## 5.3. Additional considerations, errors and uncertainties

In the previous sections the different cooling methods were compared. It should be noted that several assumptions were made in this comparison. Some of these assumptions may cause issues or introduce some uncertainty into the result. In this section some of these issues will be addressed.

### 5.3.1. Coolant inlet temperature

Within the program, it is assumed that the coolant temperature is equal to the ambient temperature and that the coolant inlet temperature stays constant throughout the burn. For long duration burns this may not be the case. It may be that there is significant heat transfer to the coolant feed lines and the propellant tank if the thruster is operating in steady state. During testing of the inconel thruster (as discussed in section 4.6.2) a thermocouple was placed on the spiral which acts as the coolant feed line. During these tests the maximum observed increase in temperature was roughly 9K. The majority of this increase in temperature occurred after shutdown of the engine and not during the burn. The assumption of a constant coolant inlet temperature thus seems reasonable. It should however be noted that for the inconel thruster only burns of up to 5 seconds were performed, it may therefore be the case that for much longer burn times this assumption is no longer valid.

### 5.3.2. Radiation heat transfer at the outside of the thruster

The model used to determine the radiation emitted by the thruster is relatively simple. Because radiation heat transfer becomes more significant as the thruster wall temperatures become higher, this may increase the error of the model as the thruster heats up. These errors may be because of the following phenomena:

- In the model it is assumed that all radiation emitted by the thruster is not reabsorbed by the thruster. In reality this is not the case and some radiation will be reabsorbed. Especially for parts which are relatively enclosed such as the nozzle throat this will lead to an increase in temperature.
- In the model it is assumed that the radiation heat transfer only occurs from the outside wall surface areas of the thruster. However, in reality radiation will also be emitted from the inside walls of the thruster. Most of this radiation will be absorbed again by the inner wall at the opposite side of the thruster. Neglecting this radiation heat transfer is thus a reasonable assumption. Close to the nozzle exit however part of the radiation emitted by the inner nozzle wall will also be radiated to the ambient environment. Because this is not taken into account, the model will likely overestimate the nozzle temperature at higher temperatures.

### 5.3.3. Thruster geometry and temperature profile

The results presented in section 5.1 were based on the reference thruster design. This design was not exactly equal to the PM200 design and several differences were present. Because of this, some considerations need to be taken into account when extrapolating the results from the reference design to the PM200. Furthermore, even when the PM200 was simulated within the model, several simplifications were still made. The impact of these differences and simplifications on the obtained results will be explained below.

- **Combustion chamber length** - The PM200 design has a shorter combustion chamber length compared to the reference design. This has two effects: the first is that the coolant channel length is shorter, resulting in a lower coolant temperature at the coolant outlet. Because of this lower coolant channel outlet temperature the cooling is more effective at the end of the channel for the PM200. Secondly, because the heat transfer coefficient is relatively high in the combustion chamber (due to the high a-coefficient here), having a shorter combustion chamber results in a lower heat transfer coefficient on average over the entire thruster body. These effects combined result in a lower predicted maximum temperature for the PM200 design. With the current non-optimised version of the cooling channel design, this already results in a lower predicted maximum temperature than the best case design for the reference case by more than 70K. With optimisation this could potentially be reduced even further, although most likely not by more than roughly 40K based on the results from section 5.1.
- **Combustion chamber wall thickness** - The PM200 thruster has a larger wall thickness at the combustion chamber and a smaller wall thickness at the nozzle. This mostly affects two things: First, the temperature difference between the outer and inner wall is larger and smaller for the combustion chamber and nozzle respectively. Secondly, while the location of the maximum temperature still occurs in the nozzle convergent, for the PM200 the location of the maximum temperature is shifted slightly more towards the nozzle throat.
- **Additional features and geometries** - The real PM200 thruster has several additional features and geometries which are not taken into account in the model. These include: the pressure sensor ports, the injector dome, the propellant feed lines, the TVC mechanism, and the mounting points. It should also be noted that the real PM200 thruster is enclosed within the (tank) module (see figure 2.1). Although from the tests performed it appears that all these factors only have a minor effect on the final temperature distribution, it may be that these effects become more significant at higher temperatures.

### 5.3.4. Asymmetry and average temperatures

The presented model has two properties which may cause issues in some specific cases. The first of these properties is that within the program the assumption was made that the temperature distribution was axisymmetric within the thruster wall material. This assumption was later confirmed for the radiation/heat-sink cooled case using experimental data in section 4.4.3. The second property of the program which should be noted is that since a finite volume method approach was used, the temperature calculated in each cell is the average temperature taken over the entire cell volume, not the local temperature in the cell centroid. This is a property of the finite volume method approach [27]. If the cell size is small enough, this average temperature approximates the real local temperature.

These two properties have the consequence that for thruster designs which are not axisymmetric, the results of the model may be less accurate. This is because for non axisymmetric designs there may be a large temperature gradient in a cell due to the cooling not being evenly distributed along the cell volume. This means that the average temperature calculated through the finite volume method may no longer be a good approximation of the maximum temperature occurring within the cell. This issue is particularly present for designs consisting of a single helical cooling channel. The results of the model appear to trend towards the best solution being a single channel with an as large as possible helix pitch (If the helix pitch is set to infinity this essentially becomes a single straight channel). One may question whether or not such a design is reasonable as it would only provide cooling to one side of the thruster. It may be true that in this scenario the average temperature indeed reaches a minimum. However, in this scenario it may also be the case that the local maximum temperature is no longer approximated closely enough anymore by the average temperature in the centroid due to the presence of high thermal gradients. Because of this, the assumptions made within the model are violated and the results are no longer valid. It thus appears that this perceived optimum solution is an exploitation of the limitations of the model, and not an actual optimum. It may therefore be the case that, even though the model shows that having only 1 helix gives the best result, having a shorter helix pitch (and thus more helices) would be (slightly) more beneficial simply due to the fact that in this case the cooling is performed more evenly over the entire thruster surface. This would limit temperatures from locally exceeding the average calculated temperature by a large margin.

As a counter argument to the preceding argumentation it should be noted that during testing of the regular PM200 (which included a cooling channel), no large temperature gradients were observed, even though this design is largely asymmetric and uses only a single helical cooling channel. It thus appears that the potential problem outlined above is not a large problem. Nevertheless, in theory problems may occur for non axisymmetric designs with large helix pitches. Therefore, to prevent users of the model from drawing incorrect conclusions the following recommendation is made: If a regeneratively cooled engine design is simulated with a single helical cooling channel, the helix pitch should always be equal to or shorter than the total cooling channel length. This is to ensure that all sides of the thruster are cooled.

## 5.4. Implications for the PM200 design

In the previous sections of this chapter the main focus was on the reference thruster, which was used to show the performance trends and the model results for each cooling method. Furthermore, the reference thruster was used as an example to explain what phenomena are occurring in small scale CubeSat thrusters. From a practical perspective it is interesting to look at what all this means for the PM200: a real life thruster. This section will therefore focus on the implications of the findings for the PM200 design. Besides discussing the model results for the PM200, this section will also focus on several observations which were made during the test campaign which did not fit well in any of the other sections of the report but which could have important consequences for the PM200 design.

### 5.4.1. The best cooling method for the PM200

For the PM200 thruster the simulation results indicate a maximum temperature of ~1320 K for the radiation/heat-sink cooled case and a maximum temperature of ~1020 K for the current regenerative cooling channel design. If it is assumed that failure of the thruster occurs at 1150 K, it can be concluded that the performance of the current regeneratively cooled thruster design is sufficient for the thruster to be able to operate in steady state. The current regeneratively cooled thruster design is most likely not the optimal design and some small performance gains could potentially still be made. The radiation/heat-sink cooled thruster design will fail unless a different wall material is used. For the radiation/heat-sink cooled thruster the model predicts that the thruster will fail after 27.1s.

Based on the results presented above it appears that the thruster will be able to run in steady state. It is recommended to perform a test campaign to validate the model result for the regeneratively cooled case. This is recommended for two reasons: firstly, while the model results match the currently available test data well, it may be that at longer burn times/higher wall temperatures the model starts to diverge from reality. In this case re-calibration of the model is required. Secondly, the 1150 K failure temperature was determined based on tests performed in house by Dawn Aerospace. These tests were performed such that they are believed to give a conservative estimate of the failure temperature. It may however be the case that this failure temperature is not correct. In this case it may be that either regenerative cooling is not feasible in steady state or that radiation cooling is also feasible depending on whether or not the failure temperature is overestimated or underestimated respectively. If it turns out that regenerative cooling is not feasible in steady state this does not necessarily mean that regenerative cooling can not be beneficial. Depending on the actual failure temperature the current regenerative cooling channel design could still be beneficial to extend the burn time as was shown in figure 5.43.

In the proposed test campaign the burn time shall be increased sequentially. Thermocouples shall be attached to the thruster, specifically at the locations where the highest temperatures are predicted according to the model, which is near the chamber and the injector. After each test (or test series), the model results shall be re-evaluated based on the test results. If it is found that the test results diverge from the model results, the model shall be re-calibrated. However, based on the current experimental results it is expected that the model will not diverge from the measurement data and that re-calibration will not be required.

### 5.4.2. Igniter heating

During tests performed with the Inconel version of the PM200 (see section 4.6.2) a thermocouple was attached to the igniter of the thruster. It was found that there was a substantial amount of heat transfer to the igniter body. For a 5s burn the maximum igniter temperature exceeded the maximum exterior throat temperature (which corresponded to the highest recorded temperature on the thruster body itself) by 8.7%. This means that even if the thruster body could survive the temperatures associated with a steady state burn, the igniter may still fail or get damaged in such a scenario.

The igniter consists of a combination of ceramic and metal components. Especially for the metal components this high temperature may be an issue at extended burn times. Estimating the igniter temperature is beyond the scope of the model presented in this study. Therefore, it is recommended that further experimental investigation is performed to determine if the heating of the igniter causes any issues at longer burn times (i.e. longer than 10s). These experiments can be combined with the experiments recommended for the test campaign described in section 5.4.1.

### 5.4.3. Pressure sensor heating

The PM200 has three pressure sensors on the thruster for measuring the injection pressures and the chamber pressure. These sensors have a maximum operational temperature of approximately 125 °C. Several tests were performed where thermocouples were mounted on the mounting points for the pressure sensors. From these tests it was found that for the 10 second burns the temperature at the mounting points exceeded the maximum operating temperature of the pressure sensors. This maximum temperature occurred after shutdown of the engine so the pressure sensors were not loaded under pressure at the time they reached this temperature. This result does not necessarily mean that the pressure sensors exceeded their maximum operating temperature and no performance degradation was noticed, even after multiple tests. It however does indicate that for extended burn times it is likely that the pressure sensors will exceed their maximum operating temperature.

It is recommended to investigate experimentally if this causes any issues and if so the severity of these issues should be established to make an estimate of the risks involved. If problems occur, this experimental campaign could also be used to determine after what burn time these issues occur.

If the problems encountered are unacceptable, it is recommended that the pressure sensors are removed if the mission profile requires long burn times. The removal of the pressure sensors could happen after acceptance testing of the thruster is completed (or even during the acceptance test campaign). This way the performance of the thruster can still be validated before flight. The pressure sensor ports could be welded shut or plugged afterwards. Ignition of the motor in orbit could still be verified by adding a thermocouple to the thruster.

### 5.4.4. Tank heating

During the test campaign performed, it was often observed that after performing several consecutive tests the propellant tank pressure would rise. This can be seen in figure 5.45 where the (normalised) chamber pressure is plotted for a number of tests performed with RT2. Tests which were performed consecutively are indicated by the same markers and trend lines are plotted through these markers. An upward trend is clearly visible for each of the test series with chamber pressures rising by as much as 15% over the course of 7 tests.

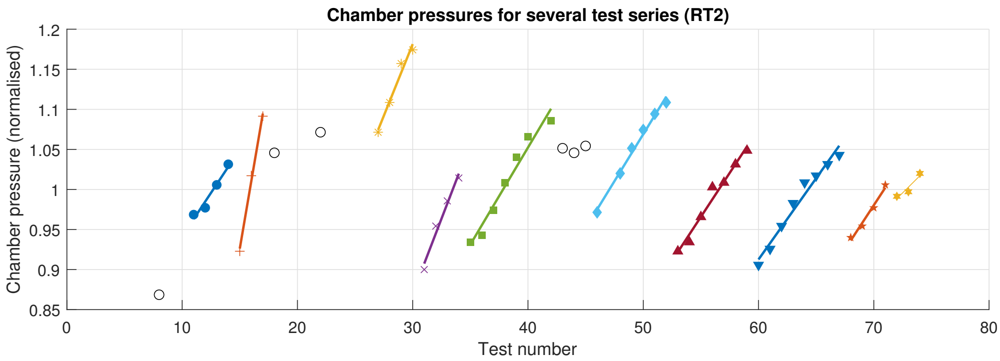


Figure 5.45: Normalised chamber pressures for RT2 for several test series

The reason for this phenomena is that because after a test the thruster radiates and conducts heat towards the tank module. As a result the tank module heats up slightly after a test, leading to a slightly higher tank pressure. This in turn results in a higher chamber pressure. While the tank heats up only slightly compared to the thruster, it retains this extra heat for much longer. This means that when the thruster has already cooled down and is ready for another firing, the tank is still at a slightly elevated temperature. This results in a positive feedback loop as the elevated tank temperature increases the chamber pressure for the next firing. Because the chamber pressure is higher the thruster heats up more, resulting in more heat transfer to the tank.

It should be noted that most of this heat transfer to the tank occurs after shutdown of the engine, and not during firing. For example, for a 5s burn the increase in tank temperature is approximately 1-1.5°C. This increase in tank temperature is only achieved approximately 400-600 seconds after ignition of the engine. The process is thus slow and does not affect thruster performance during the burn. Furthermore, during the burn the tank pressure drops more rapidly than any pressure increase which could be caused by the heating of the tank (see figures 2.3 and 4.9) so even if the tank heated up during the burn this would not be a problem.

There are multiple methods for solving the problem outlined above. The most simple solution would be to simply wait longer in between thruster firings or to limit the amount of thruster firings which are performed in sequence. For the tests plotted in figure 5.45 the time between firing was between ten and twenty minutes. Since a satellite in low earth orbit (LEO) requires approximately 90 minutes to complete a single orbit, it is easily possible to increase the wait time if burns are to be performed at the same point in the orbit. Even if burns are required in both periapsis and apoapsis (for example for raising and circularising the orbit) it can be expected that at least 45 minutes will be in between firings. The easiest solution to this problem is therefore to take this effect into account when planning manoeuvres and to execute manoeuvres in such a manner that excessive tank heating is prevented.

In some cases it may be required that multiple burns in quick succession are required or that even a small increase in tank temperature is unacceptable for mission success. Especially if long burn times are performed it could be that after shutdown of the thruster the tank still heats up quite substantially. For these cases heat transfer to the tank from the thruster should be limited. This could for example be achieved by adding thermal insulation between the thruster and the tank module. Alternatively a heat shield could be constructed around the thruster to limit the heat transfer to the rest of the module. Such concepts have also been used for other CubeSat propulsion systems, see for example the research by Tsay et al. [42].

## 5.5. Discussion of results and conclusions

In this section the results and conclusions found in this chapter will be described. This will be done by answering the research questions posed in chapter 2.

- **SQ-1: Is it possible to achieve sufficient cooling using regenerative cooling in a thrust chamber which is small enough to be used in CubeSat applications?**
  - **SSQ-1.1: How is the temperature distributed within the thruster?**

    For the radiation cooled case a peak in temperature is reached in the convergent section of the nozzle. For the reference case used in this report this peak temperature was ~1420 K. In the divergent part of the nozzle the temperature loading is lower with temperatures reaching around 960 K. Within the combustion chamber, wall temperatures range between approximately 1250 and 1400 K.

    For the regeneratively cooled case, the temperature distribution depends on the type of regenerative cooling channel chosen. Two types can be distinguished: regenerative cooling sleeves and cooling channels with ribs (including helical channels).

    For the cooling sleeves the best design for the reference case reached a maximum temperature of ~1230 K, this temperature is too high to enable steady state burn times. The maximum temperature occurs in the combustion chamber approximately at the half way point between the injector and the start of the nozzle convergent. The coolant reaches a maximum temperature of ~1140 K, this temperature is reached at the cooling channel exit. At the beginning of the cooling channel (at the nozzle exit) the cooling sleeve design is very effective; the nozzle exit reaches a temperature of only ~330 K. However, at the locations where higher heat fluxes are present (the nozzle throat and the combustion chamber) the coolant temperature rises steeply. While the cooling sleeve design reaches a lower maximum temperature than the radiation cooled design, the transient analysis shows that until a temperature point of 1158 K is reached the cooling sleeve design heats up faster than the radiation cooled design. This is because the coolant acts as an insulator and traps heat in the “inner” wall of the thruster. While the outer wall of the thruster stays relatively cold according to the simulation results (maximum temperature of ~910 K), the inner wall heats up faster than the radiation cooled design.

    For the best design utilising axial cooling channels a maximum temperature of 1094 K is reached. This temperature is reached at roughly one third of the combustion chamber length. Again, good cooling is achieved at the nozzle exit. Near areas of high heat flux the coolant temperature rises steeply. Due to the ribs heat can also be transferred to the outside wall of the thruster, leading to a more even temperature distribution. For the helical cooling channels the temperature distribution looks essentially identical, with the exception that slightly lower temperatures can be reached. For the helical cooling channel design the best case design reaches a maximum temperature of ~1090 K. For this design the maximum temperature is also reached at approximately one third of the combustion chamber length.
  - **SSQ-1.2: Is it possible to achieve sufficient cooling with gaseous nitrous oxide?**

    Yes. According to the simulations performed on the reference design a reduction of up to 23% in the maximum attained temperature can be achieved. This reduces the maximum attained temperature from ~1420 K down to ~1090 K. The thruster is expected to fail at a temperature of 1150 K, meaning that the amount of cooling achieved is sufficient.

- **SSQ-1.3: Are the thrust levels and corresponding (coolant) mass flows used in CubeSat scale propulsion systems sufficient to make regenerative cooling feasible?**

  Yes. For both the PM200 and the reference thruster design it was shown that sufficient cooling can be achieved using regenerative cooling. Both of these thrusters had a thrust level and mass flow low enough to be used in a CubeSat scale propulsion system.

Based on the results from sub questions SSQ-1.1, SSQ-1.2 and SSQ-1.3, sub question SQ-1 can now be answered. From the simulation results it has become clear that it is possible to achieve sufficient cooling using regenerative cooling in a thrust chamber which is small enough to be used in CubeSat applications.

- **SQ-2: Which design parameters are the main drivers for selecting a cooling method for a CubeSat scale propulsion system?**
  - **SSQ-2.1: What is the influence of the different design parameters on the heat loads experienced by the thruster?**
    - Chamber pressure: Heat transfer to the thruster wall scales with chamber pressure to the power 0.8 (see equation 3.8). A lower chamber pressure is thus more beneficial for achieving a lower wall temperature. Literature ([18, 38] also suggests that at low pressures typical semi-empirical relationships such as equation 3.8 overestimate the heat transfer, indicating that for low pressures using $P_c^{0.8}$ to estimate the heat transfer is an overestimation. This is in agreement with the results found in this work. It was found that for the PM200 the heat transfer was overestimated by a factor of between 2 and 3 depending on the specific location on the thruster.

    - O/F: Assuming a nominal O/F of 8, higher O/F ratios result in a lower wall temperature and lower O/F ratios result in a higher wall temperature (although likely only up to a certain point). The differences are however small, with an increase in O/F of 50% resulting in only a decrease of less than 3% in the final wall temperature. The O/F ratio can not be varied too much to ensure that ignition is still possible, therefore it can be assumed that the effect of the O/F ratio on the final temperature reached is small; typical change in the maximum final wall temperature are within 3%.

    - Propellants used: The propellants used have an effect on the heat transfer. This was not studied in detail within this study as propylene and nitrous oxide were assumed to be the propellants of choice. From equations 3.8 and 3.10 it can however be seen that in theory propellant combinations which result in reaction products with a higher heat capacity and/or a higher viscosity result in a larger amount of heat transfer. Furthermore, propellants combinations which produce higher stagnation temperatures within the combustion chamber also result in a higher amount of heat transfer.

    - Thruster geometry: The thruster geometry has an affect on the heat loading. Compared to the other factors mentioned above the effect of geometry is more complex and it is not possible to easily capture all effects present in a short set of rules. Some observations can however still be mentioned.

      Equation 3.8 indicates that the heat transfer to the thruster wall scales with a factor $(D_t/D)^{1.8}$. While this matches experimental results for the nozzle, for the combustion chamber this does not match with the experimental results. Equation 3.8 predicts that for smaller local combustion chamber diameters the temperature should be higher. Experimental results however show that near the injector the temperature decreases compared to the rest of the combustion chamber, even though the combustion chamber diameter is smaller here. The factor mentioned above is thus not applicable for the entire thruster cross section.

Equation 3.8 also indicates that a larger longitudinal throat radius results in a lower amount of heat transfer. This was not investigated in detail within this study.

It was also found that having a shorter combustion chamber wall decreases the overall temperature reached. This is because in this case the surface area of the wall in contact with the combustion gases decreases. If a regenerative cooling channel is present this also decreases the length of the channel, leading to a lower total temperature rise in the coolant fluid. This in turn results in a lower overall temperature as the cooling is more effective in this case. A too small combustion chamber length may however result in a lower combustion efficiency. Because of this, there is a limit to how small the combustion chamber length can be.

– **SSQ-2.2: What is the influence of the different design parameters on the cooling performance of each cooling method?**

  ◇ Wall material emissivity: Wall material emissivity has a small effect on the overall temperature reached. A nominal emissivity of 0.8 was assumed. Reducing this by 50% to 0.4 leads to an increase in maximum wall temperature of less than 11%. Increasing the wall material emissivity provides minimal gains with an increase in emissivity of 10% leading to less than a 2% decrease in maximum temperature.

  ◇ Wall material thermal conductivity: A higher wall material thermal conductivity results in a lower maximum final wall temperature. An increase in thermal conductivity of 50% results in a 4% lower temperature. Stainless steel (the material used for the PM200) has a relatively low thermal conductivity so by using a wall material which has a much higher thermal conductivity (100-200% more) even lower wall temperatures could be reached if all other factors are kept the same.

  ◇ Effective shape factor: The effect of the effective shape factor was not studied in detail in this study. Preliminary calculations ([45]) show that theoretically large decreases in temperature can be achieved but these also require large increases in shape factor which are difficult to achieve. Experimental results from literature have demonstrated temperature reductions of up to 111 K [4].

  ◇ Coolant heat capacity: A higher coolant heat capacity results in a lower overall wall temperature reached. A 50% increase in coolant heat capacity would result in a 4% decrease in wall temperature while a 50% decrease in heat capacity would lead to a roughly 7% increase in wall temperature. Other coolants may be available which have even higher heat capacities and which would thus provide better cooling. These were however not investigated in detail within this study.

  ◇ Cooling channel height/width: For CubeSat scale propulsion systems the cooling channel height/width has little effect on the cooling performance. Overall the model predicts that larger cooling channels perform somewhat better, however for all cooling channel shapes simulated in this study the variation in maximum temperature reached was less than 15K. This is because due to the small size of CubeSat scale propulsion systems and current additive manufacturing capabilities the design space for the cooling channel shape is very limited.

- Cooling channel inlet position: Running the coolant inlet from the nozzle exit all the way to the injector is in most cases the most optimal solution. In some cases it can be beneficial so shift the cooling channel inlet closer to the injector, leaving part of the thruster uncooled. This is for example the case for the cooling sleeve design. For the cooling channel designs with ribs changing the inlet position from the nozzle exit has little effect; all cases with shorter channels perform worse or on par with designs which use full length cooling channels.

- Helix pitch: The helix pitch appears to have little effect on the final temperature reached. For all cases simulated (1-8 helices) the variation in the results was within 37 K. A larger helix pitch appears beneficial according to the simulation results. This is because a longer helix pitch reduces the cooling channel length, leading to a lower coolant temperature at the end of the cooling channel. This in turn leads to more effective cooling at the location where the highest temperatures are predicted to occur. It should be noted that by taking the helix pitch to be too large the cooling fluid will no longer be distributed evenly over the thruster body, which violates some of the assumptions made in the model. A larger helix pitch is thus only beneficial as long as the assumptions of the model hold.

- Number of cooling channels: The number of cooling channels has little effect on the cooling performance. The variation in the maximum temperature reached for all cases simulated (3-10 channels) was less than 15 K. A smaller number of cooling channels appeared to be beneficial according to the model. This is attributed to the fact that a smaller amount of cooling channels leads to a lower combined cooling channel surface area which leads to a reduction in heat transfer to the coolant. As a result the coolant heats up less leading to more effective cooling near the end of the cooling channel.

With sub questions SSQ-2.1 and SSQ-2.2 answered it becomes possible to answer sub question SQ-2. From the results found for SSQ-2.2 several conclusions can be drawn. Changing the wall material to a material with a higher thermal conductivity or changing the coolant can be effective in lowering the thruster temperature. However, for a given wall material and a given coolant, none of the design parameters for the different cooling methods have a particularly large impact on the cooling effectiveness. The type of cooling method can still have an effect on the final temperature that is reached. Implementing a particular cooling method can thus still be beneficial, but once a particular cooling method is selected little optimisation of the design can be performed due to the small thruster size creating a very narrow design space.

The main drivers for selecting a cooling method are thus not the particular design parameters of each cooling method. Instead the main drivers are the parameters which govern how much heat comes into the system. The two parameters in particular that have a large effect are the chamber pressure and the thruster geometry. A low chamber pressure and a small combustion chamber length are beneficial for keeping the wall temperature low. For optimal performance however, a high chamber pressure and a sufficient chamber length are desirable. The choice of cooling method will thus be driven by the required system performance.

If the chamber pressure is low, regenerative cooling is an effective cooling method. As was shown in this chapter, a decrease of 23% in the maximum wall temperature can be achieved for the reference design using regenerative cooling. For the PM200, the current cooling channel design reduces the maximum wall temperature by 22%. In both cases this is sufficient to reduce the wall temperature below the failure temperature of 1150 K. If the chamber pressure is however high, the heat transfer to the wall will increase while the regenerative cooling performance will stay roughly the same. At some point regenerative cooling will thus become infeasible. Using the model, it was determined that for the PM200 this turning point lies at a chamber pressure of approximately 7.1 bar. For chamber pressures below this value regenerative cooling is feasible, for chamber pressures above this value a different wall material is required with a higher failure temperature, for example a refractory metal.

It is unlikely that a chamber pressure of 7.1 bar would ever be reached in the PM200, this is because the chamber pressure of the PM200 is related to the ambient temperature. The maximum specified operating temperature for the PM200 corresponds to an ambient temperature of 35°C, at this ambient temperature the chamber pressure is still below 5.5 bar. Furthermore, since the critical point of nitrous oxide is found at 36.4°C, this operational range can not be increased by much since the PM200 requires gaseous propellants to operate. It is thus unlikely that this chamber pressure limit of 7.1 bar would ever be reached in a real life scenario.

- **SQ-3: Is it possible to eliminate potential limitations imposed by the outcomes of sub-question 1 and 2 by changing certain design parameters? If so, what changes can be made?**

  For radiation cooled thrusters the limitations posed can most realistically only be solved by switching wall materials. The maximum predicted temperatures are around 1350-1440 K, these temperatures are well within the operational limits of several refractory metals such as Tantalum or Niobium.

  For regeneratively cooled thrusters it was found that the thrusters could survive until steady state. No limitations are thus imposed. The only regeneratively cooled design which did not reach the steady state was the regenerative cooling sleeve design. This design could be improved by decreasing the sleeve height. Using current additive manufacturing capabilities this is however impossible. A better strategy would thus be to stay clear of using regenerative cooling sleeve designs and to instead use one of the other designs which was shown to perform better.

  For the designs with ribs little improvement can be made by optimising the designs. It is however recommended to keep the cooling channel size on the larger side (0.7x0.7mm was found to give the best results for the cases considered in this study). Furthermore, the amount of channels and the amount of helices should be kept to a minimum while still keeping the coolant fluid evenly distributed across the thruster surface. This is because in contrast to cooling channels used in large scale engines, for the engines considered in this study the coolant heat transfer should be limited as much as possible at the start of the channel in order to maximise the cooling effectiveness near the end of the channel. Overall this will give the lowest maximum temperatures.

- **SQ-4: From a thermal point of view, what factors on a system level besides cooling of the thruster body should be taken into account when implementing a cooling system design for a thruster used in CubeSat applications?**

  During testing of the PM200 module, three factors were identified which may influence the overall system design of the PM200 module.

  - Igniter heating: During testing it was observed that the igniter became relatively hot. Because the igniter was not included in the simulations performed, it is unknown what temperatures can be expected in the igniter, but measurements showed that its temperature rose more quickly than the temperature of the external throat, one of the hottest parts of the thruster body. It is therefore recommended to monitor the igniter temperature at elongated burn times (>10s) to determine experimentally if the heating of the igniter causes any problems.

– Pressure sensor heating: During testing it was observed that for 10s burn times the pressure sensor mounting points would exceed the maximum operating temperature specified for the pressure sensors. While this did not cause any problems during the experiments performed in this study, it may cause problems if even longer burns are performed. It is recommended to experimentally confirm if any problems arise at longer burn times and to establish their seriousness if they do occur. If any problems arise which introduce an unacceptable risk to safe/reliable operation of the thruster it is recommended to remove the pressure sensors during the acceptance test campaign of the thruster after the thruster performance has been validated. The pressure ports could be welded shut afterwards to prevent any leakage. By adding a thermocouple to the thruster body verification of ignition could be performed while in orbit.

– Tank heating: During testing it was observed that the propellant tank heats up as a result of the thruster firing. The propellant tank cools down less quickly than the thruster body. If many firings are performed in sequence this may lead to a positive feedback loop where the thruster and propellant tank keep rising in temperature. The easiest way to solve this problem is during the operational aspect of the mission. There should be sufficient time between thruster firings to allow for cooldown of the tank, alternatively if multiple firings in sequence are required, the number of firings should be limited. If heat transfer from the tank to the remainder of the satellite is considered unacceptable or if multiple firing sequences in short succession are required a heat shield or insulation could be added to limit the heat transfer from the thruster to the tank.

# 6

# Conclusions and recommendations

The goal of this study was to assess the effectiveness of regenerative cooling and radiation cooling in a small green bi-propellant thruster in order to increase the maximum attainable burn time by developing a numerical model that simulates the heat distribution within the thruster and by implementing one of the two cooling methods in a real life thruster.

All of these goals have been met within the study. A transient numerical model was created based on the finite volume method which was used to assess the effectiveness of regenerative cooling and radiation cooling in CubeSat scale thrusters. This model was verified by comparing the model results with those from commercially available software and the results were found to be in good agreement (within 5-8%).

For calibration and validation of the model, 325 thruster firings were performed using Dawn Aerospace's PM200 thruster and a heat-sink/radiation cooled version of the PM200 specifically designed for this study. During these tests, temperature measurements were taken at various locations. It was found that the model was able to reproduce experimental results for both regeneratively cooled thrusters and radiation/heat-sink cooled thrusters within a margin of error of 15% for all cases which fell within the experimental range (excluding one particular two second burn case using heat-sink cooling).

Using the validated model, several different regenerative cooling channel designs were analysed for a reference thruster to establish the feasibility of regenerative cooling. It was found that the maximum steady state temperature reached in the wall material can be decreased by up to 23% (to a temperature of ~1090 K) using regenerative cooling. This temperature decrease is sufficient to lower the maximum wall temperature to below the allowable temperature to 1150 K (for stainless steel). It was thus shown that regenerative cooling is feasible in steady state under the conditions used in the reference case. Locally, even larger temperature reductions can be achieved using regenerative cooling; in the nozzle, temperature reductions of up to 68% are predicted for the reference design. A simulation of the PM200 design was also performed and a similar result was found. For the regeneratively cooled version of the PM200 a maximum wall temperature of ~1020 K was predicted (this corresponds to a reduction in temperature of 22%).

For a radiation/heat-sink cooled design it was shown that a different wall material would be required to operate in steady state as the wall temperature exceeded the allowable temperature of 1150 K (for stainless steel) for both the reference case (~1420 K) and for the PM200 (~1320 K). A maximum burn time of 27.1s was predicted for the radiation/heat-sink cooled PM200 design.

For the reference thruster, the best design was found to be a helical cooling channel with one helix and a square channel cross section of 0.7x0.7 mm. It was also found that due to the small dimensions of the thruster, the design of the cooling channel has very little effect on the overall maximum temperature reached. For all cooling channel designs (which included ribs) the variation in maximum temperature reached was less than 82 K. It was found that regenerative cooling sleeves perform worse than cooling channel designs which include ribs. For all but one of the cooling sleeve designs the maximum wall temperature exceeded the allowable temperature of 1150 K.

A transient analysis of the different cooling methods was also performed. From this analysis it was found that even if the maximum allowable temperature would unexpectedly be lower than 1150 K, regenerative cooling could still be used to extend the burn time of thrusters compared to heat-sink cooled thrusters. In the most favourable scenario a burn time extension of up to 33.6s could be achieved.

With the results described above the primary research question of this study can be answered. The research question was: *Is it more beneficial to use regenerative cooling or radiation cooling using refractory metals for a self-pressurising green bi-propellant rocket engine used in CubeSat applications?*

The answer to this question is: For the cases presented in this report, it is more beneficial to use regenerative cooling. This is because regenerative cooling reduces the maximum wall temperature sufficiently to make it possible to construct the PM200 out of stainless steel and to reach a steady state without exceeding the maximum allowable temperature of 1150 K. For the radiation cooled designs the steady state can not be reached when using stainless steel as the wall material. Radiation cooling would be possible if a high temperature material such as a refractory metal would be used. However, these materials are typically more expensive and this is thus not beneficial.

While for the designs presented in this report regenerative cooling is a feasible solution, it should be noted that if the chamber pressure is higher, regenerative cooling is not a feasible solution. This is because if the chamber pressure is increased, the heat transfer to the thruster wall is increased. At the same time little performance gains can be made on the coolant side, meaning that at a certain point regenerative cooling will become infeasible. Using the model, it was determined that for the PM200 this turning point is reached at a chamber pressure of approximately 7.1 bar. For chamber pressures below this value regenerative cooling is feasible, for chamber pressures above this value the wall material will exceed the maximum allowable temperature of 1150 K. Since the chamber pressure in the PM200 is dependent on the ambient temperature, it is unlikely that a chamber pressure of 7.1 bar would ever be reached in the PM200 within the specified operational envelope of the PM200 module.

Finally, several recommendations can be made. It is recommended that the outcome of the model is verified by performing a test campaign in which the burn time of the thruster is increased gradually. During this test campaign the test results should continuously be compared with the model results to ensure that the experimental results are still in agreement with the model. If it is found that the test results diverge from the model results, re-calibration of the model is required and the model results may have to be re-evaluated.

During the proposed test campaign special attention should be paid to the igniter and the pressure sensors. During the experiments performed in this study it was found that the igniter heated up relatively fast compared to other components of the thruster. The igniter was not included in the numerical model and thus the final temperature of the igniter was not predicted. Therefore, even though the model predicts that the regeneratively cooled PM200 thruster can burn in steady state, heating issues with the igniter may still cause problems. During experiments it was also found that the temperature of the pressure sensor mounts exceeded the maximum operating temperature of the pressure sensors. While this did not cause any problems, it may cause problems if even longer burn times are performed.

Lastly, during testing it was found that after a burn, the tank heated up slightly. For a 5s burn the tank temperature increased by approximately 1-1.5 K. It is expected that for longer burn times this increase may be even larger. If for a particular mission this is a problem, it is recommended to add thermal insulation between the thruster and the tank module to limit the heat transfer to the tank. Alternatively a heat shield could be constructed around the thruster to shield the tank.

(This page was intentionally left blank)

# Bibliography


[1] M. Aghaie-Khafri and A. Zargaran. High temperature tensile behavior of a PH stainless steel. *Materials Science and Engineering A*, 527(18-19):4727–4732, July 2010. doi: /10.1016/j.msea.2010.03.099.

[2] D.R. Bartz. A Simple equation for Rapid Estimation of Rocket Nozzle Convective Heat Transfer Coefficients. *Jet Propulsion*, 27(1):49–53, January 1957. doi: /10.2514/8.12572.

[3] D.R. Bartz. Factors Which Influence the Suitability of Liquid Propellants as Rocket Motor Regenerative Coolants. *Jet Propulsion*, 28(1):46–53, January 1958. doi: /10.2514/8.7223.

[4] D.R. Batha, J.G. Campbell, M.D. Carey, and A.R. Nagy. Thrust chamber cooling techniques for spacecraft engines, volume II. Technical report, National Aeronautics and Space Administration / Marquardt, 1963.

[5] J.J. Bernard and J. Génot. *Radiation Cooling of Thrust Nozzles*. NATO Advisory Group For Aerospace Research & Development, 1975.

[6] Mathieu Bernier. An Experimental Investigation of Heat Transfer to Hydrogen Peroxide in Microtubes. Master's thesis, Massachusetts Institute of Technology, 2004. Available through the MIT Library at: /1721.1/27068.

[7] Marina Campolo, Michele Andreoli, and Alfredo Soldati. Computing flow, combustion, heat transfer and thrust in a micro-rocket via hierarchical problem decomposition. *Microfluidics and Nanofluidics*, 7(1):57–73, July 2009. doi: /10.1007/s10404-008-0362-9 .

[8] Ning Hsing Chen. An Explicit Equation for Friction Factor in Pipe. *Industrial & Engineering Chemistry Fundamentals*, 18(3):296–297, 1979. doi: /10.1021/i160071a019.

[9] Izabel Cecilia Ferreira de Souza Vicentin, Carlos Henrique Marchi, Antonio Carlos Foltran, Diego Moro, Nicholas Dicati Pereira da Silva, Marcos Carvalho Campos, Luciano Kiyoshi Araki, and Alysson Nunes Diógenes. Theoretical and experimental heat transfer in solid propellant rocket engine. *Journal of Aerospace Technology and Management*, 11, 2019. doi: /10.5028/jatm.v11.1066.

[10] J. Díaz-Alvarez, J.L. Cantero, H. Miguélez, and X. Soldani. Numerical analysis of thermomechanical phenomena influencing tool wear in finishing turning of Inconel 718. *International Journal of Mechanical Sciences*, 82:161–169, May 2014. doi: /10.1016/j.ijmecsci.2014.03.010.

[11] Armin Herbertz and Markus Selzer. Analysis of coolant mass flow requirements for transpiration cooled ceramic thrust chambers. *Transactions of the Japan society for aeronautical and space sciences, Aerospace technology Japan*, 12(29):31–39, 2014. doi: /10.2322/tastj.12.Pa_31.

[12] Philip Hill and Carl Peterson. *Mechanics and Thermodynamics of Propulsion - 2nd edition*. Pearson Education, 1991. ISBN 978-0201146592.

[13] Carole Joppin. Cooling Performance of Storable Propellants for a micro rocket engine. Master's thesis, Massachusetts Institute of Technology, 2002. Available through the MIT Library at: /1721.1/8130.

[14] J.W.Cornelisse, H.F.R. Schoyer, and K.F. Wakker. *Rocket Propulsion and Spaceflight Dynamics*. Pitman Publishing Limited, 1979. ISBN 0-273-01141-3.

[15] Akira Kakami, Motoki Yamanaka, Tatsuya Matsushita, and Takeshi Tachibana. Performance of 1-N class liquefied gas propellant thruster. *49th AIAA/ASME/SAE/ASEE Joint Propulsion Conference & Exhibit, AIAA 2013-3986, San Jose, California, USA*, June 15 2013. doi: 10.2514/6.2013-3986.

[16] Arif Karabeyoglu, Jonny Dyer, Jose Stevens, and Brian Cantwell. Modeling of $N_2O$ Decomposition Events. *44th AIAA/ASME/SAE/ASEE Joint Propulsion Conference & Exhibit, AIAA 2008-4933, Hartford, Connecticut, USA*, page 29, 21 - 23 Jul 2008. doi: /10.2514/6.2008-4933.

[17] Christoph Kirchberger, Robert Wagner, Hans-Peter Kau, Sebastian Soller, Philip Martin, Marc Bouchez, and Christophe Bonzom. Prediction and analysis of heat transfer in small rocket chambers. *46th AIAA Aerospace Sciences Meeting and Exhibit, Reno, Nevada*, 7-10 January, 2008. doi: /10.2514/6.2008-1260.

[18] Christoph Ulrich Kirchberger. *Investigation on Heat Transfer in Small Hydrocarbon Rocket Combustion Chambers*. PhD thesis, Technische Universitat Munchen, Germany, 2014.

[19] Detlef Kuhl, Andrea Holzer, and Oskar J. Haidn. Computational solution of the inverse heat conduction problem of rocket combustion chambers. *35th Joint Propulsion Conference and Exhibit, AIAA-99-2913, Los Angeles, California, USA.*, page 11, 20 June 1999 - 24 June 1999. doi: /10.2514/6.1999-2913.

[20] E.V. Lebedinsky et al. *Working Processes in Liquid-Propellant Rocket Engine and Their Simulation (in Russian: Рабочие процессы в жидкостном ракетном двигателе и их моделирование)*. JSC "Mashinostroenie" Publishing House, 2008. ISBN 978-5-217-03433-8.

[21] Eric W. Lemmon and Roland Span. Short Fundamental Equations of State for 20 Industrial Fluids. *Journal of Chemical & Engineering Data*, 51:785–850, 2006. doi: /10.1021/je050186n.

[22] A.P. London, A. A. Ayon, A.H. Epstein, S.M. Spearing, T. Harrison, Y. Peles, and J.L. Kerrebrock. Microfabrication of a high pressure bipropellant rocket engine. *Sensors and Actuators A: Physical*, 92:351–357, 1 August 2001. doi: /10.1016/S0924-4247(01)00571-4.

[23] Francesco Di Matteo. *Modelling and Simulation of Liquid Rocket Engine Ignition Transients*. PhD thesis, Sapienza University of Rome, Italy, 2011.

[24] Francesco Di Matteo, Marco De Rosa, and Marcello Onofri. Semi-Empirical Heat Transfer Correlations In Combustion Chambers For Transient System Modelling. *Space Propulsion Conference, San Sebastian, Spain*, 2010.

[25] P. Miotti, M. Tajmar, C.Guraya, F.Perennes, B. Marmiroli, A. Soldati, M. Campolo, C. Kappenstein, R. Brahmi, and M. Lang. Bipropellant Micro-Rocket Engine. *40th AIAA/ASME/SAE/ASEE Joint Propulsion Conference & Exhibit, AIAA 2004-3690, Fort Lauderdale, Florida, USA*, 11 - 14 July 2004. doi: /10.2514/6.2004-3690.

[26] J.P. Moore, R.S. Graves, and R.K. Williams. Thermal Transport Properties of Niobium and Some Niobium Base Alloys from 80 to 1600 K. *European thermophysical properties conference, Antwerp, Belgium*, 11:7, 30 Jun - 4 Jul 1980.

[27] F. Moukalled, L. Mangani, and M. Darwish. *The Finite Volume Method in Computational Fluid Dynamics*. Springer, Cham, 2015. ISBN 978-3-319-16873-9. doi: /10.1007/978-3-319-16874-6.

[28] M. H. Naraghi and M. Foulon. A simple approach for thermal analysis of regenerative cooling of rocket engines. *Proceedings of IMECE2006 2008 ASME International Mechanical Engineering Congress and Exposition, Boston, Massachusetts*, October 31-November 6, 2008.

[29] Jose C. Pascoa, Odelma Teixeira, and Gustavo Filipe. A review of propulsion systems for cubesats. *Proceedings of the ASME 2018 International Mechanical Engineering Congress and Exposition, Pittsburgh, Pennsylvania , USA*, page 8, November 9-15, 2018. doi: /10.1115/IMECE2018-88174.

[30] Nikolaos Perakis and Oskar J. Haidn. Inverse heat transfer method applied to capacitively cooled rocket thrust chambers. *International Journal of Heat and Mass Transfer*, 131:150–1666, March 2019. doi: /10.1016/j.ijheatmasstransfer.2018.11.048.

[31] A. Ponomarenko. RPA: Tool for Rocket Propulsion Analysis - Thermal Analysis of Thrust Chambers. Technical report, Rocket Propulsion Software+Engineering UG, Eichendorffstr. 7, 53819 Neunkirchen-Seelscheid, Germany, June 2012.

[32] A. Ponomarenko. RPA - Tool for Rocket Propulsion Analysis. *Space Propulsion Conference, Colgone, Germany*, May 19-22, 2014.

[33] S.J. Powell. CubeSat Micro-Propulsion - Design and Validation of a Micro Bi-Propellant Rocket Motor. Master's thesis, Delft University of Technology, 2015. Available through the TU Delft Repository at: resolver.tudelft.nl/uuid:a6de0cf0-a562-41e0-8b34-b53b839385d6.

[34] Stefan Powell, Tobias Knop, and Steven Engelen. Experimental Evaluation of a Green Bi-Propellant Thruster for Small Satellite Applications. *Small Satellite Conference, Logan, USA*, 2016.

[35] Yousef Saad. *Iterative Methods for Sparse Linear Systems - 2nd edition.* Society for Industrial and Applied Mathematics, 2003. ISBN 978-0898715347.

[36] I.V. Savchenko and S.V. Stankus. Thermal conductivity and thermal diffusivity of tantalum in the temperature range from 293 to 1800 K. *Thermophysics and Aeromechanics*, 15(4):679–682, December 2008. doi: /10.1007/s11510-008-0017-z.

[37] C. Scharlemannn et al. Turbo-Pump Fed Miniature Rocket Engine. *41st AIAA/ASME/SAE/ASEE Joint Propulsion Conference & Exhibit, AIAA 2005-3654, Tucson, Arizona*, July 10th, 2005. doi: /10.2514/6.2005-3654.

[38] L. Schoenman and P. Block. Laminar boundary-layer heat transfer in low-thrust rocket nozzles. *Journal of Spacecraft and Rockets*, 5(9):1082–1089, 1968. doi: /10.2514/3.29425.

[39] B.K. Soni. Hybrid techniques in computational fluid dynamics. Technical report, Engineering Research Center for Computational Field Simulation, Mississippi State University, 1998.

[40] George P. Sutton and Oscar Biblarz. *Rocket Propulsion Elements - Eight edition.* John Wiley And Sons Ltd, 2010. ISBN 978-0-470-08024-5.

[41] C.L. Tien, M.F. Modest, and C.R. McCreight. Infrared Radiation Properties of Nitrous Oxide. *Journal of Quantitative Spectroscopy & Radiative Transfer*, 12(2):267–277, 1972. doi: /10.1016/0022-4073(72)90037-4.

[42] Michael Tsay, John Frongillo, Derek Lafko, and Jurg Zwahlen. Development Status and 1U CubeSat Application of Busek's 0.5N Green Monopropellant Thruster. *28th AIAA/USU Small Satellite Conference, Logan, USA*, 2014.

[43] Tasuku Uraoka, Yoshikazu Iwao, Yasuyuki Yano, and Akira Kakami. Improvement of combustion stability of $N_2O$/DME bipropellant in vacuum. *Transactions of The Japan Society for Aeronautical and Space Sciences, Aerospace Technology Japan*, 14:73–81, 2015. doi: /10.2322/tastj.14.Pa_73.

[44] Juan J. Valencia and Peter N. Quested. Thermophysical Properties. *ASM Handbook: Casting*, 15:468–481, 2008. doi: /10.1361/asmhba0005240.

[45] P.M. van den Berg. Thermal aspects and cooling techniques for small green bi-propellant thrusters - a literature review. Technical report, Delft University of Technology, Faculty of Aerospace Engineering, Kluyverweg 1, 2629 HS Delft, The Netherlands, 2019.

[46] H.K. Versteeg and W. Malalasekera. *An Introduction to Computational Fluid Dynamics: The Finite Volume Method, Second Edition*. Pearson, 2007. ISBN 978-0-13-127498-3.

[47] Thyrso Villela, Cesar A. Costa, Alessandra M. Brandão, Fernando T. Bueno, and Rodrigo Leonardi. Towards the Thousandth CubeSat: A Statistical Overview. *International Journal of Aerospace Engineering*, 2019:13, January 10 2019. doi: /10.1155/2019/5063145 .

[48] Jeroen Wink, Tobias Knop, Stefan Powell, and Robert Werner. Development and Ground Testing of a 200 N Vacuum thrust class thruster using a novel Nitrous Oxide/Propene propellant combination. *Space Propulsion Conference, Seville, Spain*, 2018.

[49] Jeroen Wink, Tobias Knop, Stefan Powell, Robert Werner, and Steven Engelen. Development and Ground Testing of The PM200 Bi-Propellant Propulsion Module. *Space Propulsion Conference, Seville, Spain*, 2018.

[50] H. Ziebland and R.C. Parkinson. *Heat Transfer in Rocket Engines*. NATO Advisory Group For Aerospace Research & Development, 1971.

# A
# Project Assignment from Dawn Aerospace

# BT400.10 Thermal Analysis and Optimization

# 1 Introduction

Dawn Aerospace has developed a 1N bipropellant thruster based on Nitrous Oxide and Propene for CubeSat applications. It has undergone substantial qualification testing and is due to be flown in space in August 2019. It is known as the BT400.10.

The most significant challenges in development of such a small yet high performance thruster center around thermal management and dealing with excess heat. Volume constraints mean that additive manufacturing is required and thus only a limited set of materials are available, making thermal management even more challenging. However, additive manufacturing does allow the for significant freedom in the design of otherwise difficult to implement cooling methods such as regenerative cooling, radiative fins, capacitive cooling or others. This leaves significant scope for improvement on the current design.

# 2 Problem statement

The BT400.10 thruster is currently limited to a maximum burn time of 10s. This limit is chosen to prevent damage to the thruster due to overheating. It has been experimentally determined to be safe, although longer times have not been tested due to a lack of time and resources.

While a 10s burn time is sufficient for many satellite maneuvers, there are many others still that require far longer duration burns, typically up to 60s. It is therefore desirable to extend the maximum burn time to 60s or if possible, indefinitely.

# 3 Task description

This thesis should endeavor to model, predict, optimize and evaluate the thermal design of the BT400.10 thruster. It shall achieve this through the following basic steps:

1. Develop an analytical model of the existing thruster to predict the heating rate. Validate this model through the use of existing thruster data. This model may be based on existing Dawn Aerospace analytical models
2. Conduct a sensitivity analysis to discover which design parameters have the most significant effect on the heating rate.
3. Use the information gained in 1 and 2 to propose design changes and asses the effectiveness of the proposed design changes using the developed tools.
4. Design and manufacture one of the proposed designs with assistance from Dawn Aerospace
5. Experimentally determine the performance of the new thruster design, with assistance from Dawn Aerospace

If time permits, the model developed in step 1 may be supported by CFD simulations.

(This page was intentionally left blank)

# B

# Numerical Model - Additional Information

In this appendix some additional information will be given about the numerical model which might be useful for using the program. Furthermore, some explanation will be given about the failure analysis module. This module was finished only partially but the parts which were finished can still be used in the model if required.

## B.1. User information

In this section some additional information will be given about the numerical model which might be useful for using the program. In section B.1.1 a list will be given which explains what every code module in the program does and what other modules each module calls upon. In section B.1.2 a list of all input parameters is given, these are all the parameters that a user can change when using the program. An explanation for each parameter is also given. All other parameters present in the program should not be changed.

### B.1.1. Modules within program

Table B.1: Code modules present within the numerical model

| **Module Name** | **Function** | **Calls upon** |
|---|---|---|
| Thermal_Main | Main program, used to start the code, contains most of the input parameters. Does not perform any calculations but does generate the output files. | Constants, WallMaterialDatabase, EngineGeometry, Regenerative, Radiation |
| Constants | Stores constants used throughout the code such as the ambient temperature or constants like the Stefan-Boltzmann constant | - |
| WallMaterialDatabase | Stores all the wall material and TBC properties. | - |
| EngineGeometry | Generates the engine geometry and mesh. Also specifies all cell centroids and surface vectors. | MeshGenerator, RegenGeometry |
| MeshGenerator | Determines the axial positions of the mesh. | - |

| | | |
|---|---|---|
| RegenGeometry | Generates the geometry of the regenerative cooling channel | - |
| Regenerative | Performs the main program loops (x,y and t loop) for the Regeneratively cooled case. All heat flows are calculated in this module too. | CEA, FlowParameters, EnginePerformance, GradientCalculator, HeatInCalculator, WallThermalConductivity, TimeStepCalculator, ForwardEuler, MatrixCoefficientCalculator, BackwardsEuler, DirectSteadyState, GraphicPlotter, FailureAnalysis, CoolantFlowParameters, HeatTransferCoolant |
| Radiation | Performs the main program loops (x,y and t loop) for the Radiation cooled case. All heat flows are calculated in this module too. | CEA, FlowParameters, EnginePerformance, GradientCalculator, HeatInCalculator, WallThermalConductivity, TimeStepCalculator, ForwardEuler, MatrixCoefficientCalculator, BackwardsEuler, DirectSteadyState, GraphicPlotter, FailureAnalysis |
| CEA | Creates the input file for the CEA program, runs the CEA program and reads out the CEA output file | - |
| FlowParameters | Calculates the flow parameters of the combustion gases inside the combustion chamber | - |
| EnginePerformance | Calculates the fuel and oxidiser mass flows | - |
| GradientCalculator | Calculates the temperature for all vertices, calculates the temperature gradient at every centroid | - |
| HeatInCalculator | Calculates the heat transfer coefficients for the heat transfer from the combustion gases to the chamber wall | - |
| WallThermalConductivity | Calculates the thermal conductivity of the wall based on the wall temperature | - |
| TimeStepCalculator | Calculates the maximum allowable time step for the Forward Euler case | - |

| | | |
|---|---|---|
| ForwardEuler | Performs the time stepping for the Forward Euler case | - |
| MatrixCoefficientCalculator | Generates the matrices required for the implicit and Direct steady state methods | - |
| BackwardsEuler | Performs the time stepping for the implicit method | Fluxlimiter |
| DirectSteadyState | Performs the iteration loop for the direct steady state method | - |
| GraphicPlotter | Plots (intermediate) results | - |
| FailureAnalysis | Checks if the engine will have failed already | - |
| CoolantFlowParameters | Calculates all flow parameters of the coolant not related to the heat transfer such as the coolant velocity and the pressure drop | EquationOfState |
| HeatTransferCoolant | Calculates the heat transfer coefficients for the heat transfer to and from the coolant | - |
| EquationOfState | Calculates the coolant density and heat capacity | - |
| FluxLimiter | Limits the heat fluxes and temperatures for regeneratively cooled designs to ensure that only physical solutions are calculated. | - |

## B.1.2. Input Parameters

Table B.2: Settings which can be adjusted in the model

| **Parameter** | **Options** | **Explanation** | **Set in** |
|---|---|---|---|
| enginedefinition | PM200, NP22, Custom, VerificationRegen, PM200Straight | Determines which engine should be simulated | Thermal_Main |
| outputtemps | Kelvin, Celsius | Determines if the output is given in Kelvin or Celsius | Thermal_Main |
| t_burn | - | Determines the burn time | Thermal_Main |
| t_sim | - | Determines the total simulation time | Thermal_Main |
| dt_plot | - | Determines the time step between plotting and saving data | Thermal_Main |
| timestepscheme | ForwardEuler, BackwardsEuler, SteadyState | Determines which time stepping scheme is used | Thermal_Main |
| relaxationdefault | 0-2 | Determines the default relaxation parameter for the direct steadystate approach | Thermal_Main |

| | | | |
|---|---|---|---|
| pulsemode | On, Off | Activates Pulsed operation. (Only implemented for the radiation cooled case) | Thermal_Main |
| pulsetemp | - | Determines the steady state pulsing temperature | Thermal_Main |
| pulseburntime | - | Determines the length of the pulse when in pulsed operation | Thermal_Main |
| plotsetting | Three_D_inner, Two_D_tempdistr, One_D_tempdistr, None | Determines how the program output is plotted (3D, 2D, 1D) | Thermal_Main |
| heatfluxcase | Bartz, Cornelisse, None | Determines which convective heat transfer model is used for the combustion gases to the wall | Thermal_Main |
| radheatfluxcase | Schmidt, Shack, Bonzom, None | Determines which radiation heat transfer model is used for the combustion gases to the wall | Thermal_Main |
| regencoolingtype | Rectangular_Coil, Rectangular_Axial | Determines if the cooling channels are axial or helical | Thermal_Main |
| coolingchannelshape | Rectangular, Circular | Determines the internal shape of the cooling channel | Thermal_Main |
| inlet_type | Regular, Reservoir | Determines what type of inlet condition is used for the cooling channel. If Reservoir is selected the first coolant channel cell is modelled as an annulus around the whole thruster circumference | Thermal_Main |
| reservoir_diameter | - | Determines the reservoir diameter if the reservoir inlet type is selected | Thermal_Main |
| coolantcase | Oxidizer, Fuel , Both | Determines which of the propellants is used as a coolant. Currently only the oxidizer option has been implemented. | Thermal_Main |
| coolantfluxcase | SiederTate, DittusBoelter | Determines which heat transfer model is used for the heat transfer between the coolant and the thruster wall | Thermal_Main |
| wallmaterial | StainlessSteel, Inconel, Tantalum | Determines which wall material is used | Thermal_Main |
| TBC_status | Yes, No | Determines if a TBC is used | Thermal_Main |
| TBCmaterial | YSZ | Determines the TBC material | Thermal_Main |
| t_TBC | - | Determines the thickness of the TBC | Thermal_Main |
| dy_spaceTBC | integer | Determines the amount of cells in the TBC layer | Thermal_Main |
| dx_space | integer | Determines the amount of cells in the x direction | Thermal_Main |

| | | | |
|---|---|---|---|
| dy_space | integer | Determines the amount of cells in the y (radial) direction | Thermal_Main |
| celldistribution_regen | integer | Determines the percentage of cells below and above the regenerative cooling channel | Thermal_Main |

## B.2. Additional code module: Failure analysis

In chapter 3 it was explained how the temperature profile of the thruster wall was calculated within the numerical model. The main reason to determine this temperature profile was to get an idea on whether the thruster will fail or not. Therefore, in order to get an even better idea a basic failure analysis was implemented within the model during the early stages of the project. However as the project and also the goals of the project progressed the failure analysis became redundant. As a result this module was never completely finished. Some parts were however finished and these parts can still be used within the model. The analysis was not meant to give an accurate estimation of when the thruster would fail or to pinpoint the exact failure point but rather it was implemented as a sanity check and to give the user of the program a rough estimate of the feasibility of a given design. The intention was to implement five failure modes:

- Melting of the wall material.
- Coolant decomposition.
- Radial burst failure of the combustion chamber.
- Inward failure of the cooling channel.
- Outward failure of the cooling channel.

In the end, only the first three failure modes were implemented within the model. The following methodology was used: To calculate the failure point of the thruster, the average temperature of the wall material is used for each x position. To calculate the average temperature first the volume of every cell located at the corresponding x position is calculated. The volume of every cell is multiplied with its temperature and the whole is divided by the total volume of the cells to get the weighted average temperature of all the cells at a certain x position. This temperature is then compared to the melting point of the wall material. If the calculated temperature exceeds the melting temperature of the material used the programs considers the thruster to have failed. Upon failure a dialogue box opens up on the program which prompts the user. The user can choose to continue the simulation or to stop the simulation. In case the simulation is continued the program will assume that the thruster can not fail and no further failure analysis will be performed for subsequent time steps.

To determine whether radial burst failure occurs within the thruster the stress in the wall of the thruster has to be calculated. To get a simple estimate of the stress in the wall each cross section is modelled as a cylinder. For a cylindrical structure the stress can be calculated using equation B.1.

$$\sigma_i = \frac{p_i \cdot r_i}{t_i} \tag{B.1}$$

Where $t_i$ is the wall thickness of the current wall element and $p_i$ is the local pressure as calculated from equation 3.2. The stress in the wall is compared to the yield stress of the wall material. As the wall heats up the yield stress is usually not a constant value but it instead varies with temperature. The equations describing the yield stress of a material usually take a form as can be seen in equation B.2 where the constants are dependent on the specific material used. In the model presented here relations by [1] were used.

$$\sigma_{yield,i} = B + \sum_{n=1}^{m} A_m \cdot T_i^m \tag{B.2}$$

One of the problems with the kind of equations described above is that they are often only valid for a limited temperature range. Especially for temperatures near the melting point of the material these equations are often not valid which limits their accuracy for predicting the failure point. Nevertheless some insight is still gained by using these kind of equations and a rough estimation of the failure point can still be made.

# C

# Determination of O/F and Mass Flow Measurements

For Research Thruster 2, several cold flow measurements were performed to determine the oxidiser and fuel mass flows and the Oxidiser to Fuel ratio (O/F). This was done for several reasons: first of all it was done to check whether or not the mass flows were according to the design specifications. It was also done to check if there were any leaks or issues with the thruster and lastly it was done to determine the exact O/F which was needed as an input for the model. Due to tiny manufacturing differences there will always be some small differences in O/F between each thruster, so the O/F needs to be determined for each thruster. For the same thruster, the O/F can also vary in between burns. This can for example happen if the fuel and oxidiser tank have a slightly different temperature, this in turn results in a slightly different pressure ratio between the oxidiser and fuel tanks which leads to a slightly different ratio in mass flows and therefore in O/F. The mass flow tests which are described here were performed with both tanks at the same temperature, which is the nominal case.

The test set-up used for the mass flow measurements can be seen in figure C.1. The set-up is relatively simple but was found to be very effective. The set-up used did not directly measure the mass flow, instead it measured the volume of propellant gas expelled through the nozzle. This was for two reasons: the mass flows involved were tiny, so measuring the mass directly was difficult as there was always a large amount of noise in the data. Measuring the mass directly was done by measuring the module before and after the test, the problem with this however was that if the module leaks somewhere, the mass flows from the measurement will seem like the correct mass flows, however the actual mass flows going through the combustion chamber could still be incorrect. By measuring the gas volume going through the nozzle it was certain that the correct mass flow was measured.

Two slightly different set-ups were used depending on whether the mass flow for the oxidiser or the mass flow for the fuel was measured. The main reason for this was to accommodate for the volume of gas expelled. Because the fuel mass flow is much lower than the oxidiser mass flow, the volume of propylene expelled was much smaller than the volume of nitrous oxide expelled. In figure C.1 the set-up used for measuring the oxidiser mass flow can be seen. The set-up worked as follows: RT2 was connected to the PM200 module in the same way as how it would be mounted during a normal firing test. In the nozzle of RT2 a plug was placed which was connected to a hose. This hose was connected to a T-piece which connected to a syringe on one side and a measuring cup suspended upside down in a bucket of water on the other side. To ensure that the measuring cup was level with the water level it was mounted on a wooden beam which was put on the top of the bucket. Using the syringe the air was pumped out of the measuring cup, raising the water level inside of it. Since the syringe was much smaller than the measuring cup, the syringe had to be emptied multiple times. A valve between the syringe and the T-piece was used to ensure the pressure in the measuring cup

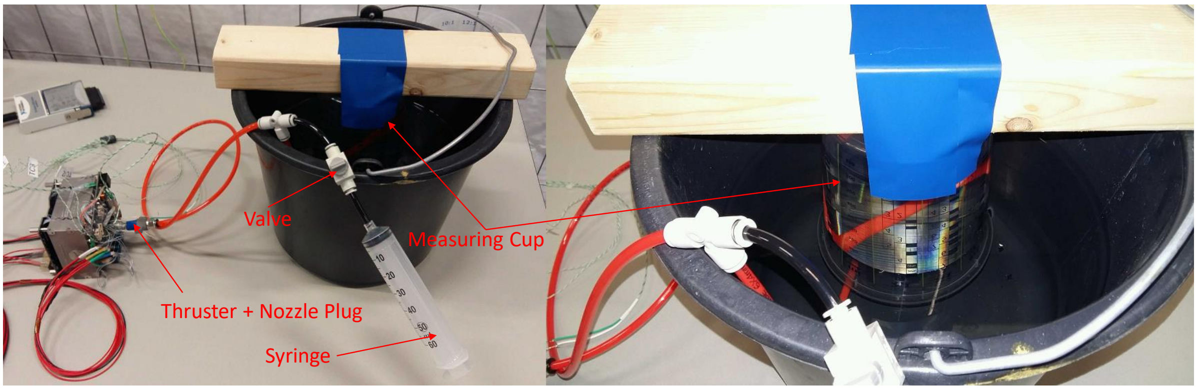


Figure C.1: Test set-up for the mass flow measurements

could not equalise with the ambient pressure. Once the water level reached a certain target level, a cold flow test was performed using either the oxidiser or fuel. By measuring the water displacement in the measurement cup, the volume of expelled gas could be measured within an accuracy of about 1 ml. The measured volume was then converted to a volume flow rate by dividing the measured volume by the “burn time”. This volume flow rate was then converted to a mass flow rate by multiplying the volume flow rate with the density. The density is equal to the saturation density under ambient pressure. For determining the fuel mass flow a similar set-up was used, in this case the measuring cup was however replaced by a second syringe to allow for a more accurate measurement of the smaller gas volume. Tests were performed with two people: one person was actuating the thruster and another person was reading off the measurement. To avoid bias, burn times were varied in a random pattern and the person reading off the measurement was not told in advance what the burn time would be.

The results from the method described above were found to be very consistent. All the measured mass flows for the fuel matched within 0.2 mg/s (0.7% of the total fuel mass flow) of each other and the oxidiser the mass flows matched within 8.3 mg/s (3.4% of the total oxidiser mass flow) of each other. The measurement error of approximately 1 ml as mentioned before corresponded to an error in the mass flow of less than 0.9 mg/s for the fuel and to an error of less than 0.5 mg/s for the oxidiser.

The final mass flows were determined by taking the average mass flow values over all tests. For RT2 a fuel mass flow of 28.55 mg/s and an oxidiser mass flow of 245.15 mg/s were found. This corresponds to an O/F of 8.587, which is close to the optimum O/F of 8.223.

# D

# Additional Test and Validation Data

In this appendix test data and additional plots from chapter 4 are presented. First the normalised raw test data from the tests performed using RT2 are presented in section D.1. Afterwards the planes of best fit for the 4s burn are shown and finally the extended error plots for the 3s burn are presented.

## D.1. Tabulated test data

In table D.1 the temperature data obtained from the tests performed with RT2 are tabulated. All temperature data is normalised with respect to the overall maximum temperature recorded over all tests. The chamber pressure data is normalised with respect to the reference pressure which can be assumed to be 3.5 bar. Measurements indicated with red text are faulty measurements where it was confirmed that the thermocouple was not attached properly. These data points were not included in the creation of the planes of best fit, nor where they used for any other analysis. The cell colours indicate at what azimuth angle the thermocouple was attached to the thruster. The meaning of the colours is shown in figures D.1-D.6. In these figures the test numbers are indicated in three colours: red means that the thermocouple position was unknown, orange means that the thermocouple position indicated is an approximation (this was done to prevent multiple points close together at similar azimuth angles), green means that the position is as exact as could be measured. All the temperature values in table D.1 are the temperature values in the reference point (the point where the interior throat reaches the maximum temperature).

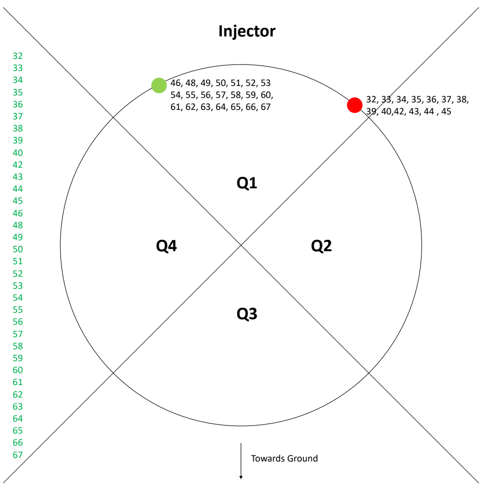


Figure D.1: Thermocouple positions for the injector

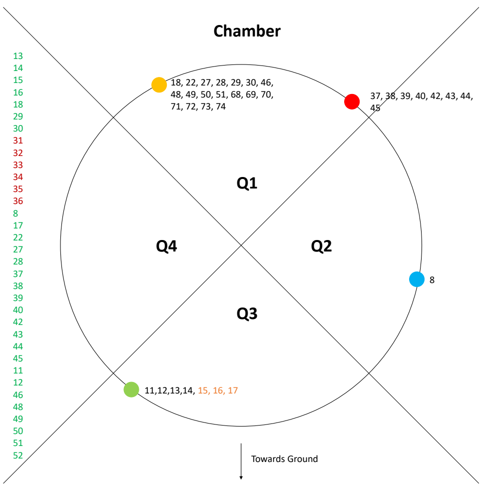


Figure D.2: Thermocouple positions for the chamber

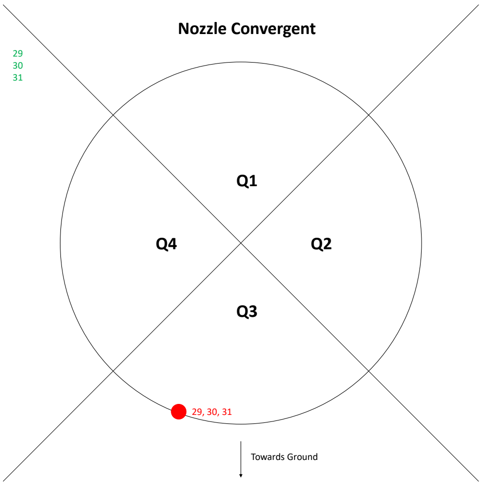


Figure D.3: Thermocouple positions for the nozzle convergent

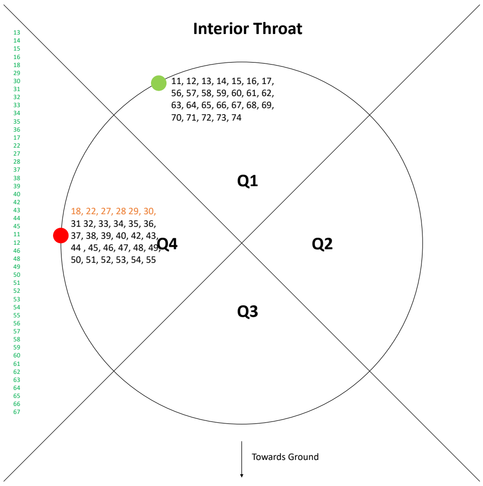


Figure D.4: Thermocouple positions for the interior throat

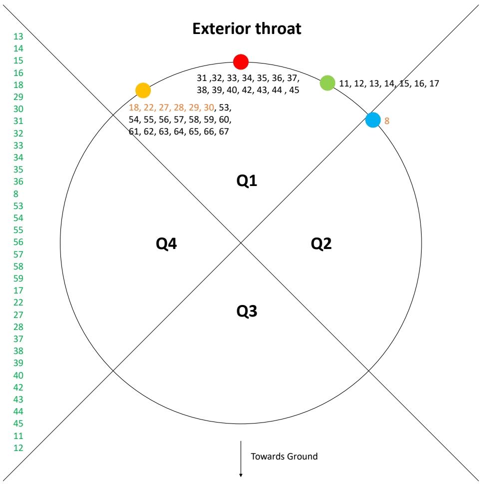


Figure D.5: Thermocouple positions for the exterior throat

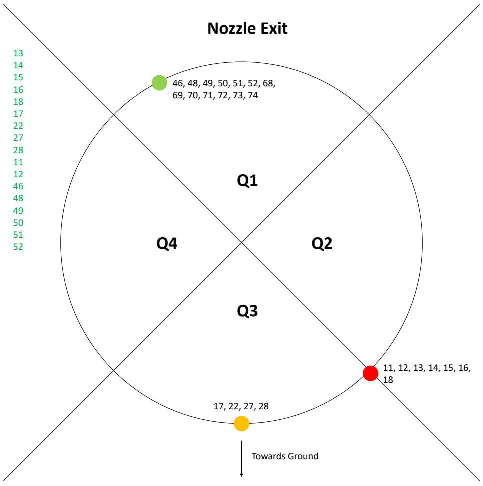


Figure D.6: Thermocouple positions for the nozzle exit

Table D.1: Temperature measurement data obtained for RT2

| Test date | Test # | Burn time | Injector | Chamber | Nozzle Convergent | Interior Throat | Exterior throat | Nozzle Exit | Chamber Pressure |
|---|---|---|---|---|---|---|---|---|---|
| x-position (normalised) | | | 0.00 | 0.20 | 0.38 | 0.50 | 0.58 | 0.97 | |
| Test 13 (22-06-2020) | 13 | 3 | N/A | 0.28 | N/A | 0.78 | 0.57 | 0.14 | 1.01 |
| Test 14 (22-06-2020) | 14 | 3 | N/A | 0.28 | N/A | 0.81 | 0.57 | 0.13 | 1.03 |
| Test 15 (23-06-2020) | 15 | 3 | N/A | 0.23 | N/A | 0.73 | 0.53 | 0.11 | 0.92 |
| Test 16 (23-06-2020) | 16 | 3 | N/A | 0.29 | N/A | 0.78 | 0.59 | 0.13 | 1.02 |
| Test 18 (26-06-2020) | 18 | 3 | N/A | 0.37 | N/A | 0.74 | 0.59 | 0.16 | 1.05 |
| Test 29 (26-06-2020) | 29 | 3 | N/A | 0.47 | 0.61 | 0.62 | 0.64 | N/A | 1.16 |
| Test 30 (26-06-2020) | 30 | 3 | N/A | 0.48 | 0.63 | 0.63 | 0.65 | N/A | 1.17 |
| Test 31 (01-07-2020) | 31 | 3 | N/A | 0.38 | 0.50 | 0.51 | 0.55 | N/A | 0.90 |
| Test 32 (01-07-2020) | 32 | 3 | 0.20 | 0.31 | N/A | 0.70 | 0.13 | N/A | 0.95 |
| Test 33 (01-07-2020) | 33 | 3 | 0.23 | 0.07 | N/A | 0.71 | 0.14 | N/A | 0.99 |
| Test 34 (01-07-2020) | 34 | 3 | 0.24 | 0.07 | N/A | 0.71 | 0.14 | N/A | 1.01 |
| Test 35 (02-07-2020) | 35 | 3 | 0.23 | 0.36 | N/A | 0.63 | 0.17 | N/A | 0.93 |
| Test 36 (02-07-2020) | 36 | 3 | 0.22 | 0.34 | N/A | 0.64 | 0.15 | N/A | 0.94 |
| Test 8 (19-06-2020) | 8 | 3 | N/A | 0.24 | N/A | N/A | 0.16 | N/A | 0.87 |
| Test 46 (03-07-2020) | 46 | 3 | 0.26 | 0.27 | N/A | 0.53 | N/A | 0.22 | 0.97 |
| Test 48 (03-07-2020) | 48 | 3 | 0.29 | 0.31 | N/A | 0.56 | N/A | 0.19 | 1.02 |
| Test 49 (03-07-2020) | 49 | 3 | 0.29 | 0.30 | N/A | 0.57 | N/A | 0.19 | 1.05 |
| Test 50 (03-07-2020) | 50 | 3 | 0.30 | 0.32 | N/A | 0.58 | N/A | 0.19 | 1.07 |
| Test 51 (03-07-2020) | 51 | 3 | 0.29 | 0.31 | N/A | 0.58 | N/A | 0.19 | 1.09 |
| Test 53 (07-07-2020) | 53 | 3 | 0.24 | N/A | N/A | 0.54 | 0.55 | N/A | 0.92 |
| Test 54 (07-07-2020) | 54 | 3 | 0.27 | N/A | N/A | 0.56 | 0.57 | N/A | 0.93 |
| Test 55 (07-07-2020) | 55 | 3 | 0.27 | N/A | N/A | 0.59 | 0.58 | N/A | 0.97 |
| Test 56 (07-07-2020) | 56 | 3 | 0.21 | N/A | N/A | 0.64 | 0.64 | N/A | 1.00 |
| Test 57 (07-07-2020) | 57 | 3 | 0.22 | N/A | N/A | 0.65 | 0.64 | N/A | 1.01 |
| Test 58 (07-07-2020) | 58 | 3 | 0.23 | N/A | N/A | 0.66 | 0.63 | N/A | 1.03 |
| Test 59 (07-07-2020) | 59 | 3 | 0.23 | N/A | N/A | 0.67 | 0.61 | N/A | 1.05 |
| Test 60 (08-07-2020) | 60 | 3 | 0.19 | N/A | N/A | 0.58 | 0.53 | N/A | 0.91 |
| Test 61 (08-07-2020) | 61 | 3 | 0.21 | N/A | N/A | 0.60 | 0.55 | N/A | 0.93 |
| Test 62 (08-07-2020) | 62 | 3 | 0.21 | N/A | N/A | 0.62 | 0.56 | N/A | 0.95 |
| Test 63 (08-07-2020) | 63 | 3 | 0.22 | N/A | N/A | 0.63 | 0.57 | N/A | 0.98 |
| Test 64 (08-07-2020) | 64 | 3 | 0.21 | N/A | N/A | 0.63 | 0.56 | N/A | 1.01 |
| Test 65 (08-07-2020) | 65 | 3 | 0.22 | N/A | N/A | 0.64 | 0.57 | N/A | 1.02 |
| Test 66 (08-07-2020) | 66 | 3 | 0.22 | N/A | N/A | 0.65 | 0.57 | N/A | 1.03 |
| Test 67 (08-07-2020) | 67 | 3 | 0.22 | N/A | N/A | 0.65 | 0.58 | N/A | 1.04 |
| Test 68 (09-07-2020) | 68 | 3 | N/A | 0.38 | N/A | 0.56 | N/A | 0.17 | 0.94 |
| Test 69 (09-07-2020) | 69 | 3 | N/A | 0.35 | N/A | 0.60 | N/A | 0.16 | 0.95 |
| Test 70 (09-07-2020) | 70 | 3 | N/A | 0.37 | N/A | 0.62 | N/A | 0.17 | 0.98 |
| Test 71 (09-07-2020) | 71 | 3 | N/A | 0.37 | N/A | 0.63 | N/A | 0.15 | 1.01 |
| Test 72 (09-07-2020) | 72 | 3 | N/A | 0.34 | N/A | 0.62 | N/A | 0.14 | 0.99 |
| Test 73 (09-07-2020) | 73 | 3 | N/A | 0.38 | N/A | 0.62 | N/A | 0.14 | 1.00 |
| Test 74 (09-07-2020) | 74 | 3 | N/A | 0.38 | N/A | 0.63 | N/A | 0.15 | 1.02 |
| Test 17 (23-06-2020) | 17 | 4 | N/A | 0.42 | N/A | 1.00 | 0.79 | 0.15 | 1.09 |
| Test 22 (26-06-2020) | 22 | 4 | N/A | 0.50 | N/A | 0.83 | 0.79 | 0.22 | 1.07 |
| Test 27 (26-06-2020) | 27 | 4 | N/A | 0.53 | N/A | 0.81 | 0.79 | 0.23 | 1.07 |
| Test 28 (26-06-2020) | 28 | 4 | N/A | 0.55 | N/A | 0.83 | 0.81 | 0.24 | 1.11 |
| Test 37 (02-07-2020) | 37 | 4 | 0.32 | 0.49 | N/A | 0.79 | 0.17 | N/A | 0.97 |
| Test 38 (02-07-2020) | 38 | 4 | 0.35 | 0.54 | N/A | 0.79 | 0.22 | N/A | 1.01 |
| Test 39 (02-07-2020) | 39 | 4 | 0.36 | 0.56 | N/A | 0.79 | 0.21 | N/A | 1.04 |
| Test 40 (02-07-2020) | 40 | 4 | 0.38 | 0.58 | N/A | 0.79 | 0.22 | N/A | 1.07 |
| Test 52 (03-07-2020) | 52 | 4 | 0.37 | 0.40 | N/A | 0.74 | N/A | 0.23 | 1.11 |
| Test 42 (02-07-2020) | 42 | 2 | 0.24 | 0.35 | N/A | 0.46 | 0.16 | N/A | 1.09 |
| Test 43 (02-07-2020) | 43 | 2 | 0.22 | 0.33 | N/A | 0.43 | 0.17 | N/A | 1.05 |
| Test 44 (02-07-2020) | 44 | 2 | 0.23 | 0.35 | N/A | 0.44 | 0.16 | N/A | 1.05 |
| Test 45 (02-07-2020) | 45 | 2 | 0.24 | 0.35 | N/A | 0.45 | 0.17 | N/A | 1.05 |
| Test 11 (22-06-2020) | 11 | 2 | N/A | 0.16 | N/A | 0.54 | 0.36 | 0.10 | 0.97 |
| Test 12 (22-06-2020) | 12 | 2 | N/A | 0.21 | N/A | 0.57 | 0.40 | 0.11 | 0.98 |

# D.2. Planes of best fit and extended validation plots

In figures D.7, D.8 and D.9 the planes of best fit for the test data from the 4s burns can be seen. It can be seen that less data points were used for these planes due to the fact that less 4s burns were performed during the study. It can also be seen that the planes show the same overall trends as the planes for the 3s burn cases.

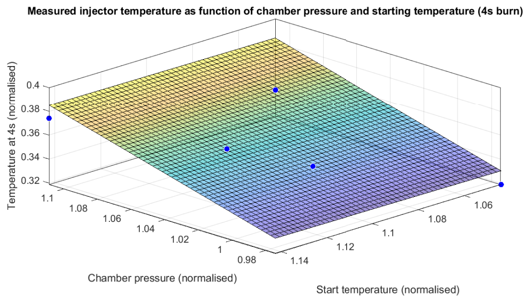


Figure D.7: Normalised temperatures after 4s as recorded at the injector for RT2 as function of chamber pressure and starting temperature.

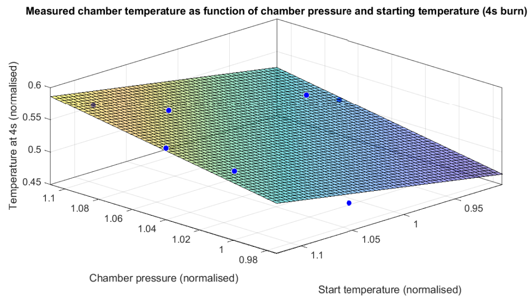


Figure D.8: Normalised temperatures after 4s as recorded at the chamber for RT2 as function of chamber pressure and starting temperature.

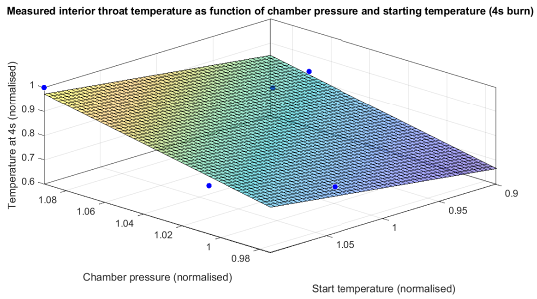


Figure D.9: Normalised temperatures after 4s as recorded at the interior throat for RT2 as function of chamber pressure and starting temperature.

.

In figures D.10-D.15 the errors as calculated by comparing the model results with the extrapolated test data can be seen. It can be seen that in general the predicted errors are still relatively small, except for the combustion chamber and for the nozzle exit. For the combustion chamber in particular a large error is predicted for the combination of a low chamber pressure and a low starting temperature.

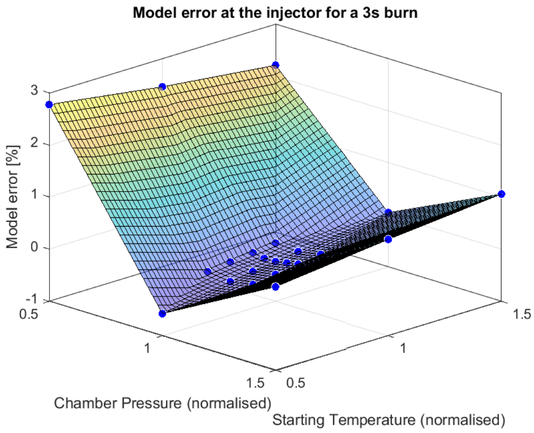


Figure D.10: Model error at the injector compared to test data as function of chamber pressure and starting temperature, extrapolated beyond the validity range based of the test data (NOTE: Starting temperature axis is inverted for readability)

.

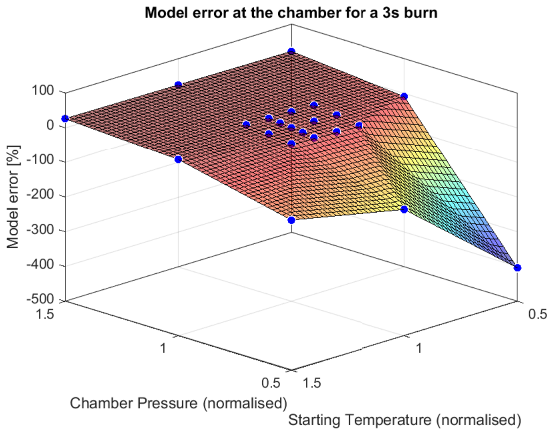


Figure D.11: Model error at the chamber compared to test data as function of chamber pressure and starting temperature, extrapolated beyond the validity range of the test data.

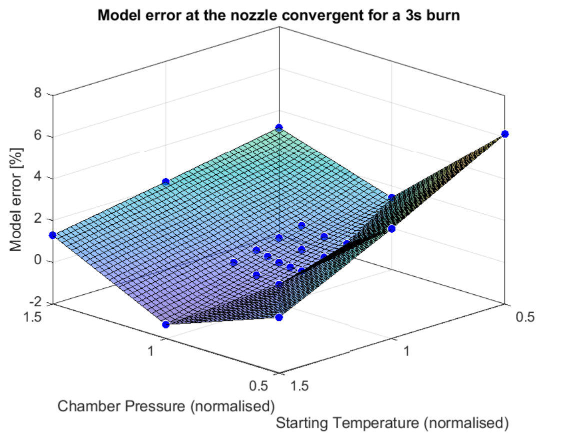


Figure D.12: Model error at the nozzle convergent compared to test data as function of chamber pressure and starting temperature, extrapolated beyond the validity range of the test data.

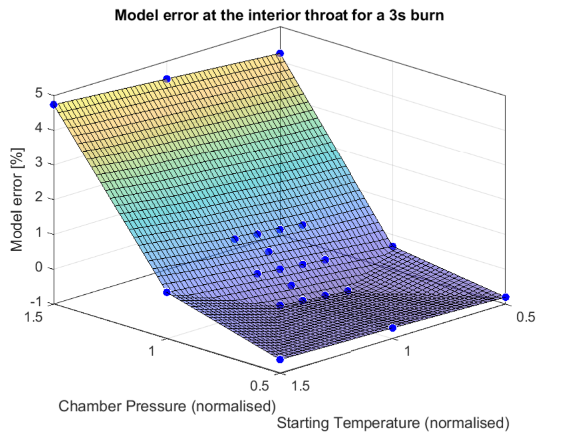


Figure D.13: Model error at the internal throat compared to test data as function of chamber pressure and starting temperature, extrapolated beyond the validity range of the test data.

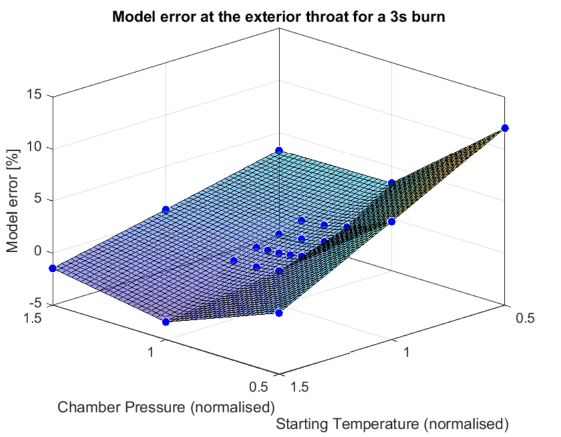


Figure D.14: Model error at the exterior throat compared to test data as function of chamber pressure and starting temperature, extrapolated beyond the validity range of the test data.

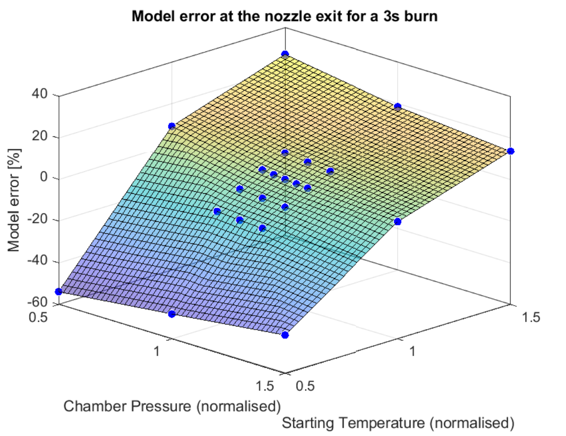


Figure D.15: Model error at the nozzle exit compared to test data as function of chamber pressure and starting temperature, extrapolated beyond the validity range of the test data (NOTE: Starting temperature axis is inverted for readability).

(This page was intentionally left blank)

# E

# Space Propulsion Conference 2020 abstract

The research conducted within this thesis study was summarised in a conference paper for the Space Propulsion Conference which was set to take place in October 2020.[1] The title of the conference paper is: "Investigation of Thermal Behaviour of Additively Manufactured Green Bi-Propellant Thrusters in CubeSat Applications Using Transient Thermal Modelling". The paper was submitted as part of the Spacecraft propulsion symposium in the category 'Flow and Systems Modelling'. On the 15th of April 2020 the abstract was accepted by the organisation. Below, the originally submitted extended abstract is reproduced.

#**00082**
**Investigation of Thermal Behaviour of Additively Manufactured Green Bi-Propellant Thrusters in CubeSat Applications Using Transient Thermal Modelling**
1. SPACECRAFT PROPULSION
1.15. Flow and Systems Modelling (all propulsion systems design and performance evaluation)

P.M. Van Den Berg[1], B.V.S. Jyoti[1], R.J.G. Hermsen[2].
[1]Delft University Of Technology - Delft (Netherlands), [2]Dawn Aerospace - Delfgauw (Netherlands)

**Introduction**

Dawn Aerospace has developed a 0.5 N additively manufactured green bi-propellant thruster called the PM200 for use in CubeSat applications [1]. Due to the high combustion temperatures associated with bi-propellants, the burn time of this thruster is currently limited to approximately 15 seconds after which cool down of the thruster is required. In recent years, CubeSat missions have however become increasingly complex and therefore the need has arisen to be able to perform longer duration burns. In order to achieve such longer burn times a cooling method has to be implemented in the PM200 system.

**Discussion**

Because the thermal behaviour of small scale propulsion systems is slightly different than that of their larger counterparts, the first step to implementing a cooling method in the PM200 is to gain insight in the thermal behaviour of the system. Therefore, a transient thermal model was developed which could be used to analyze the effectiveness and feasibility of several cooling methods in CubeSat scale propulsion systems by determining the wall temperature

[1]Due to the ongoing situation with COVID-19 the Space Propulsion Conference 2020 was delayed to February 2021. The paper is however still accepted.

distribution for a given cooling method. The developed model uses a finite volume method approach in combination with simpler semi-empirical relationships to reduce the computational time required. Besides studying the effectiveness of several cooling methods, the model was also used to analyze the performance of several construction materials by determining their respective heating rates. These heating rates could then be used to predict the failure point of the thruster. The model was verified by comparing it to simpler commercially available software and validated using data from over one-hundred static fire tests which were performed using the PM200 and several other thrusters developed by Dawn Aerospace. In this paper the numerical model will be presented and the model outcomes will be compared to test data from static fire tests. An example outcome of the model can be seen in Fig 1.

## Conclusion

It will be shown that the model predicts the thermal behaviour of the PM200 thruster and other small scale thrusters developed at Dawn Aerospace with an accuracy of within 15%. Furthermore, simulation results for a reference case will be presented.

## Bibliography

[1] J. Wink, T. Knop, S. Powell, R. Werner and S. Engelen, ”Development and Ground Testing of the PM200 Bi-Propellant Propulsion Module,” in 3AF Space Propulsion Conference, Seville, Spain, 2018.

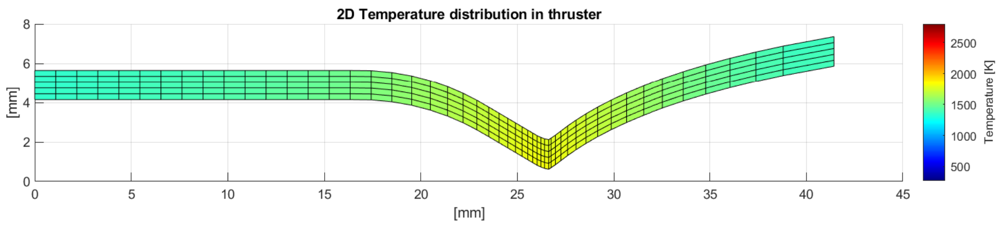


Fig 1: Example output for a 2D thruster cross section.